Structural and Thermodynamic Studies of Mixed Metal Halides for Ammonia Absorption Applications

Jonathan Betteridge

Jesus College



A thesis submitted for the degree of

Doctor of Philosophy

Inorganic Chemistry Laboratory, University of Oxford

June 2024

Contents

Abstract **xvi**

Acknowledgements **xviii**

Abbreviations **xxi**

1 Introduction **1**

1.1 The Climate Crisis 2

1.1.1 Energy Generation 4

1.1.2 Energy Storage Requirements 8

1.2 Chemical Energy Storage Methods 18

1.2.1 Batteries 18

1.2.2 Hydrogen 22

1.2.3 Synthetic Carbon Fuels 25

1.2.4 Ammonia 28

1.3 Thermal Energy Storage Methods 31

1.3.1 Sensible Heat Storage 32

1.3.2 Latent Heat Storage 33

1.3.3 Thermochemical Energy Storage 34

1.4 Ammonia Sorption 36

1.4.1 Ammonia Separation 36
1.4.2 Ammonia Storage 37
1.4.3 Thermal Applications 39

2 Ammonia Sorbents **42**

2.1 Deep Eutectic Solvents and Ionic Liquids 42
2.2 Metal Organic Frameworks 48
2.3 Metal Borohydrides 51
2.4 Metal Halides 53
2.5 Material Reasoning 60
2.6 Thesis Aims 61

3 Experimental Methods **62**

3.1 Solid State Synthetic Techniques 63
3.1.1 Tube Furnace 63
3.1.2 Ball Milling 64
3.2 Solid-Gas Reactions and Analysis 65
3.2.1 Gas Flow Setup 65
3.2.2 Simultaneous Thermal Analysis 67
3.3 Material Syntheses 70
3.4 Temperature Cycling Experiments 72
3.5 Structural Analysis - Diffraction 73
3.5.1 X-ray Diffraction 73
3.5.2 Neutron Diffraction 82
3.5.3 Rietveld Analysis 88
3.6 Computational Chemistry 91
3.6.1 Density Functional Theory 91
3.6.2 CASTEP 94
3.6.3 Madelung Energy 98

4 Ammonia Absorption of $CaCl_2$ and CaBr2 **101**

4.1 Structural Analysis of Phases Involved in Ammonia Absorption . . . 102

4.1.1 Anhydrous Phases . . . 102

4.1.2 Ammonia Absorption . . . 105

4.1.3 $CaCl_2$ and $CaBr_2$ Mono-ammoniates . . . 107

4.1.4 $CaCl_2$ and $CaBr_2$ Di-ammoniates . . . 124

4.1.5 $CaCl_2$ Tetra-ammoniate . . . 145

4.1.6 $CaBr_2$ Hexa-ammoniate . . . 153

4.1.7 $CaCl_2$ and $CaBr_2$ Octa-ammoniates . . . 161

4.2 Ammonia Absorption Pathways and Energetics . . . 167

4.3 *In-Situ* Powder Neutron Diffraction . . . 183

4.3.1 $CaCl_2$ . . . 183

4.3.2 $CaBr_2$ . . . 188

4.4 Conclusions and Future Work . . . 192

5 Ammonia Absorption of $CaCl_xBr_{2-x}$ Solid Solutions **194**

5.1 Stability of Solid Solution Phases . . . 195

5.2 Interactions of $CaCl_xBr_{2-x}$ Solid Solutions with NH_3 . . . 203

5.3 *In-Situ* Powder Neutron Diffraction . . . 221

5.4 Conclusions and Future Work . . . 233

6 Eutectic Mixtures **235**

6.1 Thermodynamics of Molten Salt Ammonia Absorption . . . 238

6.2 Ammonia Absorption into Molten Salt Mixtures . . . 242

6.2.1 Pure Salt Ammonia Absorption . . . 244

6.2.2 Mixed Molten Salts Containing Zinc Chloride . . . 249

6.2.3 Pressure Swing Absorption . . . 252

6.2.4 Mixed Molten Salts Without Zinc Chloride . . . 263

6.3 Conclusions and Future Work . . . 268

7 Periodic Trends in Ammoniate Formation of Metal Halides 270

7.1 Scope of the Work 271

7.2 Trends in Ammoniate Stability Within Metal Groups 274

7.2.1 Group I 274

7.2.2 Group II/XII 276

7.2.3 Group III/XIII 281

7.2.4 Group IV 283

7.3 Trends in Ammoniate Stability Within Periods 285

7.4 Conclusions and Future Work 292

8 Conclusion 294

Bibliography 298

Appendix A 310

Appendix B 322

Appendix C 329

Appendix D 351

List of Figures

1.1 Mean Wind Speed by Location 3
1.2 Solar PV Potential by Location 4
1.3 Price of Solar Power by Year 5
1.4 Average Monthly Variation in Electricity Generation of Solar and Wind Power 9
1.5 Average Hourly Variation in Electricity Generation of Solar and Wind Power 9
1.6 Monthly Variation in Electricity Generation of Solar and Wind Power 10
1.7 Possible Renewable Energy Supply between Europe, the Middle East and North Africa 11
1.8 Breakdown of Energy Consumption by Sector 13
1.9 Breakdown of Energy Source for the Transport Sector 14
1.10 Breakdown of Carbon Emissions by Mode of Transport 15
1.11 Breakdown of Domestic Energy Consumption 17
1.12 Energy Density of Different Energy Stores 24
1.13 Hydrogen Capacities and Release Temperatures of Different Hydrogen Storage Methods. 24
1.14 Efficiency Losses of Power to Methane/Methanol Systems 27
1.15 Heat Loss from a Domestic Heat Storage System 33

1.16 Vapour Pressure of Liquid NH_3 and an Ammonia Sorbent 38

2.1 Imidazolium Cations in ILs 43
2.2 Pressure-Composition Isotherms for ILs 44
2.3 Ammonia Absorption for various MILs 45
2.4 Ammonia Absorption for various Metal-containing DESs 47
2.5 Structural Change on Ammonia Absorption in M(BDC) MOFs 49
2.6 NH_3 Absorption in MFM-300(V^{IV}) 50
2.7 NH_3 Absorption in Cu(cyhdc) 51
2.8 Decomposition Temperatures of Various Metal Borohydride Ammoniates 52
2.9 TGA/MS of $CaBH_4(NH_3)_4$ 53
2.10 TPD of $MgX_2(NH_3)_6$ 56
2.11 Crystal Structures of $MgCl_2(NH_3)_n$ 57
2.12 Pressure-Composition Isotherms for Ammonia-CaX_2 Systems 57
2.13 Ammonia Storage Capacity of $CaCl_{2-x}Br_x$ Samples 59

3.1 Tube Furnace Schematic 63
3.2 Atmospheric Pressure Gas Rig Setup 66
3.3 Elevated Pressure Gas Rig Setup 67
3.4 STA Setup 69
3.5 X-ray Scattering from One, Two and Four Isolated Electrons 74
3.6 The POLARIS Chopper and Detector Setup 85
3.7 The Sample Cell used on POLARIS 87
3.8 **k**-point Convergence Testing in CASTEP 96
3.9 Geometry Optimisation Process in CASTEP 97
3.10 Conditional Convergence of a Madelung Constant 99
3.11 Comparison of Experimental Lattice Enthalpies and Theoretical Madelung Energies 100

4.1 $CaCl_2$ Crystal Structures . . . 102
4.2 PXRD Pattern of $CaCl_2$ . . . 103
4.3 CaI_2 Crystal Structure . . . 104
4.4 Ammonia Desorption Pathways for $CaCl_2$ and $CaBr_2$ . . . 106
4.5 Ammonia's Trigonal Pyramidal Geometry . . . 109
4.6 Definition of 'Equivalent' Deuterium Sites in the Mono-ammoniate Structure . . . 111
4.7 $CaX_2(NH_3)$ Structure . . . 117
4.8 PND Pattern of $CaBr_2(ND_3)$ . . . 118
4.9 PND Pattern of $CaCl_2(ND_3)$ . . . 119
4.10 PXRD Pattern of $CaBr_2(NH_3)$ . . . 120
4.11 Hydrogen Bonding Motif of the Mono-ammoniate . . . 121
4.12 Deuterium Site Occupancies in the Mono-ammoniate Structure . . . 122
4.13 Goodness-of-fit Results for Mono-ammoniate Stacking Fault Model . 123
4.14 Mono-ammoniate PXRD Pattern Fitted to Stacking Fault Model . . 123
4.15 Reported Crystal Structure of $CaCl_2(NH_3)_2$ . . . 124
4.16 I11 PXRD of $CaCl_2(NH_3)_2$ . . . 125
4.17 POLARIS PND Pattern of $CaCl_2(ND_3)_2$ . . . 127
4.18 *Cmmm* Structure of $CaCl_2(ND_3)_2$ . . . 127
4.19 PXRD Pattern of $CaBr_2(NH_3)_2$ . . . 129
4.20 PND Pattern of $CaBr_2(ND_3)_2$ . . . 130
4.21 *Cmce* Structure of $CaBr_2(ND_3)_2$ . . . 130
4.22 Hydrogen Bonding in $CaCl_2(NH_3)_2$ Phases . . . 133
4.23 Hydrogen Bonding in $CaBr_2(NH_3)_2$ Phases . . . 134
4.24 Structure of Hydrogen Bonding in Di-ammoniate Phases . . . 135
4.25 Interlayer Anion Distances in Di-ammoniate Phases . . . 136
4.26 Depiction of 'Between-Layer' and 'In-Layer' Hydrogen Bonding in the *Cmce* Di-ammoniate Phase . . . 137

4.27 Rotational Energy Changes in the *Cmmm* Di-ammoniate Structure. . 137
4.28 Structure of Energy Minima of an Ammonia Molecule Rotating in the *Cmmm* Di-ammoniate Phase 139
4.29 Structure of Energy Maxima of an Ammonia Molecule Rotating in the *Cmmm* Di-ammoniate Phase 140
4.30 Rotational Energy Changes in the *Cmce* Di-ammoniate Structure. . . 141
4.31 Deuterium Site Occupancies in the *Cmce* Di-ammoniate Structure . . 144
4.32 AA Stacked $CaCl_2(ND_3)_4$ PND Data 146
4.33 AB Stacked $CaCl_2(ND_3)_4$ PND Data 147
4.34 AA Stacked $CaCl_2(ND_3)_4$ Structure 147
4.35 AB Stacked $CaCl_2(ND_3)_4$ Structure 149
4.36 CASTEP Geometry Optimised AA Stacked $CaCl_2(NH_3)_4$ Structure . 151
4.37 CASTEP Geometry Optimised AB Stacked $CaCl_2(NH_3)_4$ Structure . 152
4.38 Crystal Structure of $CaI_2(NH_3)_6$ 153
4.39 PND Pattern of $CaBr_2(ND_3)_6$ 154
4.40 Hydrogen Bonding in $CaX_2(NH_3)_6$ 156
4.41 The 'Ammonia Cube' in the $CaX_2(NH_3)_6$ Structure 157
4.42 Energies of Hydrogen-Bonded $CaX_2(NH_3)_6$ Motifs 157
4.43 Energy and Hydrogen Bond Variance in $CaX_2(NH_3)_6$ Structures . . . 159
4.44 Relationship between Ca-X Distance and Hydrogen Bonding between $Ca(NH_3)_6{}^{2+}$ Octahedra and X^- in $CaX_2(NH_3)_6$ Motifs 160
4.45 Relationship between Energy and Halide Movement in the $CaX_2(NH_3)_6$ Motifs 160
4.46 $CaX_2(NH_3)_8$ Crystal Structure 162
4.47 POLARIS PND Pattern of $CaBr_2(ND_3)_8$ 163
4.48 POLARIS PND Pattern of a Mixture of $CaCl_2(ND_3)_8$ and $CaCl_2(ND_3)_4$ 163
4.49 $CaX_2(NH_3)_8$ Hydrogen Bonding 164
4.50 STA of $CaCl_2$ Ammonia Cycling at Various Pressures 168

4.51 STA of $CaCl_2$ Ammonia Cycling at Various Pressures 169
4.52 STA of $CaBr_2$ Ammonia Cycling at Various Pressures 171
4.53 STA of $CaBr_2$ Ammonia Cycling at Various Pressures 172
4.54 4.5 bar NH_3 Desorption Cycle from $CaBr_2$ 173
4.55 Integration of the Extra Peak in the 4.5 bar NH_3 Desorption Cycle of $CaBr_2$ 174
4.56 Clausius-Clapeyron Fits for CaX_2 Ammoniates 176
4.57 CaX_2 Ammoniate Coexistence Curves 176
4.58 CASTEP Calculated Energies for CaX_2 Ammoniates 181
4.59 Madelung Energies for CaX_2 Ammoniates 181
4.60 Contour Plot of PND data for $CaCl_2$. 184
4.61 Mole Percent of Phases in $CaCl_2$ PND Data 185
4.62 Mole Percent of Phases in $CaCl_2$ PND Data During Temperature Ramp 186
4.63 Contour Plot of PND data for $CaBr_2$ 189
4.64 Mole Percent of Phases in $CaBr_2$ PND Data 190
4.65 Mole Percent of Phases in $CaBr_2$ PND Data During Temperature Ramp 191

5.1 CASTEP Calculated Energies of $CaCl_xBr_{2-x}$ Cells 195
5.2 CASTEP Calculated Energies of $CaCl_xBr_{2-x}$ Cells Plotted Against Bond Length Deviations 197
5.3 CASTEP Calculated Energies of $CaCl_xBr_{2-x}(NH_3)_n$ Cells 198
5.4 CASTEP Calculated Energies of $CaCl_xBr_{2-x}(NH_3)_n$ Cells Plotted Against Bond Length Deviations 199
5.5 PXRD Patterns of $CaCl_xBr_{2-x}$ Syntheses 200
5.6 Lattice Parameters of $CaCl_xBr_{2-x}$ Phases 201
5.7 PXRD Patterns of $CaCl_{0.4}Br_{1.6}$ and $CaCl_{0.2}Br_{1.8}$ 202

5.8 Onset and Peak Desorption Temperatures for Di-ammoniate and Mono-ammoniate Desorptions 205
5.9 PXRD Patterns of $CaCl_xBr_{2-x}$ Samples after Exposure to Ammonia . 206
5.10 PXRD Patterns of $CaCl_xBr_{2-x}$ Samples after Exposure to Ammonia . 207
5.11 Volumes of $CaX_2(NH_3)_2$ Cells in Rietveld Analyses 210
5.12 STA of CaClBr Ammonia Cycling at Various Pressures 211
5.13 STA of CaClBr Ammonia Cycling at Various Pressures 212
5.14 Peak Fitting for the $2 \rightarrow 1$ Desorption in the CaClBr STA 214
5.15 STA of $CaCl_{0.4}Br_{1.6}$ Ammonia Desorption 216
5.16 STA of $CaCl_{0.8}Br_{1.2}$ Ammonia Desorption 217
5.17 STA of $CaCl_{1.2}Br_{0.8}$ Ammonia Desorption 218
5.18 STA of $CaCl_{1.6}Br_{0.4}$ Ammonia Desorption 219
5.19 Ammonia Desorption STAs of $x = 0.4$, 0.8, 1.2 and 1.6 Samples . . . 220
5.20 Contour Plot of PND data for CaClBr from POLARIS 222
5.21 Mole Percent of Phases in CaClBr PND Data 223
5.22 Mole Percent of Phases in CaClBr PND Data During the First Temperature Ramp 224
5.23 Mole Percent of Phases in CaClBr PND Data During the Second Temperature Ramp 225
5.24 Expansion of the CaClBr Mono-ammoniate During Di-ammoniate Desorption 227
5.25 Expansion of the CaClBr Hexa-ammoniate During Desorption 231
5.26 PND Data of $CaClBr(ND_3)_8$ 232
5.27 PND Data of $CaClBr(ND_3)$ 232

6.1 Suggested Ammonia Separation Procedure using Solid Sorbents . . . 236
6.2 Suggested Ammonia Separation Procedure using Liquid Sorbents . . 237
6.3 Hess Cycle of Absorption into a Molten Metal Halide Salt 238
6.4 Colour Map of $T_{\mathrm{des,\,1}}$. 241

6.5 $ZnCl_2$ Ammonia Desorption 245
6.6 $MnCl_2$ Ammonia Desorption 248
6.7 NH_3 Absorption Capacity of Molten Salt Samples from 250–300 °C . . 250
6.8 NH_3 Absorption Capacity at 300 °C for Different Zn Mole Percentages in $ZnCl_2$: NaCl + KCl Melts 252
6.9 300 °C PSA Experiment for a $MnCl_2$ Sample 254
6.10 300 °C PSA Experiment for 60:40 Zn : Na Chloride Sample 255
6.11 300 °C PSA Experiment for 60:40 Zn : K Chloride Sample 256
6.12 300 °C PSA Experiment for 60:20:20 Zn : Na : K Chloride Sample . . . 257
6.13 300 °C PSA Experiment for 70:15:15 Zn : Na : K Chloride Sample . . . 258
6.14 300 °C PSA Experiment for 80:10:10 Zn : Na : K Chloride Sample . . . 259
6.15 300 °C PSA Experiment for a $ZnCl_2$ Sample 260
6.16 Melting Point Test for 40:40:10:10 Mn : Ca : Na : K Chloride Sample . 264
6.17 PSA Cycling Data for 40:40:10:10 Mn : Ca : Na : K Chloride Sample . . 265
6.18 PSA Cycling at 400 °C for the 40:40:10:10 Mn : Ca : Na : K Chloride Sample 266
6.19 PSA Cycling at 400 °C for a $MnCl_2$ Sample 267

7.1 Absorption Enthalpies of Group I Metal Halides 275
7.2 Absorption Enthalpies of Group II/XII Metal Halides (Be, Mg, Zn) . 277
7.3 Absorption Enthalpies of Group II Metal Halides (Ca, Sr, Ba) 279
7.4 Absorption Enthalpies of Group III/XIII Metal Halides (Al, Sc, Y, Lu) 282
7.5 Absorption Enthalpies of Group IV Metal Halides (Ti, Zr, Hf) 284
7.6 Absorption Enthalpies of Period 3 Metal Halides (Na, Mg, Al) 286
7.7 Absorption Enthalpies of Period 4 Metal Halides (Ca, Sc, Ti) 289

A.1 Definition of 'Equivalent' Deuterium Sites in the Cmmm Di-ammoniate Structure 311

A.2 Definition of 'Equivalent' Deuterium Sites in the Cmce Di-ammoniate Structure . . . 312
A.3 Definition of 'Equivalent' Deuterium Sites in the Tetra-ammoniate Structure . . . 313
A.4 Definition of 'Equivalent' Deuterium Sites in the Hexa-ammoniate Structure . . . 314
A.5 Definition of 'Equivalent' Deuterium Sites in the Octa-ammoniate Structure . . . 315
A.6 Variable Pressure Desorption Cycles for $CaCl_2$ . . . 318
A.7 Variable Pressure Desorption Cycles for $CaBr_2$ . . . 319
A.8 Weight Percent of Phases in $CaCl_2$ PND Data . . . 320
A.9 Weight Percent of Phases in $CaBr_2$ PND Data . . . 321

B.1 Gas Outflow during Temperature Cycling of $x = 0$ Sample . . . 322
B.2 Gas Outflow during Temperature Cycling of $x = 0.2$ Sample . . . 323
B.3 Gas Outflow during Temperature Cycling of $x = 0.4$ Sample . . . 323
B.4 Gas Outflow during Temperature Cycling of $x = 0.6$ Sample . . . 324
B.5 Gas Outflow during Temperature Cycling of $x = 0.8$ Sample . . . 324
B.6 Gas Outflow during Temperature Cycling of $x = 1$ Sample . . . 325
B.7 Gas Outflow during Temperature Cycling of $x = 1.2$ Sample . . . 325
B.8 Gas Outflow during Temperature Cycling of $x = 1.4$ Sample . . . 326
B.9 Gas Outflow during Temperature Cycling of $x = 1.6$ Sample . . . 326
B.10 Gas Outflow during Temperature Cycling of $x = 1.8$ Sample . . . 327
B.11 Gas Outflow during Temperature Cycling of $x = 2$ Sample . . . 327
B.12 Weight Percent of Phases in CaClBr PND Data . . . 328

C.1 Colour Map of $T_{\mathrm{des,\,1}}$. . . . 330
C.2 Colour Map of $T_{\mathrm{des,\,1}}$. . . . 331
C.3 $ZnCl_2$ Ammonia Absorption . . . 332

C.4 $MnCl_2$ Ammonia Absorption 333
C.5 NaCl Ammonia Absorption 334
C.6 KCl Ammonia Absorption 335
C.7 60:40 Zn : Na Chloride Melting Point 336
C.8 60:40 Zn : K Chloride Melting Point 336
C.9 60:20:20 Zn : Na : K Chloride Melting Point 337
C.10 70:15:15 Zn : Na : K Chloride Melting Point 337
C.11 80:10:10 Zn : Na : K Chloride Melting Point 338
C.12 Zinc Chloride Melting Point 338
C.13 NH_3 Absorption as a Function of Temperature for the 60:40 Zn : Na Chloride Sample 339
C.14 NH_3 Absorption as a Function of Temperature for the 60:40 Zn : K Chloride Sample 340
C.15 NH_3 Absorption as a Function of Temperature for the 60:20:20 Zn : Na : K Chloride Sample 341
C.16 NH_3 Absorption as a Function of Temperature for the 70:15:15 Zn : Na : K Chloride Sample 342
C.17 NH_3 Absorption as a Function of Temperature for the 80:10:10 Zn : Na : K Chloride Sample 343
C.18 PSA Cycling Data for 60:40 Zn : Na Chloride 344
C.19 PSA Cycling Data for 60:40 Zn : K Chloride 345
C.20 PSA Cycling Data for 60:20:20 Zn : Na : K Chloride 346
C.21 PSA Cycling Data for 70:15:15 Zn : Na : K Chloride 347
C.22 PSA Cycling Data for 80:10:10 Zn : Na : K Chloride 348
C.23 PSA Cycling Data for $ZnCl_2$ 349
C.24 PSA Cycling Data for $MnCl_2$ 350

List of Tables

1.1 Comparison of Hydrogen Production Methods 23

2.1 Ammoniation Numbers of Various Group II Metal Halides 55

3.1 Starting Materials Used in Syntheses 70
3.2 Lattice Systems and Bravais Lattices 77
3.3 Neutron Scattering Cross Sections of Relevant Nuclei 82

4.1 Relative Energies of CaX_2 Structures 104
4.2 Output Data from Refinement of the Mono-ammoniate Structure . . 112
4.3 Computationally Calculated Energies of Mono-ammoniate Structures 114
4.4 Output Data from PND Refinement of $CaCl_2(ND_3)_2$ 128
4.5 Output Data from PND Refinement of $CaBr_2(ND_3)_2$ 131
4.6 Madelung Energies of Di-ammoniate Structures 132
4.7 Ca-X-Ca Angle in $CaX_2(NH_3)_2$ Phases 135
4.8 Output Data from PND Refinement of $CaCl_2(ND_3)_4$ Structures . . . 148
4.9 Data from CASTEP Geometry Optimisations of Different $CaCl_2(NH_3)_4$ Structures 148
4.10 Output Data from PND Refinement of $CaBr_2(ND_3)_6$ 154
4.11 Output Data from PND Refinements of $CaX_2(ND_3)_8$ 165
4.12 Ammonia Sorption Enthalpies for CaX_2 Ammoniate Phases 177

4.13 Literature Values of Ammonia Sorption Enthalpies for CaX_2 Ammoniate Phases . . . 177
4.14 CASTEP Calculated Enthalpy Changes for CaX_2 . . . 178
4.15 $CaCl_2(NH_3)_n$ Desorption Onset Temperatures from PND Data . . . 187
4.16 $CaBr_2(NH_3)_n$ Desorption Onset Temperatures from PND Data . . . 191

5.1 $CaClBr(NH_3)_n$ Desorption Onset Temperatures from PND Data . . . 229

6.1 Information on Metal Chlorides Considered for Inclusion in Eutectic Mixtures . . . 243
6.2 Liquidus Temperatures of Zinc-Containing Eutectic Samples . . . 249
6.3 Output Data from PSA Experiments at 300 °C . . . 262

7.1 Formation Enthalpies of Zinc Halide Ammoniates . . . 278
7.2 Selected Formation Enthalpies of CaX_2, SrX_2 and BaX_2 . . . 280
7.3 Ammoniation Numbers of Various Group II Metal Halides . . . 280
7.4 Scaled Madelung Energy for Various Salts . . . 288
7.5 Formation Enthalpies of Selected Group II and III Metal Halide Ammoniates . . . 291

A.1 Hydrogen Bonds in $CaCl_2(NH_3)_2$ Phases . . . 316
A.2 Hydrogen Bonds in $CaBr_2(NH_3)_2$ Phases . . . 317

D.1 Ammoniate Structures Used for Each Group I Cation-Anion Pair . . . 351
D.2 Ammoniate Structures Used for Each Group II/XII Cation-Anion Pair . . . 352
D.3 Ammoniate Structures Used for Each Group III/XIII Cation-Anion Pair . . . 353
D.4 Ammoniate Structures Used for Each Group IV Cation-Anion Pair . 354

Abstract

This thesis examines the interactions of ammonia with pure and mixed metal halides. Through detailed crystallographic and structural analysis, alongside DFT calculations, these interactions are studied in detail.

Calcium halides have been explored previously as ammonia absorption materials due to their large gravimetric and volumetric ammonia absorption densities, and the high abundance of calcium within the Earth's crust. Within this work, the thermodynamics and structural chemistry of calcium chloride and calcium bromide ammoniates is studied comprehensively. While the decomposition temperatures of ammoniate phases are primarily controlled by anionic size, it was shown that this relationship breaks down for the octa-ammoniate phase due to the expansion of the coordination environment.

Solid solutions of calcium chloride-bromide were examined also, with a focus on the possibility of controlling ammoniate phase equilibria through a change in the composition of the material. Through a combination of STA and *in-situ* PND, this was shown to be possible for the mono-ammoniate phase. However, much more complicated ammoniation pathways occur for higher ammoniate phases due to halide separation. With the aid of DFT calculations, this was shown to be the result of differing structural preferences for chloride and bromide ions, as opposed to direct issues with the mixing of halides.

Eutectic mixtures of metal halides were also investigated for the application of high temperature ammonia purification, through the use of STA. The addition of zinc chloride permitted a low liquidus temperature, enabling the application of these liquid sorbents at ∼300 °C. However, it was observed that greater temperatures would lead to significant evaporation of the sample. The removal of zinc chloride increased the liquidus temperature significantly, while limiting the evaporation rate from the sample. In essence, this shifts the operational temperature range, possibly enabling ammonia absorption *in situ* from the Haber-Bosch process. With further research, this may replace the need for gas recycling in Haber-Bosch with sorbent recycling.

Through DFT calculations in CASTEP, a systematic survey of the thermodynamics of ammoniate formation in metal halides across the periodic table was undertaken. Rationalisation of trends across periods and down groups explained why certain phases are unstable for certain combinations of metal and halide. Alongside this, it was shown that the enthalpy of absorption is significantly increased for higher charge metal halides due to a combination of M-N bonding, the reduced loss of Madelung energy upon absorption, and hydrogen bonding.

The crystallographic, structural and thermodynamic analyses undertaken in this thesis provide a detailed understanding of the driving forces of ammoniate phase formation in pure and mixed metal halides. This understanding is taken forward into the study of specific materials, namely calcium halide ammoniates, and eutectic mixtures for high temperature ammonia separation.

Acknowledgements

We always have the opportunity to appreciate those around us, that make us who we are, yet we rarely take it. People come and go in life for a myriad of reasons. This is not a sad fact. I feel lucky to be able to put my feelings into words, immortalising these people in my eyes. Thank you to all who made me who I am today. The list is far longer than those who are mentioned by name.

Prior to joining Bill David's group as a Part II, I had not even considered a DPhil. Bill's passion for research, and the trust and independence placed on me to make my Part II project my own was a large part of the reason I applied to continue as a member of his group. He has been an inspiration and a constant source of support throughout my DPhil. For all this, I cannot thank him enough.

Thanks must also go to Josh Makepeace, who had a large part in making my Part II year so enjoyable. The early years of my DPhil would not have looked the same had I not been able to follow the example set by Jake Brittain. He was always willing to help, and this had a big hand as I settled into DPhil life.

While meetings with my second supervisor, Simon Clarke, were few and far between, these always provided a great opportunity to step back from my project and look at the bigger picture. I gained much more from our short meetings than he probably realises.

I would like to thank all of the David group. This DPhil thesis would not exist without you. In particular though, thanks must go to Tom Wood and Matt Cummings. At times in COVID, Matt would be the only person I would speak to in person outside of my household. Seeing Matt in the lab three times a week in December 2020–March 2021 might have been the only thing keeping me in the DPhil. Though he might claim not to like helping people (me), Matt will always be the first into the lab to help solve an issue with the gas rigs.

I've been deliberating for a while about how to thank Tom. Tom had such a big hand in the early stages of my project, though thanking him exclusively for work aspects would never feel right. He's one of few people I could listen to for hours. Your discussions of algorithms, maths, computation and everything keep me enthralled for days. I may not be able to remember what the largest n-dimensional sphere that can fit into a n-dimensional cube is, but I know who to ask to find out.

Great thanks must also go to James Taylor, the lab manager. You were always happy to receive questions about what might be possible with the lab equipment, accommodating my needs where you could. Thank you to Ron Smith, Chris Goodway, Adam Sears and Paul McIntyre for their help with running a smooth POLARIS experiment. Thank you also to Zoë, Emma and Matt, for their dutiful monitoring of the beamline during my POLARIS experiment.

I must also thank everyone at Sunborne Systems Ltd. I thoroughly enjoyed my two months there, and learnt so much about the life of research beyond the laboratory scale.

So many friends, old and new, have contributed to my education and my life. It's not possible to name them all, but thank you. Special thanks must go to Oli Whitaker. Living together throughout the DPhil, it is hard to explain how much you supported me. From barely watching Below Deck every night, to discussing our projects every day, thank you.

For my family, the words I wrote in my Part II thesis still feel apt. Without your push to believe in myself, I would never have applied to Oxford. Everything I have written above and below would not have happened were it not for the support you've given me.

The love from Meg has been a huge part of getting me to where I am today. Despite the long distance, you have supported me better than anyone. I cannot thank you enough for the patience you have shown during the tougher times of my DPhil. I hope I can do the same as you progress through your PhD.

These people and many more have contributed as much to this thesis as I ever could.

Abbreviations

BEV	battery electric vehicle
CASTEP	CAmbridge Serial Total Energy Package
CCP	cubic close packing
CNG	compressed natural gas
DES	deep eutectic solvent
DFT	density functional theory
DSC	differential scanning calorimetry
FCV	fuel cell vehicle
FWHM	full width half maximum
GCF	gas conversion factor
HCP	hexagonal close packing
HFCV	hydrogen fuel cell vehicle
ICE	internal combustion engine
ICSD	Inorganic Crystal Structure Database
IEA	International Energy Agency
IL	ionic liquid
LHS	latent heat storage
LUMO	lowest unoccupied molecular orbital
MFC	mass flow controller
MFM	mass flow meter
MOF	metal-organic framework
MS	mass spectrometry

NMR	nuclear magnetic resonance
OECD	Organisation for Economic Co-operation and Development
OPEC	Organisation of Petroleum Exporting Countries
PEM	polymer electrolyte membrane
ppm	part(s) per million
PSA	pressure swing absorption
PSD	position sensitive detector
PV	photovoltaic
SAF	sustainable aviation fuel
sccm	standard cubic centimetres per minute
SCR	selective catalytic reduction
SHS	sensible heat storage
SMR	small modular reactor
SRM	steam reforming of methane
STA	simultaneous thermal analysis
TCS	thermochemical energy storage
TGA	thermogravimetric analysis
TPD	temperature programmed desorption
λ	wavelength
PND	powder neutron diffraction
PXRD	powder X-ray diffraction

1 Introduction

Rapid, global implementation of renewable energy generation, storage and transportation technologies must be achieved in order to avoid the worst effects of climate change. While the importance of achieving this aim is undeniable, it does bring a host of challenges. Fossil fuels have been used historically due to their high energy density, ease of combustion and responsiveness to demand. Renewable energy generation technologies tend to have higher setup costs, spatial footprints and problems with intermittency. As such, green energy storage technologies are essential to balancing out the supply and demand mismatch of the energy grid. Importantly also, many renewable energy generation methods are location dependent and are, due to their low power density[1], unsuitable for mobile energy generation (e.g. land, air or sea travel), hence the importance of energy storage in mobile applications.

While various energy storage methods are burgeoning, storage systems involving ammonia offer several advantages including a high energy density, an established production and distribution network, and, in certain applications, the possibility of retrofitting internal combustion engines.

This thesis explores the structural and thermodynamic properties of various metal halide-based solid ammonia sorbents, and mixtures thereof, with a view to the applications of these materials. The mixing and formation of solid solutions of these materials may allow for new and/or tuneable properties based on the composition of the mixture/solid solution. Detailed structural chemistry, accompanied by DFT calculations, is used to examine the driving forces and bonding interactions in these materials, and to explain trends in ammoniate formation across the range of metal halides.

1.1 The Climate Crisis

The Climate Crisis is one of the gravest threats to human civilisation in the 21st century. The Paris Agreement, signed by 175 nations in 2015, legally binds countries to limit global warming to well below 2 °C above pre-industrial levels, while reaching net-zero carbon emissions by 2050. The Paris Agreement also stipulates that further efforts must be made to limit warming to 1.5 °C[2]. Despite this, global greenhouse gas emissions are still rising[3], and as of October 2022, the United Nations Environment Programme has stated there is no 'credible pathway' to limit warming to 1.5 °C[4]. However, every inch of warming is crucial, and drastic reductions in carbon emissions must still be made rapidly. Between 2030 and 2050, climate change is estimated to cause 250,000 additional deaths per year according to the World Health Organisation[5], with the effects of climate change to worsen throughout the 21st century. These estimates will only rise as cumulative greenhouse gas emissions climb and the degree of warming increases.

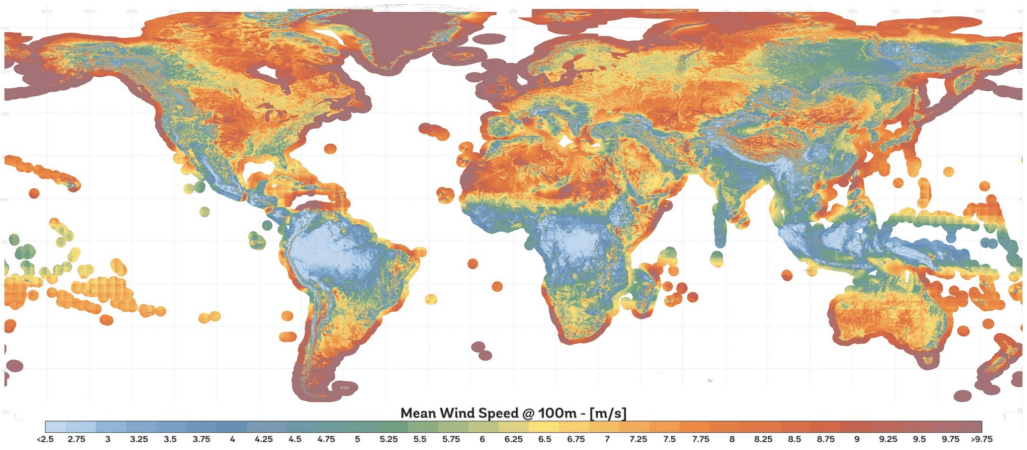


Figure 1.1: Mean wind speed measured 100 m above surface level by location. White areas are those not measured. Wind speed is typically higher in coastal areas and deserts. Image provided by GlobalWindAtlas.info[6]

The climate crisis is a global problem, requiring global solutions. However, it will undoubtedly hit countries in the 'poor global south' the hardest; countries in regions like Africa and Asia[7]. Coupled with the greater historic carbon emissions per capita in 'rich global north' countries[8], it is crucial that global north countries, with their greater fiscal power, enable poorer countries to transition, with a corresponding democratisation of energy production. Fortunately, areas more susceptible to the effects of climate change often have the greatest capacity for renewable energy generation (see Figures 1.1 and 1.2). This drastically changes the geopolitics of energy generation, with a move away from OPEC and towards countries with high renewable energy generation potential, such as in North Africa. If done fairly, the global energy transition can also be an opportunity to greatly improve the living standards of global south populations by becoming exporters of green energy. However, for global trade of renewable energy to occur, green energy storage and transportation methods must be developed.

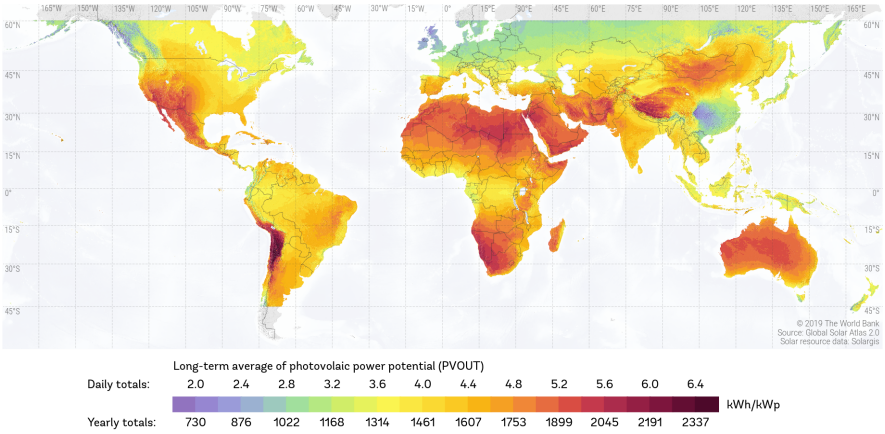


Figure 1.2: Solar photovoltaic potential by location. Solar potential is significantly greater near equatorial regions. Image provided by GlobalSolarAtlas.info [9]

1.1.1 Energy Generation

The retirement of fossil fuels and scale-up of renewable energy technologies requires various barriers to be overcome. The largest of these is ensuring that energy supply meets demand, both temporally and spatially, including mobile applications where renewable energy generation technology lacks. Nuclear, hydroelectric, wind and solar power are all viable alternatives to fossil fuels that do not emit carbon or other greenhouse gases, and, due to the differing nature of these, all are needed for a smooth and rapid energy transition.

Solar Power

Solar power is a great source of renewable energy, with extremely low running costs and no pollution, waste or greenhouse gas emissions associated with its operation. However, solar power is very intermittent, location dependent (Figure 1.2), and has no ability to respond to demand changes. The price of solar panel installation has been dropping rapidly as the installed capacity increases (Figure 1.3), and is currently very cheap when compared with other renewables. Coupled with the distribution of solar irradiance, this makes solar power a very attractive option for developing countries, even if this price trend does not continue.

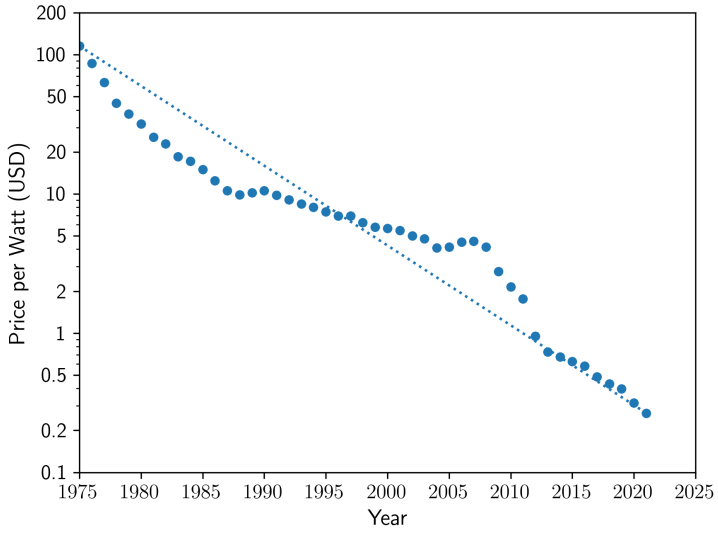


Figure 1.3: Price per Watt against the year for solar PV power generation. Data provided by Our World In Data[10].

The world's largest solar park is located at Bhadla, India, with 2,245 MW of generation capacity[11]. The Bhadla solar park is located in a dry, arid region where the closest habitation is 50 km away, the village of Bap. This is in part due to the large spatial footprint required for solar power[12], meaning that large solar installations usually use uninhabitable or otherwise undeveloped land. Despite the large space requirement, there is ample opportunity for development of solar parks in uninhabitable land. According to Forbes, an area of 110,000 km^2 of solar panels could power the world's energy use[13]. While not every inch of the Sahara desert is uninhabited, nor should every inch be covered in solar panels, this area spans 9.2 million km^2 (80× the Forbes estimate) and illustrates the possibility of solar parks in otherwise unusable land. However, large solar installations in uninhabited areas will require energy storage and transportation methods.

Wind Power

Similar to solar power, wind power is an affordable renewable energy option for developing countries, and has no pollution, emissions or waste issues during operation. Again, wind power is highly intermittent and location dependent, with areas with uninterrupted air flow, such as coastal, offshore, high altitude and desert regions seeing far higher wind speeds, as can be deduced from Figure 1.1. Wind power also has a significant spatial footprint[12] (though typically less than solar). However, this is not such an issue when considering offshore wind energy generation, similar to placing solar panels in uninhabitable areas.

The world's largest wind farm, recently becoming operational, is Hornsea 2. Located in the North Sea, Hornsea 2 is around 90 km off the Yorkshire coast[14] and can generate up to 1.3 GW of electricity for the national grid, equivalent to over 1.4 million UK homes. The intermittency of wind power, while it has a different temporal profile to solar intermittency, also requires energy storage technology to balance out the demand and supply requirements.

Nuclear Power

Nuclear power is one of the safest methods of energy generation[15], despite public concerns about nuclear power due to previous nuclear disasters such as Chernobyl and Fukushima. Attention has also been brought to the large amounts of nuclear waste generated by nuclear power, which can remain radioactive for thousands of years. However, scientific and political consensus is that this waste is not harmful if buried deep underground[16]. The primary benefits of nuclear power lie in its large energy density (greatest of any zero-carbon energy technology) and location independence.

Perhaps the most prohibitive aspect of nuclear power, is cost. Nuclear reactors are expensive and time-consuming to build, hence their higher prevalence in rich countries such as the US and China. This tends to make large nuclear power stations unsuitable for the energy transition of developing countries.

To bring down the high cost of nuclear power, small modular reactors (SMRs) have been developed in recent years. Although only 3 SMRs were in operation in the year 2022, over 40 SMR designs exist, with varying numbers of these in each of the design, licensing and construction stage[17] [18]. Rolls Royce have a commercial SMR design, occupying 40,000 square meters (0.4 km^2), generating 450 MW of electricity, and costing £1.8 billion (£3.8 million per MW)[19]. Sizewell C, a nuclear power station on the east coast of England with construction intended to begin shortly, will cost £20 billion and generate 3,300 MW of electricity (£6.1 million per MW)[20]. The smaller scale of SMRs, allowing for more widely distributed energy generation infrastructure and faster and cheaper construction, makes them a key part of the future of green electricity, for both developed and developing countries.

However, despite the large electrical power output, nuclear power is actually very inefficient, generating huge amounts of thermal energy alongside the large amount of electricity. Only around a third of the thermal energy generated by a Rolls Royce SMR is successfully converted into electricity (450 MWe from 1350 MWth)[19]. The 900 MW of wasted heat opens up the possibility of distribution of this thermal energy, using methods such as district heating or thermal energy storage systems, enabling a reduction in heating requirements in surrounding areas.

Hydroelectric Power

Hydroelectric power generated one-sixth of the world's electricity in 2020, accounting for almost 4500 TWh[21]. Hydroelectric power has a number of advantages, including high energy conversion efficiences (even as high as 90%) and fast responsiveness to energy demand (seconds to minutes). Hydroelectric power generation is easy to

modulate, due to the rate of water flow, which is easily controlled, being directly proportional to the power output. Hydroelectric power stations can be expensive to build, often making them unsuitable for less developed countries. However, they have long lifetimes and very low running costs once operational. The biggest downfalls of hydroelectric power are the geographical constraints and the environmental impact associated with damming a section of river, causing flooding and changing habitats upstream. The Three Gorges Dam in Hubei, China has the largest capacity of all hydroelectric power stations, with a maximum capacity of 25 GW, enough to power 150 million Chinese homes when running at full capacity [22].

1.1.2 Energy Storage Requirements

Due to the ease of use and fast response times of fossil fuels, few reversible energy storage technologies have been required, with fossil fuels simply allowing energy generation on demand. This can be seen in the electricity grid, with power stations running on natural gas or coal, or in mobile applications, such as petrol or diesel for cars, and kerosene for jet engines. The move away from fossil fuels brings a host of challenges, all serving the requirement of matching energy demand and supply temporally and spatially.

Balancing the Grid - Stationary Storage and Energy Trade

Figures 1.4 and 1.5 show the mean energy generation of a solar park in Spain and a wind turbine in the North Sea, for each month of the year and hour of the day, with capacities of 8 MW each [23]. Solar power has a much larger daily variation in energy generation (for obvious reasons), while wind power in the North Sea shows stronger variation on a yearly scale. From these two datasets, the requirement for energy storage technologies to balance supply and demand of the electricity grid is clear.

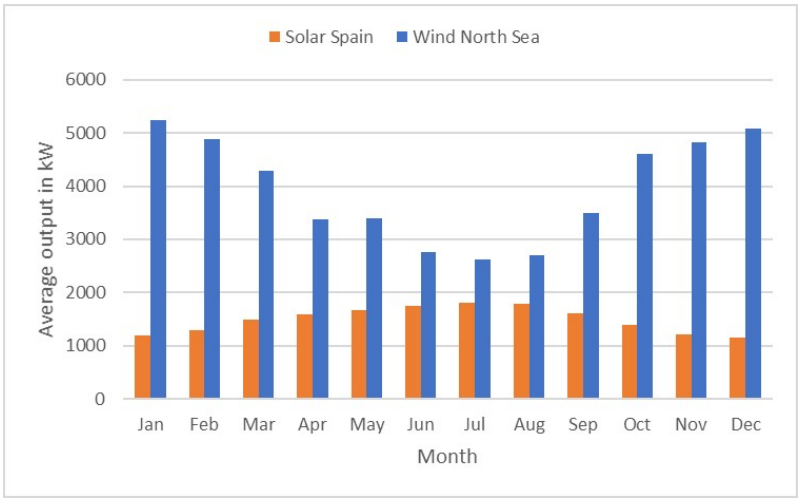


Figure 1.4: Variation in the mean monthly electricity generation of a solar park in Spain and a wind turbine in the North Sea. Both have capacities of 8 MW. Data are for the period 2005–2016.[23]

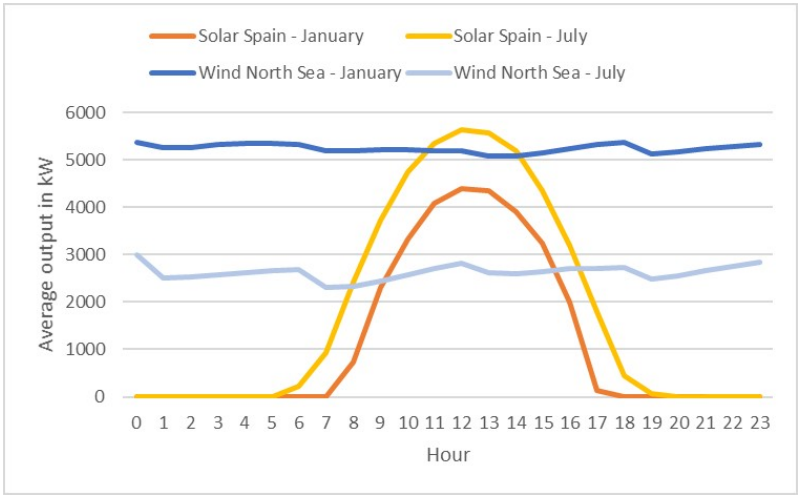


Figure 1.5: Variation in the mean hourly electricity generation of a solar park in Spain and a wind turbine in the North Sea. Both have capacities of 8 MW. Data are for the period 2005–2016.[23]

While average variations throughout the day and year are important to study, the use of a mean value removes the effect of short term fluctuations in solar irradiance and wind speed. Figure 1.6 shows the electricity generation of the solar and wind installations each month, for the period 2005–2016. Mean monthly outputs for wind power vary from approximately 2.6 to 5.3 MW, while actual monthly output varies from 1.6 to 7.0 MW, a difference twice as large. A similar effect is seen for solar, with mean monthly output varying from 1.2 to 1.8 MW and actual monthly output varying from 0.7 to 1.9 MW. Again, the difference between maximum and minimum is roughly doubled when comparing actual values with mean values. Daily variations in energy generation will also occur, which are similarly masked in Figure 1.5. Diverse and complementary energy sources will be required to partially handle intermittency. However, energy storage solutions will still be necessary to balance out the electricity grid. These solutions must be flexible enough to smooth out variations on both long (days to months) and short (seconds to minutes) timescales. This will require multiple different energy storage technologies, due to the vastly different response times.

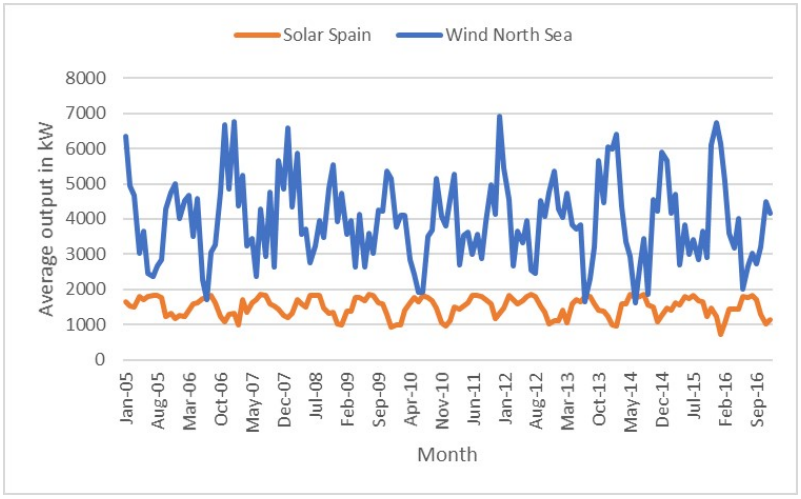


Figure 1.6: Monthly electricity generation of a solar park in Spain and a wind turbine in the North Sea. Both have capacities of 8 MW. Data are for the period 2005–2016.[23]

As discussed in Section 1.1, the distribution of renewable energy generation potential around the globe is not equal, nor is energy demand at present day, with rich countries using far more energy per capita than developing countries. Matching supply and demand temporally is crucial. However, matching supply and demand spatially is equally important. Submarine power cables are an effective way to balance the grid between nations separated by water. Medgrid is a project seeking to promote and develop a Euro-Mediterranean electricity network, providing North Africa and Europe with cheap, renewable electricity, by making use of submarine power cables and solar installations in the Sahara Desert. Figure 1.7 shows a schematic of possible renewable energy supply infrastructure between Europe, the Middle East and North Africa.

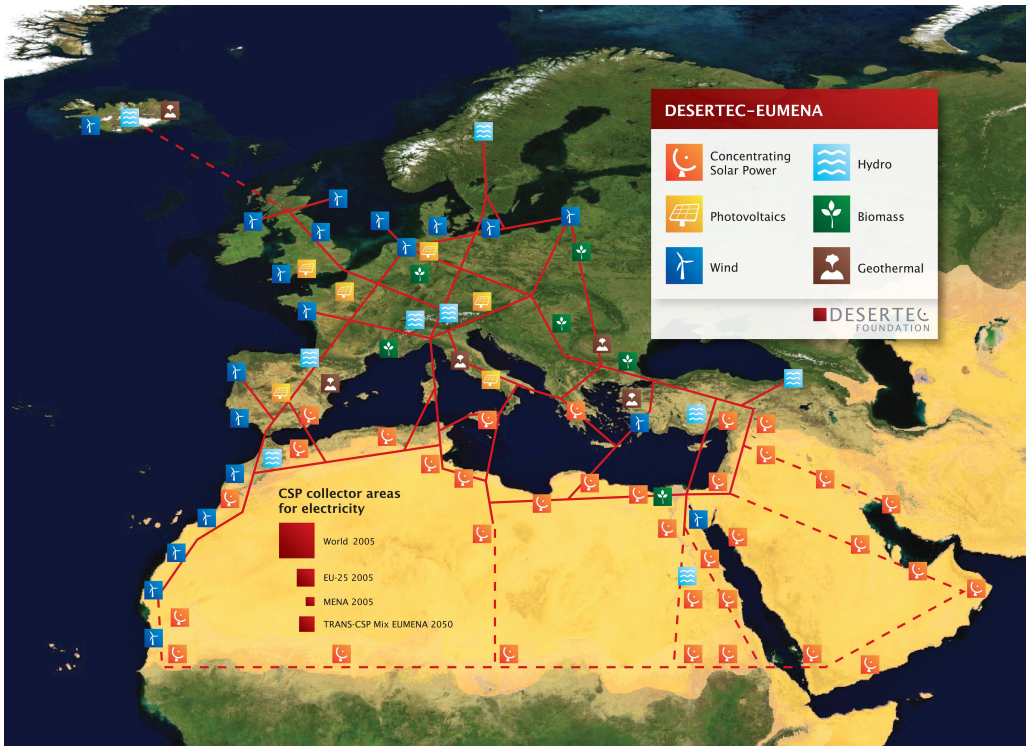


Figure 1.7: Schematic showing the possibility of renewable energy generation and supply infrastructure between Europe, the Middle East and North Africa. Red lines indicate possible placement of high voltage direct current (HVDC) cables to transmit electricity between Europe, the Middle East and North Africa. Image produced by DESERTEC. [24]

Temporal and spatial energy demands cannot be completely disentangled. Submarine power cables installed to date span only relatively short distances e.g. across the English channel or Mediterranean Sea. However, in part due to different peak electricity demand times between time zones, a techno-economic analysis of a potential power cable between North America and Northern Europe has shown the benefits of intercontinental electricity trade, allowing for the smoothing of demand variations both daily and seasonally [25]. Similarly, one could imagine electricity networks travelling north to south, rather than east to west, enabling greater seasonal variations in electricity demand to be smoothed. While there is a large benefit to long-distance submarine power cables, it is estimated a North America to Europe power cable would take 12 years to prepare, produce and install [25], rendering the possibility of direct electricity trade between these continents impossible until at least 2036.

An alternative to direct electricity transport is chemical energy storage technologies. For example, a chemical energy store such as ammonia is easily transported and can be produced where and when there is a surplus of electricity. Ammonia can be shipped around the world and used as an energy source where and when energy demand outstrips supply. Using a combination of direct electricity transport and chemical energy stores, developing countries with high renewable energy generation potentials can fund their own green industrial revolutions by exporting renewable energy and green fuels.

Mobile Storage - Transportation

The transportation sector accounts for over 30 % of global energy consumption (Figure 1.8) [26]. Due to its high reliance on fossil fuels, with 90 % of its energy consumption originating from oil products (Figure 1.9), transportation accounts for over a third of global carbon emissions. Renewable energy alone has always been insufficient for transport applications due to the large spatial footprints required for

renewables such as wind and solar power[1], thus preventing their installation on vehicles as the sole power source. While nuclear power does have a high spatial energy density and has been trialled previously in civilian cargo ships, price and safety concerns have prevented its persistence as an option.

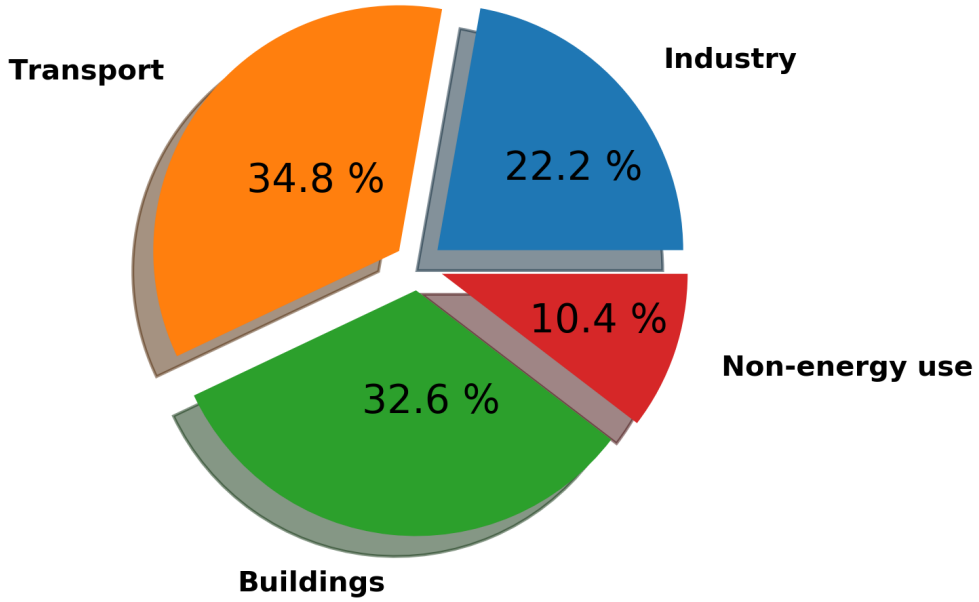


Figure 1.8: A breakdown of energy consumption by sector for OECD countries. Non-energy use refers to fossil fuel (a store of energy) consumption for any purpose outside of energy generation e.g. feedstock for chemical synthesis. Data provided by the IEA[26].

In 2012, over 55 % of transportation energy consumption was used for passenger travel[28], with the rest being freight travel. The majority of passenger transport energy use is for light-duty vehicles (e.g. cars) and air travel, with them making up 45 % and 12 % of transportation sector energy use respectively. The proliferation, and electrification, of public transport, alongside a changing culture of travel requirements brought about by the COVID-19 pandemic can lower energy consumption for passenger travel. However, green technologies for transportation will remain a necessity to reach net-zero. Battery electric vehicles (BEVs) currently lead the way in zero-carbon (at the point of use) personal transport. At present day however, only a small proportion of transportation is electrically powered, as can be seen in

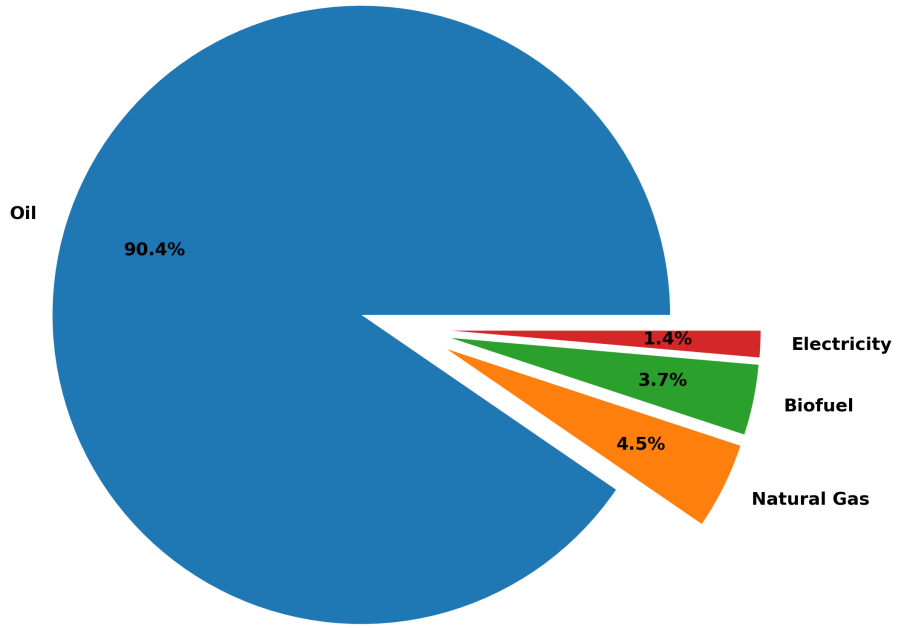


Figure 1.9: A breakdown of energy source for the transportation sector in OECD countries. Data provided by the IEA.[27]

Figure 1.9. This percentage must be increased dramatically for net-zero to be within reach, although the current form of BEVs has many other issues associated, which will be discussed further in Section 1.2.1.

At present day, there are no commercially available zero-carbon flights. However, the world's first net-zero transatlantic flight took place in 2023, flying from London, using sustainable aviation fuel (SAF) derived from waste biomass[29]. Due to the carbon emissions associated with the production, transportation and refining of SAFs, they only reduce life cycle emissions by up to 80 % relative to fossil fuels, and as such, carbon capture will be used for this flight to be truly carbon-neutral. As decarbonisation occurs across various sectors however, carbon emissions associated with SAFs can reduce further, while emissions from fossil fuels are inherent to their use. While biomass is a suitable zero-carbon fuel in the future, currently a maximum of 50 % SAF blended with kerosene can be used in commercial jet engines, though testing of higher SAF percentages as 'drop in' fuels (i.e. no requirement to change other components) is underway. Despite the green credentials of SAF/biomass, the

land requirements for these fuels are large. With a harvesting cycle of three years, a spatial energy density of 2.13 GWh/km^2 [12], and aviation sector energy consumption of 14 EJ in 2019 [30], replacing all aviation fuel with biomass would require 5.5 million km^2. This is 82 % of the area of the Amazon Rainforest (or 3.7 % of the land area of Earth). Considering aviation contributes to 2 % of global carbon emissions [30], this is a huge amount of land to dedicate to such a task, and alternative solutions must be found to the 'Jet Zero' problem.

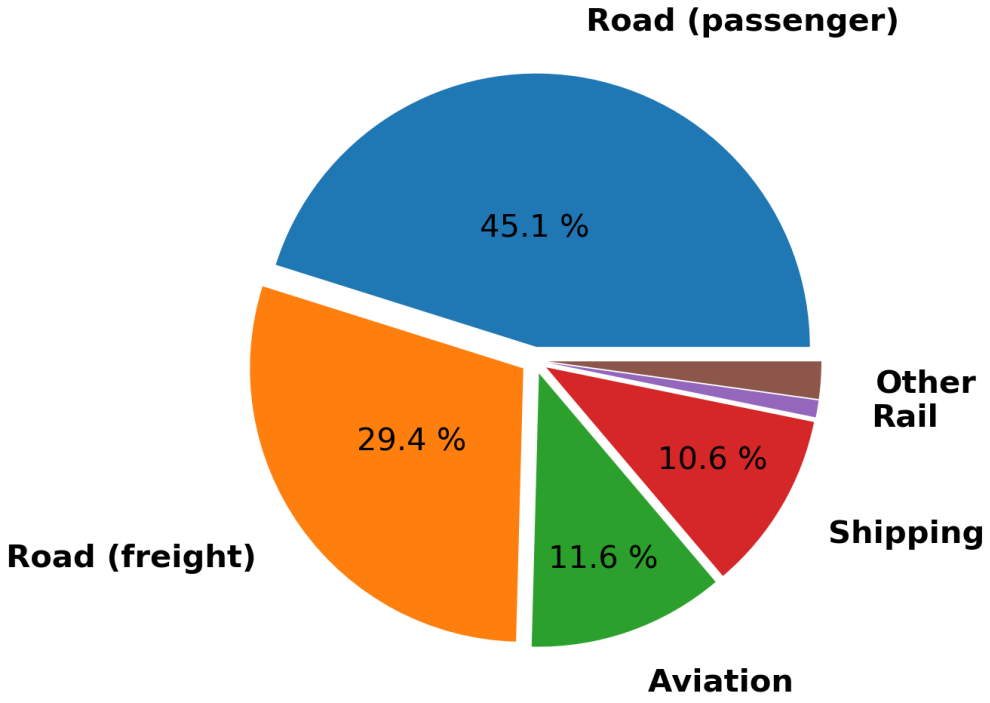


Figure 1.10: A breakdown of carbon emissions by transportation mode. Data provided by Our World in Data [28].

Alongside passenger travel, freight transportation must transition also. In 2015, shipping accounted for 70 % of the 108 trillion tonne-km travelled by freight, with 18 % of travel by road, and 9 % by rail [31]. Despite this, carbon emissions for freight travel by trucks and lorries were nearly three times that of freight travel by ship in

2018 (Figure 1.10). In an increasingly globalised world, freight travel requirements are only going to increase, with maritime trade volume in 2050 predicted to be three times that of today[31].

Decarbonisation of the transportation sector requires decarbonisation of shipping, aviation, rail and road transport, for both passenger and freight travel. This will require various energy storage solutions, due to the diverse requirements for each transportation system.

Waste Heat Storage and Use

Domestic energy accounted for 23 % of energy use in the U.K. in 2021[32]. Figure 1.11 shows the breakdown of domestic energy consumption for IEA countries. Just under 70 % of domestic energy use is for low temperature heating (water and space heating). Insulation of homes and buildings can massively reduce space heating requirements, though progress on this issue has stalled in recent years, prompting action by protest groups such as Insulate Britain. It is estimated that 80 % of the housing that will be used in the U.K. in 2050 is already built[33], and will need upgrading to net-zero standard. This means 26 million U.K. homes need to be retrofitted with proper insulation by 2050 (1 million each year).

Aside from reducing energy losses, switching away from gas boilers allows for reduction in carbon emissions. Air and ground source heat pumps allow for both space and water heating, powered by electricity from the grid. Alongside decarbonisation of the electricity grid, these can produce no greenhouse gas emissions through their operation. Another alternative is district heating systems, which distribute heat generated in a centralised location. This heat could be obtained from nuclear power plants, or geothermally, if the location allows (e.g. Iceland). However, heat generated by solar towers or troughs, which focus the sun's rays on a single point to increase their intensity, along with appropriate storage and distribution methods can contribute to the heating requirements of homes almost anywhere on

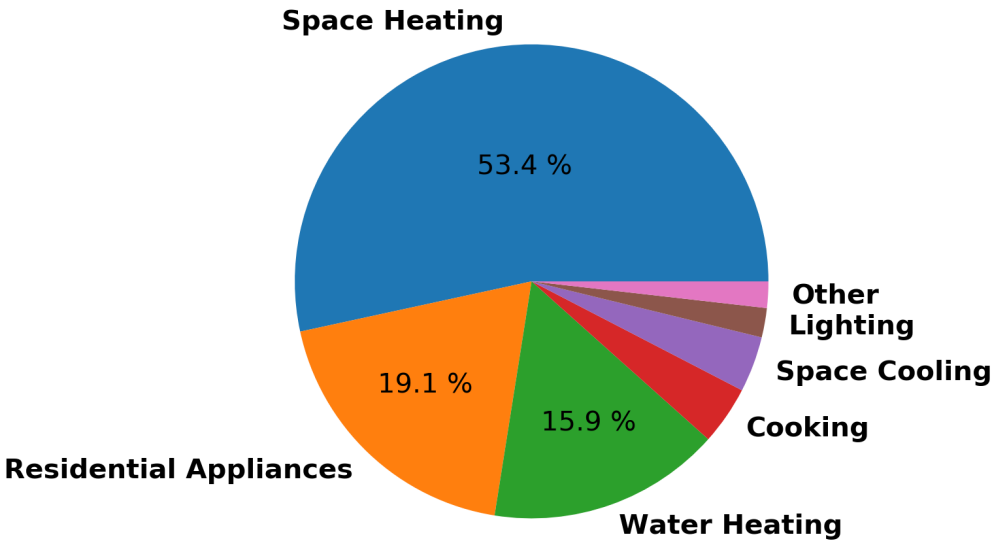


Figure 1.11: A breakdown of domestic energy consumption by use. Heating and cooling constitute the majority of domestic energy use. Data provided by the IEA for selected IEA countries in the year 2019 [34].

the planet. For example, in Büsingen, a village in Germany, between 10 and 20% of the heat in winter, and all of the required space and water heating during summer is powered by just 1090 m^2 of solar collectors [35]. While successful in the village of Büsingen, these systems are much more beneficial in urban areas, where the density of heat requirements is much higher.

Efficiency improvements and zero-carbon generation technologies for heating homes are vital. However, there are other sectors producing large amounts of heat, which can be utilised. For example, it is estimated there are 300 TWh of waste thermal energy from industrial processes each year in the EU, with a third of this below 200 °C [36]. As mentioned previously, nuclear power generates huge amounts of thermal energy as waste. Similar to electrical power, supply and demand of heat must be matched temporally and spatially. In the case of heat, the temperature of the thermal energy supply matters too. Technologies to capture heat (e.g. thermal energy storage systems), distribute heat (e.g. district heating systems) and transform heat (e.g. chemical heat pumps) are all required in order to match demand

and supply. It should also be noted that energy storage from thermal energy has been suggested as one of the solutions for balancing the grid, as waste heat can be used to generate electricity. Pumped thermal electricity storage is promising as a large-scale energy storage technology due to its long lifetime and lack of geographical constraints[37].

1.2 Chemical Energy Storage Methods

The requirements for energy storage vary greatly in terms of timescale, capacity and responsiveness. Various technologies have been, and are being developed, and a net-zero future will require a diverse range of these.

1.2.1 Batteries

Batteries are ubiquitous in modern life, with uses multiple times a day passing by unnoticed to the consumer. Over time, the development of different types of battery, the decreasing cost of batteries, and the increasing requirement for energy storage has led to diversification of their uses. Initially just used for small scale applications such as handheld devices, lithium-ion batteries (LIBs) have grown to be used in battery electric vehicles (BEVs) and even in balancing the electricity grid.

Batteries have a very low energy density, which may appear to make them unsuitable for mobile energy storage applications such as BEVs. However, batteries are used due to their extremely high round trip efficiency compared with other energy storage technologies[38]. The combination of high round trip efficiencies, the possibility of regenerative braking, and the low efficiency of internal combustion engines (around 20–25 %[39]) means BEVs are actually much more energy efficient than conventional ICE cars during operation. Despite this, most BEVs have ranges lower than the average ICE car, due to the weight and cost associated with large batteries. BEVs also have much longer recharge/refuelling times compared with petrol

or diesel cars. This makes them suitable for the average consumer, who usually travels less than the range of the car, but unsuitable for long-haul freight transport. Among all this, the main advantage of BEVs is the lack of emissions at the point of use. This eliminates air pollution from the tailpipe (though not from the tyres[40]) in urban areas and, if the electricity grid is decarbonised, makes personal transport by road zero-carbon during operation (i.e. ignoring manufacture of the vehicle).

Due to the well-defined and regular stopping points of public transportation, electric buses are a viable option. Although these buses will travel long distances each day, they can make use of 'opportunity charging' due to the defined route. Transport for London began opportunity charging in 2023, with a 15 mile bus route containing rapid charging points at each end, ensuring the bus can run all day without returning to the garage for a full charge[41]. Similarly, China has introduced various Capabuses, which make use of supercapacitors, and charging points at every stop to enable electric public transportation[42]. Supercapacitors have around 10× lower capacity (Wh/kg) than batteries, but around 10× higher power (W/g) than batteries. This means that, coupled with regular charging, only a small mass of supercapacitor is needed to enable the required power for a bus.

While suitable for road transport, batteries are unsuitable for air travel, due to their low gravimetric energy density. For example, the battery found in a Tesla Model 3 (a BEV) has an energy density of 260 Wh/kg[43], while research has estimated the energy density required to enable regional flights to be over 500 Wh/kg[44]. This would represent almost a doubling in capacity to enable short-haul flights. It's clear that batteries alone will not solve the issue of 'Jet Zero'.

Australia is commissioning a number of big battery projects, for the purpose of stabilising the electricity grid. Batteries can be good for this purpose, due to their high round trip efficiency, ensuring minimal energy loss. However, due to the low energy density of batteries, they can only be used for smoothing supply and demand on very short timescales. The new batteries, currently planned to be operational

in 2025, represent 4.2 GWh of capacity[45]. With an annual electricity consumption of around 250 TWh (average of 28.5 GW)[46], these batteries can only power the Australian grid for 8 minutes and 50 seconds. Of course these projects are aimed at smoothing supply and demand, not powering the country entirely. However, it shows the requirement for alternative, larger capacity energy storage technologies. Despite this, batteries can help enable these alternative energy storage methods. Due to the rapid responsiveness of batteries, these projects can supply power to the grid while other energy storage systems are still responding.

With the proliferation of domestic solar panels in recent years, many homes now have domestic batteries installed alongside. This is for storing the energy generated by the rooftop solar panels for later use. However, this is simply time shifting demand and supply in the same way that big battery projects would. The fundamental difference is in who owns, and who makes money from, the battery storage (for domestic batteries this would be the home owner/occupier). Domestic batteries do not require links with a solar panel; they can easily be used by consumers to save money on their electricity bills by shifting electricity demand times.

While batteries have their place in the green energy transition, there are a host of social and environmental issues associated with LIBs (currently the leading battery technology). Lithium extraction in Chile has placed pressure on water supply in the Salar de Atacama region, with lithium and other mining activities using 65 % of the region's water supply. With an estimated 1.9 million litres of water required per tonne of lithium extracted[47], this is having a huge impact on local farmers and indigenous communities in the surrounding area. The mining of cobalt, an element used in many types of LIBs, can lead to pollution of rivers and drinking water when sulphur-containing minerals are exposed to air and water[47]. Alongside this, most cobalt is mined in the Democratic Republic of Congo, where it is estimated up to 40,000 children work in mines with inadequate safety equipment[47].

Aside from the issues associated with its production, cobalt is a particularly scarce element in the Earth's crust, and a single BEV can contain 14 kg of cobalt [48]. With global cobalt production of 190,000 tonnes in 2022 [49], fewer than 14 million BEVs can be produced each year. At this rate, it would take 103 years to replace all of the 1.45 billion road vehicles [50] in the world with BEVs. This is under the assumption that all road vehicles are cars, not trucks which require larger/more battery packs, and also does not account for the lifetime of the battery in a BEV (typically up to 20 years [48]). Accounting for a 20 year battery life (with no recycling), current cobalt production can only sustain 270 million operational BEVs globally. Lithium and cobalt-based BEVs clearly cannot tackle the emissions of road transport alone. Nonetheless, production and recycling of lithium and cobalt will need significant growth in coming years, while simultaneously ensuring the social and environmental issues are overcome.

Sodium-ion batteries (SIBs) fundamentally work on the same principles as LIBs, except lithium is replaced with sodium, a much more environmentally friendly and abundant element. Also, research into these focuses on layered cathode materials which avoid the environmentally destructive elements associated with LIBs such as cobalt. SIBs generally show lower energy densities and shorter cycle lives than LIBs, though it should be noted that they are at an earlier stage of development [51]. Despite this, their cheaper and more environmentally friendly manufacture could allow for much greater production of SIBs in the future. Due to the inherently lower energy densities, SIBs may be considered less suitable for the electric vehicle market. However, the lower cost and reduced environmental damage allows for larger/more battery packs to be used in BEVs in order to increase the driving range. Energy density is not as important for stationary storage applications, and as such SIBs also show promise for big battery projects similar to those commissioned in Australia,

or even for domestic battery storage. Transportation and grid stabilisation utilising batteries is part of the zero-carbon future and SIBs will play a role as we look away from environmentally destructive materials to supply the transition.

1.2.2 Hydrogen

Hydrogen has commonly been touted as the green fuel of the future, with its synthesis from water and renewable energy, and its combustion (or use in a fuel cell) providing large quantities of energy and releasing only water. However, storage of hydrogen is a thorny issue, with attempts to overcome the safety concerns of storing pure hydrogen (a high risk of explosion) failing thus far.

Hydrogen can be easily produced via electrolysis of water, enabling easy connection to the electricity grid and renewable energy sources. However, the majority of hydrogen is currently produced via steam reforming of methane (SRM) or coal gasification, both high temperature processes releasing large amounts of carbon dioxide, due to the currently high cost of water electrolysis[52]. An alternative method, in its earlier stages of development, is methane pyrolysis. Methane pyrolysis involves cracking methane at high temperatures, forming solid carbon and hydrogen gas. Due to the methane feedstock, and solid carbon produced (which can be used in other carbon consuming industries), this is a low cost method without the carbon emissions associated with SRM or coal gasification. In fact, if biomethane is used, this is actually a carbon negative process, removing carbon that would otherwise enter the atmosphere.

While hydrogen is currently produced from carbon intensive processes, the falling cost of renewable energy over the coming years will enable electrolysis to become competitive, and alongside the potential maturation of methane pyrolysis, this could allow for an expansion of green hydrogen production.

Table 1.1: A comparison of hydrogen production methods. While zero-carbon hydrogen production is possible, it is currently small scale and is not competitive with carbon emitting methods.[52]

Process	Feedstock	Byproducts	tCO_2 / tH_2	\$ per kg H_2	% H_2 production (2018)
Steam Reforming of Methane	Natural Gas, Water	CO_2	7.5	0.43	76% (53 Mt)
Coal Gasification	Coal, Water	CO_2	13.4	0.24	23% (16 Mt)
Electrolysis	Water	O_2	0–16.4[a]	2.76	2% (1 Mt)
Methane Pyrolysis	Natural Gas	Solid Carbon	-10.9–0[b]	0.72	0%

[a] Dependent on the carbon intensity of the electricity source.

[b] Dependent on the methane source.

Hydrogen has a very large gravimetric energy density (Figure 1.12), in part due to its extremely low mass, which could make it an ideal fuel for transportation applications. However, storage of hydrogen to an acceptable volumetric density is a tricky problem to solve. Storage of pure hydrogen can be achieved either by compression to 700 bar (as was used in the Toyota Mirai) or by liquefaction at $-253\,^{\circ}C$. Both of these require expensive and bulky engineering solutions which reduce the effective energy density of hydrogen, while still not fully alleviating the safety risks of highly concentrated hydrogen. An alternative to pure hydrogen storage is solid state hydrogen storage, where hydrogen can be incorporated into, or adsorbed onto the surface of, a solid material. However, molecular hydrogen, due to its low number of electrons and lack of polarity or lone pairs, tends to bind weakly while retaining the hydrogen bond, leading to low hydrogen capacities, or the requirement of extremely high pressures and/or low temperatures. An alternative approach is to break the hydrogen bond for storage. Unfortunately, hydrogen tends to bond strongly to materials when found in an atomic/ionic state, leading to slow recharge times, high hydrogen release temperatures or limited reversibility. Figure 1.13 shows the hydrogen capacities and release temperatures of various proposed hydrogen storage methods. Porous materials, simple metal hydrides and complex metal hydrides have all been studied over previous decades for hydrogen storage, but materials with sufficient hydrogen densities have not met the required standards in other areas.

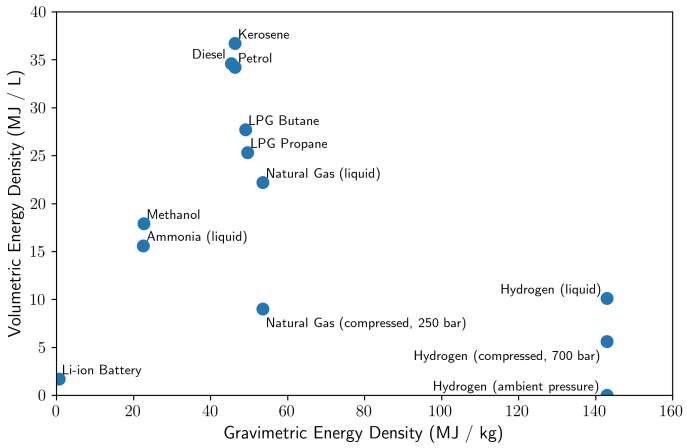


Figure 1.12: Gravimetric and volumetric energy densities of select energy stores. While hydrogen provides a great gravimetric energy density, safe, high density storage of hydrogen remains a challenge.[53] [54] [55]

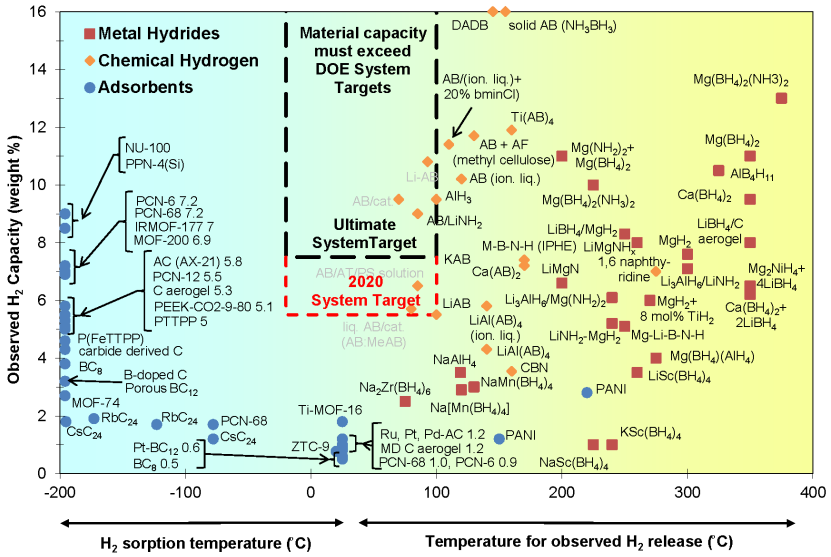


Figure 1.13: Hydrogen capacities and release temperatures of different hydrogen storage methods. In general, adsorbents (which bond molecular hydrogen) require extremely low temperatures, while metal hydrides (which bond ionic hydride) and chemical hydrogen (which bond atomic hydrogen) generally have high hydrogen release temperatures. Figure produced by the Hydrogen and Fuel Cell Technologies Office at the U.S. Department of Energy[56].

Despite this, hydrogen has been explored as a transportation fuel for passenger vehicles, with two hydrogen fuel cell vehicles (HFCV's) on the market currently, the Toyota Mirai and the Hyundai Nexo. HFCV's offer the range of a petrol car, with a much higher energy efficiency and without the associated carbon emissions of their operation. However, a severe lack of hydrogen distribution and refuelling infrastructure has prevented the widespread adoption of HFCV's. For example, there are only 11 hydrogen refuelling stations operational in Britain[57]. The long journey between these refuelling stations signifies the difficulty of operating a HFCV as a passenger vehicle.

Aeronautical companies such as Airbus are investigating hydrogen powered flight using tanks of liquid hydrogen as their solution to the hydrogen storage problem. Airbus use modified gas turbine engines, alongside electrical power from hydrogen fuel cells to get this project off the ground, aiming to fly commercial hydrogen aircraft by 2035[58]. While the hydrogen distribution and refuelling infrastructure is not yet ready for commercial hydrogen flight, scaling up of infrastructure for the purposes of flight is likely to be much easier, as hydrogen can remain in the hands of trained professionals at all stages of production, transport and usage.

1.2.3 Synthetic Carbon Fuels

Using excess electricity in the grid, hydrogen can be electrolysed from water (Equation 1.1), and then used as a feedstock for methane (CH_4) and methanol (CH_3OH) synthesis (Equations 1.2 and 1.3). Upon combustion of these fuels, carbon dioxide and water is produced (Equations 1.4 and 1.5), thus making a zero-carbon loop.

$$2\,H_2O \longrightarrow 2\,H_2 + O_2 \tag{1.1}$$

$$CO_2 + 4\,H_2 \longrightarrow CH_4 + 2\,H_2O \tag{1.2}$$

$$CO_2 + 3\,H_2 \longrightarrow CH_3OH + H_2O \tag{1.3}$$

$$CH_4 + 2\,O_2 \longrightarrow CO_2 + 2\,H_2O \tag{1.4}$$

$$2\,CH_3OH + 3\,O_2 \longrightarrow 2\,CO_2 + 4\,H_2O \tag{1.5}$$

Figure 1.14 shows the efficiency losses of methanol and methane at each stage of such a system. Due to the requirement for compression of methane (a gas), methane has much greater efficiency losses in the storage and transportation stage than methanol, a liquid at room temperature and pressure. CHP refers to the combined heat and power output of the chemical fuels. For the purposes of grid stabilisation, this is not the most useful metric, as only power can be effectively fed into the electricity grid. As such, we can only expect around 30 % and 22 % electrical round trip efficiencies for methanol and methane respectively. This signifies a common issue with grid stabilisation using chemical energy stores: the power output is significantly less than the power input. The big advantage of chemical fuels is the long term stability, with virtually no energy losses over time.

Crucially however, Figure 1.14 assumes a pure source of CO_2. In reality, CO_2 purification requires energy and will lower the efficiency estimates further. If carbon is captured from higher concentration sources such as flue gas, this will be more energy efficient than attempting direct air capture, where only 400 ppm are CO_2.

Both methane and methanol have applicability as transportation fuels, with the possibility of compressed natural gas (CNG) and methanol usage either in small concentrations in traditional engines, or as the main fuel in dedicated CNG or methanol engines[59]. Alongside this, due to the use of both methane (primarily as a fuel) and methanol (as a fuel and a chemical feedstock) over the past century, the infrastructure for transportation and storage of these chemicals is already well established.

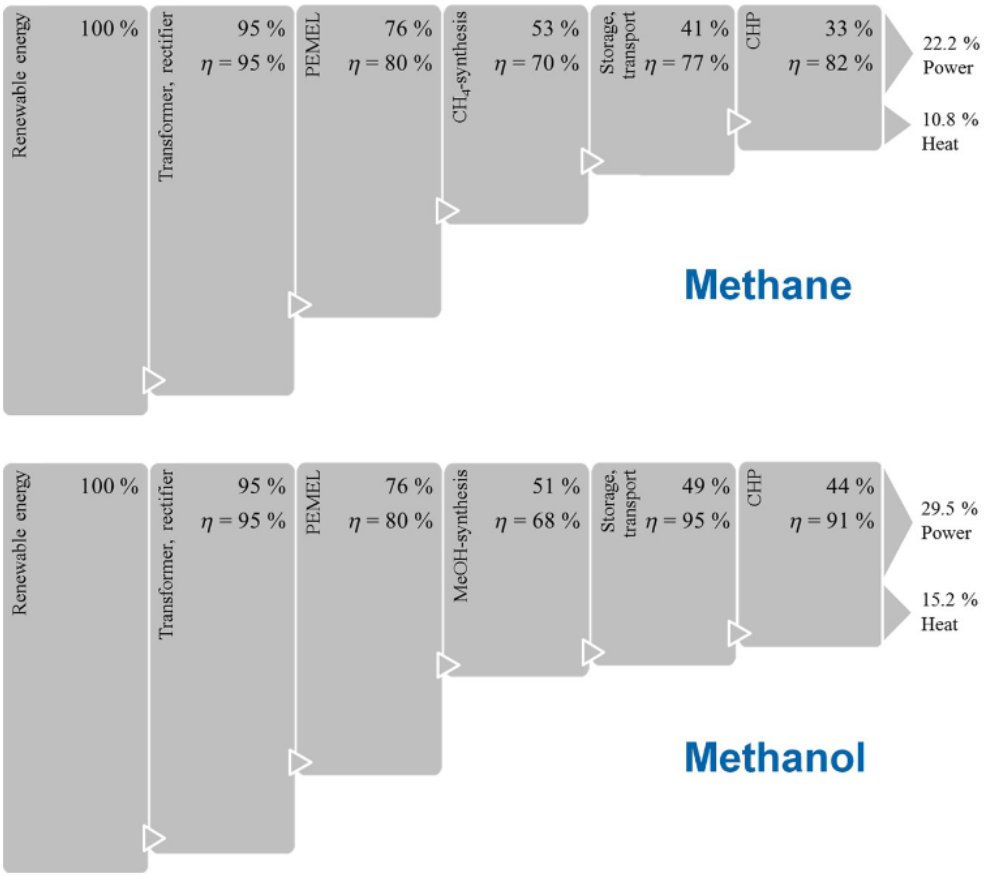


Figure 1.14: Efficiency losses through the power to chemical fuel to power system. η represents the efficiency of each process. PEMEL - Polymer electrolyte membrane electrolysis (H_2 production). It is assumed each fuel is transported 500 km. CHP - Combined heat and power output. Figure adapted from Raüchle *et al.*[59]

1.2.4 Ammonia

Due to its role as a fertiliser feedstock, ammonia is one of the most widely produced and shipped chemicals. While ammonia is a toxic gas and has a risk of explosion near ignition sources, these challenges have been overcome in industry, as evidenced by ammonia's ubiquity over the last century.

Ammonia is primarily produced by the Haber-Bosch process (Equation 1.6), invented in 1913. As the Haber-Bosch process involves a reversible reaction, pressure and temperature will affect the yield of ammonia. As ammonia synthesis is exothermic, temperature increases reduce ammonia yield. However, high temperatures (500 °C), along with an iron catalyst, are required to reach a sufficient reaction rate. High pressures (200 bar) are used to increase the yield of ammonia. Despite this, ammonia separation techniques are still required. Traditionally this has been done by cooling, utilising the different boiling points of N_2, H_2 and NH_3 to separate ammonia as a liquid[60]. Recently, in an attempt to prevent the energy loss associated with repeated heating and cooling cycles, research has been conducted into ammonia sorbents[61,62,60,63,64], allowing separation at higher temperatures, and membrane reactors[65], where ammonia can selectively pass through a membrane, leaving nitrogen and hydrogen behind in the reactor.

$$N_2 + 3\,H_2 \rightleftharpoons 2\,NH_3 \tag{1.6}$$

The Haber-Bosch process requires pure sources of nitrogen (separated from air, of which it constitutes 78 %) and hydrogen, which is currently obtained mainly from steam reforming of methane but can also be obtained by electrolysis powered by renewable energy, as explained in Section 1.2.2.

Electrochemical synthesis of ammonia from nitrogen and a proton source (e.g. H_2O) is an alternative to the Haber-Bosch process. This enables ammonia synthesis at low temperature, and without the need for pure hydrogen feedstock. N_2 is a relatively inert molecule, due to the triply bonded nitrogen atoms, and has very low

solubility in polar solvents such as water, due to its lack of polarity. As a result, the rate of electrochemical ammonia synthesis is low, and the hydrogen evolution reaction (Equation 1.7) is competitive with the nitrogen reduction reaction (Equation 1.8)[66]. As such, both the rate and selectivity of electrochemical ammonia synthesis is not yet at the level required for industrial production of NH_3.

$$2\,H^+ + 2\,e^- \longrightarrow H_2 \tag{1.7}$$

$$N_2 + 6\,H^+ + 6\,e^- \longrightarrow 2\,NH_3 \tag{1.8}$$

While ammonia is a gas under standard conditions, ammonia will condense when pressurised to 7 bar or cooled to −33 °C. This removes the necessity for overly expensive, bulky and potentially unsafe storage solutions associated with other proposed energy stores, such as hydrogen at 700 bar. Ammonia will not match the gravimetric energy density of a light fuel such as hydrogen. However, in part due to its ease of liquefaction, ammonia shows a high volumetric energy density among potential green fuels (Figure 1.12), a crucial factor when considering the size of a fuel tank for transportation applications.

One of the key advantages of ammonia as a green fuel is its ubiquity. Rapid decarbonisation, in line with climate goals, necessitates minimising required development. With ammonia being used in the synthesis of fertilisers, plastics, textiles, dyes, pesticides and explosives, and also as a refrigerant and a component in many household cleaning products, its usage is well understood. Alongside this, ammonia has an established global network of shipping and bunkering infrastructure.

There are various ways to release the energy stored within ammonia. Ammonia can be decomposed at high temperatures with a suitable catalyst, in the reverse reaction to Equation 1.6, to release hydrogen. As such, the uses of hydrogen discussed in Section 1.2.2 will, in general, apply to hydrogen produced from ammonia. However, for use in PEM (polymer electrolyte membrane) fuel cells, ammonia con-

centration must be as low as 1 ppm, to avoid poisoning the membrane. At 550 °C and 1 bar, equilibrium consists of around 800 ppm NH_3 [67], and as such any use of ammonia as a carrier of hydrogen for PEM fuel cells will require post-decomposition treatment to remove remaining ammonia from the gas stream. This has usually been demonstrated using ammonia sorbents [67].

Alternatively, ammonia can be used directly in a solid oxide fuel cell to produce electricity. However, these require very high operating temperatures (>600 °C) [68], causing issues with initial startup.

One of the most promising methods of energy release from ammonia is use in internal combustion engines. One of the key advantages is the established nature of engines, and the possibility of retrofitting existing vehicles. Ammonia does not combust easily, and requires heating prior to ignition. Similar to solid oxide fuel cells, this can prevent ignition of a cold engine with pure ammonia. Alongside this, attempted combustion of pure ammonia tends to produce high amounts of NOx emissions (greenhouse gases with very high global warming potentials) and has issues with 'ammonia slip' (where unreacted ammonia is released in the exhaust gas) [69]. However, ammonia can be used to scrub NOx emissions in post combustion treatment of exhaust gas [70]. In theory, the issues of NOx emissions and ammonia slip can resolve each other, though further research into processes such as selective catalytic reduction (SCR) is required to achieve this.

An alternative proposed method to pure ammonia combustion is the use of dual fuels. For example, an engine could be run on ammonia-hydrogen mixtures. The hydrogen is used to aid combustion, in turn reducing ammonia slip, pre-heating requirements and NOx emissions [69]. The combustion benefits of a dual fuel approach are clear, and as ammonia is a hydrogen carrier this does not require a separate hydrogen fuel tank, but rather a system designed to partially crack ammonia.

1.3 Thermal Energy Storage Methods

Thermal energy storage is used to capture heat, for use at a later time. Heat is transferred to a storage medium during the charging phase, and transferred out of the storage medium during the discharging phase. In this way, thermal energy storage is akin to a 'heat battery'.

Media used in thermal energy storage applications can also be used for an array of other thermal applications, such as refrigeration, heat pumps and even electricity generation. However, while theoretically possible, the properties possessed by each material may only be suitable for certain applications. Further discussion of this is given in Section 1.4.

There are three different types of thermal energy storage: sensible, latent, and thermochemical. Sensible heat storage (SHS) simply stores thermal energy in the form of a temperature increase. Latent heat storage (LHS) stores thermal energy via a material's phase change. Thermochemical energy storage (TCS) utilises a chemical reaction to store heat. Both LHS and TCS are able to store sensible heat alongside their chemical changes, and as such the amount of heat stored for SHS, LHS and TCS is shown in Equations 1.9, 1.10 and 1.11. m is the mass of the storage material, C_p is the heat capacity of the material(s), T_C is the lower temperature, T_H is the higher temperature, and T_m and T_r are melting and reaction temperatures. These equations become significantly simplified over small temperature changes, where C_p can be assumed to be constant, as shown in Equation 1.12.

$$Q = m \int_{T_C}^{T_H} C_p \, dT \tag{1.9}$$

$$Q = m\Delta H_m + m \int_{T_C}^{T_m} C_{p,s} \, dT + m \int_{T_m}^{T_H} C_{p,l} \, dT \tag{1.10}$$

$$Q = m\Delta H_r + m \int_{T_C}^{T_r} C_{p,1} \, dT + m \int_{T_r}^{T_H} C_{p,2} \, dT \tag{1.11}$$

$$\text{When } C_p \text{ is a constant: } \int_{T_1}^{T_2} C_p \, dT = C_p(T_2 - T_1) = C_p \, \Delta T \tag{1.12}$$

1.3.1 Sensible Heat Storage

Sensible heat storage tends to focus on cheap materials with large heat capacities, due to the simplicity of the process and the dependence on heat capacity shown in Equation 1.9. One of the cheapest and most commonly used methods is hot water due to its abundance and heat capacity ($4.2\,\text{kJ kg}^{-1}\,\text{K}^{-1}$). However, due to the low boiling point of water (100 °C) it is unsuitable for higher temperature applications. Rocks, sand, concrete and molten salt mixtures are stable to higher temperatures and have been used for solar thermal energy storage. This allows the decoupling of heat demand and solar heat production, via an intermediate storage system.

In Hamburg-Altenwerder, Germany, 1000 tonnes of volcanic rock is used to store up to 130 MWh of heat for a week[71]. Built by Siemens-Gamesa, the facility uses excess electrical energy to heat air to 750 °C, which is then passed through the rock. Due to the low thermal conductivity associated with grain boundaries in solids, a heat transfer fluid is needed for sufficient heating rates; air is used in this example. When required, the thermal energy is then used for heating requirements, or converted back to electrical energy by use of a steam turbine.

During sensible heat storage, the material is at a higher temperature than its surroundings, and will begin to cool down. This illustrates both the large amounts of insulation required for sensible heat storage to be efficient, and the short timescales (hours to days) over which heat can be stored by this method, as shown in Figure 1.15. With the exception of domestic heat storage, sensible heat storage facilities tend to be fairly large installations due to the scaling of surface area (which affects the rate of thermal energy loss) relative to volume (which affects thermal energy storage capacity).

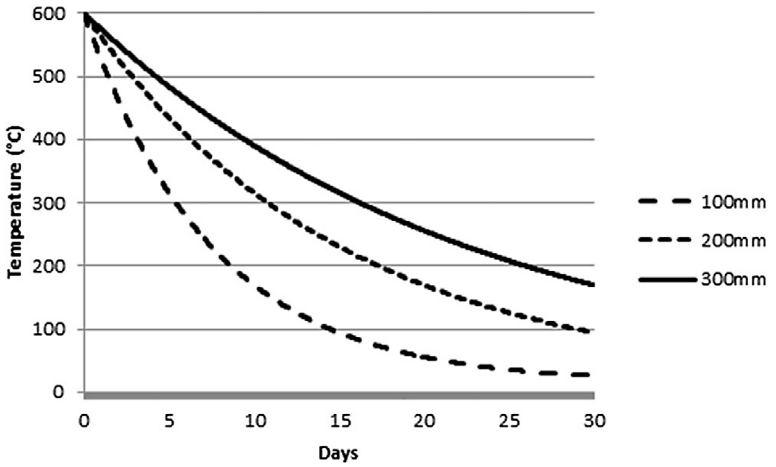


Figure 1.15: Simulated heat loss from a domestic heat storage system using a high temperature magnetite block with different fabric insulation thicknesses. The volume of the magnetite block is such that the amount of heat passed to the brick is enough to balance variation in seasonal heat demand for a typical U.K. home. However, the stored heat rapidly dissipates, preventing seasonal heat storage in this manner. Adapted from Allison *et al.*[72]

1.3.2 Latent Heat Storage

Latent heat storage involves the use of a phase change to store and release heat. While phase changes involving gases would generally be expected to give the greatest enthalpy change, vaporisation and sublimation processes are not used for latent heat storage due to the large volume change associated with them. Instead, solid to liquid transitions are almost exclusively used for latent heat storage. Latent heat storage allows for a greater energy capacity over a smaller temperature range when compared with sensible heat storage.

A wide array of materials melt at appropriate temperatures for latent heat storage, and as such many materials have been studied for this application. A class of material commonly used for solar thermal energy storage is eutectic salt mixtures, particularly those of metal nitrates. Eutectic salts show various preferable qualities for solar thermal energy storage such as moderate phase transition ranges, high

stability and low vapour pressures. However, they often require additives such as Al_2O_3 nanoparticles to overcome the shortfall in thermal conductivity[73]. Similar to sensible heat storage, heat loss can be an issue, requiring good insulation of these systems and limiting the storage time.

1.3.3 Thermochemical Energy Storage

Thermochemical energy storage uses a chemical reaction to store heat. The main benefit of thermochemical energy storage over LHS or SHS is the ability to store heat over long time periods. As TCS uses a chemical reaction, the products of the charging reaction can be separated, for recombination at a later date. While the sensible heat stored will be lost, the heat of reaction will remain stored until the components are recombined. This enables thermal energy storage across seasons.

Commonly, due to the ease of separation associated with a gas evolution reaction, TCS systems have been focused on gas sorbents. As mentioned in Section 1.3.2, this could result in large storage volumes being required to store the released gas. For TCS, there are two main ways around this issue. Firstly, the gas released can be an abundant, easily accessible gas, such that it does not need to be stored. For example, the decomposition of transition metal oxides, occurring at high temperatures and shown in Equation 1.13, is easily reversed using atmospheric oxygen instead of stored oxygen gas[74]. Alternatively, the gas given off can be separated prior to storage as a liquid, as is the case for closed salt hydrate systems (open systems using atmospheric water or externally supplied water are possible too). An example of a general salt hydrate system is shown in Equation 1.14. As water condenses at modest temperatures and pressures, it can be easily condensed in a separate vessel for storage. However, storage of the gas as a liquid can lower energy capacities, as heat must be absorbed to vapourise the gas prior to absorption. Despite this, there is no requirement for the liquid storage tank to be in precisely the same location as the absorber. For example, if used for domestic heating requirements it would be

possible to store the liquid absorbent outside the home, allowing slow heat uptake from the air to vapourise the liquid before allowing gas absorption to occur closer to the desired heating location.

$$M_xO_{y+z} \longrightarrow M_xO_y + \frac{z}{2}O_2 \tag{1.13}$$

$$MX(H_2O)_n \longrightarrow MX + nH_2O \tag{1.14}$$

Many salt hydrate systems have been studied extensively for the possibility of low temperature thermochemical energy storage[75]. While they have a simple operation process in theory, many have shown to be plagued by various stability issues. For example, some salts have been shown to be deliquescent (they absorb water to the point of forming a solution) even at low vapour pressures ($< 20\,\text{mbar}$)[75]. Similarly, some of the higher hydrates ($n = 4$ or $n = 6$) of salts such as $MgCl_2$ and $CaCl_2$ have very low melting points (30–45 °C) and will form a liquid if the temperature rises[75]. Deliquescence and melting will lead to grain clogging and a change in porosity in the reactor after re-solidification of the salts, which can greatly affect power in-/output[75].

Alongside these issues, the chemical stability of some salts can be an issue. In the presence of water (crystallised or gaseous) and heat, metal chlorides can slowly decompose to form HCl gas, as shown for $MgCl_2$ in Equation 1.15. HCl gas will be harmful to humans in an open system, and corrosive in a closed system. However, the kinetics and thermodynamics of this process will vary depending on the salt, with $MgCl_2$ in particular prone to this decomposition[76].

$$MgCl_2 + H_2O \longrightarrow MgClOH + HCl \tag{1.15}$$

$$MX(NH_3)_n \longrightarrow MX + nNH_3 \tag{1.16}$$

$$MgCl_2 + NH_3 \longrightarrow MgClNH_2 + HCl \tag{1.17}$$

Similar to salt hydrate systems are salt ammoniate systems. These operate on an identical principle to salt hydrates, as shown in Equation 1.16. While ammonia can be harder to liquefy, requiring −33 °C or 7 bar, this does reduce the propensity for deliquescence or melting of higher ammoniates, removing issues with grain clumping. Similarly, due to the instability of the amide ion (NH_2^-) relative to the hydroxide ion, there are no issues with HCl release at higher temperatures (the hypothetical reaction is shown in Equation 1.17). The main drawback of salt ammoniate systems when compared with hydrates is the requirement of a closed system, and the high pressure required to liquefy ammonia for long term storage. Both ammoniates and hydrates can have issues with agglomeration due to the volume change induced upon sorption. However, dispersion on supports can help overcome this issue[77].

1.4 Ammonia Sorption

Due to its well established synthesis, transportation and storage infrastructure, ammonia is uniquely positioned to take on the challenges of being a fuel of the future. However, further research is still needed to improve all aspects of ammonia's use, whether in the form of synthesis and decomposition catalysts, improved methods of storage, or new and improved ammonia purification techniques.

1.4.1 Ammonia Separation

Ammonia synthesis via the Haber-Bosch process requires separation of ammonia from unreacted nitrogen and hydrogen. Traditionally this has been performed by cooling, utilising the different boiling points of NH_3, N_2 and H_2. High temperature ammonia sorbents (> 300 °C) allow for ammonia separation closer to/at the temperature of the reaction, minimising the energy usage for repeated cooling and

heating. In fact, if the temperature of the reaction can be lowered with highly active catalysts, then it is possible to exceed the equilibrium constant of the reaction by ammonia absorption directly within the reactor, as shown by Smith *et al*[60].

Polymer electrolyte membrane fuel cells convert hydrogen and oxygen to electrical power and water. However, they require $< 0.1\,\text{ppm}$ NH_3 concentration to work effectively without poisoning[78]. Hydrogen produced by ammonia decomposition will thus require separation before use in a PEM fuel cell. However, many sources of hydrogen production, such as steam methane reforming and coal gasification, can lead to small amounts of ammonia production also, due to nitrogen impurities and the high temperatures involved[78]. As such, even when hydrogen has not originated from ammonia, separation techniques may be needed to remove small amounts of ammonia from a hydrogen stream.

Ammonia is commonly used as a reactant gas in many industrial processes, for example the production of nylon. Release of ammonia to the atmosphere can lead to diminished air quality and facilitate the formation of particulate matter by reaction with NOx or SOx[79]. Ammonia capture and recycling methods can prevent ammonia release from industrial processes and improve the efficiency of these processes.

1.4.2 Ammonia Storage

For ammonia storage as a liquid, the storage system must operate somewhere on the vapour pressure curve of NH_3, shown in Figure 1.16. As such, storage must be done at elevated pressure ($10\,\text{bar}$ at $25\,^\circ\text{C}$) or with active cooling ($-33\,^\circ\text{C}$ at $1\,\text{bar}$), or some combination of the two (known as semi-refrigerated ammonia storage). In the case of a leak, pressurised storage leads to worse safety outcomes, due to the rapid release of ammonia into the environment, which can also lead to rapid cooling

and the subsequent settling of ammonia clouds close to the ground. Refrigerated ammonia storage, while much safer, requires active energy use to maintain the liquid state of the ammonia, which can be costly over long periods of time.

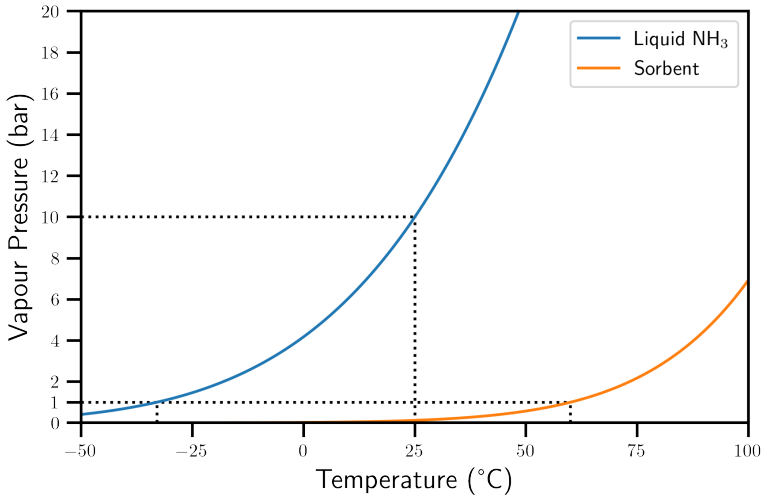


Figure 1.16: Ammonia vapour pressure of liquid NH_3 and a hypothetical ammonia sorbent. Use of ammonia sorbents can enable ammonia storage at ambient temperature and low pressure (enhancing safety outcomes in the event of a leak).

Despite ammonia's high toxicity, its global use for fertilisers, refrigerants and much more show that these safety challenges can be overcome. However, safety improvements are always welcome. Ammonia sorbents will have a different vapour pressure curve to that of liquid NH_3; a hypothetical example is shown in Figure 1.16. This enables ammonia storage at ambient temperature and pressure, drastically limiting ammonia release in the event of a leak, and removing the need for active cooling (greatly reducing the cost of long term storage). However, the binding of ammonia to solid sorbents means that heating will be required in order to release the ammonia for use as a gas.

1.4.3 Thermal Applications

As discussed in Section 1.3, ammonia sorbents can be used to store thermal energy. Generally, ammonia sorbents are suitable for thermal energy storage below around 400 °C, due to the weaker binding when compared with processes involving oxides. Thermal energy storage can be used for heat generation, as in solar thermal energy storage, or the capture of waste heat, for example from industrial processes. The temperature of the sorption process should be matched to that of the heat being captured, and selection of an appropriate ammonia sorbent should consider this. Other important considerations include possible degradation of the material over many cycles, heat transfer rates and the kinetics of ammonia sorption. Aside from purely storing thermal energy, it is possible to convert the stored thermal energy into electricity, usually by use of heating steam to drive a steam turbine.

Thermally powered cooling can also be performed with ammonia sorbents. The principle behind this revolves around a sorbent chamber, a condenser chamber, and an evaporation chamber, all separated from one another to ensure heat exchange between the chambers is minimised. The sorbent chamber will be filled with an ammonia sorbent, such as $CaCl_2$, while the condenser and evaporator chambers are for the working fluid, ammonia. The simple cycle process works as below:

1. The sorbent chamber is heated with an external heat source. This causes an increase in temperature and pressure (through both heating and desorption of ammonia from the sorbent).

2. The sorbent and the condenser chambers are connected, and heating of the sorbent chamber continues. This causes ammonia to be continually released in the sorbent chamber, and to condense in the cool condenser chamber due to the increased pressure. The condenser chamber is kept at room temperature during this condensation process by water cooling.

3. The liquid ammonia is passed to the evaporator. As the sorbent chamber cools naturally after heating, the pressure in the system drops (through both cooling and absorption of ammonia by the sorbent). The pressure drop causes liquid ammonia in the evaporator to evaporate, cooling it down. This cooling of the evaporator and subsequent heat absorption from the surroundings is the refrigeration effect desired.

More complex cycling methods are possible to overcome the intermittent nature of cooling. The primary benefit of this method is the use of heat for refrigeration, as opposed to the electricity required in traditional refrigerators. This allows for the use of waste heat or solar thermal energy and does not require connection to the electricity grid, a crucial aspect for use in remote locations or many developing countries.

Ammonia is a good working fluid for thermally powered cooling due to its low boiling point (−33 °C). This enables evaporative cooling to work down to sub-zero temperatures. The optimal ammonia sorbent will have a large ammonia storage capacity, which is released at relatively low temperatures, minimising the thermal energy required to begin the process. Considerations must also be given to stability, lifetime and kinetics of ammonia sorption.

Chemical heat pumps can be used to upgrade the temperature of thermal energy. When upgrading heat from ambient temperature, as is found for heat pumps used in homes, they are commonly referred to as heat pumps. They are referred to as thermal transformers when the supplied heat is above ambient temperature. Despite the difference in name, the operation principles of heat pumps and thermal transformers are identical. In fact, chemical heat pumps are very similar to thermally powered coolers; both do work to create a temperature gradient. However, as the goal is to obtain high temperature heat, the sorbent chamber is used to release heat at the desired location.

Heat pumps and thermal transformers using ammonia-salt working pairs must ensure the desorption temperature of the salt-ammonia complexes are close to the desired input and output temperature respectively. For heat pumps in homes this would usually be liquid ammonia for input (as it will easily evaporate at ambient temperature), and a salt-ammonia complex with a desorption temperature slightly above ambient. For thermal transformers this will vary depending on the application, but may involve two ammonia-salt working pairs.

2

Ammonia Sorbents

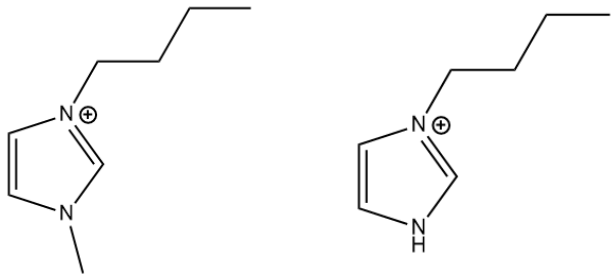
Ammonia sorption has been approached from multiple directions, ranging from dissolution to absorption and adsorption methods. The binding strength, and hence the pressure-temperature-composition surface, varies greatly depending on the sorption method and the material.

2.1 Deep Eutectic Solvents and Ionic Liquids

Ionic liquids (ILs) and deep eutectic solvents (DESs) work by dissolution of gaseous ammonia into a liquid; those typically used as solvents for DESs and organic salts with a low melting point for ILs. The bonding interactions for conventional ILs and DESs driving this dissolution are the same as those in liquid ammonia or water:

polar/ionic interactions and hydrogen bonding. Due to these relatively weak bonding interactions, ILs and DESs tend to work best for low temperature applications, such as ammonia storage, thermal processes or ammonia capture from the waste gas of certain industrial processes (typically not Haber-Bosch due to the higher temperature requirements). In fact, absorption of NH_3 by water, which works in the same way as ILs or DESs, has often been used for low temperature ammonia capture. However, water's volatility and high heat capacity (leading to high energy input when regenerating the sorbent) has left alternatives to be sought[79].

Many studies of ionic liquids have focused on an imidazolium backbone[80]. Initially, research on ILs focused on their use as hydrogen bond acceptors, with large anions such as PF_6^- and BF_4^- used to bond to the positively charged hydrogens of NH_3. However, absorption capacities were limited without elevated pressure (0.2 mol NH_3 per mol of IL). Shang *et al.*[81] showed much greater ammonia absorption capacities could be achieved by use of a protic ionic liquid, such as [bim][NTf2]. The use of an ionic liquid which can act as both a hydrogen bond acceptor and a hydrogen bond donor increased ammonia capacity around 10× (2.69 mol NH_3 per mol of IL) for ambient pressure and temperature.



(a) **(b)**

Figure 2.1: Imidazolium cations used in ILs. (a) shows 1-butyl-3-methylimidazolium (bmim), a conventional IL cation. (b) shows N-butylimidazolium (bim), a protic IL cation. The removal of the methyl group in place of a hydrogen allows for strong hydrogen bonding to the NH_3 lone pair.

The next generation of ILs, metallic ILs, combined the strong bonding of metal cations to ammonia with the better mass transfer characteristics of a liquid. By use of imidazolium cations with complex anions containing metals, even stronger NH_3 bonding could be achieved. Chen *et al.*[82] showed the far greater ammonia binding achieved using MILs (Figure 2.2) by studying [bmim]Zn_2Cl_5. Wang *et al.*[83] took this further, studying a range of MILs based on [bmim] with a metal chloride complex anion. This showed MILs could achieve up to 50× gravimetric capacity of NH_3 compared to conventional ILs (Figure 2.3), with a $NiCl_4^{2-}$ anion producing the greatest NH_3 capacity.

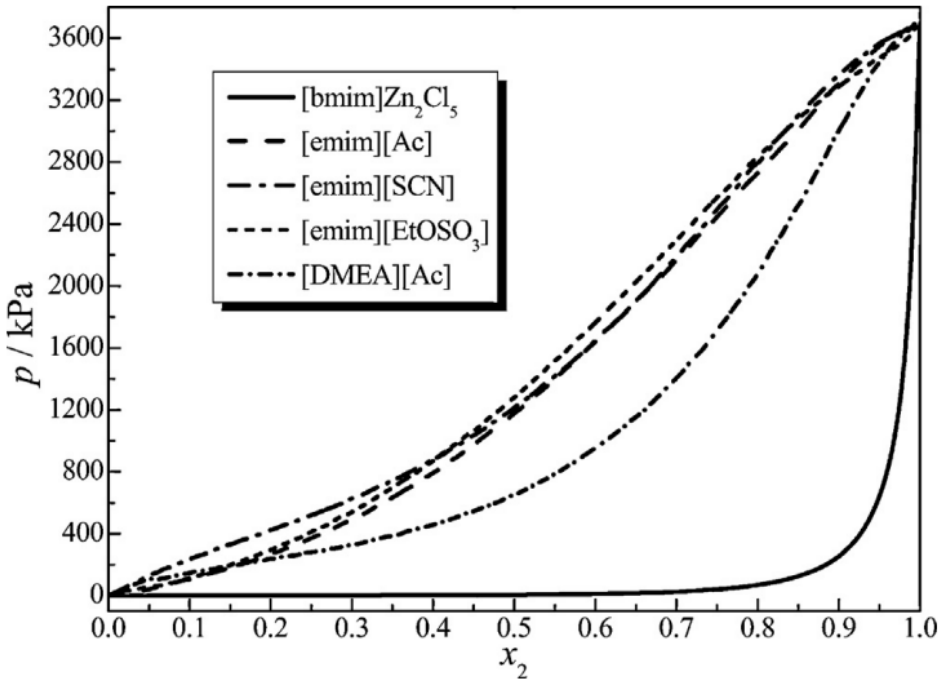


Figure 2.2: Pressure-composition isotherms for various ILs at 348 K. x_2 is the molar fraction of NH_3. The extreme deviation from linearity for [bmim]Zn_2Cl_5 indicates chemical absorption, as opposed to physical absorption. Figure adapted from Chen *et al.*[82]

The extreme deviation from linearity for ammonia absorption in [bmim]Zn_2Cl_5 (Figure 2.2) signifies chemical absorption of ammonia (i.e. a significant rearrangement of atoms/ions is occurring) compared to typically physical absorption shown for conventional ILs. By use of DFT, Wang *et al.*[83] showed the method of this chemical

absorption, with ammonia typically replacing the chloride ligands and forming ammoniate complexes such as $[Ni(NH_3)_6]^{2+}$ or $[Cu(NH_3)_4]^{2+}$. In fact, for some metals such as Cu, this binding was so strong that it significantly affected the reversibility of the process, leading to a significant loss of performance on each cycle. For other, weaker coordinating metals, such as Sn, ammoniate complexes did not form, lowering the ammonia sorption capacity, but greatly improving reversibility. For Sn, the bonding interaction was primarily hydrogen bonding from $[SnCl_4]^{2-}$ to the NH_3. Metallic ILs are commonly solid until slightly above room temperature, and as such many can only be used at slightly elevated temperatures.

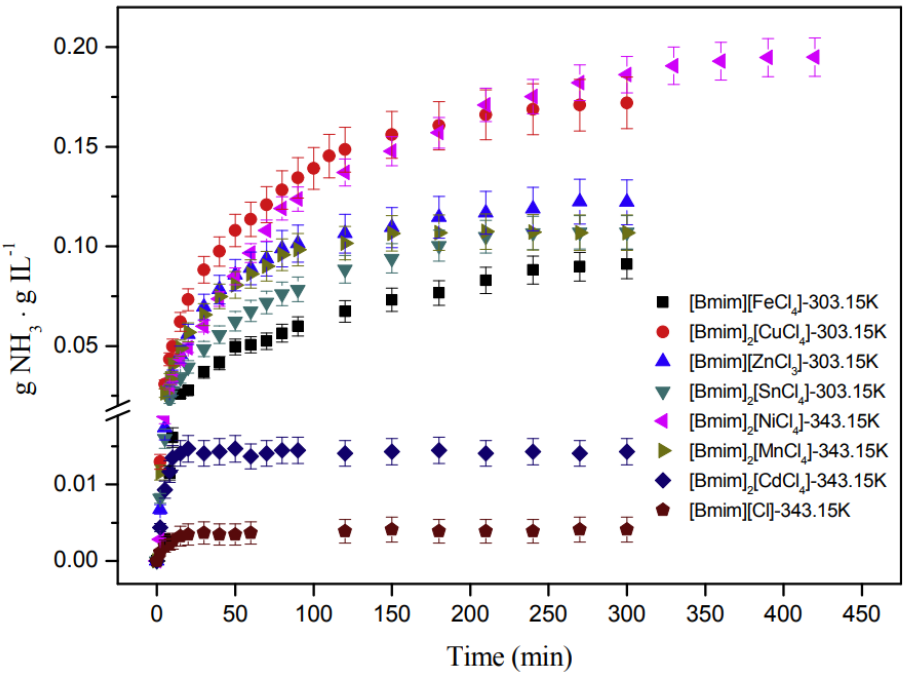


Figure 2.3: Ammonia absorption into various MILs as a function of time at an ammonia pressure of 100 kPa. It is clear to see that the inclusion of metal cations increases the ammonia absorption capacity of the liquid. Figure adapted from Wang *et al.*[83]

Deep eutectic solvents are an alternative to ILs, aiming to overcome some of the shortfalls of ILs. DESs are typically cheaper, more sustainable and more biocompatible than ILs. Importantly, they also show lower viscosities compared to ILs, due to their weaker electrostatic interactions, though this generally comes with increased volatility.

Deep eutectic solvents commonly use a similar hydrogen bond acceptor and donor approach to ensure NH_3 absorption is favourable. However, similar to conventional ILs, there are no clearly defined active sites (as in many MILs), and so absorption capacity tends to vary smoothly with pressure. Hydrogen bond acceptors are often chloride (e.g. choline chloride) or nitrogen based (azoles), while hydrogen bond donors are often oxygen (e.g. phenol or glycerol) or nitrogen based. Zhong *et al.*[84] have demonstrated an ammonia absorption capacity of 130 g/kg at 313 K and 100 kPa for a 1:7:4 mixture of choline chloride, phenol and ethylene glycol; a much higher ammonia absorption capacity than many other DESs.

Similar to ILs, various studies have examined incorporating metal chlorides into the DES. Rather than being a complex anion, as in MILs, metal-containing DESs simply mix the metal chloride into the solvent mixture. As shown for ILs, this can lead to much greater ammonia absorption capacities due to the strong Lewis acid-base interaction for metal cations and ammonia. Again, this will change physical absorption to chemical absorption, leading to diminished binding once metal sites are saturated. Sun *et al.*[85] studied a range of resorcinol-ethylene glycol (1:2 molar ratio) mixtures with and without 3.33 mol% of dissolved MCl_2 compounds. As shown in Figure 2.4, even a small amount of metal chloride can make a significant difference to the ammonia absorption capacity of the mixture. While effective, it should be noted that the solubility of metal chlorides in organic solvents is likely limited, and so increasing the mol % of metal chlorides beyond 3.3 % may be difficult. In fact, Sun *et al.* were unable to form a homogeneous mixture when using $CuCl_2$.

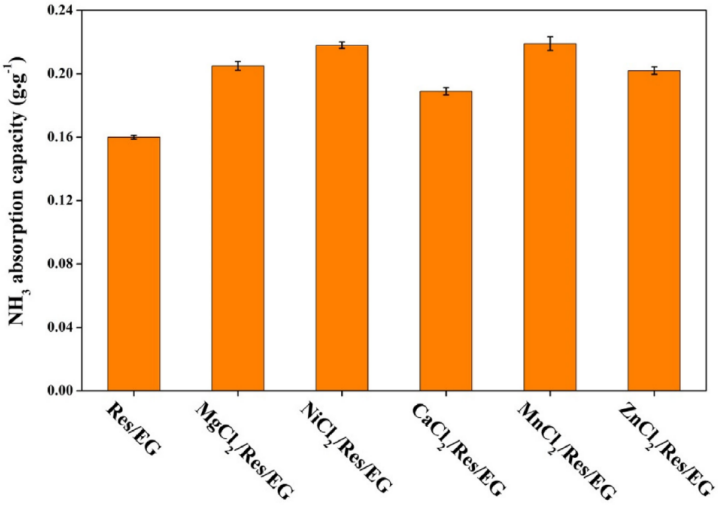


Figure 2.4: Ammonia absorption capacity into various metal-containing DESs at 313 K and 100 kPa. Molar ratio of components was 0.1:1:2 MCl_2 : resorcinol : ethylene glycol. Figure adapted from Sun *et al.*[85]

Sun *et al.*[85] also investigated the effect of increasing $MgCl_2$ content on the ammonia absorption capacity of their DESs. This showed increasing capacity with increasing $MgCl_2$ concentration, with a maximum capacity of 239 g/kg at 100 kPa and 313 K achieved for a 0.25:1:2 ratio of MCl_2 : resorcinol : ethylene glycol. However, they did not investigate greater $MgCl_2$ concentrations, which may show even higher capacities (although the concern about solubility of salts in organic solvents remains).

It is important to note that deep eutectic solvents and ionic liquids have been studied for the capture of various harmful gases, including NOx, SOx and CO_2. However, through design, high selectivity for NH_3 can be achieved due to ammonia's high basicity and hydrogen bonding ability compared to many other gases.

2.2 Metal Organic Frameworks

Adsorption is the process of binding onto the surface of a material. Traditional adsorption materials such as zeolites and porous carbon work by having very large internal surface areas, allowing for many molecules to interact with a surface simultaneously. Zeolites primarily consist of aluminium, silicon and oxygen in very large, porous structures. The bonding between ammonia and adsorption materials is often weak physisorption, and thus applications can be limited to the low temperature regime.

Metal organic frameworks (MOFs) are large, porous structures composed of a metal cation and an organic linker molecule. The porous structure, and high internal surface area of MOFs allows for fast kinetics and limited hysteresis in their application. While the porous structure allows for fast kinetics, it does greatly increase the volume occupied by MOFs. MOFs typically work by surface adsorption, and the wide array of possible cations and organic ligands allows for extensive design of active sites and precise engineering of pores. Design can therefore enable enhanced gas adsorption properties and enhanced selectivity. However, some MOFs can degrade in the presence of corrosive gases such as ammonia[86], and the chemical stability of any MOF-based ammonia sorbent must be studied carefully.

Various design strategies have been used for enhancing ammonia absorption, including open metal sites, structural transformations, charge transfer and NH_3 incorporation into the ligand. An open metal sites strategy refers to the synthesis of a MOF with a coordinated solvent molecule, which is then removed under vacuum, leaving a coordinatively unsaturated metal site. As there is very little reorganisation associated with ammonia binding to an open site, the binding strength is increased. Rieth *et al.*[86] demonstrated the enhanced absorption capacity of an open metal site MOF with their design (manganese ions connected by bisbenzenetriazolate linkers) achieving 263 g/kg at ambient pressure and temperature. These results were demonstrated to be reversible for 3 cycles, but no further cycling data was obtained.

MOFs based off a metal (M = Cu, Zn, Cd) with a 1,4-benzenedicarboxylic acid (BDC) linker undergo structural transformations when exposed to small coordinating molecules such as ammonia. Figure 2.5 (adapted from Chen *et al.*[87]) shows the reversible structural transformations occurring to enable ammonia binding. The Cu variant of this MOF showed the greatest absorption capacity, achieving 292 gNH_3/kg under standard conditions. Likely in part due to the significant structural change occurring on sorption, these MOFs required vacuum and temperatures up to 200 °C in order to regenerate the original MOF. However, despite the high regeneration temperature (which can also lead to degradation of MOFs), this process was shown to be reversible for at least 3 adsorption cycles for Zn and Cd (no further data obtained) and at least 10 cycles for Cu (no further data obtained).

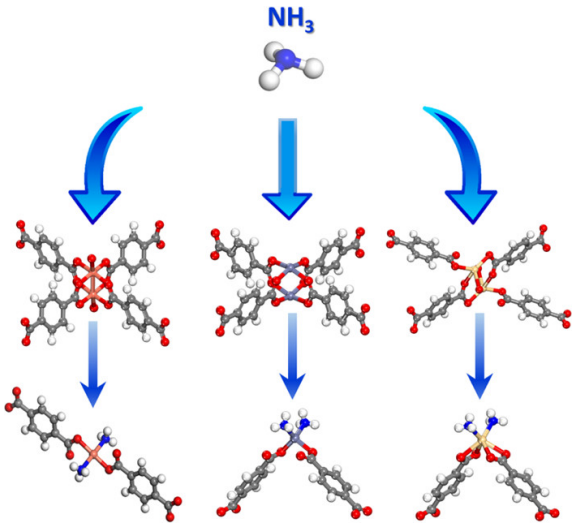


Figure 2.5: Structural Change on Ammonia Absorption in M(BDC) MOFs where M = Cu, Zn, Cd (left to right). The BDC ligands initially bridge between metals, but are displaced by NH_3. Adapted from Chen *et al.*[87]

MFM-300(V^{IV}) shows a very interesting mechanism of ammonia absorption, allowing it to achieve 294 g/kg ammonia sorption capacity. This is enabled by conversion of ammonia into hydrazine (N_2H_4) and ammonium (NH_4^+) on absorption, with an associated reduction of V^{IV} to V^{III}. This conversion is stabilised by an extensive hydrogen bonding network within the pores of MFM-300, as shown in Figure 2.6[88].

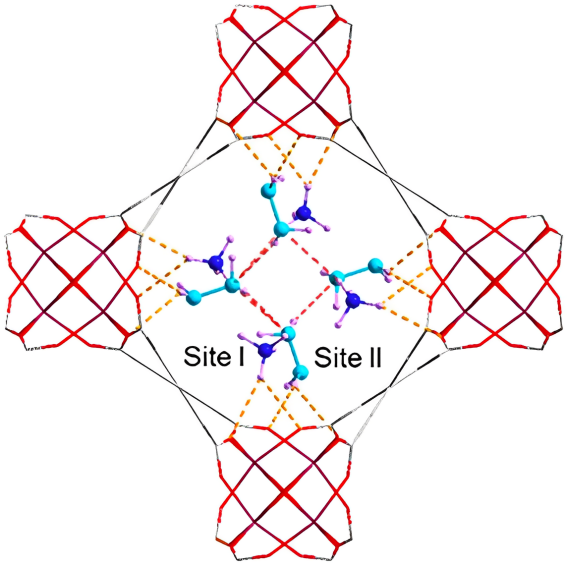


Figure 2.6: NH_3 Absorption in MFM-300(V^{IV}). Light blue atoms are nitrogen atoms of N_2H_4 while dark blue atoms are those of NH_4^+. The occupancies of each site were seen to be variable depending on the amount of ammonia absorbed. Adapted from Han *et al.*[88]

Another recent breakthrough in ammonia absorption by MOF materials came from Snyder *et al.*[89]. By use of a MOF formed from 1,4-cyclohexanedicarboxylate (cyhdc) and Cu^{2+}, they were able to show high ammonia absorption capacities (289 g/kg) at very low pressures (200 mbar) and room temperature. In this MOF, the Cu site is coordinatively saturated, and one of the Cu-O bonds must be displaced to enable NH_3 bonding. However, due to the strong hydrogen bonding between NH_3 and the now displaced carboxylate group, this is better seen as an insertion into the Cu-O bond. This can be seen in Figure 2.7.

While MOFs can show good gravimetric ammonia capacity at ambient temperatures and pressures, due to the large porous structures exhibited they often show limited volumetric capacity. Their stability over many cycles must be studied further before they find significant use in applications.

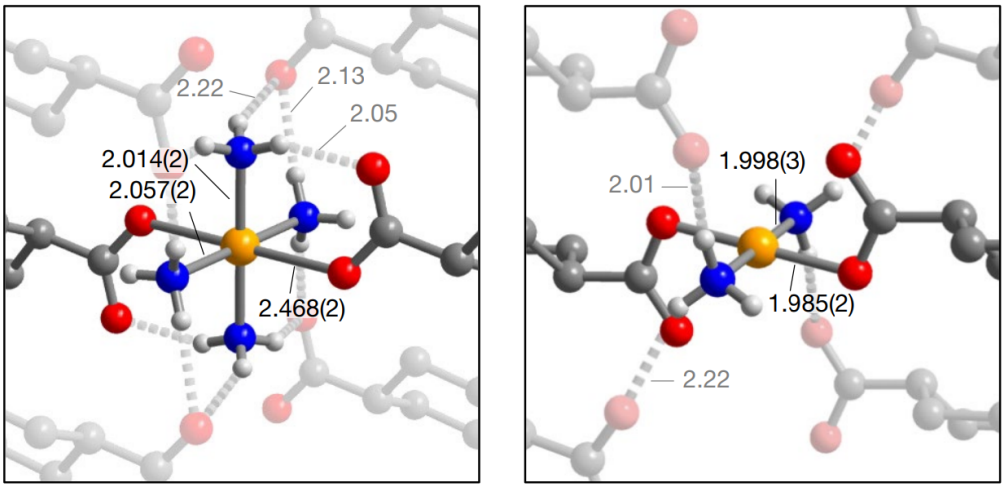


Figure 2.7: NH_3 Absorption in Cu(cyhdc). The left image shows the coordination environment when 4 NH_3 molecules are bound, and the right image shows the environment when 2 NH_3 molecules are bound. Cu is shown in yellow, O in red, N in blue, C in dark grey and H in light grey. Adapted from Snyder *et al.*[89]

2.3 Metal Borohydrides

Metal borohydrides have previously been studied for hydrogen storage due to their high hydrogen capacity (up to and over 10 wt% H_2). However, issues with the reversibility of the hydrogen release process have prevented their use thus far. Metal borohydrides have since been studied as ammonia storage materials. Metal borohydrides form crystalline structures with bridging BH_4^- units. When coordinated by ammonia in a metal borohydride ammoniate, the bonding is significantly more flexible. The NH_3 can be viewed to insert itself into the M-HBH_3^- bond, replacing this interaction with bonding to the metal cation via the N lone pair, and bonding to the BH_4^- ion via di-hydrogen bonds ($H^{\delta+}$ of NH_3 to $H^{\delta-}$ of BH_4^-).

Compared to MOFs and DESs or ILs, metal borohydrides typically undergo much greater structural changes upon ammonia absorption. Correspondingly, metal borohydrides form ammoniates of integer numbers of ammonia and, due to the stronger bonding, with much higher release temperatures than MOFs or DESs/ILs.

Metal borohydrides, in part due to the low mass of the borohydride counterion, show much larger ammonia capacities than DESs/ILs, reaching 1460 gNH_3/kg sorbent for $Ca(BH_4)_2$, an order of magnitude higher than MOFs or DESs/ILs.

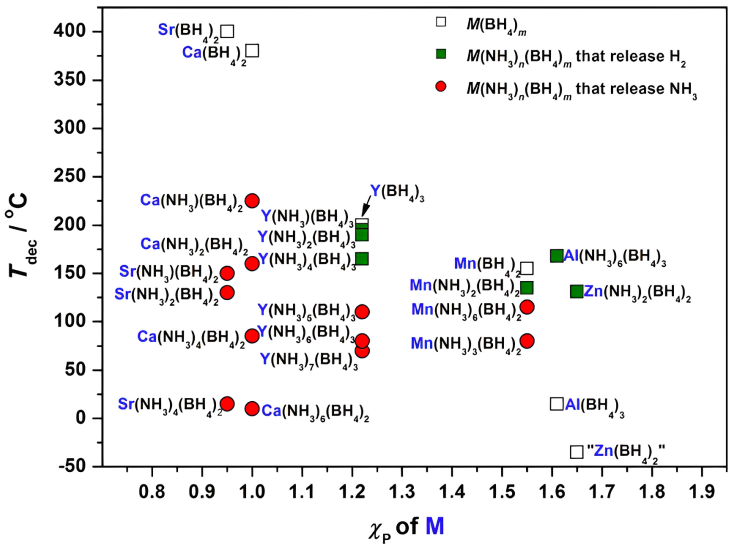


Figure 2.8: Decomposition temperatures of various metal borohydride ammoniates against the electronegativity of the metal cation. Figure adapted from Jepsen *et al.*[90]

Due to the di-hydrogen bonds in metal borohydride ammoniates, it is kinetically feasible that heating of a metal borohydride ammoniate leads directly to hydrogen release, as opposed to ammonia release. It has been suggested this is more likely for less stable metal borohydrides with higher electronegativity cations such as Al, Zn, Mn and Y. This is consistent with the data shown in Figure 2.8 (adapted from Jepsen *et al.*[90]). Similarly, electronegativity of the metal cation has been suggested as a key factor in the room temperature ammonia vapour pressure of metal borohydrides, with lower metal electronegativity giving greater vapour pressures (implying weaker ammonia bonding).

While the ammonia absorption ability of certain metal borohydrides is strong, care must be taken in their use, due to their instability to heat and moisture. Figure 2.9 shows the decomposition process of $Ca(BH_4)_2(NH_3)_4$ as it is heated from room

temperature to 500 °C. It is clear to see the 3 step ammonia release undergone by this compound. However, if heated to > 350 °C, there is a risk of irreversible decomposition of the borohydride itself.

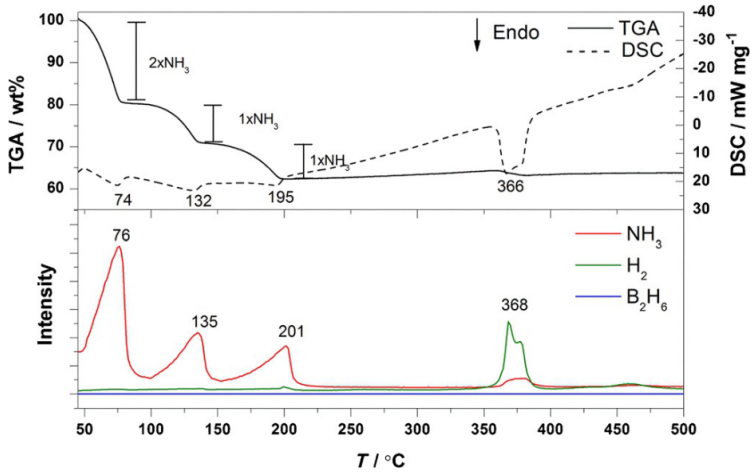


Figure 2.9: Thermogravimetric analysis, differential scanning calorimetry and mass spectrometry of $Ca(BH_4)_2(NH_3)_4$ heated to 500 °C. Integer quantities of NH_3 are released, prior to decomposition of the borohydride itself at 368 °C. Figure adapted from Jepsen *et al.* [90]

2.4 Metal Halides

Ammonia absorption into metal halides fundamentally works in a similar way to metal borohydrides. The primary difference is the anion involved. However, this can affect the properties in important ways. BH_4^- has a mass of 14.8 amu while Cl^-, the smallest halide that generally allows absorption, has a mass of 35.5 amu. This can lead to slightly lower gravimetric ammonia absorption capacities in metal halides compared to metal borohydrides, but still vastly higher than MOFs and DESs/ILs. However, in general, metal halides are much more stable than metal borohydrides and do not suffer from facile decomposition from heat or moisture. Similarly, due to the lack of di-hydrogen bonding in metal halides, they do not show hydrogen release upon heating.

As was observed for metal borohydrides, there is a general correlation between the vapour pressure of ammonia over a salt, and the electronegativity of the metal and halide. Aoki *et al.* found that the greater the electronegativity of the metal, and the lower the electronegativity of the halide, the lower the NH_3 vapour pressure. While Aoki *et al.*[91] observed the correlation between cation and anion electronegativities and ammonia vapour pressure, no explanation was offered for either trend. Jones *et al.*[92] observed a similar trend in the desorption temperatures of the $MgX_2(NH_3)_n$ series (X = Cl, Br, I), with larger, less electronegative anions leading to greater desorption temperatures. Their explanation was not focused on electronegativity as solid state NMR showed minimal effect from the halide on Mg-N bonding. Instead, it was rationalised as an effect on the change in lattice enthalpy upon removal/insertion of ammonia. As ammonia absorption increases the size of the cation (Mg^{2+} forms $Mg(NH_3)_n{}^{2+}$), this lowers the lattice enthalpy of the solid. However, as lattice enthalpy generally scales with the reciprocal of the interionic separation (according to the approximations of the Kapustinskii Equation[93]), this change in lattice enthalpy is less significant for larger halides, leading to larger ammonia sorption enthalpies. This also explains why no solid group I or II metal fluoride (HF gas will) absorbs ammonia at room temperature and pressure, due to the high ionic bonding enthalpy which will be interrupted upon ammonia insertion.

In general, it is observed that group I metal halides do not absorb ammonia into a solid phase, with the exception of lithium[94] and hydrogen (NH_4X being the absorbed phase). All group II metal halides (except radium and fluorides)[95,96] and many 2+ transition metal halides[97] have been shown to absorb ammonia into the solid state. This is mostly consistent with the electronegativity correlation observed. However, electronegativity is likely an oversimplification, due to the observation of $BaCl_2$ absorbing to form $BaCl_2(NH_3)_8$ at a little over 1 bar and room temperature,

while NaCl has not been shown to absorb ammonia at room temperature and elevated pressures, despite sodium possessing a higher Pauling electronegativity value (0.93 vs 0.89)[98].

Following the observed electronegativity trend, it is logical to expect group III/XIII and IV metal halides to bond even more strongly to ammonia than group II metal halides, and possibly even some metal fluorides to absorb ammonia at close to ambient temperature and pressure. Indeed, ammoniates of aluminium fluoride and zirconium fluoride have been synthesised under extreme conditions[99,100]. Despite the extreme synthesis conditions, these have been studied by single crystal X-ray diffraction under ambient conditions, suggesting stability of these phases. Various other group III/XIII and IV metal halide ammoniates have been observed, but the majority of metal halide ammoniate research has focused on group II metal halides or transition metal (2+) halides, likely due to their lower molar mass and volume (MX_2 vs MX_3 or MX_4), and hence greater ammonia capacity.

Table 2.1: Ammoniation numbers of various group II metal halides, $MX_2(NH_3)_n$[95,96].

	Be	Mg	Ca	Sr	Ba
Cl	2, 4	1, 2, 6	1, 2, 4, 8	1, 2, 8	8
Br	2, 4	1, 2, 6	1, 2, 6, 8	1, 2, 8	1, 2, 4, 8
I	2, 4	2, 6	1, 2, 6, 8	1, 2, 6, 8	2, 4, 6, 8

Table 2.1 shows the metal halide ammoniates experimentally observed for group II metal halides of the form $MX_2(NH_3)_n$. The greatest ammoniation number of each salt tracks with the highest coordination number possible for the metal i.e. 4 for Be, 6 for Mg, 8 for Ca, Sr, Ba. Beyond this however, there is limited correlation to be examined within or between groups.

Due to the relatively strong M-N bonding, the high abundance of Mg and Ca and the low mass of the chlorine atom, $MgCl_2$ and $CaCl_2$ are two of the most well studied metal halides for ammonia absorption applications. $MgCl_2$ releases ammonia in 3 steps (as shown in Figure 2.10), with $n = 1$, 2, 6 of $MgCl_2(NH_3)_n$ being stable. The structures of the $n = 2$ and $n = 6$ phases are shown in Figure 2.11 [101,92].

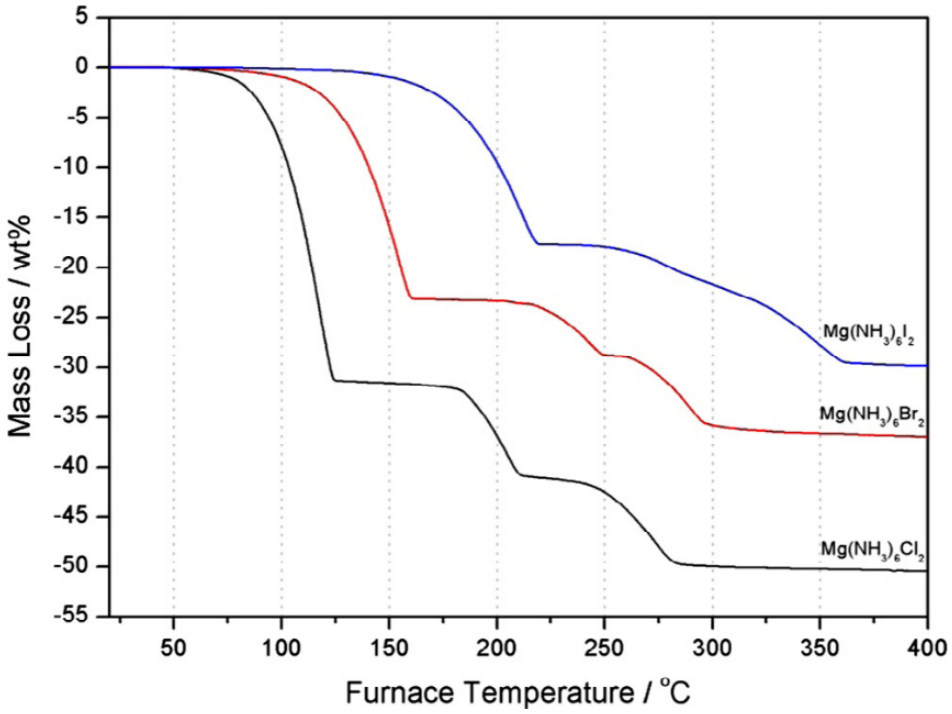
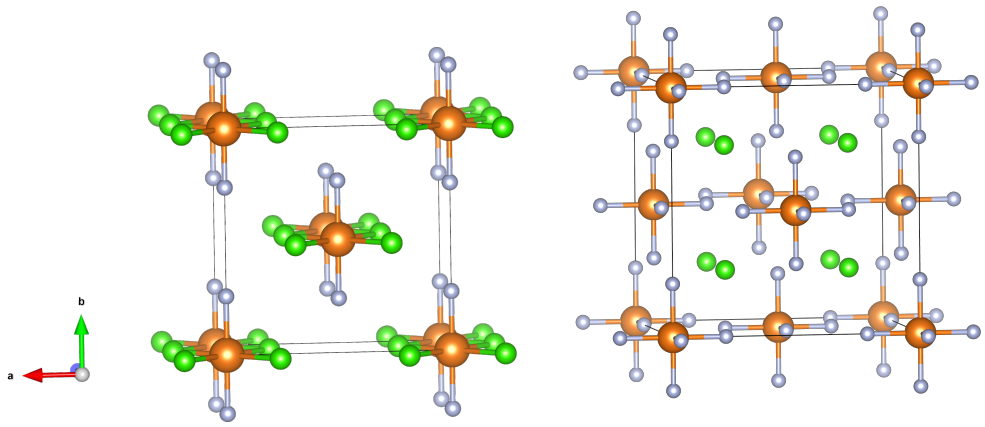


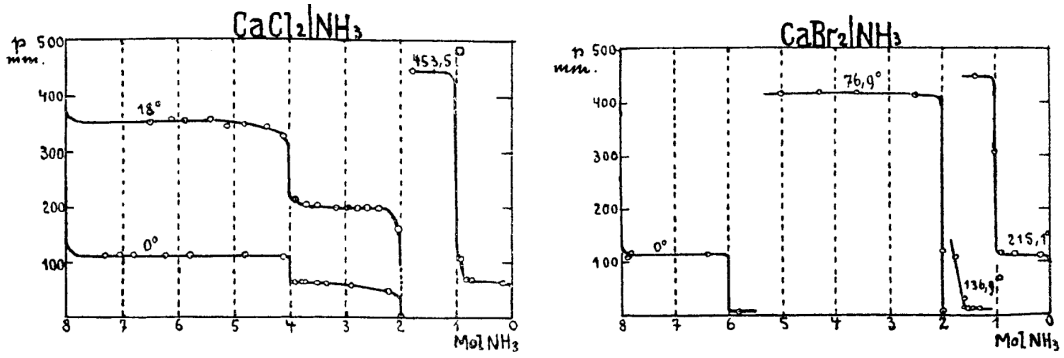
Figure 2.10: TGA of the desorption process of $MgX_2(NH_3)_6$ (X = Cl, Br, I) under a flowing argon atmosphere. Heavier halides lead to greater temperature stability of ammoniate phases. Figure adapted from Jones *et al.* [92]

While limited progress has been made in the fundamental understanding of metal halide ammoniate phase formation, there is extensive research into the use of these materials. Yan *et al.* [103] studied the use of manganese chloride ammoniates for thermochemical energy storage, achieving energy storage densities of 1391 kJ/kg and 644 MJ / m^3. With charging temperatures of 150–174 °C and discharge temperatures of 50 °C, this study was aimed at capturing low grade waste heat from industrial processes, though the temperatures used are also appropriate for solar collectors. In



(a) **(b)**

Figure 2.11: Crystal Structures of $MgCl_2(NH_3)_n$. (a) shows the structure of $n = 2$ $(Cmmm)$[101], while (b) shows the structure of $n = 6$ $(Fm\bar{3}m)$[92]. Mg ions are depicted in orange, while chlorine is green and nitrogen is light blue/grey. Hydrogen atoms are omitted due to uncertainty about their position in the crystal structure determination.



(a) **(b)**

Figure 2.12: Pressure-composition isotherms for the (a) $CaCl_2$-NH_3 and (b) $CaBr_2$-NH_3 systems. Vertical lines indicate stable ammoniate phases. Figure adapted from Hüttig[102].

order to improve the heat and mass transfer properties, and avoid agglomeration of ammoniate materials, expanded graphite was used as an additive (15% of final solid sample by mass) to the $MnCl_2$ sample. As a result, for a charging temperature of 174 °C, the average power achieved during discharge reached 2.62 kW per kg of solid material with an energy storage efficiency of 48%. The high storage efficiency, power and storage density illustrate the possibilities of this technology for heat recovery, conversion and long term (e.g. seasonal) energy storage.

Various studies have examined the possibility of ammonia synthesis utilising metal halide absorption-based separation methods[62,104,105,63,61]. These have typically focused on metal halides showing strong ammonia binding, primarily $MgCl_2$ and $MnCl_2$. Smith *et al.*[60] demonstrated the possibility of simultaneous synthesis and absorption by integrating the catalyst (Ru/Cs supported on CeO_2 nanoparticles) and absorbent ($MnCl_2$ supported on SiO_2) setup. With absorption of ammonia *in-situ*, the equilibrium of the synthesis reaction is never reached (by continuous removal of synthesised ammonia), and gas recycling is not required. The system consisted of an initial reactor with only catalyst present, followed by a reactor with both catalyst and sorbent present. Using a pressure of 20 bar, a 3:1 mixture of H_2:N_2 and a temperature of 360 °C, the percentage conversion to ammonia after reactor 1 was 15%, improving to 25% after the integrated reactor-absorber. Under these conditions without absorber present, equilibrium is equivalent to 22% conversion. It is important to consider the pressure reduction possible through the use of integrated reaction-absorption. With reaction-absorption exceeding the typical gas equilibrium mixture, the need for high pressure in ammonia synthesis is potentially removed. However, the absorption rates of sorbents in these systems have been consistently reported as highly dependent on ammonia pressure[64,60,62]. As such, excessive pressure decreases may produce insufficient ammonia production rates even in an integrated reactor-absorber.

While the strong binding of $MgCl_2$ and $MnCl_2$ to ammonia has led to its preference for higher temperature applications, such as ammonia separation from Haber-Bosch, calcium chloride has commonly been touted as a potential ammonia storage compound due to its large ammonia storage density and ease of decomposition for phases with $n > 2$. In a series of papers, Liu *et al.*[106,107,108,109] demonstrated the possibility of calcium halides (in particular calcium chloride) for ammonia storage through simple pressure swing absorption, taking advantage of the low stability of the higher ammoniate phases. With a modest reversible pressure swing of 10–80 kPa (at 298 K), they were able to demonstrate an ammonia storage capacity of 15.3 mmol g^{-1} for $CaCl_2$.

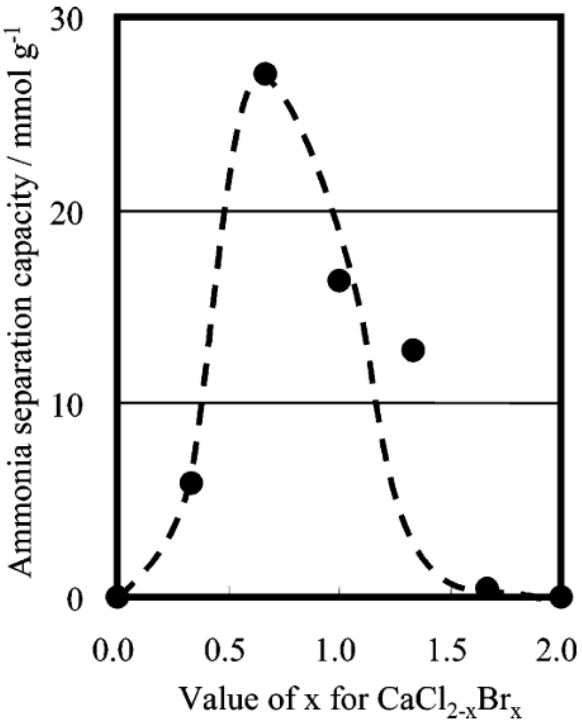


Figure 2.13: Ammonia storage capacity of $CaCl_{2-x}Br_x$ samples under a PSA method from 10–60 kPa at 298 K.

Through the use of mixed calcium chloride-bromide materials, Liu *et al.* were able to optimise the absorption and desorption equilibria to achieve even greater ammonia storage capacities for pressure swings of 10–60 kPa at 298 K. The results

of this are presented in Figure 2.13. The control of sample composition allows for optimisation of the process given certain PSA conditions. However, this study only examined PSA at low pressure, and thus did not examine the effect of sample composition on ammoniate formation at elevated temperatures.

2.5 Material Reasoning

For any technology to be a significant part of the solution to climate change, it must be based around abundant, cheap, environmentally friendly materials. As discussed in Section 1.2.1, it is unlikely that the current most common form of battery, the lithium ion battery, will take over the transportation market, due to issues accessing enough of the resources needed to produce these batteries on a global scale.

Similarly, developing ammonia absorption materials from rare minerals is unlikely to lead to their use on a global scale. As such, the materials studied within this thesis in the context of applications are all earth abundant and cheap where possible. Many other metal halides have been studied using computational methods, in order to enhance the understanding of structure and bonding in ammoniates.

It is also crucial that materials do not irreversibly nitride during operation. Stable metal nitrides are limited in the s-block of the periodic table, but common in the first row of the transition metals; early transition metals can lose 3 electrons to form stoichiometric nitrides, while later transition metals form interstitial nitrides with significant metal-metal bonding. Nitrides of the s-block have only been reported to form from the pure metal at high temperatures, and as such nitridation should not be considered a concern for metal halide ammoniates of the s-block. However, there have been reports of transition metal nitride formation at elevated but modest temperatures when transition metal chlorides are exposed to ammonia. Widenmeyer *et al.*[110] reported formation of various iron nitride phases alongside NH_4Cl after thermal decomposition of $Fe(NH_3)_2Cl_2$ under an ammonia atmosphere. With decomposition of the final mole of ammonia around 300 °C and formation of

the nitrides around 340 °C, the nitridation reaction may not be avoidable during the long term usage of iron chloride ammoniates in some applications. Juza *et al.*[111,112] reported similar observations for nickel and cobalt chlorides, leading to formation of Ni_3N and Co_3N respectively. The possibility of nitridation of other transition metal halides in the presence of ammonia is unclear, but must be considered prior to their usage.

With a view to all of these aspects, experimental work in this thesis is primarily focused on sodium, potassium, manganese, zinc and calcium halides.

2.6 Thesis Aims

This thesis investigates ammonia absorption into metal halide systems, focusing on the fundamental chemical changes occurring during ammonia absorption and desorption. With many metal halide systems studied for ammonia absorption applications previously, this work seeks to extend the field in the following ways:

1. To identify and analyse the structure of all calcium halide ammoniate phases.
2. To analyse and understand the stability of calcium halide and mixed calcium halide systems under varying ammonia sorption conditions.
3. To examine the possibility of ammonia absorption into liquid metal halide systems at ammonia synthesis conditions.
4. To understand the trends in energetics and phase stability of solid ammoniate phases of a range of metal halides.

3

Experimental Methods

This chapter outlines the scientific methods used to study the materials involved in this thesis. All weighing, grinding and packaging of samples took place in an argon-filled Unilab mBraun glove box ($O_2 < 0.1\,\text{ppm}$, $H_2O < 0.1\,\text{ppm}$), before transfer to appropriate equipment.

3.1 Solid State Synthetic Techniques

3.1.1 Tube Furnace

The majority of solid-solid syntheses performed in this thesis were completed by use of a tube furnace. This involved weighing of appropriate masses of reactants, followed by grinding in a pestle and mortar for 5 minutes, before transfer to an alumina boat, which was then placed inside a cylindrical quartz glass tube, sealed at one end. The other end of the tube was then sealed using a metal adaptor fitted with a rubber O-ring and connected to a glass T-piece with three Young's taps.

Once removed from the glovebox, the tube was connected up to argon flow via the T-piece, and placed inside a horizontal tube furnace (Carbolite). The tube furnace was then set up with the appropriate temperature program and argon flow rate. Argon flow was qualitatively measured by use of a mineral oil bubbler and controlled via a pressure regulator. After reaction, the argon flow was removed and the tube furnace placed back into the argon-filled glovebox for removal of the boat and powder. The tube furnace setup is shown in Figure 3.1.

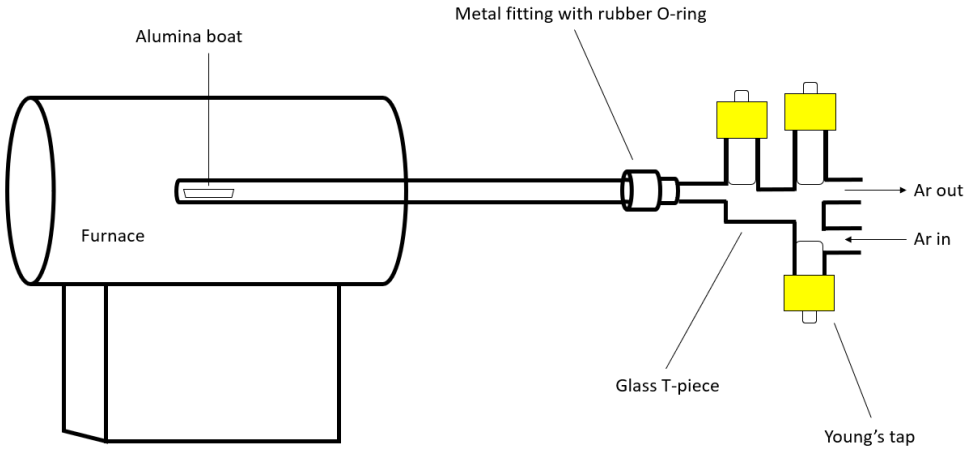


Figure 3.1: Schematic of the tube furnace setup. A glass T-piece is used to control gas flow.

3.1.2 Ball Milling

A Retsch Planetary Mill 100 was used at times in this work to reduce particle size (in order to aid future solid-solid or solid-gas reactions) or for mechanochemical synthesis purposes. The appropriate powder(s) would be weighed (0.5–1.5 g total) then transferred to a pestle and mortar for a grinding period of 5 minutes, in order to ensure homogeneity (particularly important when two powders were mixed). After grinding, the powder was transferred to a stainless steel grinding jar (Retsch, 125 mL) with a tungsten carbide interior. Alongside the powder, 5 mm radius tungsten carbide balls were also placed in the grinding jar. The number of balls used was determined by the desired ball : powder mass ratio (typically 5:1).

The grinding jar was sealed inside the glovebox, transferred to the planetary mill and clamped in place. The counterweight was set to the same mass as the grinding jar, in order to keep the mill balanced as the jar rotated around the 'Sun Wheel' (referred to as such because the 'planets' orbit around the centre of the wheel). As the grinding jar rotates around the centre of the Sun Wheel, the centrifugal force causes the balls and powder to fly around in the jar, leading to an effect similar to extensive grinding in a pestle and mortar. The ball-mill program used varied in duration (0.5–16 hr) and rotation speed (150–400 rpm) depending on the desired outcome of milling. In all scheduled ball-milling, the direction of rotation was reversed periodically to keep the sample as homogeneous as possible, with a break period between these reversals.

After the program was completed, the jar was removed from the planetary mill and transferred to the glovebox for unpacking of the sample. A small magnetic stirrer bar was used to remove the tungsten carbide balls from the sample.

3.2 Solid-Gas Reactions and Analysis

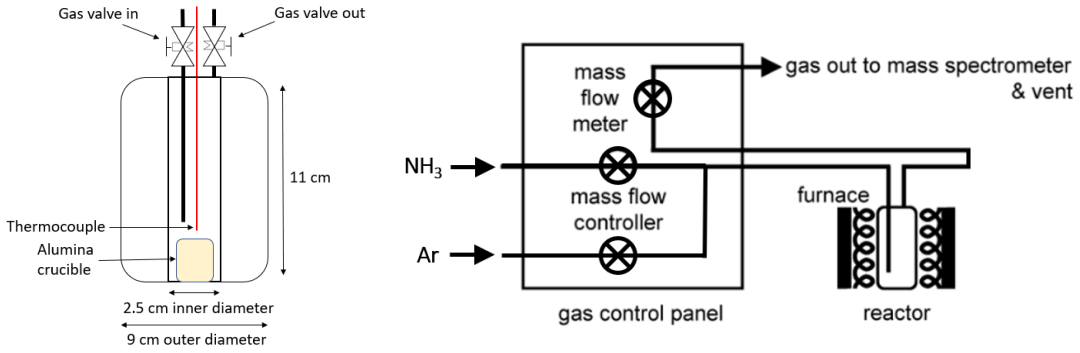
Various experimental set-ups were used in order to synthesise materials containing ammonia, and analyse the ammonia sorption properties of materials of interest.

3.2.1 Gas Flow Setup

Atmospheric Pressure

Atmospheric pressure experiments were performed using a custom-designed stainless-steel reactor with a pressure relief valve and fittings to allow gas flow in, gas flow out, and the insertion of a thermocouple for temperature measurement. After loading the sample into an alumina crucible, and placing the crucible into the reactor, the reactor was removed from the glovebox, placed in a vertical tube furnace (Severn Thermal Solutions) and connected to a custom-designed gas flow panel. The gas flow panel consists of Swagelok tubing and fittings, with HFC-302 mass flow controllers (MFCs) to control gas inflow and an HFM-300 mass flow meter (MFM) to measure outflow, all sourced from Teledyne Hastings Instruments. While pressure control was not possible during the experiments, a pressure gauge was fitted to allow measurement of pressure, particularly useful when evacuation of the panel was required. The gas outlet was connected to a T-piece, allowing some gas to escape into the fumehood for ventilation, and some to travel to the Hiden Analytical HPR-20 QIC R&D mass spectrometer (MS).

Prior to the experiment, the panel was flushed with argon, then a slight overpressure introduced by sealing of valves. The taps to the reactor were then opened, and the slight overpressure (slight to avoid scattering the powdered sample) pushed any remaining air downstream away from the reactor. The furnace and MFCs could be controlled via an associated computer, allowing for temperature and gas flows



(a) **(b)**

Figure 3.2: Atmospheric pressure gas rig setup. (a) shows a detailed view of the reactor, with the location of gas in/outlets and the thermocouple. (b) shows a wider view of the gas flow panel and associated mass flow controllers and mass flow meters (edited from Makepeace *et al*[113]).

to be coordinated to the user's desired program. After the experiment was complete, the reactor was flushed with argon, before removal to the glovebox for sample unpacking.

Elevated Pressure

A second gas flow rig setup was used for experiments requiring elevated pressure (≤ 5 bar). The gas control panel is identical to the atmospheric pressure equipment except for the inclusion of a back pressure regulator, in order to control the pressure within the panel and reactor. The reactor used was a cylindrical stainless steel reactor (Cambridge Reactor Design), with a thermocouple and gas in/outlets similar to that of the custom reactor in Figure 3.2a. Due to the different dimensions of this reactor, a Cambridge Reactor Design Polar Bear Plus furnace was used to ensure

good thermal contact between furnace and reactor. This reactor was used without an alumina crucible, though the process of loading was similar to that described for the atmospheric pressure reactor. The gas flow panel setup is shown in Figure 3.3.

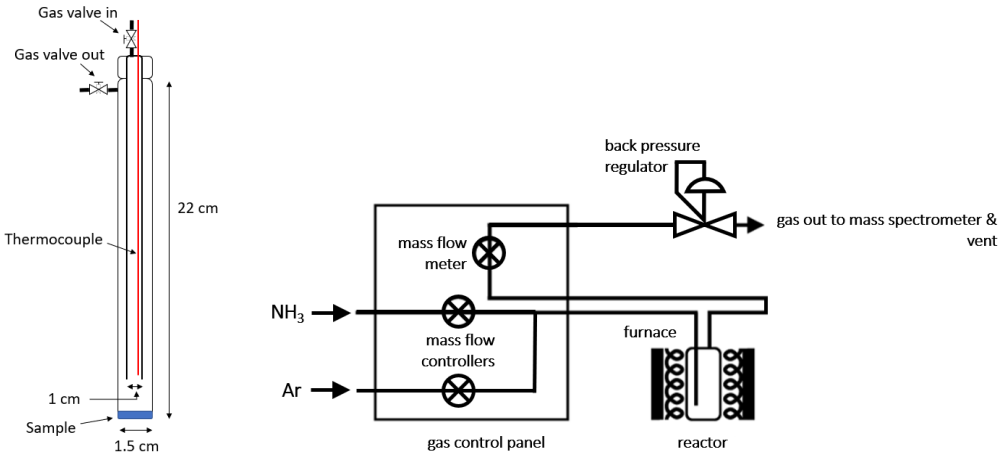


Figure 3.3: Elevated pressure gas rig setup. (a) shows a detailed view of the reactor, with the location of gas in/outlets and the thermocouple. Gas flow is directed down the inside of the inner tube onto the sample, before returning up the outside of the inner tube and through the outlet. (b) shows a wider view of the gas flow panel and associated mass flow controllers and mass flow meters (edited from Makepeace *et al* [113]).

The gas flow setups described above were used to synthesise ammoniated phases for further study and in order to directly probe the ammonia absorption properties of materials of interest.

3.2.2 Simultaneous Thermal Analysis

Thermogravimetric analysis (TGA) is the measurement of mass and temperature data simultaneously, allowing for the facile detection of chemical changes involving gas releases or absorption. Simultaneous thermal analysis (STA) is the collection of TGA data alongside differential scanning calorimetry (DSC) data. DSC is the measurement of heat changes to a sample, allowing for the detection of events asso-

ciated with an enthalpy change, and thus chemical events not associated with gas releases or absorption, such as melting or structural changes within solids, are also detectable.

STA data were collected using a Netzsch STA 449 F3 Jupiter. The STA sample carrier contains space for two pans, one reference and one sample, each with their own heater. The difference in heat flow between the sample and reference pans thus removes contributions from the pan, leaving only the heat flow due to the sample. Corrections were run prior to sample measurement, to ensure measured mass changes accurately represent the mass change of the sample. The STA allows for up to 3 gases to flow simultaneously, by use of MFCs as described in Section 3.2.1. For the majority of experiments performed, a mixture of ammonia (usually 50 ml/min) and argon (usually 10 ml/min) was used. While often preferential to use pure ammonia, Netzsch advise using an inert carrier gas such as argon in order to prevent damage to sensitive components.

Experiments were performed at atmospheric pressure, and according to pre-defined temperature programs. Sample pans were loaded with sample (∼10 mg) in the glovebox, before being transferred carefully to the instrument. An aluminium pan (∼40 mg) was used for most experiments, allowing for cold welding of a lid in the glovebox, thus sealing the pan for transfer. Immediately before placement on the sample stage, a hole was pierced in the pan lid, in order to allow gas flow in and out of the pan. This means the samples were exposed to air very briefly (∼10 seconds), though the samples used in this thesis are not sufficiently air- or moisture-sensitive enough for short exposure to have a significant impact.

For samples containing zinc chloride, a platinum crucible (∼160 mg) was used instead of aluminium. Aluminium is more reactive than zinc, leading to reaction with the crucible (Reaction 3.1). A lid was not used in these experiments. Instead,

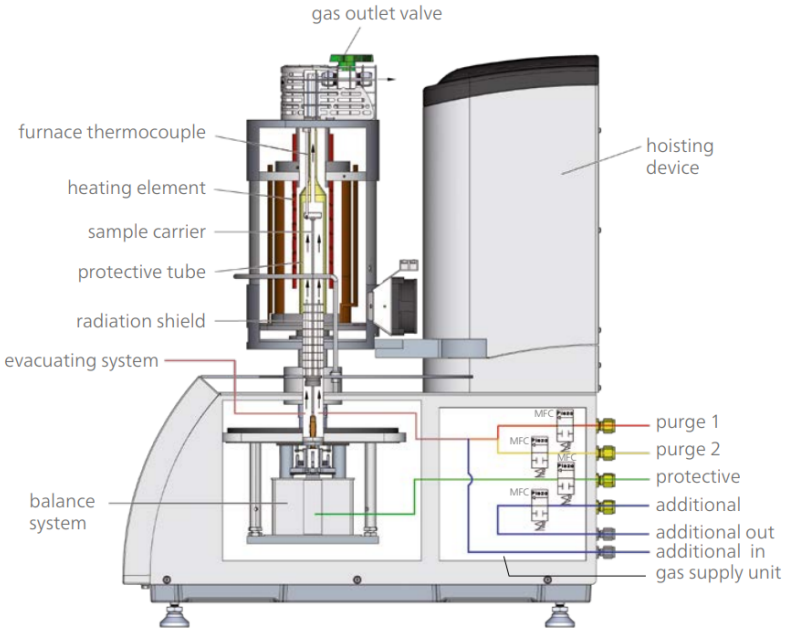


Figure 3.4: Schematic of the interior of the Netzsch STA 449 F3 Jupiter. Gas enters through the bottom of the sample chamber, flowing over the sample pan before leaving via the gas outlet at the top of the instrument. Image produced by Netzsch [114].

the loaded crucibles were removed from the glovebox in a sealed vial for transport to the instrument. Similar to the aluminium pans, the sample will have been exposed to air briefly (∼10 seconds) upon transfer of the crucible to the sample carrier.

$$3\,ZnCl_2 + 2\,Al \longrightarrow 2\,AlCl_3 + 3\,Zn \tag{3.1}$$

Experiments involving solid materials would typically involve observing absorption and desorption of ammonia as temperature is varied between room temperature and $> 350\,°C$. Experiments involving eutectic liquids would often involve switching ammonia gas flow on and off, akin to 'pressure swing absorption' methods, where a change in ammonia pressure leads to changes in the amount of ammonia absorbed into a condensed phase. Typical pressure swing absorption (PSA) methods involve atmospheric and elevated pressure (as this is generally preferable at an application scale). However, as the STA can only operate at atmospheric pressure and below, experiments were mandated to use a sub-atmospheric pressure PSA method.

3.3 Material Syntheses

Appropriate masses (totalling 1.0–1.3 g) of $CaCl_2(H_2O)_2$ and $CaBr_2$ were ground in a pestle and mortar inside an argon-filled glovebox for five minutes, prior to addition to an appropriate reactor. Initially, for syntheses from $x = 0$–2 in steps of 0.2, the heating step was performed in a tube furnace. However, this was subsequently discovered to not be fully airtight, and subsequent syntheses were performed on the atmospheric pressure gas rig described in Section 3.2.1. After addition of the ground sample to the chosen reactor, the reactor would be connected to ∼20 sccm argon flow before heating to 550 °C at a ramp rate of 5 K/min. After 40 hours at 550 °C, the reactor would be cooled to room temperature at a ramp rate of 5 K/min. The reactor was sealed and returned to the glovebox, where the sample was unloaded and ground for a further five minutes.

Table 3.1 shows the starting materials used in the work in this thesis.

Table 3.1: The starting materials used in the work in this thesis.

Material	Supplier	Purity (%)
$CaCl_2(H_2O)_2$	Sigma-Aldrich	99.0
$CaBr_2$	Fluorochem	99.5
$MnCl_2$	Thermo Scientific	97.0
NaCl	VWR Chemicals	99.5
KCl	Sigma-Aldrich	99.0
$ZnCl_2$	Fluorochem	98.0

Samples studied on POLARIS underwent the same treatment as described above. These samples were then ball milled for 30 minutes, with a 5 minute interval, 30 second break period and a 5:1 mass ratio of tungsten carbide balls : powder. This

was done to ensure homogeneity and small crystallite size, speeding up absorption of ammonia. These samples were mixed with amorphous silica prior to use on POLARIS, as described in Section 3.5.2.

Synthesis of pure ammoniate phases for structural analysis was typically performed on one of the gas flow rigs, enabling solid-gas reaction. The sample (0.2–0.5 g) was ground in a pestle and mortar for two minutes in an argon-filled glovebox before loading into the chosen reactor. Argon and ammonia flow was connected, however a pre-heating step (usually up to 300 °C) was performed under argon flow to ensure all water was driven off prior to contact with ammonia gas. The precise temperature program following this pre-heating step varied depending on the desired phase and usually consisted of cooling to room temperature under ammonia flow. Once sufficient ammonia was absorbed, ammonia flow was replaced with argon flow. This induces desorption, as some phases are only stable under ammonia pressure at room temperature. Then, the sample was heated to an appropriate region of the phase diagram in which the desired phase is stable. It was important to maintain argon flow throughout this step for two reasons. Firstly, upon cooldown, it was necessary that the sample did not absorb any ammonia. Secondly, the temperature stability of ammoniate phases is dependent on the ammonia partial pressure, and as such removing the partial pressure of ammonia can also induce decomposition of the desired phase when the temperature is elevated. It is significantly more reliable to simply decompose unwanted phases under argon flow, rather than attempt to manage the temperature and ammonia partial pressure in the reactor carefully.

Mixed-metal halide samples for study as molten salt ammonia absorbers (Chapter 6) were simply ground in a pestle and mortar for five minutes in an argon-filled glovebox. While only small masses were needed for analysis via STA (∼10 mg), samples were generally made up to 0.7–1 g to ensure error in measurement and transfer of powders was limited. Pre-analysis dehydration and melting were performed *in-situ* on the STA when these samples underwent analysis.

3.4 Temperature Cycling Experiments

The gas flow setups described in Section 3.2 were used to study the ammonia absorption properties of materials across a range of temperatures and pressures. A typical experiment would involve pressure being set to the desired value, before a temperature program consisting of multiple cycles of heating and cooling with gas inflows usually held constant. The data collected (gas inflows, outflows and MS data) informed about the identity of the sample and changes occurring within it as a function of temperature.

MFCs and MFMs do not directly measure gas flow. MFCs and MFMs actually introduce a small amount of heat to the gas stream, and measure the temperature difference at the start and end of the gas stream. This leads to a dependence on the heat capacity of the gas. The MFCs and MFMs used in these experiments were calibrated to ammonia so that, when measuring pure ammonia, the observed gas flow value is the true gas flow value. As such, the value must be adjusted when measuring any other gas e.g. argon or ammonia-argon mixtures. Gas conversion factors (GCFs) allow for conversion between the calibrated gas and other gases. While measured experimentally, GCFs closely match the ratio of heat capacities of different gases. Equation 3.2 shows the calculation of the actual gas flow. A similar equation can be formulated for gas mixtures using an adjusted GCF (which would be the weighted average of the GCFs of the individual gases), though the composition of the gas mixture must be known quantitatively.

$$\text{True Gas Flow} = \text{Measured Gas Flow} \times \frac{\text{GCF}_{\text{gas}}}{\text{GCF}_{\text{calib. gas}}} \tag{3.2}$$

With constant gas inflows throughout large periods of each experiment, any deviation between the MFM and MFC must be due to the sample or reactor. While the reactor walls (which consist mainly of iron) have been known to nitride and denitride in some experiments performed by the David group, the temperatures used in this thesis ($< 350\,^{\circ}\text{C}$) typically were not high enough to induce changes to

the reactor walls which would be measurable by gas flow analysis. As such, it is assumed that deviation between MFC and MFM is almost entirely due to interaction of the gas phase with the sample, or gas releases from the sample.

Mass spectrometry data were also collected for the majority of these experiments using a Hiden Analytical HPR-20 QIC R& D mass spectrometer. A few experiments were conducted without MS data due to repairs and maintenance being carried out on the mass spectrometers available. Many experiments were conducted under pure ammonia inflow and, as the materials of interest typically only absorb and desorb ammonia (i.e. no decomposition or chemical changes occurring to the gas stream), MS data were used in a fairly limited capacity, though it can confirm the absence of any leaks in the flow setup.

3.5 Structural Analysis - Diffraction

3.5.1 X-ray Diffraction

X-ray wavelengths are comparable to the interatomic spacings in crystalline materials, and as such, diffract when interacting with the electrons in these materials. A diffraction pattern is the measurement of X-ray intensity as a function of angle between the diffracted and incident beam. Due to constructive interference at certain angles, a crystalline material (due to the high degree of order) produces peaks at these angles. For disordered solids and liquids, the diffraction pattern contains no sharp peaks, due to the absence of crystalline order.

Figure 3.5 shows the scattering of X-rays from a single electron (left), two electrons (middle) and a square of four electrons (right). While scattering from one electron cannot show any interference pattern, the scattered waves from two and four electrons interact constructively and destructively along certain directions. Figure

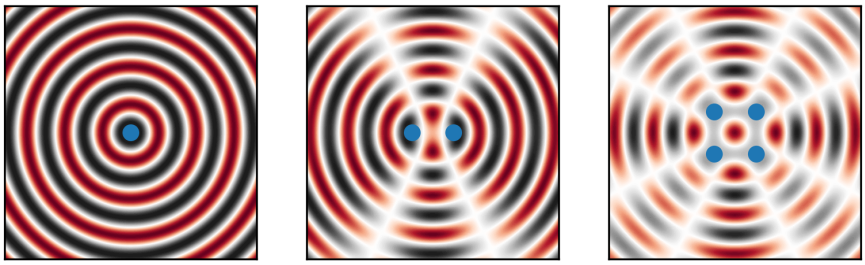


Figure 3.5: A depiction of scattering of X-rays from one (left), two (middle), and a square of four (right) isolated electrons. Electrons are shown as blue dots. The X-rays are assumed to scatter equally in all directions from each electron. For scattering from two and four electrons, constructive and destructive interference leads to the modification of wave amplitude in certain directions. The colour represents the displacement of the wave. Destructive interference is seen as white lines emanating from between the two electrons, as the waves are perfectly out of phase. Constructive interference in a certain direction is seen as a repetitive colour change (representing the maximally changing displacement of the resulting wave).

3.5 assumes the scattered waves leaving each electron begin with the same phase. This is analogous to the incident beam arriving perpendicular to the view shown in Figure 3.5.

When a monochromatic X-ray beam is directed at a periodic crystal, the incident wave and the elastically scattered wave can be represented as:

$$f_{\text{in}}(t, \mathbf{x}) = A_{\text{in}} \cos(\omega t - \mathbf{k}_{\text{in}} \cdot \mathbf{x} + \psi_{\text{in}}) \tag{3.3}$$

$$f_{\text{out}}(t, \mathbf{x}) = A_{\text{out}} \cos(\omega t - \mathbf{k}_{\text{out}} \cdot \mathbf{x} + \psi_{\text{out}}) \tag{3.4}$$

where ω is the angular frequency, $\mathbf{k}$ represents the wave vectors, $\mathbf{x}$ is the position vector and ψ represents the initial phases of the waves. These waves propagate independently. However, they must coincide at the point at which the incident wave was scattered. Therefore:

$$\omega t - \mathbf{k}_{\text{in}} \cdot \mathbf{x} + \psi_{\text{in}} = \omega t - \mathbf{k}_{\text{out}} \cdot \mathbf{x} + \psi_{\text{out}} + 2\pi n \tag{3.5}$$

where n is an integer. This equation must hold for $\mathbf{x} = 0$, therefore:

$$\psi_{\text{in}} = \psi_{\text{out}} + 2\pi n' \tag{3.6}$$

where n' is an integer. By rearranging, and subsuming n' into n:

$$(\mathbf{k}_{\text{out}} - \mathbf{k}_{\text{in}}) \cdot \mathbf{x} = \boldsymbol{\Delta}\mathbf{k} \cdot \mathbf{x} = 2\pi n \tag{3.7}$$

For the incident and scattered wave to have an identical phase at any lattice point $\mathbf{x}$, with $\mathbf{x} = p\mathbf{a} + q\mathbf{b} + r\mathbf{c}$, and $\mathbf{a}, \mathbf{b}$ and $\mathbf{c}$ as the lattice vectors of the unit cell, then:

$$\boldsymbol{\Delta}\mathbf{k} \cdot \mathbf{x} = \boldsymbol{\Delta}\mathbf{k} \cdot (p\mathbf{a} + q\mathbf{b} + r\mathbf{c}) = p(\boldsymbol{\Delta}\mathbf{k} \cdot \mathbf{a}) + q(\boldsymbol{\Delta}\mathbf{k} \cdot \mathbf{b}) + r(\boldsymbol{\Delta}\mathbf{k} \cdot \mathbf{c}) = 2\pi n \tag{3.8}$$

This equation must hold for all lattice points, and therefore any integer values of p, q and r. Due to the separation of terms in Equation 3.8, this leads to the three Laue conditions[115]:

$$\boldsymbol{\Delta}\mathbf{k} \cdot \mathbf{a} = 2\pi h \tag{3.9}$$

$$\boldsymbol{\Delta}\mathbf{k} \cdot \mathbf{b} = 2\pi k \tag{3.10}$$

$$\boldsymbol{\Delta}\mathbf{k} \cdot \mathbf{c} = 2\pi l \tag{3.11}$$

where h, k and l are integers. Each choice of integers (Miller indices) determines a different scattering vector $\boldsymbol{\Delta}\mathbf{k}$. If the Laue equations are satisfied, the incoming and outgoing wave have the same phase at each point of the crystal lattice.

William Lawrence Bragg and William Henry Bragg later derived Braggs' law [116], relating the distance between successive planes (Miller planes) of atoms in a crystalline material with the condition for constructive interference:

$$\lambda = 2d_{hkl} \sin\theta \tag{3.12}$$

λ is the X-ray wavelength, θ is the angle between the incident X-ray beam and the directions of constructive interference, and d_{hkl} is the distance between successive Miller planes.

For single crystals, in which the unit cells of a crystal are all oriented in the same direction, the observed reflections are entirely dependent on the direction of the incident beam. As such, measurement of a single crystal diffraction pattern typically involves re-orientation of the crystal multiple times to ensure all allowed reflections are captured. Powdered samples (as used in this thesis) consist of many crystallites oriented in random directions. As a result, diffraction from these randomly-oriented crystallites leads to a cone (the Debye-Scherrer cone) of constructively interfering X-rays, and re-orientation of the sample is not required.

Single crystal diffraction experiments will use a 2D detector, as the diffracted beams from each possible reflection occur in only one direction, so a full area must be collected in order to detect all reflections. Powder diffractometers tend to use a 1D detector, which moves in an arc, allowing for collection of data across the range of 2θ values. However, this means much of the Debye-Scherrer cone produced from powder diffraction is missed. 2D detectors are sometimes used in order to gain extra information on the sample, and greatly improve diffraction intensity. The conversion of a 2D powder diffraction pattern to a 1D pattern is done by integration of the intensity of the Bragg rings. It is important to note that a powder with a small number of crystallites, such as one which has been insufficiently ground, may lead to diffraction in preferential directions on the Debye-Scherrer cone (each crystallite gives one precise direction for each of its reflections, but the sum of many

crystallites leads to the conical diffraction observed for a powder). When measured with a 1D detector, this can lead to inaccurate peak intensities, often referred to as 'preferred orientation' effects.

A diffraction pattern is the Fourier transform of the real space electron density, and thus contains a great deal of information about a crystalline material. Obtaining this information can be tricky however. As the detector in an X-ray diffraction experiment can only measure the intensity of diffracted X-rays, not the phase, there is no direct method to obtain a crystal structure from a powder diffraction pattern. This is known as the 'phase problem'. The physics of diffraction is well understood, and the calculation of a diffraction pattern from a known crystal structure is facile with modern diffraction programs. As a result, typical analysis of a diffraction pattern involves adjusting a model crystal structure in order to obtain the best fit between the calculated and the experimental diffraction pattern. This will be developed further in Section 3.5.3.

Due to the constraint that the unit cells of a crystalline material must tessellate, only 7 lattice systems (geometry of the unit cell) and 14 Bravais lattices (arrangement of lattice points in the crystal structure) are possible. These are shown in Table 3.2, with the associated symmetry constraints imposed on lattice parameters.

Table 3.2: Lattice Systems and Bravais Lattices.

Crystal System	**Lattice Centring**	**Axial Lengths**	**Unit Cell Angles**
Cubic	Primitive, Face-centred, Body-centred	$a = b = c$	$\alpha = \beta = \gamma = 90^\circ$
Tetragonal	Primitive, Body-centred	$a = b \neq c$	$\alpha = \beta = \gamma = 90^\circ$
Orthorhombic	Primitive, Face-centred, Body-centred, Base-centred	$a \neq b \neq c$	$\alpha = \beta = \gamma = 90^\circ$
Hexagonal	Primitive	$a = b \neq c$	$\alpha = \beta = 90^\circ, \gamma = 120^\circ$
Rhombohedral	Primitive	$a = b = c$	$\alpha = \beta = \gamma \neq 90^\circ$
Monoclinic	Primitive, Base-centred	$a \neq b \neq c$	$\alpha = \beta = 90^\circ, \gamma \neq 90^\circ$
Triclinic	Primitive	$a \neq b \neq c$	$\alpha \neq \beta \neq \gamma \neq 90^\circ$

Within each of the lattice systems are a number of space groups. In total, there are 230 three-dimensional space groups, split up among each lattice system. The Bravais lattice and space group of a given crystal determines which reflections will appear in the powder diffraction pattern.

For a given crystalline phase, a set of Bragg peaks will be produced at well defined positions (determined by the unit-cell size and shape) in the diffraction pattern. The intensity of these peaks are defined by I_{hkl}, as shown in Equation 3.13.

$$I_{hkl} = |F_{hkl}|^2 \tag{3.13}$$

$$F_{hkl} = \sum_j f_j \, e^{2\pi i(hx_j + ky_j + lz_j)} \tag{3.14}$$

h, k and l are the Miller indices of the given planes of atoms. These planes of atoms are defined as the planes perpendicular to the vector $\mathbf{v} = h\mathbf{a}^* + k\mathbf{b}^* + l\mathbf{c}^*$, where $\mathbf{a}^*$ is the $\mathbf{a}$ lattice vector of the reciprocal unit cell (i.e. it is the reciprocal lattice vector of the real unit cell). Each combination of (hkl) denotes a different set of planes. F_{hkl} is the structure factor for the (hkl) reflection while f_j is the scattering factor for the j^{th} atom. As X-rays interact with the electrons in materials, f_j scales with the number of electrons in atom j. x_j, y_j and z_j refer to the coordinates of atoms within the unit cell.

The positions of the Bragg peaks are determined by the unit cell, while the intensity of those peaks is typically determined by atomic identity and position. One of the consequences of Equation 3.14 is the dependence of intensity on the symmetry of the crystal. For example, in a body centred crystal, an atom at (x, y, z) mandates an atom at ($x + \frac{1}{2}$, $y + \frac{1}{2}$, $z + \frac{1}{2}$) due to the lattice centring. The structure factor is therefore:

$$F_{hkl} = fe^{2\pi i(hx+ky+lz)} + fe^{2\pi i(h(x+\frac{1}{2})+k(y+\frac{1}{2})+l(z+\frac{1}{2}))} \tag{3.15}$$

$$F_{hkl} = fe^{2\pi i(hx+ky+lz)}(1 + e^{\pi i(h+k+l)}) \tag{3.16}$$

As $e^{\pi i} = -1$:

$$F_{hkl} = fe^{2\pi i(hx+ky+lz)}(1 + (-1)^{h+k+l}) \tag{3.17}$$

Therefore, when $h + k + l$ is even, $F_{hkl} = 2fe^{2\pi i(hx+ky+lz)}$, while $F_{hkl} = 0$ when $h + k + l$ is odd. Similar forbidden reflections occur throughout crystallography, mandated by the symmetry of the crystal, and derived from the structure factor. As such, the relative peak positions observed can inform the user about the symmetry of their crystalline material, a process known as 'indexing'. While the symmetry of the cell is deduced from relative peak positions, the location of atoms within the unit cell can be determined by the relative intensities of the peaks (note the x, y and z dependence in Equation 3.14).

Many of the X-ray diffraction patterns in this work were recorded using a Malvern PANalytical X'Pert Diffractometer, located in the Chemistry Department at the University of Oxford. Diffraction patterns recorded using this instrument were primarily used for phase identification before and after reaction. The resolution and signal : noise ratio of this instrument is sufficient for known phase identification. However, crystal structure solution is challenging.

The Malvern PANalytical X'Pert uses a copper anode. Electrons are produced by passing a current through a filament, before acceleration of these electrons through a high voltage tube. As the electrons collide with the copper anode, they lose energy and thus emit electromagnetic radiation with various wavelengths. Some of these wavelengths correspond to electronic transitions in copper. As the copper electrons transition to a higher energy level, higher energy level electrons can transition to the lower energy level. In doing so, they will lose energy in the form of X-rays. One

of these transitions releases copper $K_{\alpha 1}$ radiation ($\lambda = 1.540\,51$ Å). Radiation from other copper transitions (not of the appropriate wavelength/energy) is removed by use of a germanium monochromator, placed between the anode and the sample.

Diffraction experiments using the PANalytical were performed with a flat plate sample holder. The sample was ground in an argon-filled glovebox, before sprinkling onto a microscope slide lightly covered in vacuum grease. The slide was shaken to remove any excess sample and ensure as flat a surface as possible (i.e. any powder not touching the grease should fall off). The slide was placed into an airtight sample holder with a thin mylar film window, which allows X-ray transmission. Diffraction data were generally collected with a 2θ range of 10–80°.

For samples of particular interest, where greater resolution or signal : noise ratio was required, diffraction patterns were recorded on the I11 beamline at Diamond Light Source. Diamond Light Source is a synchrotron, where electrons are accelerated to extremely high energies, travelling close to the speed of light. Electrons are generated in an electron gun, before acceleration through a linear accelerator. These accelerated electrons are then passed to the booster synchrotron, where magnetic fields are used to bend the electrons round a near-circular (48 sided polygon) path. While moving through this path, electric fields are used to accelerate the electrons further until they reach the desired energy. Once at the desired energy, the electrons are passed to the storage ring of Diamond Light Source. The storage ring contains various magnetic and electric fields in order to bend the path and maintain the high energy of the electrons. When the electrons are bent round the storage ring using magnetic fields, they lose energy by releasing light (controlling the magnetic field allows for control of the wavelength emitted). In order to regain this energy, they must be accelerated through electric fields within the storage ring, such that the electron energy is kept constant.

The light emitted during each bend is directed towards one of the instruments at Diamond Light Source. The I11 beamline receives X-rays for high intensity powder X-ray diffraction. Due to the extremely high intensities at Diamond Light Source, high quality diffraction patterns can be collected in seconds and minutes on the I11 beamline.

I11 has two detector setups. The first setup consists of five MACs (multi-analyser crystals), each containing nine individual detectors, which form an arc around the sample, allowing collection of diffraction data for $2\theta = 3$–150°. Before each detector, the scattered X-rays must pass through a silicon (111) crystal to ensure only X-rays scattered at exactly the right angle are able to reach the detector. The second setup consists of a position sensitive detector (PSD), again shaped as an arc around the sample, which can determine the position of the scattered X-rays that collide with it. As such, this can be converted into a diffraction pattern. The PSD has 0.25° gaps every 5°, and so two scans are typically taken, with the detector slightly shifted between scans, allowing for collection of the full data range for $2\theta = 3$–90°.

For all diffraction data collected on the I11 beamline, samples were loaded into borosilicate capillaries (of various sizes, $\leq 0.7\,\text{mm}$ inner diameter) inside an argon-filled glovebox, before temporary sealing with vacuum grease. Once removed from the glovebox, a propane torch was used to melt the borosilicate glass and thus seal the capillary reliably. The capillary was then mounted on to a brass sample holder and attached to a magnetic base, allowing the I11 robot to run samples rapidly with minimal human oversight. While data are collected, the capillary is spun to minimise preferred orientation effects, which can affect observed peak intensities.

3.5.2 Neutron Diffraction

As X-rays interact with the electrons of a material, scattering intensity is proportional to the number of electrons in a material/atom. As such, detection of light atoms (particularly hydrogen) becomes extremely difficult, even with high quality synchrotron data. This is a problem for this thesis, as it is focused on solid, crystalline materials containing NH_3.

In neutron diffraction, neutrons interact with the atomic nuclei of materials, and as such the dependence on the number of electrons is removed. Table 3.3 shows the neutron scattering cross sections of nuclei relevant to the neutron diffraction experiments performed in this thesis.

Table 3.3: Neutron scattering cross sections of relevant nuclei [117]. Where a mass number is not given for the nucleus, the values are relevant for natural abundance of individual nuclei i.e. Cl refers to the scattering observed for a mixture of 76% ^{35}Cl and 24% ^{37}Cl.

Nucleus	Coherent Scattering Cross Section (barn)	Incoherent Scattering Cross Section (barn)
Ca	2.78	0.05
Br	5.80	0.10
Cl	11.53	5.30
N	11.01	0.50
^{1}H	1.76	80.27
^{2}H/D	5.59	2.05
Si	2.16	0.004
O	4.23	0.0008

Coherent scattering refers to scattering events in which the relative phase of the waves is unchanged. As such, these waves can constructively interfere according to Braggs' Law (Equation 3.12). Incoherent scattering refers to scattering events in which the relative phase of the wave changes. As a result, interference patterns are not well-defined in incoherent scattering events. Incoherent scattering therefore contributes significantly to the background in a diffraction experiment. If possible, nuclei with large incoherent scattering cross sections should be avoided in order to improve data quality.

Most of the nuclei (or elements) relevant to the neutron diffraction work contained within this thesis have small incoherent scattering cross sections, with the important exception of ^{1}H, which has a very large incoherent scattering cross section and a relatively small coherent scattering cross section. To avoid issues inherent with incoherent scattering, ND_3 gas was used instead of NH_3. All materials studied in the neutron diffraction experiments therefore contain no ^{1}H nuclei. While isotopes of the same element are generally considered chemically identical, changes in mass do slightly affect bonding properties, primarily due to the mass dependence of the zero point energy associated with the ground vibrational state. As hydrogen is the lightest element, the addition of one or more neutrons to its nucleus affects bonding more significantly than for isotopes of other elements. For example, T_2O melts at 4.5 °C, D_2O melts at 3.8 °C and H_2O melts at 0 °C[118], showing the subtle effect of large relative mass changes on bonding properties. While rare, significant structural effects have also been observed. Ammonium hexachlorotellurate ($(NH_4)_2TeCl_6$) shows just one phase transition on cooling from 120 K to 10 K, while deuterated ammonium hexachlorotellurate ($(ND_4)_2TeCl_6$) shows three phase transitions over the same temperature range[119]. Conclusions drawn from analyses of neutron diffraction data should consider the effects of using deuterium in place of hydrogen.

The POLARIS diffractometer at the ISIS Neutron and Muon source was used for the neutron diffraction experiments in this thesis. ISIS is a spallation neutron and muon source, where neutrons are produced by collision of protons with tungsten nuclei. Initially, hydride ions are produced at the ion source, before acceleration through a linear accelerator. As they enter the synchrotron, they pass through a thin sheet of aluminium oxide, removing them of their electrons. In the synchrotron, these protons are accelerated to 800 MeV before being guided to one of the two target stations. 50 proton pulses are produced each second, with 40 of these directed to Target Station 1 (where POLARIS is situated) and 10 directed to Target Station

2. The extremely high energy protons then strike a tungsten target, leading to spallation of the nuclei, generating neutrons. The neutrons produced have too much energy to be useful for many experiments, and must pass through a moderator in order to slow them down prior to interaction with a sample. In the case of POLARIS, a water (ambient temperature) moderator is used, causing neutrons to slow down through collision with the water molecules.

POLARIS is a time-of-flight neutron diffractometer. Most X-ray diffraction experiments use a constant wavelength and measure the angle of diffraction in Equation 3.12. However, as the energy, speed and wavelength of the neutrons approaching the sample at POLARIS is variable, five detector banks are used at fixed values of 2θ. For each detector bank, θ is kept constant while wavelength is measured indirectly by measuring the time taken for the neutron to reach the detector.

Starting from Braggs' Law (Equation 3.12) and the de Broglie relation, $\lambda = \frac{h}{mv}$:

$$\frac{h}{mv} = 2d\sin\theta \tag{3.18}$$

As $v = \frac{L}{t}$:

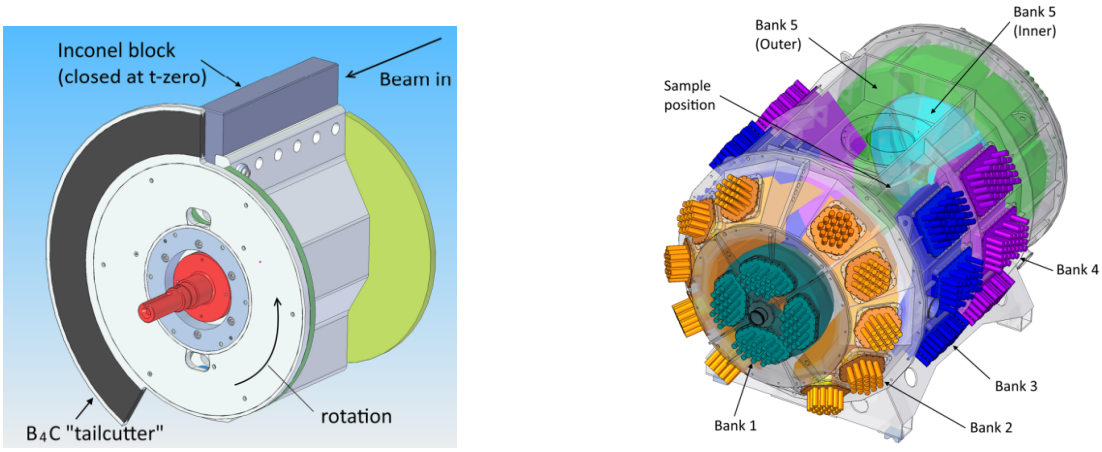
$$\frac{ht}{mL} = 2d\sin\theta \tag{3.19}$$

Therefore:

$$d = \frac{ht}{2mL\sin\theta} \tag{3.20}$$

where h is Planck's constant and m is the mass of a neutron. As shown in Equation 3.20, a known distance (L, the distance between moderation and detection) and angle (θ) allows for direct conversion between time-of-flight and d spacing. However, this process of measurement must be very rapid, due to the pulses occurring 50 times each second. As such, low energy (slow) neutrons from an earlier pulse can arrive at the detectors during detection of the current pulse. Similarly, the high energy (fast)

neutrons which have not been slowed by the moderator are undesirable in a diffraction experiment, due to their small wavelength. The POLARIS chopper (Figure 3.6a), placed between the moderator and the sample, is used to solve these issues. The chopper simply consists of an inconel alloy block, followed by a gap (to allow the desired neutrons through), followed by a curved B_4C tail cutter. The chopper is temporally aligned with the proton pulses of ISIS, rotating at 50 Hz (identical to the pulse frequency). The inconel alloy prevents the passage of high energy neutrons immediately after the proton pulse while the tail cutter prevents the passage of low energy neutrons from the previous pulse. This ensures no crossover between pulses.



(a) **(b)**

Figure 3.6: (a) shows the POLARIS chopper. The inconel block prevents high energy (fast) neutrons passing too quickly, while the B_4C tailcutter prevents low energy (slow) neutrons from a previous pulse passing. (b) shows the detector banks at POLARIS. Each detector bank is at a different fixed angle in order to collectively cover a large range of d spacings. Adapted from Smith *et al.*[120]

POLARIS has five detector banks (Figure 3.6b) in order to collect data across a range of d spacings (shown in Figure 3.6b). Due to their relatively high resolution and range of d spacings, banks 3 and 4 were the most useful in the determination of unknown crystal structures and sample composition throughout chemical reaction.

Three calcium halide samples and one pure silica sample were examined on the POLARIS diffractometer. Samples were housed in a cylindrical quartz glass sample stick (shown in Figure 3.7) with fittings for gas inflow, outflow, and thermocouples. The sample rested on top of a quartz frit, requiring gas to pass through the sample and frit in order to reach the gas outlet. A 'flow through' system was used to ensure good contact between gas and all of the sample. Calcium chloride and calcium bromide undergo absorption in contact with ammonia, leading to large changes in crystal structure volume (calculation from known crystal structure data suggests up to $\sim 4\times$ [121,122]). As such, expansion of a pure calcium halide sample would be likely to close any gaps in the powdered sample, preventing the flow through of gas and risking large regions of powder being unreachable by ND_3, or worse, causing overpressurisation and sample cell failure. To avoid these consequences, all calcium halide samples were mixed with porous, amorphous silica in order to ensure gas could flow through all of the sample at all stages of the experiment. Due to the lack of long range order, the use of amorphous silica does not produce Bragg peaks, but leads to a larger background and reduced calcium halide signal observed in the data. Alongside the CaX_2-SiO_2 samples, a pure silica sample was recorded in order to enable the removal of the silica contribution from the final data.

The three calcium halide samples examined on POLARIS were $CaCl_2$, $CaBr_2$ and CaClBr. All three samples were mixed with porous SiO_2 in an approximate 2:1 $SiO_2 : CaX_2$ volume ratio by using their densities to calculate the appropriate mass required. Samples were loaded into the quartz sample cell in an argon-filled glovebox, before the metal lid was secured. The gas flow panel shown in Figure 3.2b was used in these experiments with two modifications. Due to the price of ND_3 gas, it was important to use low gas flow rates in order to avoid wastage. However, this means that the outflow may not be high enough to prevent air entering the sample cell. To avoid this issue, a paraffin bubbler setup was fitted after the gas outflow, to prevent air diffusing back through the pipework. The second modification was

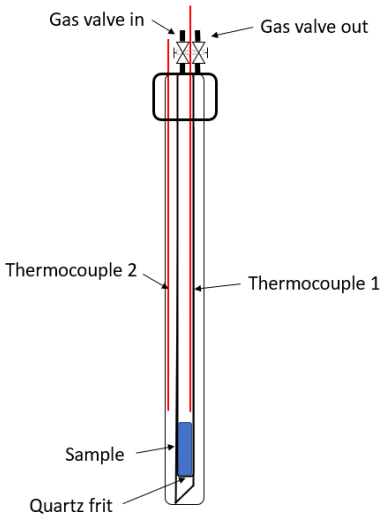


Figure 3.7: The sample cell used on the POLARIS diffractometer. Gas flow enters through the top of the inner tube, passes through the sample and quartz frit, before travelling back up between the walls of the inner and outer tube and leaving via the exhaust valve. A flow-through system ensured gas could interact effectively with all of the sample.

the lack of a mass spectrometer. Mass spectrometry data were not important for this experiment as the gases themselves were not expected to undergo any chemical changes other than absorption and desorption.

After connection of the sample cell to the appropriate gas pipework, the system was leak tested and the sample cell lowered into the POLARIS furnace for the experiment to begin. Exact flow rates, time lengths and temperature programs for each sample were somewhat dictated based on feedback during the experiment. Gas flow rates were typically 10 sccm. However, if pressure was rising due to difficulty with gas diffusion through the sample, then the gas inflow rate was lowered. Despite experimental constraints preventing full consistency, all samples were given ample time to absorb deuterated ammonia at room temperature and atmospheric ammonia pressure, before heating to 300 °C at a ramp rate of 2 °C per minute. After heating to

300 °C, samples would begin cooldown to room temperature and subsequent reuptake of ND_3. $CaCl_2$ and $CaBr_2$ samples only performed this cycle once due to time constraints, while the CaClBr sample performed two full cycles.

Unfortunately, due to the high silica volume fraction in each sample and repeated beam shutdowns, PND data quality for each observed phase was often limited.

3.5.3 Rietveld Analysis

As mentioned in Section 3.5.1, direct calculation of a structure from a powder diffraction pattern is challenging because of the 'phase problem'. However, direct calculation of a powder diffraction pattern from a structure is straightforward. The most commonly used method for analysis of powder diffraction data is the Rietveld method[123]. Rietveld analysis is predicated on the availability of a crystal structure which is an approximate estimation of the correct structure. The calculated powder diffraction pattern is then compared with the observed pattern, and parameters are modified before recalculation and comparison. This is an iterative process that finishes when observed and calculated patterns are sufficiently statistically similar.

Structural input includes lattice parameters, atomic positions, thermal parameters, and crystallite size and strain parameters, alongside experimental parameters such as the wavelength of radiation used, in order to accurately calculate a diffraction pattern. Comparison of the calculated pattern with the observed data is performed by mathematical examination of the weighted profile R-factor:

$$R_{\mathrm{wp}} = \sqrt{\frac{\sum_i w_i (Y_{\mathrm{o},i} - Y_{\mathrm{c},i})^2}{\sum_i w_i Y_{\mathrm{o},i}^2}} \tag{3.21}$$

where w_i is the weighting applied to data point i. w_i is typically defined as $\frac{1}{\sigma^2} = \frac{1}{y_{o,i}}$. The weighted profile R-factor is a comparison between two sets of data, based on how well each data point matches. The dependence on the square of

$Y_{o,i} - Y_{c,i}$ ensures that small deviations (such as noise in the data) do not affect the value of R_{wp} greatly, while large deviations (such as unfitted Bragg peaks) do. During Rietveld analysis, R_{wp} is minimised iteratively.

A second function, R_{exp} is used to quantify the target value of R_{wp}:

$$R_{exp} = \sqrt{\frac{N-P}{\sum_i w_i Y_{o,i}^2}} \tag{3.22}$$

where N is the number of data points and P is the number of parameters in the model. It should be noted that N will almost always be significantly greater than P. The goodness-of-fit function should approach unity for a good fit:

$$\chi^2 = \frac{R_{wp}}{R_{exp}} = \sqrt{\frac{\sum_i w_i (Y_{o,i} - Y_{c,i})^2}{N-P}} \tag{3.23}$$

The goodness-of-fit is thus a measure of how well the calculated pattern fits the experimental pattern, taking into account the quality of the data through the use of R_{exp}. As such it is applicable to both high and low quality datasets. While in almost all cases, $N >> P$, the dependence of R_{exp}, and hence the goodness-of-fit, on the number of parameters is important. If the number of parameters is large, then the goodness-of-fit will significantly increase. This protects against overfitting, where a model is too complex and begins significantly fitting noise.

A large goodness-of-fit implies a bad fit to the data, while a goodness-of-fit approaching 1 implies an excellent fit to the data. A $\chi^2 < 1$ means that the mean absolute value of the residuals is less than the uncertainty. For any dataset of a reasonable size, this should not happen and implies either an overfitted model, or overestimated uncertainties. It should be noted that while mathematical methods of determining the quality of a fit are important, there is no well-defined range for a 'good' fit and these are, at best, indicators. Visual inspection of calculated patterns should always be performed to ensure reliable fits, and thus reliable output structures.

Rietveld analysis of diffraction data was performed using TOPAS Academic v6[124]. Initial structure attempts were entered, before successive refinement of parameters. In general, scale and lattice parameters would be refined first alongside a Chebyshev polynomial function for background fitting, with all other structural parameters fixed, in order to center the calculated peaks on the observed peaks. For data recorded on I11, fits to previously recorded air and empty capillary scattering patterns would be included to ensure accurate background fitting. After this, atomic positions, thermal parameters and crystallite size and strain parameters can be allowed to refine. Chemical intuition must be applied to ensure parameters are reasonable. For example, if the initial structural estimate is poor, this may lead to nonsensical interatomic distances in the refined structural model. At times, minimum and maximum limits were set on parameters to ensure they were kept chemically reasonable throughout refinement e.g. the N-D bond length during analysis of the neutron diffraction data.

Beyond Rietveld analysis of individual diffraction patterns, TOPAS is a very powerful program with a large range of functionality. TOPAS utilises its own purpose built scripting language, allowing derivation of atomic positions and other parameters in terms of user-defined variables. This functionality was used extensively during structure solution and Rietveld refinement of ammoniate phases from POLARIS datasets, enabling the definition of ammonia molecules based on calcium positions and bond lengths and angles. TOPAS also allows for the refinement of more than one dataset simultaneously, a very useful function for analysis of POLARIS data from multiple banks.

Control of TOPAS via Python was used for analysis of the *in-situ* absorption/desorption experiments performed on POLARIS. Over 2,500 datasets were recorded for each POLARIS bank (over 12,500 total patterns), prohibiting manual refinement of individual datasets. As such, once structure solution or refinement was complete for all phases visible in the data, batch refinement was performed in

order to analyse each dataset individually. This was achieved by use of a python script modified from code originally written by Dr. Tom Wood. The python script enables recursive writing of input files and execution of the TOPAS program. The input file for iteration $n+1$ is written from the output file for dataset n, in order to ensure only small changes occur on each refinement and thus refinements are more likely to remain accurate.

As manual refinement/visual inspection of all datasets is not possible, care must be taken to ensure parameters remain reasonable. For example, crystallite size and strain parameters can have a large effect on peak width, and as such when a phase only constitutes a very small percentage of the material, refinement can lead to excessively broad peaks which are actually fitting background features. This can lead to inaccurate outputted values for this phase. Similar effects can be seen with all parameters e.g. lattice parameters may also vary wildly if Bragg peaks from a phase are not present/visible above the background. To avoid this, batch refinement was performed with atomic coordinates and crystallite size, strain, and thermal parameters held constant. Lattice parameters were allowed to vary within minimum and maximum limits, to ensure recovery of accurate values if Bragg peaks from the designated phase were to return. After batch refinement R_{exp}, R_{wp} and goodness-of-fit values were checked for all datasets, and any abnormalities/inconsistencies were manually checked to ensure appropriate fits had been found.

3.6 Computational Chemistry

3.6.1 Density Functional Theory

Density functional theory (DFT) is a quantum mechanical modelling method used to examine the electron density of many-body systems. The many-electron time-independent Schrödinger equation (after application of the Born-Oppenheimer approximation) is as follows:

$$\hat{H}\Psi = \left[\hat{T}+\hat{V}+\hat{U}\right]\Psi = \left[\sum_{i=1}^{N}\left(-\frac{\hbar^2}{2m_i}\nabla_i^2\right)+\sum_{i=1}^{N}V(\mathbf{r}_i)+\sum_{i<j}^{N}U(\mathbf{r}_i,\mathbf{r}_j)\right]\Psi = E\Psi \quad (3.24)$$

E is the total energy and $\hat{H}$ is the Hamiltonian operator, which can be broken down into operators for the kinetic energy ($\hat{T}$) and the potential energy ($\hat{V}+\hat{U}$). $\hat{V}$ is the potential energy arising from interaction of the electrons with the positively charged nuclei. The electric field from the nuclei is treated as constant under the Born-Oppenheimer approximation, and as such this term only depends on individual electronic wavefunctions (which are then summed). $\hat{U}$ is the electron-electron interaction energy, and thus depends on two electronic wavefunctions for each term in the sum. For single-electron atoms, the electron-electron interaction term is non-existent and the equation can be solved analytically. For many-electron systems, electron-electron repulsions are significant and the equation cannot be broken down into many single-particle equations. As such, the equation cannot be solved analytically.

In order to get around this issue, DFT uses the electron density, $n(\mathbf{r})$, rather than calculating many interacting electrons, and the associated difficulties with their movement. The Kohn-Sham approach[125] represents the interacting many-electron system with many non-interacting electrons that experience an effective potential, averaged from the electron density. The orbitals calculated by the Kohn-Sham equations reproduce the electron density of the interacting system.

The Kohn-Sham equations are as follows:

$$\left(-\frac{\hbar^2}{2m_i}\nabla_i^2 + V_{\text{eff}}(\mathbf{r})\right)\psi_i(\mathbf{r}) = \varepsilon_i\psi_i(\mathbf{r}) \quad (3.25)$$

where $\psi_i(\mathbf{r})$ is the Kohn-Sham orbital for the i^{th} electron, ε_i is the energy eigenvalue for the i^{th} electron, and $V_{\text{eff}}(\mathbf{r})$ is the effective potential, which includes the potential from the static nuclei ($V_{\text{ext}}(\mathbf{r})$), the potential from interaction with the other electrons in the system ($V_{\text{ee}}(\mathbf{r})$), and an exchange-correlation potential which

approximates the many-body effects ($V_{\mathrm{xc}}(\mathbf{r})$). The exchange-correlation potential is effectively a correction factor applied to the non-interacting system, such that it more closely resembles the real, interacting system.

The electronic repulsion potential energy is calculated by the following equation:

$$E_{\mathrm{ee}} = \frac{1}{2}\int\int \frac{n(\mathbf{r})n(\mathbf{r}')}{|\mathbf{r}-\mathbf{r}'|}d\mathbf{r}\; d\mathbf{r}' \tag{3.26}$$

This is effectively a sum over all pairs of spatial points in the system. The electron density is determined by the Kohn-Sham orbitals:

$$n(\mathbf{r}) = \sum_{i}^{N} |\psi_i(\mathbf{r})|^2 \tag{3.27}$$

Thus, the electronic repulsion energy is:

$$E_{\mathrm{ee}} = \frac{1}{2}\int\int \frac{\sum_i^N |\psi_i(\mathbf{r})|^2 \; \sum_j^N |\psi_j(\mathbf{r}')|^2}{|\mathbf{r}-\mathbf{r}'|}d\mathbf{r}\; d\mathbf{r}' \tag{3.28}$$

As the Kohn-Sham orbitals are orthogonal, all cross terms (i.e. when i $\neq$ j) equal 0, greatly reducing the intensity of this calculation:

$$E_{\mathrm{ee}} = \frac{1}{2}\sum_{i}^{N}\int\int \frac{|\psi_i(\mathbf{r})|^2 \; |\psi_i(\mathbf{r}')|^2}{|\mathbf{r}-\mathbf{r}'|}d\mathbf{r}\; d\mathbf{r}' \tag{3.29}$$

Electrostatic interactions calculated in E_{ext} and E_{ee} represent the non-interacting system of electrons perfectly. This energy accounts for the vast majority of the energy of a system. However, the exchange and correlation effects introduced in a real, interacting system can have large effects on the energy of the system, and must be calculated also.

The exchange-correlation potential is a combination of exchange and correlation effects of the calculated electron density. The exchange term accounts for the effects of the Pauli exclusion principle (e.g. Fermi heaps and Fermi holes) and the requirement of electronic wavefunctions to be antisymmetric with respect to the exchange of particles. The correlation term represents deviations from the mean field

applied in the electron-electron repulsion calculation. Put simply, the repulsions calculated in $V_{ee}(\mathbf{r})$ are performed using the overall electron density distribution. In reality, as electrons move, this will affect the position of the other electrons in the system, causing deviations from this 'mean field' approximation (i.e. electrons are correlated/they interact). The correlation term attempts to account for this.

The local density approximation (LDA) is a method used to approximate $V_{xc}(\mathbf{r})$. Under the LDA, $V_{xc}(\mathbf{r})$ depends only on the electron density at each point in space. LDA functionals have been typically derived from the hypothetical 'homogeneous electron gas', with great success in both speed of calculation and accuracy. However, in an improved method, GGA (generalised gradient approximation) functionals, $V_{xc}(\mathbf{r})$ depends on both the electron density and the local gradient of the electron density. As such, it is more responsive to the geometry of the system than LDA functionals, and generally considered more accurate. The computational work throughout this thesis was performed using the Perdew-Burke-Ernzerhof (PBE) functional[126], a GGA functional.

To obtain the ground state electron density of a system, an initial attempt at the electron density is made. Then, the Kohn-Sham equations are solved for this electron density in order to obtain orbitals and eigenvalues. The electron density is updated based on these new Kohn-Sham orbitals. This process is repeated until the electron density and Kohn-Sham orbitals do not change significantly between iterations (an appropriate tolerance value can be set). This electron density is then the ground state electron density of the system, which can be used to calculate many other properties of the system.

3.6.2 CASTEP

Cambridge Serial Total Energy Program (CASTEP)[127], a program for the implementation of DFT calculations, was used throughout this thesis in order to calculate energies and optimise geometries of crystalline materials.

Real crystalline materials contain an astronomical number of electrons. As such, the modelling of crystalline materials is best performed using an infinitely large lattice (i.e. no end point/surface) and the imposition of periodic boundary conditions (Bloch's theorem). This allows for the separation of the wavefunction into a periodic function ($u_{\mathbf{k}}$), which describes the spatial variation of the wavefunction within a unit cell, and a plane wave part ($e^{i\mathbf{k}\cdot\mathbf{r}}$), representing the periodicity associated with the crystalline material:

$$\psi_{\mathbf{k}}(\mathbf{r}) = u_{\mathbf{k}}(\mathbf{r})e^{i\mathbf{k}\cdot\mathbf{r}} \tag{3.30}$$

As a result, calculations can focus solely on the wavefunction within the first Brillouin zone, greatly simplifying DFT calculations. In theory, an infinite number of **k**-points are required to describe the total wavefunction. However, if the **k**-points are sufficiently close together, they represent the wavefunction accurately. As such, it is common to use a discrete grid of **k**-points for DFT calculations within CASTEP (known as a Monkhorst-Pack grid). To determine the appropriate spacing of **k**-points, convergence testing is performed. Multiple different **k**-point grids are used, and then the results subsequently checked for the point of convergence (i.e. when greater numbers of **k**-points no longer lead to a significant increase in accuracy). Figure 3.8 shows the cell pressure during convergence testing for a NaCl cell. A greater number of **k**-points leads to a greater degree of accuracy. However, this comes at the expense of increased computational time.

Despite these approximations, calculation of all electrons is still very computationally expensive. It is well understood that not all electrons contribute to bonding equally. To take an extreme example, the electrons in the 1s orbital of a calcium atom are clearly too close to the nucleus to be significantly affected by any surrounding atoms. As such, core electrons can be approximated by pseudopotentials in order to improve computational speed. Norm-conserving pseudopotentials ensure that the charge within a certain radius is equal to that of the all-electron calculation.

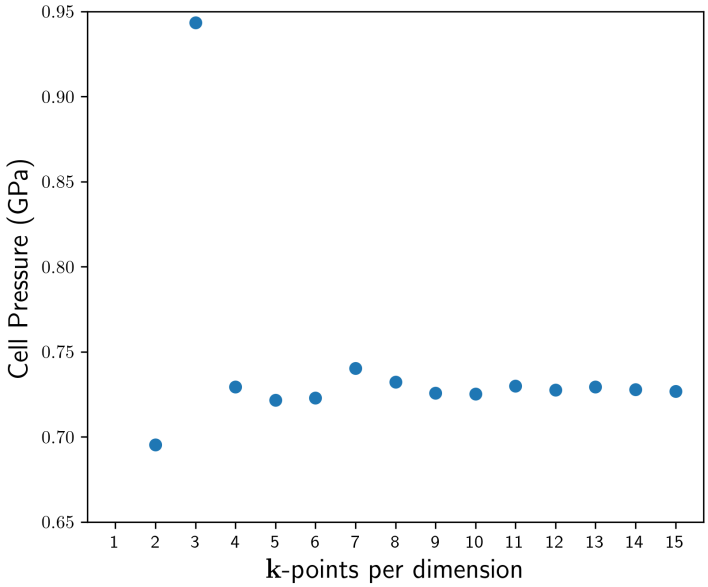


Figure 3.8: **k**-point convergence testing for NaCl rocksalt structure. The cell pressure calculated for 1 **k**-point per cell axis was 25.42 GPa. 8 **k**-points per cell axis was chosen as a suitable trade-off between speed and accuracy.

However, this strict rule can lead to discontinuities, especially near the cutoff radius. As such, ultrasoft pseudopotentials were used throughout the work in this thesis, as these have much smoother behaviour near atomic nuclei.

Similar to the Monkhorst-Pack grid, an appropriate degree of accuracy must be chosen, balancing computational speed and accuracy. Convergence testing for the cutoff energy is implemented in the same way; single-point energy calculations are run with varying cutoff energies, and the stress on the cell is checked to determine the appropriate cutoff energy for further calculations. The cutoff energy determines the energy range for which electrons are considered 'core' and 'valence'.

After appropriate parameters have been chosen, CASTEP can be used to geometry optimise an input unit cell. Using the inputted atomic positions, CASTEP will solve for the electronic ground state using the Kohn-Sham approach, as described

in Section 3.6.1. After solution of the electronic ground state (electron density), the forces on atoms can then be computed using this electronic ground state and the Hellmann-Feynman theorem:

$$\mathbf{F}_i = -\frac{\partial E}{\partial \mathbf{r}_i} \tag{3.31}$$

where $\mathbf{F}_i$ is the force on atom i, calculated using the derivative (gradient) of energy with respect to the x, y and z directions respectively. After force calculation, the atoms are moved in the direction of these forces, and a new electronic ground state is calculated according to the Kohn-Sham approach. Upon each iteration of this process, the system is checked for convergence. The process of geometry optimisation is shown in Figure 3.9.

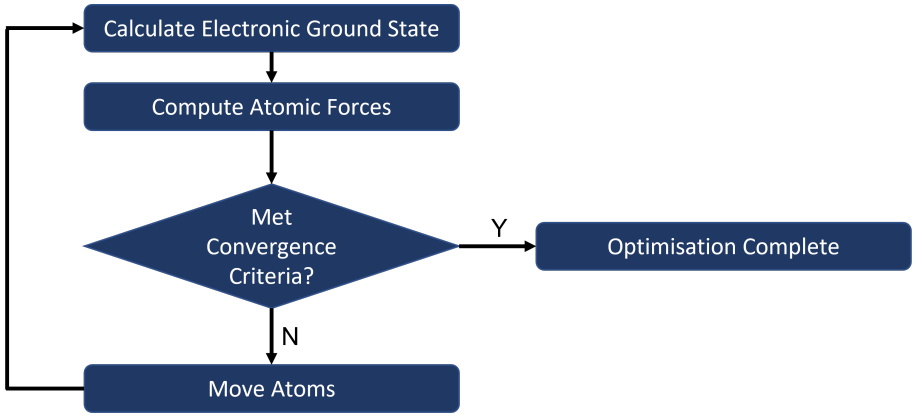


Figure 3.9: A flowchart depicting the process undertaken during a CASTEP geometry optimisation. The electronic ground state must be recalculated and updated each time atoms are moved.

Various criteria are used in CASTEP to determine whether an optimisation is complete. This includes the energy change between iterations, the distance moved by atoms in the last iteration, the forces on the atoms, and the stress on the unit cell. Various optimisation algorithms are available in CASTEP; the Broyden-Fletcher-Goldfarb-Shanno (BFGS) algorithm was used throughout the work in this thesis. Some optimisation algorithms, such as steepest descent, can be inefficient when

interacting with curved surfaces. Given the large number of parameters involved in geometry optimisation of most crystalline materials, the energy surface will certainly be very complex. The BFGS algorithm uses both first (gradient) and second (curvature) order derivatives to inform the step direction, leading to more efficient optimisation.

CASTEP was used primarily for geometry optimisations, but also for single point energy calculations when the location of atoms was desired to be controlled tightly. Single-point energy calculations simply calculate the electronic ground state within the inputted atomic framework.

3.6.3 Madelung Energy

Ewald summations[128] are a method of quantifying electrostatic interactions within an infinite crystalline material. They are akin to the calculation of a Madelung constant[129]. However, Madelung constants are calculated using real-space methods, which leads to slow convergence or divergence dependent on the method used for calculation (see Figure 3.10).

To avoid similar issues and greatly improve the speed of calculation, Ewald sums break the electrostatic interactions down into short-range and long-range interactions:

$$E_{\text{tot}} = E_{\text{sr}} + E_{\text{lr}} \tag{3.32}$$

The short-range calculation is performed in real space, and is straightforward with modern computation. The long-range calculation is computationally expensive in real space, but rapidly converges in reciprocal space. By calculation of the long-range interactions in reciprocal space using Fourier transforms, the term is evaluated much more quickly. A cutoff radius is chosen to determine whether an interaction is considered short or long range.

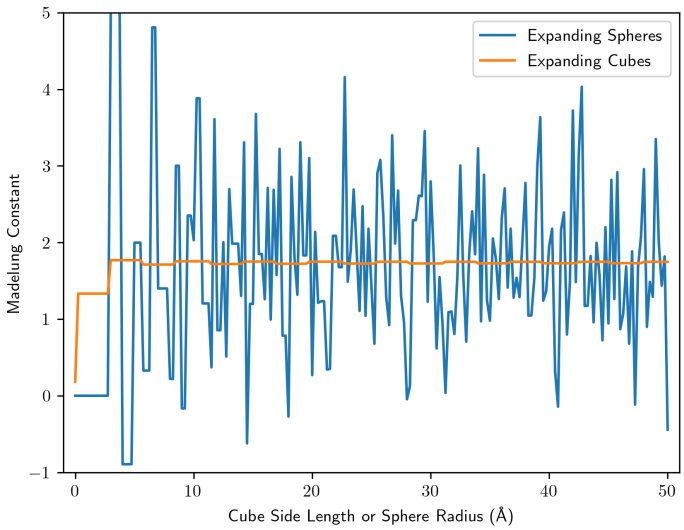


Figure 3.10: Convergence of the Madelung constant for NaCl using the 'expanding spheres' and 'expanding cubes' method. Note the lack of convergence when the 'expanding spheres' method is used.

Madelung energy calculations treat ions as point charges with no electronic structure, and as such it is not an accurate representation of many materials. It is useful for studying the ionic interactions/ionic bonding strength of materials, but should be seen as an approximation for energetics or structural arguments. Madelung energy was calculated using the pymatgen Python module[130] for many of the computationally determined structures in this thesis as part of rationalising results and trends in ammoniate materials.

Within this thesis, Madelung energy was used as a method of separating ionic bonding effects from other bonding interactions, such as hydrogen bonding, within the materials studied. Figure 3.11 shows the correlation between experimentally determined lattice enthalpies[131,132] and theoretically calculated Madelung energies for a selection of ionic materials. Group I halides show a very strong correlation between theoretical and experimental lattice enthalpies. While group II halides show a larger variation, this exemplifies the use of this approach in highlighting deviations from ionic behaviour. All data points below the trend line (CaI_2, $MgCl_2$, $MgBr_2$

and MgI_2) adopt layered structures, which show significant halide-halide bonding. As halide-halide bonding effects are not accounted for under a Madelung approach, this is observed in the data as Madelung energy underestimating the experimental lattice enthalpy. Removal of these layered structures leads to a significantly stronger correlation.

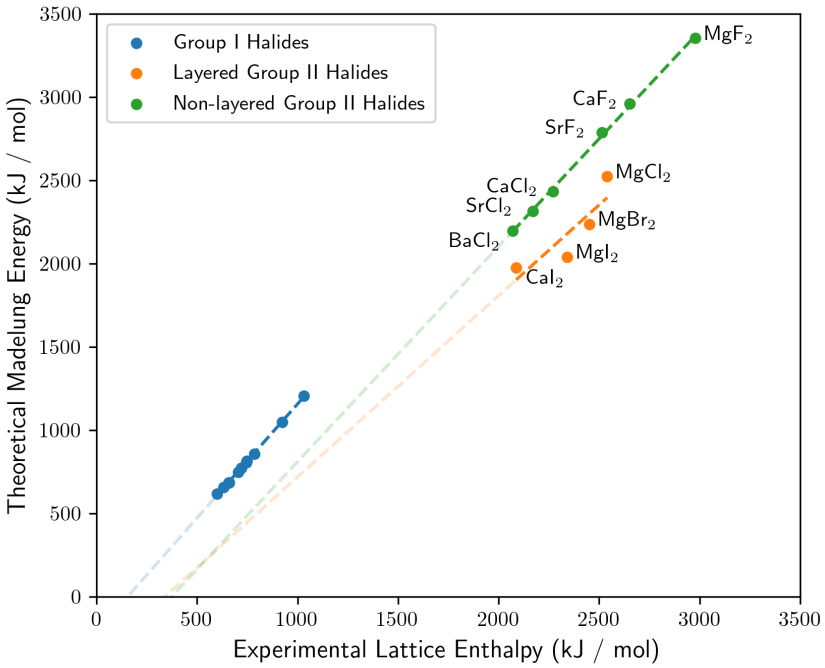


Figure 3.11: Comparison between experimental lattice enthalpies[131,132] and theoretical Madelung energies calculated using the Ewald method for a selection of ionic solids. Very strong correlation is seen for group I metal halides. While, group II metal halides show significant variation, non-layered group II metal halides show a strong correlation. Group II metal halides (CaI_2, $MgCl_2$, $MgBr_2$ and MgI_2) which adopt layered crystal structures show significant halide-halide bonding, leading to deviation from purely ionic behaviour and only a weak correlation between experimental and theoretical Madelung lattice enthalpies. Group I halides are fitted to $E_{th} = -212 + 1.37E_{exp}$. Group II halides are fitted to $E_{th} = -810 + 1.37E_{exp}$ while non-layered group II halides are fitted to $E_{th} = -482 + 1.29E_{exp}$.

4

Ammonia Absorption of $CaCl_2$ and CaBr2

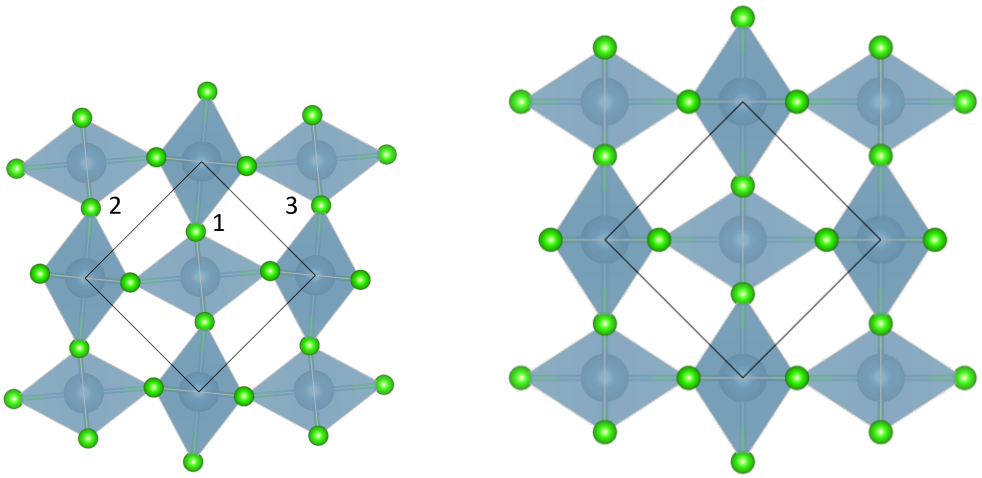
For over 100 years, calcium halides (with the exception of fluoride) have been understood to absorb large amounts of ammonia under mild conditions[102]. This chapter explores the structural chemistry and thermodynamic driving forces of the various phases observed in the ammonia absorption pathway of calcium halides, particularly chloride and bromide, through the use of STA, gas flow measurements, PXRD, PND and DFT calculations in CASTEP.

4.1 Structural Analysis of Phases Involved in Ammonia Absorption

A detailed analysis of the driving forces affecting the ammonia absorption properties of $CaCl_2$ and $CaBr_2$ is required in order to understand the ammonia absorption properties of solid solutions of $CaCl_xBr_{2-x}$.

4.1.1 Anhydrous Phases

Calcium chloride and calcium bromide have long been known to crystallise in a distorted rutile structure ($Pnnm$ space group) at room temperature, undergoing phase transition to rutile ($P4_2/mnm$ space group) at elevated temperatures[121]. Figure 4.1 shows the rutile and distorted rutile structures of $CaCl_2$. Figure 4.2 shows a PXRD pattern of the distorted rutile structure of calcium chloride.



(a) **(b)**

Figure 4.1: The crystal structures of $CaCl_2$. $CaBr_2$ adopts these crystal structures also. (a) shows the distorted rutile $Pnnm$ phase. (b) shows the rutile $P4_2/mnm$ phase. Ca = blue, Cl = green. Note that the distortion consists of a rotation of the $CaCl_6$ octahedra, bringing Cl atom 1 closer to Cl atom 2, but further from Cl atom 3.

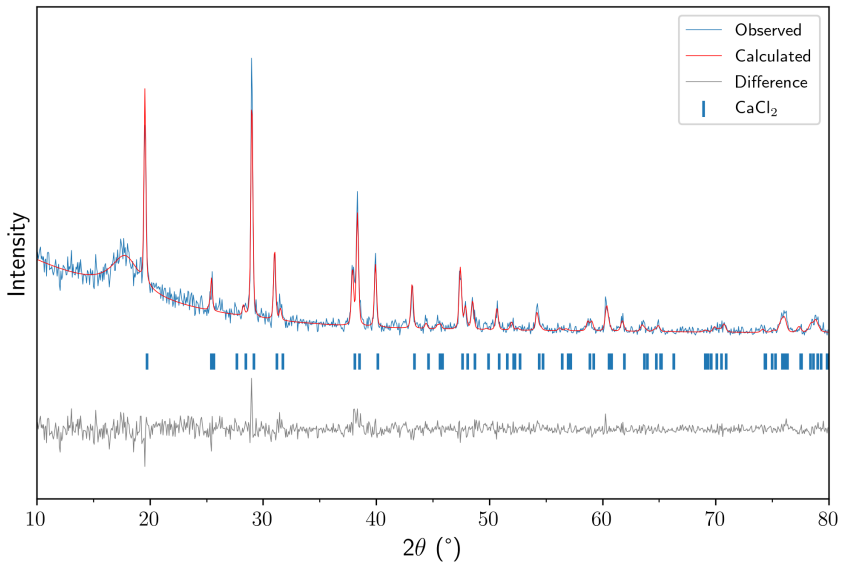


Figure 4.2: PXRD pattern of $CaCl_2$, fitted to the distorted rutile *Pnnm* structure, and recorded on the Malvern PANalytical X'Pert Diffractometer in the Oxford Chemistry Department. $\chi^2 = 1.12$.

It may appear surprising for a highly ionic crystal such as $CaCl_2$ or $CaBr_2$ to show distortions from the high symmetry of the rutile structure, though the distortion is subtle. Rather than adopting the distorted rutile phase, CaI_2 crystallises in a layered $P\bar{3}m1$ structure (Figure 4.3) due to the polarising nature of Ca^{2+} and the high polarisability of I^-, which minimises the electronic repulsions between iodide ions in successive layers. Due to the high strength of dispersion forces for anions with large numbers of electrons (such as iodide), this allows the layered structure to be stable relative to rutile or the distorted rutile phase. This is a well understood phenomenon across chemistry. A highly polarising cation such as Mg^{2+} or Cd^{2+} bonded to highly polarisable anions such as I^- commonly leads to this form of structure.

The available literature does not speculate on the reasoning for distortions to the rutile structure in $CaCl_2$ and $CaBr_2$. CASTEP geometry optimisations were performed, with a cutoff energy of 850 eV, to investigate the origin of this distortion.

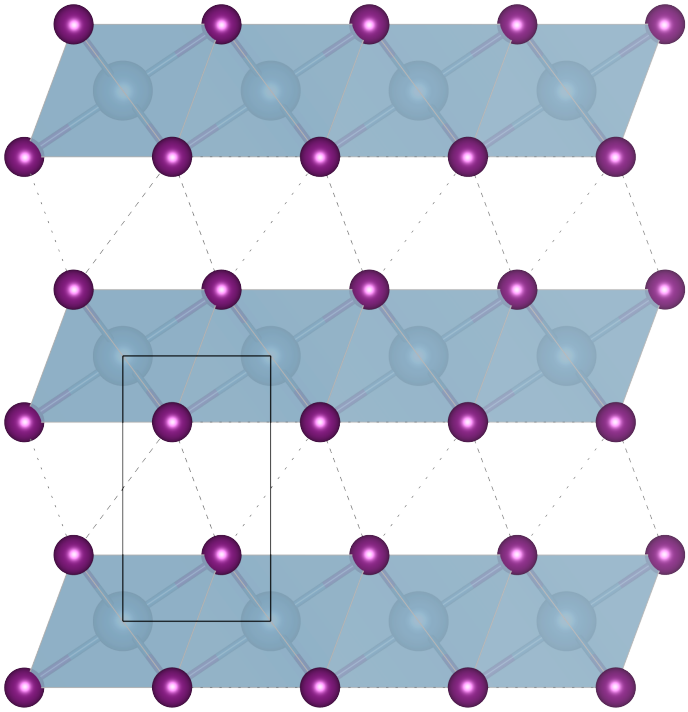


Figure 4.3: The crystal structure of CaI_2. The boundaries of the unit cell are shown as black lines. Dashed lines indicate halide-halide bonding between layers of edge-sharing CaI_6 octahedra. Ca = blue, I = purple.

Table 4.1: The energy change associated with distorting the rutile structure. Energy values are given in kJ mol Ca^{-1}. Note the effect of including dispersion forces on the stability of the distorted *Pnnm* phase.

Dispersion?	Anion	ΔE (kJ / mol Ca)
No	Cl	0.06
	Br	-0.20
	I	-0.69
Yes	Cl	-2.69
	Br	-3.82
	I	-5.64

As shown in Table 4.1, when dispersion forces are ignored, the distortion produces a very minimal energy change, well within acceptable error for DFT calculations. However, when dispersion forces are included, the distortion is clearly favourable. It appears that dispersion forces significantly contribute to the favourability of this distortion. As shown in Figure 4.1, this distortion leads to an increase in some Cl-Cl distances and a decrease in an equivalent number of Cl-Cl distances. Dispersion forces are generally considered approximately proportional to $-\frac{1}{r^6}$ at large distances[133]. The curvature of this function is always negative ($\frac{\partial^2 E}{\partial r^2} \propto -\frac{1}{r^8}$), and as such simultaneous distance increases and decreases will lower the energy of the system. This must be balanced with the ionic repulsion of chloride ions, which prefers maximal distance between ions (Coulomb's Law scales with $\frac{1}{r^2}$, curvature is always positive for like-charge ions). While not layered like CaI_2, it is likely that small amounts of polarisation induced on X^- by Ca^{2+} contribute to the reduction of repulsion between anions, allowing for the dispersion effect to become significant in comparison to a purely ionic model, leading to the subtle distortion observed.

The change in energy values upon application of dispersion forces is greater for larger halides, as larger atoms/ions are more polarisable, allowing for both reduced ionic repulsions between anions and greater dispersion forces. This difference in the favourability of distortion is reflected in the temperatures at which the phase transition from *Pnnm* to rutile occurs (235 °C for $CaCl_2$, 553 °C for $CaBr_2$[121]).

4.1.2 Ammonia Absorption

The ammonia absorption pathways for $CaCl_2$, $CaBr_2$ and CaI_2 have been known for over 100 years, first comprehensively studied in 1922 by Gustav Hüttig[102]. All of these calcium halides show 4 ammoniate phases up to an octa-ammoniate ($CaX_2(NH_3)_8$). While $CaCl_2$ exhibits stable phases for n = 1, 2, 4, 8, ammoniates of $CaBr_2$ and CaI_2 are observed for n = 1, 2, 6, 8 (in $CaX_2(NH_3)_n$). The inves-

tigation of calcium halides in this thesis is focused on $CaCl_2$ and $CaBr_2$ due to their higher ammonia absorption densities (gravimetric and volumetric), and hence greater likelihood of application.

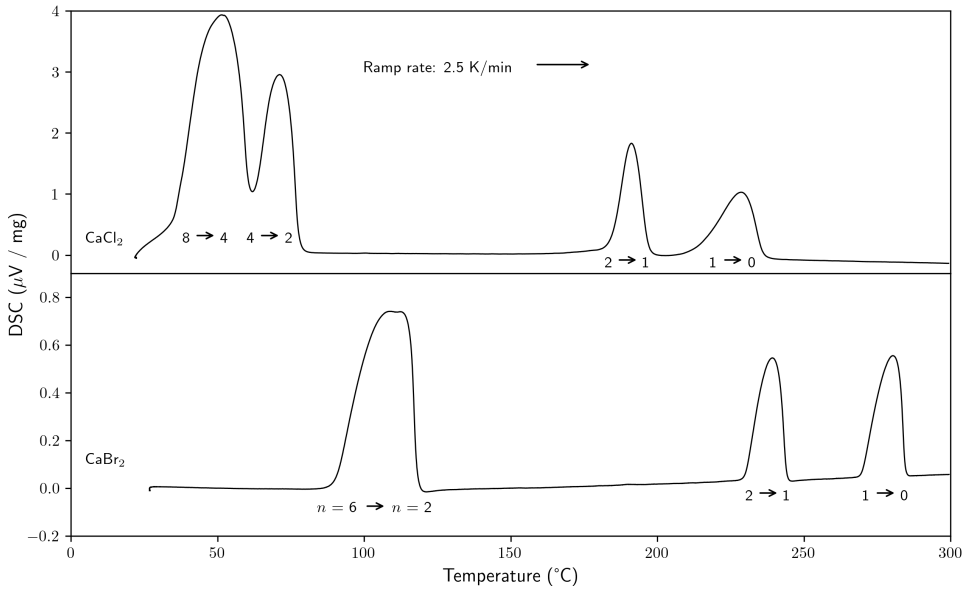


Figure 4.4: The ammonia desorption pathways of $CaCl_2(NH_3)_n$ and $CaBr_2(NH_3)_n$ after exposure to 0.83 bar NH_3 (flowing 50 sccm NH_3 and 10 sccm Ar at atmospheric pressure). DSC data is presented, tracking the heat change associated with each transition. Corresponding mass data were simultaneously recorded and agree closely with transitions observed by DSC.

Figure 4.4 shows the ammonia desorption transitions from $CaCl_2$ and $CaBr_2$ after ammonia absorption at room temperature and 0.83 bar. This is consistent with the transitions described above from Hüttig's original work. The octa-ammoniate of calcium bromide is stable at room temperature but requires slightly higher pressure than used in this experiment.

It is clear from Figure 4.4 that the desorption temperature of calcium bromide ammoniate phases is generally greater than for calcium chloride ammoniates, with the exception of the octa-ammoniate phase. An equivalent trend has been explained

previously for MgX_2 ammoniates[92] on the basis of ionic bonding using the Kapustinskii Equation (Section 2.4), and similar is likely to be at play here. The rationalisation of trends and driving forces for ammoniate formation, both general and specific to calcium halides, will be developed further throughout this thesis, after a detailed study of the structures of calcium halide ammoniate phases.

4.1.3 $CaCl_2$ and $CaBr_2$ Mono-ammoniates

Prior to this work, no characterisation of the mono-ammoniate of $CaCl_2$ or $CaBr_2$ has been reported in the literature. The mono-ammoniates are fleetingly stable in a TPD experiment, particularly if performed without NH_3 present.

Indexing of early PXRD data believed to be a mixture of calcium bromide mono-ammoniate and calcium bromide di-ammoniate suggested the mono-ammoniate crystallises in an orthorhombic unit cell with lattice parameters: $a = 18.665(2)$ Å, $b = 6.6790(5)$ Å, $c = 4.2742(4)$ Å. The volume of this unit cell is $532.8(1)$ Å^3. Given that the crystal structures of $CaBr_2$ and $CaBr_2(NH_3)_2$ have volumes of 97.5 Å^3 and 166.9 Å^3 per calcium ion, the volume of the mono-ammoniate per calcium ion is likely $\sim$132 Å^3. This suggested there were 4 formula units in the unit cell ($132 \times 4 = 528$).

PND data collected *in-situ* on the POLARIS diffractometer allowed for a diffraction pattern of pure mono-ammoniate to be analysed. Importantly, these data were fitted by the Pawley method using the aforementioned unit cell and confirm that the previous phase observed was the mono-ammoniate. A Pawley analysis simply fits peak positions using unit cell parameters and a given space group to check for forbidden reflections, thereby confirming the unit cell deduced from PXRD data was likely correct.

It was initially considered, from the systematic absences observed, that the unit cell adopted *Pnnm* symmetry. This allowed use of the Wyckoff sites in order to determine the likely positions of atoms. It was noted that both the b ($\sim$6.6 Å) and c ($\sim$4.3 Å) axes of the unit cell are too short to accommodate more than one

Br^- ion along the (010) or (001) direction (ionic radius of $Br^- \approx 1.85$ Å), preventing placement of bromide ions on 8h, 4e or 4f Wyckoff sites, and certain combinations of two-fold Wyckoff sites. Despite these assertions, PXRD data alone was insufficient to determine the full crystal structure.

As discussed in Section 3.5.2, ND_3 moieties contribute far more to peak intensity in PND data than in PXRD data, where heavy atoms such as Br dominate scattering. In order to solve the mono-ammoniate structure, identification of the position of the ND_3 moiety was performed as a first step. Ammonia molecules are rarely without significant motion, commonly seen to spin around their threefold rotation axis within solid materials. To account for the motion of the deuterium atoms, an appropriate method of modelling this was required. This method, an entirely general way of defining deuterium atom positions based on only the Ca-N vector, D-N-D bond angle and N-D bond distance, was used throughout the analysis of the PND data in this thesis.

As an ammonia molecule spins, the deuterium atoms map out a circle, perpendicular to the Ca-N vector, in 3D space. A circle can be defined parametrically in 3D space using the centre and radius of the circle, and two perpendicular unit vectors which are parallel to radii when placed at the centre of the circle:

$$\mathrm{P} = \mathrm{C}(x, y, z) + \mathbf{a}r\cos(\theta) + \mathbf{b}r\sin(\theta) \tag{4.1}$$

Point P is a point on the circle, point C is the centre of the circle, r is the radius of the circle and $\mathbf{a}$ and $\mathbf{b}$ are the perpendicular unit vectors. By varying θ, the circle is traced out by the coordinates of P. This neatly allows the production of evenly spaced deuterium atoms around the circle, by setting up θ as a series e.g. $\theta = 0, \frac{\pi}{6}, \frac{2\pi}{6} ... \frac{11\pi}{6}$.

Vector $\mathbf{a}$ can be chosen using the dot product and the Ca-N vector:

$$\mathbf{a} \cdot \mathbf{k} = |\mathbf{a}||\mathbf{k}|\cos(\theta) = \sum_{i=1}^{3} a_i k_i = 0 \tag{4.2}$$

where **k** is the Ca-N vector. In 3D space, there are infinitely many vectors perpendicular to another vector, hence **a** must be chosen (this can be done by choosing two of the components, followed by calculation of the third). In order to calculate the direction of **b**, the cross product must be used to ensure **b** is perpendicular to both **a** and the Ca-N vector:

$$\mathbf{b} = \mathbf{a} \times \mathbf{k} = (a_y k_z - a_z k_y, a_z k_x - a_x k_z, a_x k_y - a_y k_x) \tag{4.3}$$

Vectors **a** and **b** must be scaled to unit length before use. To determine the radius and centre of the circle, an ammonia molecule can be viewed as a trigonal pyramid (Figure 4.5).

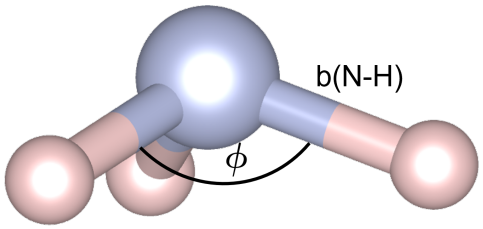


Figure 4.5: The view of an ammonia molecule as a trigonal pyramid. The H-N-H bond angle is defined as ϕ and the N-H bond length is b(N-H).

The H-H distance is thus determined by the cosine rule:

$$\text{H-H distance} = \sqrt{2\text{b(N-H)}^2 - 2\text{b(N-H)}\cos(\phi)} \tag{4.4}$$

The distance of a hydrogen atom from the centre of the base of the pyramid (equivalent to the radius of the circle) is then determined using the sine rule on an isosceles triangle with a unique angle of 120° and unique side equal to the H-H distance:

$$r = \frac{\text{H-H distance} \times \sin(\frac{\pi}{6})}{\sin(\frac{4\pi}{6})} = \frac{\text{H-H distance}}{\sqrt{3}} \tag{4.5}$$

With the radius of the circle and N-H bond length known, Pythagoras' theorem can be used to determine the distance of the centre of the circle from the nitrogen atom. Given a distance from the nitrogen atom and a direction in 3D space (the Ca-N vector), determining the position of the centre of the circle, $C(x, y, z)$, is facile.

This method allows for the definition of ND_3 molecular positions in terms of bond lengths and distances regardless of the orientation. Alongside this, circular harmonic functions were used throughout PND analysis to refine occupancies of deuterium atoms while preserving both the local three-fold symmetry of the ND_3 molecule (the occupancy of the deuterium atom at θ is equivalent to the occupancy of the deuterium atoms at $\theta \pm 120°$) and the symmetry of the space group (e.g. deuterium atoms reflected in a mirror plane should have identical energies and thus identical occupancies). This is shown for the mono-ammoniate in Figure 4.6 and for other ammoniate phases in Figures A.1–A.5. This allows for a search of the parameter space while keeping bond lengths and angles reasonable through the use of limits. This definition of deuterium positions and occupancies was used throughout the PND analysis of ammoniate phases presented in this thesis.

This analysis was performed in order to solve the mono-ammoniate crystal structure. Initially, a Ca and N atom were placed on separate 4g Wyckoff sites in the *Pnnm* unit cell. D-N-D bond angles were constrained between 105 and 114°, the Ca-N bond length constrained between 2.3 and 2.8 Å and the N-D bond length constrained between 0.98 and 1.03 Å. Deuterium positions every 30° were computed and placed in the structure also. TOPAS was used to refine the positions of the N and Ca and the ring of D atoms and obtain the best fit to the PND data from this rudimentary structure. After convergence, a Br atom was placed on another 4g Wyckoff site and the structure refined, before a final Br atom was placed on a second 4g site and refined in TOPAS.

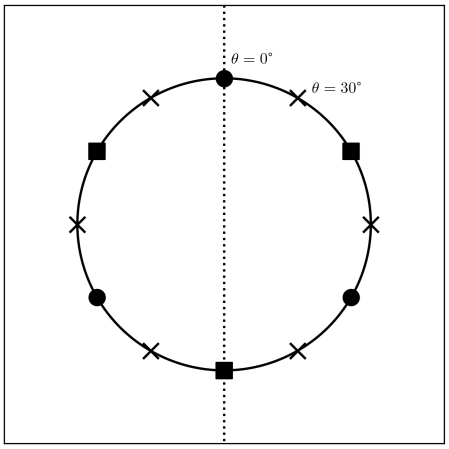


Figure 4.6: The definition of 'equivalent' deuterium sites in the mono-ammoniate structure. The circle depicts the circle of possible deuterium positions (viewed along the N-Ca vector). The markers denote positions used in refinement (every 30°). Positions with the same marker were assigned the same occupancy. The local three fold rotational symmetry of the ND_3 molecule, and the symmetry of the space group (mirror plane denoted as a dotted line), is preserved under this approach.

This yielded the structure shown in Figure 4.7a, and while fits to PND data appeared good, fits to PXRD data recorded on the I11 beamline clearly showed the structure was incorrect, with various peaks clearly absent from the observed data but present in the calculated pattern. After re-analysis of the structure and data, the mono-ammoniate appears to crystallise in the $Cmc2_1$ space group. This mono-ammoniate structure (Figure 4.7b) consists of the same layering determined for the hypothetical $Pnnm$ structure. However, in the $Cmc2_1$ structure, these layers are oriented in the same direction, leading to a polar crystal.

Figures 4.8 and 4.10 show PND and PXRD data of $CaBr_2(NH_3)$, with fits to the hypothetical $Pnnm$ and actual $Cmc2_1$ structures. Table 4.2 shows the crystal structure data output from these structural refinements. Figure 4.9 shows the PND data of $CaCl_2(NH_3)$ with fitting to the $Cmc2_1$ structure.

Table 4.2: Data output from refinement of $CaBr_2(ND_3)$ (PND) and $CaBr_2(NH_3)$ (PXRD).

Parameter	PND	PXRD
Temperature (°C)	238–275 (*in-situ*, ramp rate of 2 K/min)	25
χ^2	1.39	4.32
R_{wp}	1.01	0.72
R_{exp}	0.73	0.17
a-lattice parameter (Å)	4.2572(5)	4.2440(3)
b-lattice parameter (Å)	18.828(3)	18.629(1)
c-lattice parameter (Å)	6.6133(8)	6.5718(6)
N-D bond length (Å)	0.98(2)	N/A
D-N-D bond angle (°)	105(3)	N/A
Ca-N bond length (Å)	2.39(3)	2.22(2)
Space Group	$Cmc2_1$	$Cmc2_1$
Br-fractional coordinates	(0, 0.087(1), 0.705(3))	(0, 0.0736(3), 0.7014(5))
Br-fractional coordinates	(0, 0.2451(6), 0.062(2))	(0, 0.2441(3), 0.0284(9))
Ca-fractional coordinates	(0, 0.346(2), 0.405(2))	(0, 0.3514(5), 0.3849(9))
N-fractional coordinates	(0, 0.414(1), 0.710(7))	(0, 0.4122(8), 0.675(3))

The obtention of a polar crystal is somewhat surprising. It is important to recall that the systematic absences of $Cmc2_1$ are identical to those of the $Cmcm$ space group, and thus they can appear identical in diffraction techniques. However, the conversion from $Cmc2_1$ to $Cmcm$ requires the placement of a mirror plane perpendicular to the c axis. As the c axis is oriented upwards in Figure 4.7b, there is no clear way to place a mirror plane here. Any mirror plane placed must either cut directly through Ca-N bonds (to prevent the addition of an extra bond) or be placed perfectly between two Ca-N bonds (thus reflecting them onto one another). This is clearly not possible in the structural motif shown for the $Cmc2_1$ structure, and thus high confidence is placed in this space group determination, despite the polar nature.

One aspect of the mono-ammoniate structure is the strong hydrogen bonding motif obtained. While many subsequent ammoniate structures (see Sections 4.1.4 and 4.1.6) show local hydrogen bonding from an ammonia molecule to four anions, which can lead to more complicated energy changes upon ammonia rotation, the mono-ammoniate achieves a triangular arrangement of anions around each NH_3 moiety. As hydrogen bonding is the most significant attractive force between the layers, this is a crucial aspect of the structure. Figure 4.11 shows this hydrogen bonding motif as viewed down the Ca-N bond.

Table 4.3 shows the CASTEP calculated energies and Madelung energies of each plausible mono-ammoniate structure. These data are in agreement with the diffraction data, suggesting the polar $Cmc2_1$ structure is marginally more stable (though the energy difference is well within the uncertainty associated with such a calculation).

The difference in Madelung energy is clear, though it is much larger than that of the CASTEP calculated energy. As such, it would be naive to place the stability difference as purely due to the arrangement of formally charged ions. However, it

Table 4.3: CASTEP and Madelung energies of possible mono-ammoniate structures. Madelung energy was calculated assuming point charges on only calcium and bromide ions. Values for Madelung energy are absolute, while values for CASTEP calculations are given relative to the lowest energy structure.

	$Pnnm$	$Cmc2_1$
CASTEP Calculated (kJ / mol $CaBr_2$)	0.32	0
Madelung Energy (kJ / mol $CaBr_2$)	-2128.6	-2137.5
CASTEP Calculated (kJ / mol $CaCl_2$)	0.31	0
Madelung Energy (kJ / mol $CaCl_2$)	-2259.2	-2266.1

should be noted that the distance between calcium ions in successive layers is much larger for the $Cmc2_1$ structure (see Figure 4.7), possibly explaining the difference in Madelung energy.

Figure 4.12 shows the deuterium site occupancies refined against the PND data of $CaBr_2(ND_3)$, along with the energy associated with rotating a singular NH_3 molecule in a static framework of the $CaBr_2(NH_3)$ structure. Limited correlation is observed, alongside large uncertainties in the occupancy values. While the lowest site occupancy corresponds to an energy maximum as expected, a low site occupancy is also seen for the minimum energy in the rotation. This may be due to limited PND data quality when only small amounts of ND_3 (the strongest neutron scatterers) are present. While more complex rotational energy changes are observed for other ammoniate phases, the triangle of anions surrounding each NH_3 leads to a very straightforward explanation of the minima (shown in Figure 4.11) and maxima (repetition is seen every 120° due to the three-fold symmetry of an NH_3 molecule) in the DFT calculations.

With large energy changes upon rotation of the ammonia molecule in the mono-ammoniate structure ($\sim$6.5 kJ/mol, $RT = 3.93$ kJ/mol at 200 °C) and zero site occupancy refined from PND data at these energy maxima, it is likely that full rotation of the ND_3 molecule is not occurring, but the ND_3 molecule is merely oscillating around its minimum energy position.

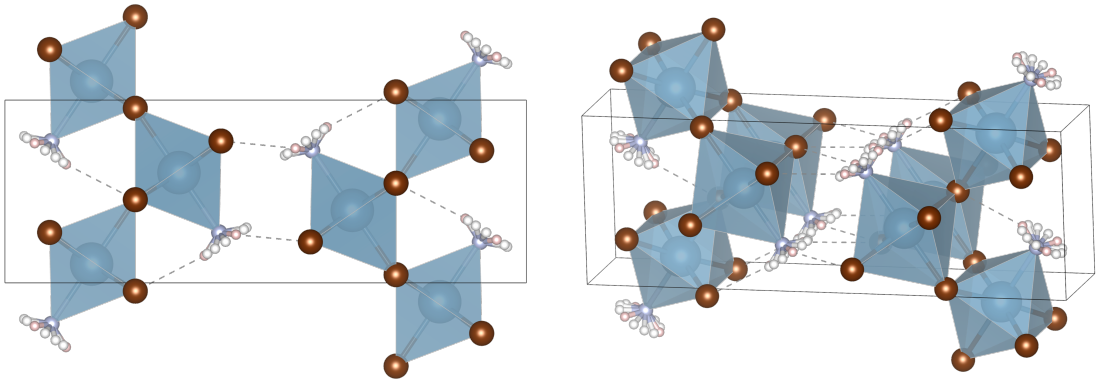
Given the minimal energy differences between the hypothetical $Pnnm$ structure and the $Cmc2_1$ structure, it is plausible that, on a local level, both are present. This could present itself as stacking faults or micro-domains, whereby many layers are oriented in the same direction (i.e. the $Cmc2_1$ structure) then the next n layers are oriented in the opposite direction (n does not have to be constant, of course). It is unclear the distribution with which n would follow. However, if n is rarely or never small, then the structure would correspond to almost all layers oriented identically to their neighbouring layer, except at the boundary where the switch from 'up' to 'down' occurs. This would lead to the diffraction pattern of this material appearing largely similar to a crystal in which no switch from 'up' to 'down' occurs. This is what is observed, as the Bragg features in the data overwhelmingly fit to the $Cmc2_1$ structure. However, non-Bragg features do occur, which may be a sign that this switch of layer orientation does occur.

A stochastic stacking fault model was built in Python to analyse the possibility of stacking faults. Built probabilistically, the model adds one layer in sequence with a set probability of switching the layer orientation. Figure 4.13 shows the results from this analysis using a model 300 layers thick. Figure 4.13a shows a broad search of the parameter space, while Figure 4.13b shows a detailed search within the best results of the broad search. As the model is built probabilistically, and the switching probabilities examined in detail are very low, it was important to run multiple refinements to ensure random error could be (mostly) eliminated. The boxplots in Figure 4.13b are used to represent the distribution of goodness-of-fit values obtained for each probability of switching layer orientation.

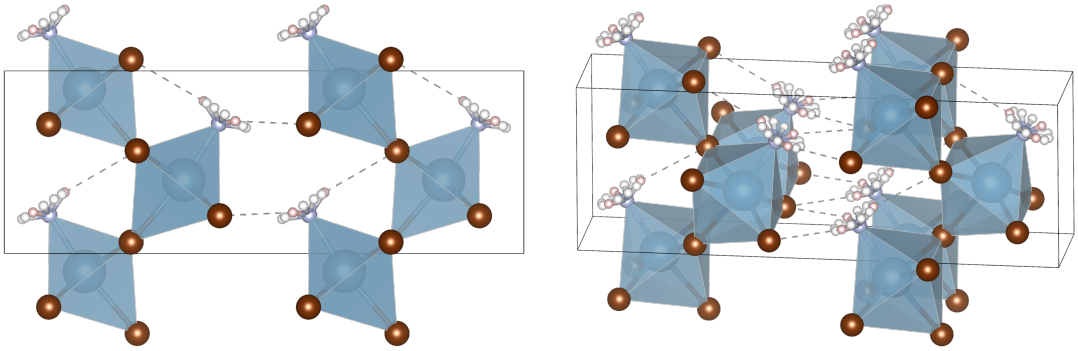
Figure 4.14 shows the PXRD pattern recorded from 2θ = 10–20°, focusing on non-Bragg features, with fits to the best stacking fault model (top) and the $Cmc2_1$ structure (bottom). The peaks around 11.5 and 12.5° show tails at higher angle, alongside similar, but subtle tails in other peaks (e.g. 18.5°). Similarly, a broad feature is seen around 16.5°. It is clear to see from the calculated PXRD patterns and the modest decreases in χ^2 that this stacking fault model does not account sufficiently for these features.

More complex stacking fault models are possible, whereby the next layer added depends on the previous n layers, rather than just the previous layer as used above. A model was built for dependence on the previous two layers (requiring two defined probabilities), but again no significant improvement was observed. Further models were not investigated, due to the inference from these results that the non-Bragg features are not a result of stacking faults or micro-domains. Alongside this, the number of probabilities requiring definition is 2^{n-1}, where n is the number of layers considered when the next layer is added to the model. This makes the search of the parameter space very computationally expensive when $n > 2$.

While the non-Bragg features remain of unknown origin, it is suggested that these may be due to defects in the structure. This could perhaps result from incomplete decomposition during the synthesis of the mono-ammoniate, leading to non-stoichiometric ammonia content, and thus the introduction of defects into the structure. It is important to note that, while PND data quality was limited, there was no clear evidence of non-Bragg features in the *in-situ* PND pattern (beyond the silica background), suggesting these features may result from this particular sample, rather than being inherent to the mono-ammoniate structure.

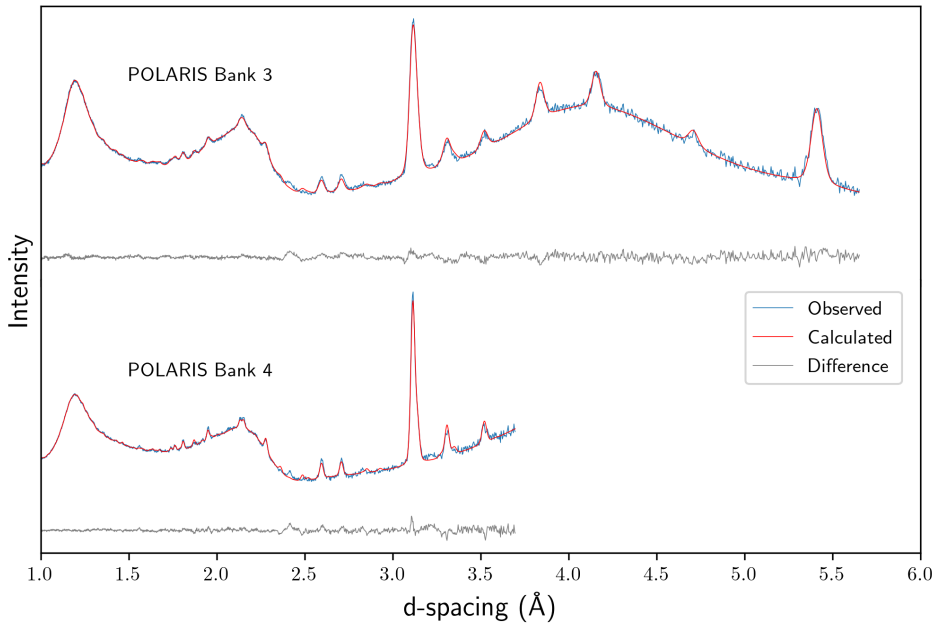


(a)

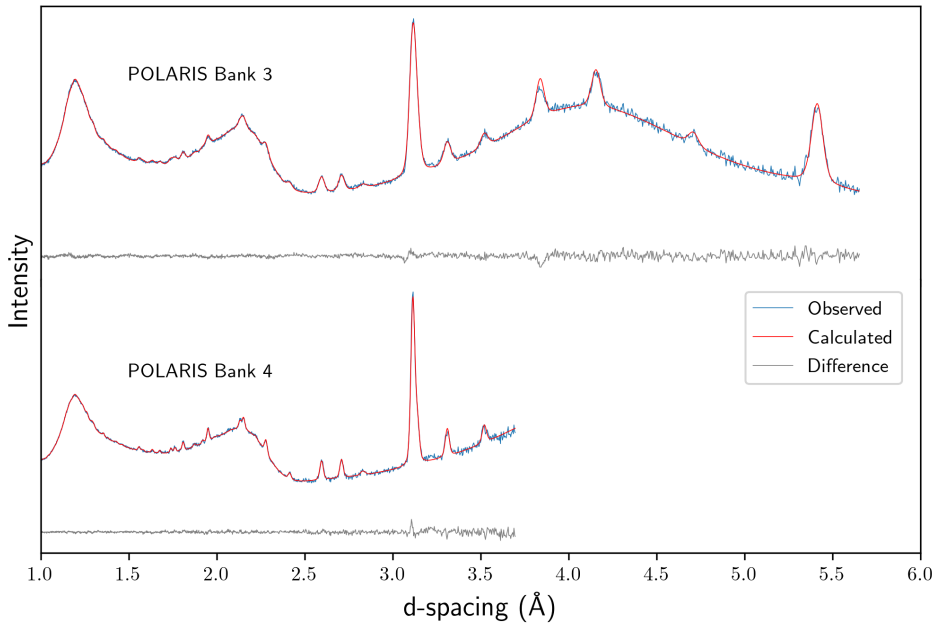


(b)

Figure 4.7: (a) shows the *Pnnm* structure originally derived from PND data. (b) shows the $Cmc2_1$ structure determined after comparison with PXRD data. The two structures are identical within the layers. However, they differ in the relative directionality of consecutive layers. Blue = Ca, grey = N, brown = Br. Due to the likelihood of rotation of ND_3 moieties in the material, deuterium atoms were modelled at evenly-spaced positions on a ring during PND analysis. These deuterium atom positions are shown in white, with pink representing the lowest energy conformation of the rotating ND_3 moiety (according to results from CASTEP simulations).



(a)



(b)

Figure 4.8: PND data recorded on the POLARIS diffractometer for $CaBr_2(ND_3)$. (a) shows fitting to the *Pnnm* structure ($\chi^2 = 1.55$), while (b) shows fitting to the $Cmc2_1$ structure ($\chi^2 = 1.40$).

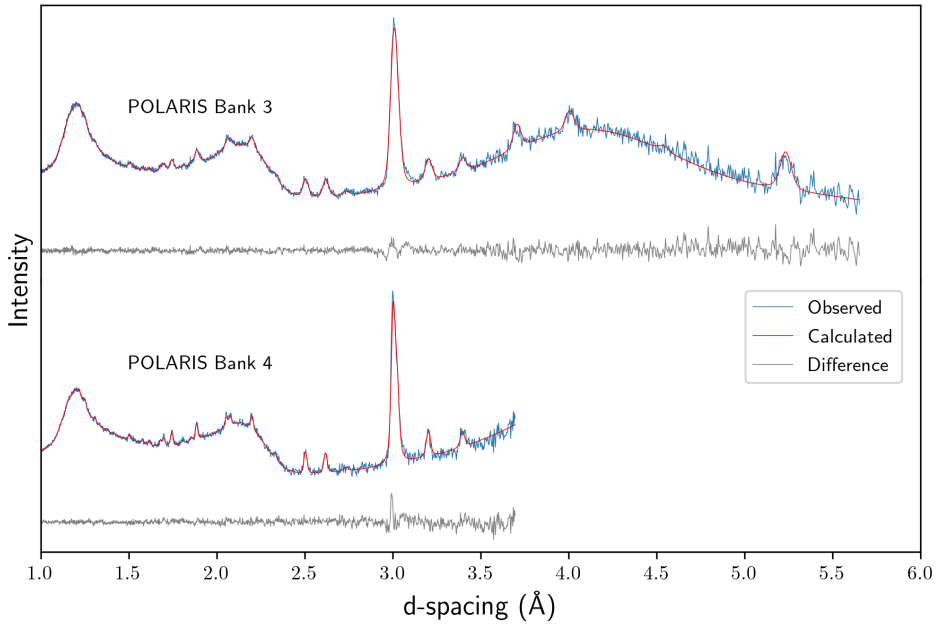


Figure 4.9: PND data recorded on the POLARIS diffractometer for $CaCl_2(ND_3)$ with fitting to the $Cmc2_1$ structure ($\chi^2 = 1.04$).

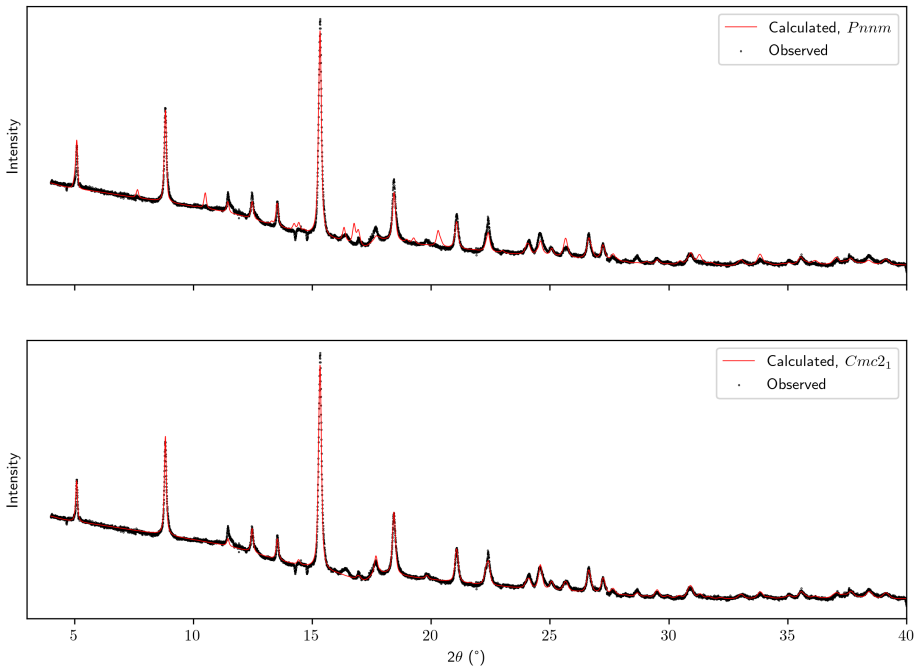


Figure 4.10: PXRD patterns of $CaBr_2(NH_3)$ recorded on the I11 beamline at Diamond Light Source. Fits to the *Pnnm* and $Cmc2_1$ structures are shown (χ^2 = 7.66 and 4.38 respectively). Note the absence of significant peaks in the observed data for the fit to the *Pnnm* structure. The 'drop down' features (14.2 and 14.7°) and complex background is understood to be related to absorption effects. These features were observed across all X-ray diffraction patterns recorded for this sample.

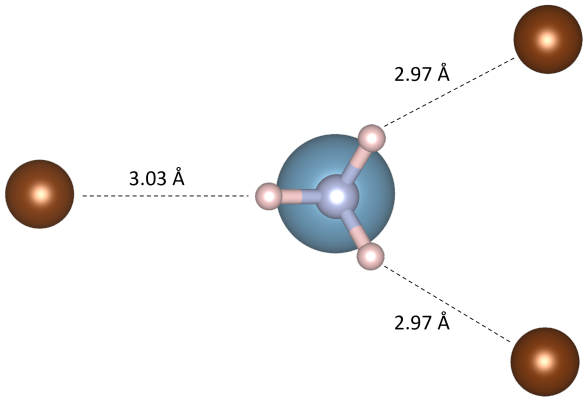


Figure 4.11: Hydrogen bonding motif of the mono-ammoniate as viewed down the Ca-N bond. Bonding between the NH_3 and the two anions on the right is between successive layers, while bonding to the bromide on the left is hydrogen bonding within the layers. Brown = Br, Grey = N, Blue = Ca, Pink = H.

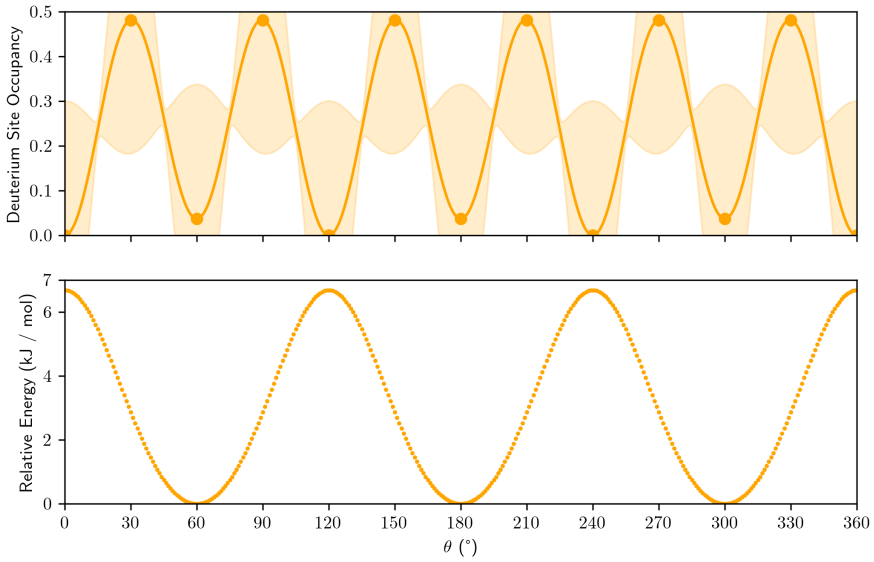
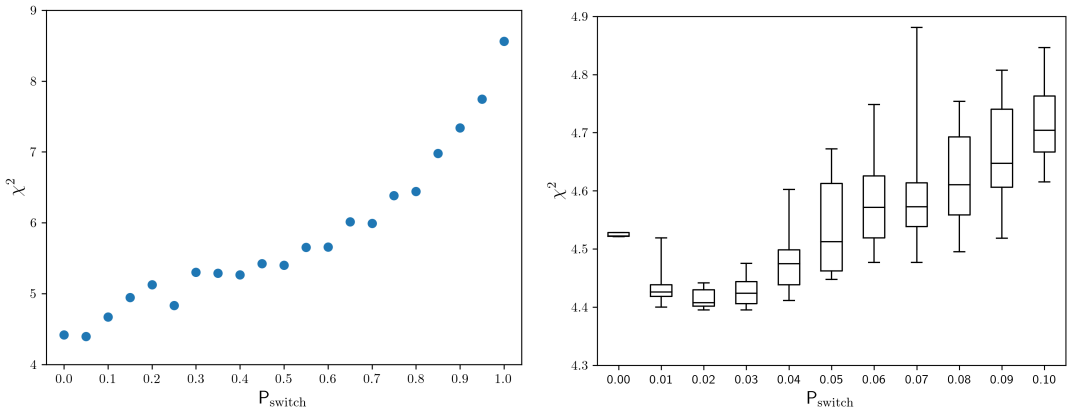


Figure 4.12: Refined deuterium site occupancies in the mono-ammoniate structure plotted above corresponding energy changes according to DFT calculations. The site occupancies were fitted to a circular harmonic function of the form $\text{occ} = \frac{1}{6}\big(1.5 + \alpha_3 \cos(3\theta) + \alpha_6 \cos(6\theta)\big)$, which preserves the three-fold and mirror plane symmetry. $\alpha_3 = -0.11(23)$, $\alpha_6 = -1.4(1.8)$. θ is the angle of rotation of the ND_3 ligand (rotated around the Ca-N vector). A mathematical justification for the use of this equation is given in Appendix A (Equation 1). Uncertainty values are shown as filled areas. Deuterium sites used in refinement are shown as dots. Significant uncertainty in occupancy values at the deuterium sites used is seen, likely explaining why there is little correlation between the CASTEP results and PND analysis. However, uncertainties are small at $\theta = 30\text{n} + 15°$ as the largest uncertainty is associated with α_6, and $\cos(6\theta) = 0$ at these points. The PND pattern was recorded from 238 to 275 °C with a temperature ramp of 2 K / min.



(a) **(b)**

Figure 4.13: Goodness-of-fit results for the mono-ammoniate stacking fault model. It is clear to see that limited improvement to the fit is made for $P_{switch} = 0.02$ when compared with $P_{switch} = 0.00$ (the $Cmc2_1$ structure). Box and whisker plots are used to show the distribution of χ^2 values obtained from this approach for each probability in which multiple structures were tested.

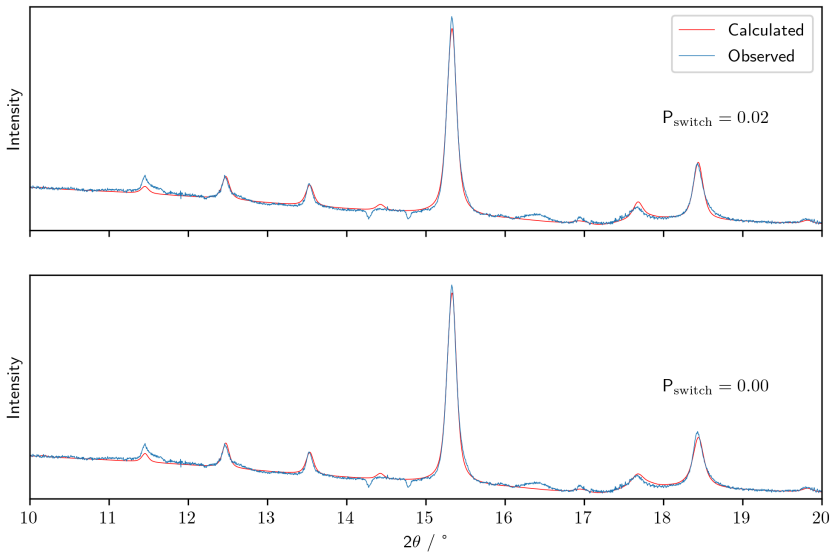


Figure 4.14: The mono-ammoniate PXRD pattern fitted to the best stacking fault model (top, $\chi^2 = 4.40$) and the $Cmc2_1$ structure (bottom, $\chi^2 = 4.52$). Limited improvement is seen, with many non-Bragg features remaining unfitted.

4.1.4 $CaCl_2$ and $CaBr_2$ Di-ammoniates

Both $CaCl_2$ and $CaBr_2$ form a di-ammoniate phase, with the crystal structure of $CaCl_2(NH_3)_2$ reported as an *Aem*2 phase by Westman *et al.*[95] in 1981. Figure 4.15 shows the crystal structure reported. The bending of N-Ca-N angles in Westman's structure leads to a descent in symmetry from *Aema* (equivalent to *Cmce*) to *Aem*2 symmetry. This bending is surprising from a chemical standpoint, though hydrogen bonding was offered as an explanation by the authors.

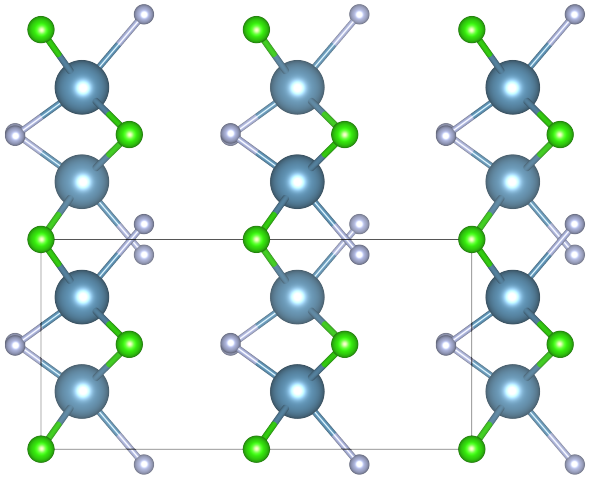


Figure 4.15: The *Aem*2 crystal structure of $CaCl_2(NH_3)_2$ as reported by Westman *et al*[95]. Note the bending of the N-Ca-N angle, hypothesised to be a result of hydrogen bonding by the authors. Cl = green, Ca = blue, N = grey.

Figure 4.16 shows the PXRD pattern of a mixture of $CaCl_2$ and $CaCl_2(NH_3)_2$ recorded on the I11 beamline. Importantly, Westman *et al's* structure did not fit to the data. Instead, the reported crystal structure of the di-ammoniate of $MgCl_2$ (Leineweber *et al.*[101]) fitted well. It should be noted that the FWHM of peaks produced by the di-ammoniate is significantly greater than that produced by the pure $CaCl_2$. While some variation was seen depending on the exact phase and synthesis procedure, the appearance of broader diffraction peaks after absorption processes was a general observation throughout this work. Clearly it is not feasible for a crystal structure to incorporate large amounts of ammonia instantaneously, and

so this phenomenon is likely related to ammonia molecules interrupting the bonding network upon absorption, leading to fragmentation of crystallites. This is likely to lead to much smaller crystallite sizes and much higher levels of strain within the powder; two factors greatly affecting peak width in PXRD patterns. This is consistent with visual observations after experiments, where powders were typically much finer with higher flowability after exposure to ammonia.

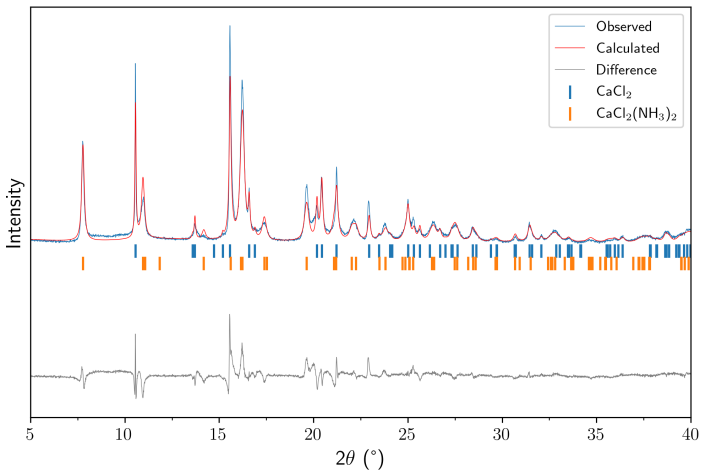


Figure 4.16: PXRD recorded on the I11 beamline showing the diffraction patterns of $CaCl_2$ and $CaCl_2(NH_3)_2$. $CaCl_2$ was fitted to the distorted rutile *Pnnm* structure, while $CaCl_2(NH_3)_2$ was fitted to the $MgCl_2$ di-ammoniate *Cmmm* structure. Blue = observed data, red = calculated data. $\chi^2 = 5.41$.

It is interesting to note the lack of mono-ammoniate phase present in the PXRD data shown in Figure 4.16, given that the sample was simply produced by exposure of $CaCl_2$ to flowing ammonia at room temperature and 1 bar. This suggests that absorption of the second mole of ammonia is extremely rapid in comparison with absorption of the first mole of ammonia, such that the concentration of mono-ammoniate phase in the sample is too low to be visible above the background in the PXRD data. While much work available in the literature examines ammoniation equilibria independently, similar results have been observed in pressure-composition isotherms by Liu *et al*[108]. Testing the absorption of various salts ($CaCl_2$, $CaBr_2$,

$SrCl_2$ and $SrBr_2$) at room temperature under slowly increasing ammonia pressure (from 0–80 kPa) revealed a common hysteretic effect. While many intermediate phases are known to be stable, the coordination number of the salt would remain at zero, then absorption would occur rapidly to a higher ammoniate phase, seemingly 'skipping' certain intermediate phases. This was seen for $CaCl_2$, which absorbed directly to the di-ammoniate phase, $CaBr_2$ and $SrBr_2$, both of which absorbed directly to the hexa-ammoniate phase after absorption started.

The origin of this is not clear, but does not appear to be exclusive to $CaCl_2$ or these ammoniate phases. Given that absorption of the first mole of NH_3 releases large quantities of heat, this may lead to faster reaction speeds locally. This would cause intermediate ammoniate phases to react quickly immediately after formation and could be the origin of the mono-ammoniate phase being undetectable in Figure 4.16.

Figure 4.17 shows the PND pattern of $CaCl_2(NH_3)_2$ recorded *in-situ* on the POLARIS diffractometer at ISIS Neutron and Muon Source. This pattern was recorded during a temperature ramp from 107–142 °C at a rate of 2 °C/min. While this did not appear to greatly affect the structure used for fitting, it should be considered when drawing comparisons with the PXRD data in Figure 4.16, which was recorded at room temperature. Again, good agreement between observed and calculated data was found for the *Cmmm* structure, while poor agreement was seen for the previously reported *Aem*2 structure (or the higher symmetry version, the equivalent *Cmce* structure). The method described in Section 4.1.3 for the calculation of deuterium positions was used, with deuterium atoms evenly spaced every 30° to account for the rotation of ND_3 molecules.

The data output from the refinement of the *Cmmm* structure is presented in Table 4.4, and the structure is shown in Figure 4.18.

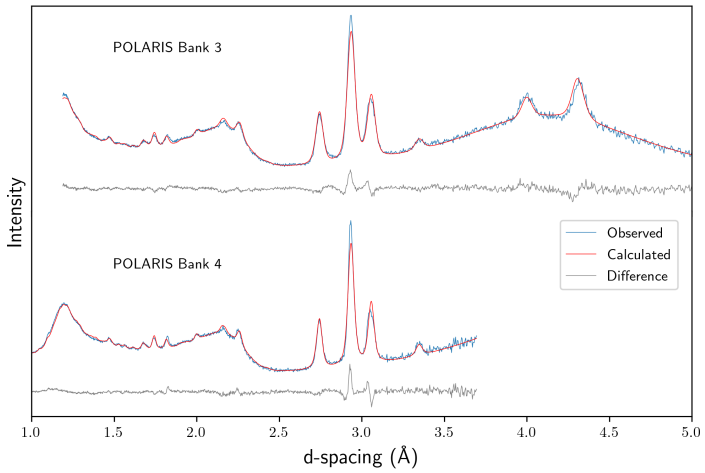


Figure 4.17: PND pattern of $CaCl_2(ND_3)_2$ recorded on the POLARIS diffractometer. The data is fitted to the *Cmmm* structure of $CaCl_2(ND_3)_2$. Blue = observed data, red = calculated data. $\chi^2 = 1.79$.

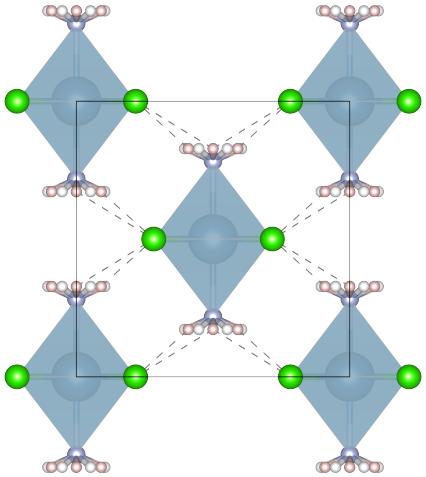


Figure 4.18: Structure of $CaCl_2(ND_3)_2$ in the *Cmmm* space group, refined from PND data. The two energetic minima of ND_3 ligands are shown in pink (from CASTEP results), with dashed lines indicating hydrogen bonding. Blue = Ca, grey = N, brown = Br. Due to the likelihood of rotation of ND_3 moieties in the material, deuterium atoms were modelled at evenly-spaced positions on a ring during PND analysis. These deuterium atom positions are shown in white, with pink representing the lowest energy conformation of the rotating ND_3 moiety (according to results from CASTEP simulations).

Table 4.4: Data output from PND refinement of $CaCl_2(ND_3)_2$ in the $Cmmm$ structure.

Parameter	Value
χ^2	1.79
R_{wp}	1.75
R_{exp}	0.98
a-lattice parameter (Å)	8.622(2)
b-lattice parameter (Å)	8.698(1)
c-lattice parameter (Å)	4.005(1)
N-D bond length (Å)	0.98(2)
D-N-D bond angle (°)	105(2)
Ca-N bond length (Å)	2.46(2)
Space Group	$Cmmm$
Cl-fractional coordinates	(0.217(1), 0, 0.5)
Ca-fractional coordinates	(0, 0, 0)
N-fractional coordinates	(0, 0.283(2), 0)

No crystal structure has been previously reported in the literature for $CaBr_2(NH_3)_2$. However, Westman *et al.*'s *Aem*2 structure[95] reported for $CaCl_2(NH_3)_2$ fits well to all recorded diffraction data for $CaBr_2(NH_3)_2$ in this thesis. The higher symmetry *Cmce* structure (*Aema*) was used throughout this work, as the likelihood of a distortion to the polar *Aem*2 structure was deemed low. Figure 4.19 shows the PXRD pattern of $CaBr_2(NH_3)_2$ recorded on the I11 beamline at Diamond Light Source. As seen for $CaCl_2(NH_3)_2$, broad peaks indicate small crystallites and high levels of strain within the powder, a result of the absorption and desorption processes of these materials.

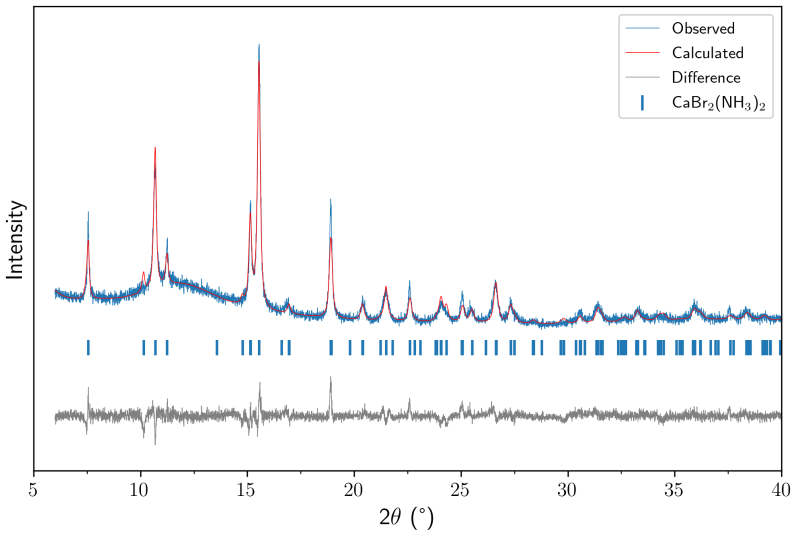


Figure 4.19: PXRD pattern of $CaBr_2(NH_3)_2$ recorded on the I11 diffractometer at Diamond Light Source, with fitting to the *Cmce* structure of $CaBr_2(NH_3)_2$. $\chi^2 = 1.53$.

Table 4.5 shows the data output from structural refinement against PND data in TOPAS. Westman *et al*'s *Aem*2 structure has Ca-N bonds of length 2.36 and 2.74 Å, while the *Cmce* structure refined from PND data gives a bond length of around 2.40 Å, similar to the refined value for the *Cmmm* structure of $CaCl_2(NH_3)_2$ of around 2.46 Å.

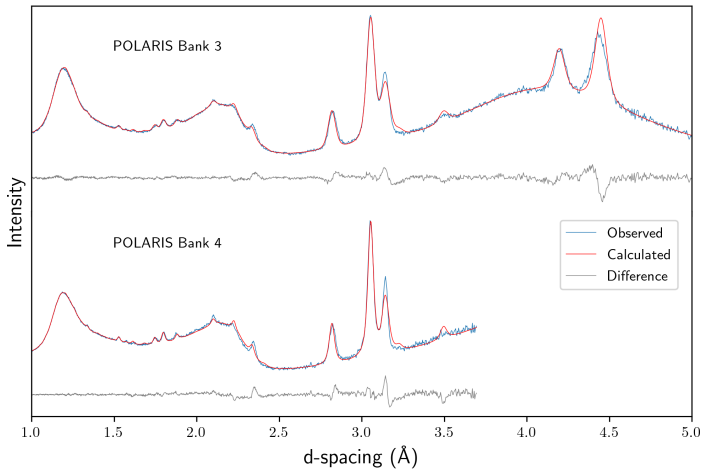


Figure 4.20: PND pattern of $CaBr_2(ND_3)_2$ recorded on the POLARIS diffractometer at ISIS Neutron and Muon Source, with fitting to the *Cmce* structure of $CaBr_2(NH_3)_2$. χ^2 = 1.81.

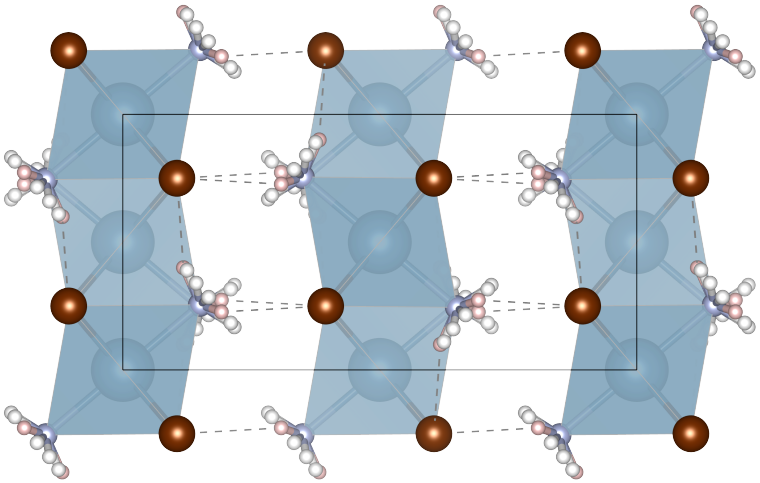


Figure 4.21: Structure of $CaBr_2(ND_3)_2$ in the *Cmce* space group, refined from PND data. Blue = Ca, grey = N, brown = Br. Due to the likelihood of rotation of ND_3 moieties in the material, deuterium atoms were modelled at evenly-spaced positions on a ring during PND analysis. These deuterium atom positions are shown in white, with pink representing the lowest energy conformation of the rotating ND_3 moiety (according to results from CASTEP simulations).

Table 4.5: Data output from PND refinement of $CaBr_2(ND_3)_2$ in the *Cmce* structure.

Parameter	Value
χ^2	1.81
R_{wp}	1.16
R_{exp}	0.64
a-lattice parameter (Å)	8.407(1)
b-lattice parameter (Å)	12.643(2)
c-lattice parameter (Å)	6.286(1)
N-D bond length (Å)	0.98(3)
D-N-D bond angle (°)	105(3)
Ca-N bond length (Å)	2.40(4)
Space Group	*Cmce*
Br-fractional coordinates	(0.25, 0.8998(8), 0.25)
Ca-fractional coordinates	(0, 0, 0)
N-fractional coordinates	(0, 0.852(2), 0.760(4))

The structural diversity seen within the di-ammoniate phases is important to understand prior to analysis of the ammonia absorption properties of mixed halide phases. For this purpose, these structures were studied using Madelung energy and CASTEP calculations.

Jones *et al.*[92] already showed the strong effect that ionic bonding can play in ammoniate formation with their study on $MgX_2(NH_3)_n$ ammoniates. Similar to the invocation of the Kapustinskii equation, Ewald summations are used here to study the strength of simple ionic bonding within each structure. It should be noted that ionic bonding alone is not an accurate description of the materials, and should only form part of the explanation of the structural preference. Table 4.6 shows the Madelung energies calculated for each structure and anion. Structures were geometry optimised in CASTEP using a cutoff energy of 950 eV prior to analysis.

Table 4.6: Madelung energies of CASTEP geometry optimised di-ammoniate structures of $CaX_2(NH_3)_2$. Energies were calculated assuming point charges on Ca^{2+} and X^-. No charge was assigned to N and H atoms.

	Cl	Br
E_{Cmce} (kJ/mol Ca)	-2171.3	-2043.5
E_{Cmmm} (kJ/mol Ca)	-2134.9	-2011.4
ΔE (kJ/mol Ca)	-36.4	-32.1

From the perspective of pure ionic bonding, the *Cmce* structure should be favoured. Cl generally shows greater magnitude of Madelung energy, due to its smaller size. In fact, the ratios between the calculated Madelung energies (E_{Cl}/E_{Br}) match well with the expected ratio from the Kapustinskii equation (0.94 vs 0.95) when Shannon ionic radii[134] are used for Ca^{2+} and X^-. Bonding between Ca and N atoms is likely to be of very similar strength, regardless of the anion and wider structure, as shown previously for $MgX_2(NH_3)_2$ phases by Jones *et al.*[92] using solid state NMR spectroscopy.

Hydrogen bonding is an important, and heavily anion-dependent, aspect of bonding in ammoniate phases. Structural analysis of CASTEP geometry optimised crystal structures allows insight into the hydrogen bonding network of these phases.

Figures 4.22 and 4.23, and Tables A.1 and A.2 show the data associated with the hydrogen bonding within each of the possible di-ammoniate structures.

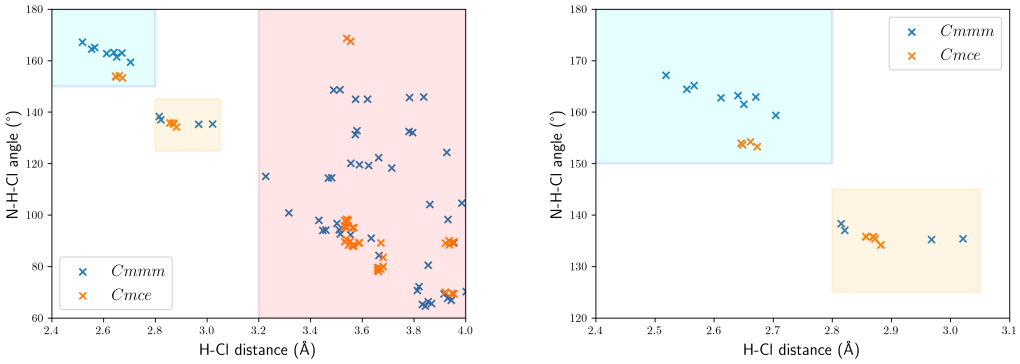


Figure 4.22: Hydrogen bonding in geometry optimised $CaCl_2(NH_3)_2$ Phases. Data points in the blue rectangle represent strong hydrogen bonds. Those in the orange rectangle represent weaker hydrogen bonds, while those in the red rectangle are functionally insignificant hydrogen bonds. (a) shows an overview, while (b) shows a zoomed view on the hydrogen bonds deemed notable.

Aside from obvious trends such as lower H-X distances when X = Cl, there are subtleties within these data that may inform structural preferences. In this analysis, it should be noted that these geometry optimised structures consist of static ions/atoms, which effectively give a snapshot of the ground state structure. While this is informative, real systems will consist of rotating and vibrating NH_3 molecules. Figure 4.24 shows representations of the local ground state hydrogen bonding network for each of the diammoniate structures.

From Figure 4.22, it appears that hydrogen bonding in the *Cmmm* structure is likely to be stronger, due to generally shorter H-Cl distances, and consistently straighter N-H-Cl angles (closer to 180°). N-H-X angles closer to 180° lead to

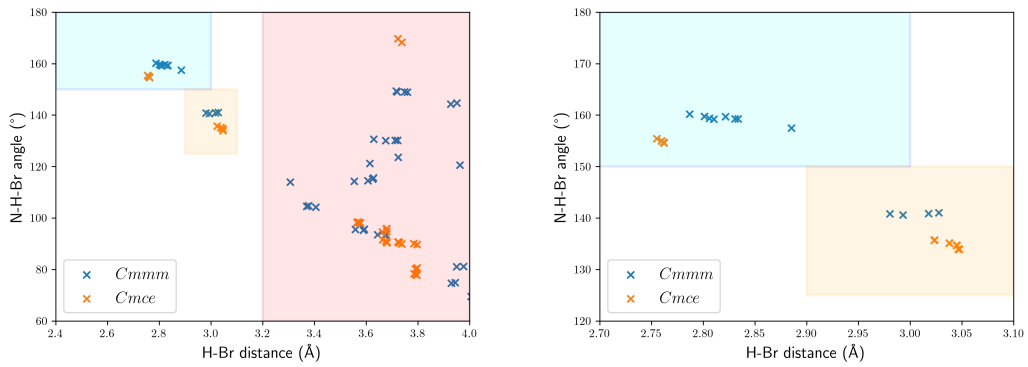
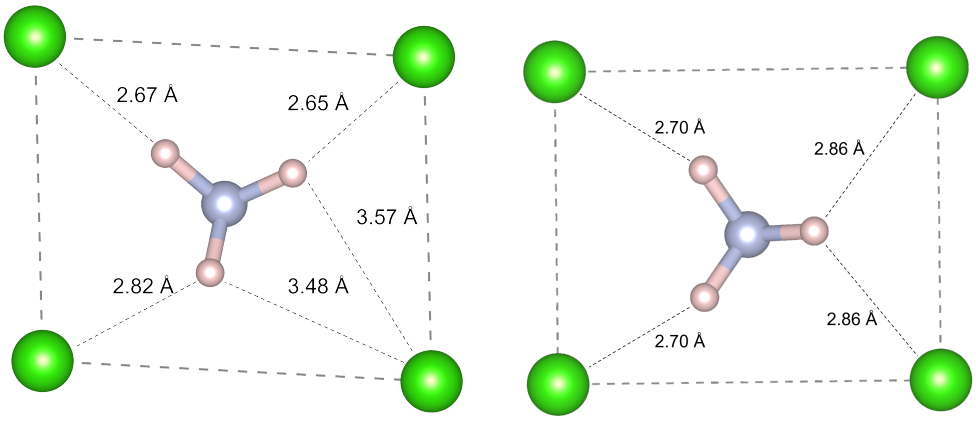


Figure 4.23: Hydrogen bonding in geometry optimised $CaBr_2(NH_3)_2$ Phases. Data points in the blue rectangle represent strong hydrogen bonds. Those in the orange rectangle represent weaker hydrogen bonds, while those in the red rectangle are functionally insignificant hydrogen bonds. (a) shows an overview, while (b) shows a zoomed view on the hydrogen bonds deemed notable.

stronger hydrogen bonding due to better orbital overlap with the N-H σ^* orbital. However, Figure 4.23 shows consistently longer H-Br distances for the 'strong' hydrogen bonds in the *Cmmm* structure, compared to the *Cmce* structure. Clearly structure type is not a single decisive factor controlling H-X distances. This is likely due to the orientation of hydrogen bonding within the wider network of anions in each structure.

Alongside the data presented thus far, it should be noted that the Ca-X-Ca angle in the *Cmmm* structure is much tighter than observed for the *Cmce* structure (see Table 4.7), allowing greater hydrogen bonding strength through limiting repulsion between $H^{\delta+}$ and Ca^{2+}.

While the *Cmmm* structure has more favourable N-H-X and Ca-X-Ca angles for hydrogen bonding, it appears these can only be taken advantage of by an appropriately sized anion, such as chloride. The staggered arrangement of anions between layers in the *Cmce* structure (see Figure 4.25) likely allows this structure the flexibility to modify the 'between-layer' hydrogen bond distances as required (see Figure



(a) **(b)**

Figure 4.24: The ground state hydrogen bonding structure in di-ammoniate phases, calculated via CASTEP geometry optimisations. Distances are given for chloride ions. Dashed lines indicate the anion rectangle, while dotted lines indicate hydrogen bonding. (a) shows the local hydrogen bonding in the *Cmmm* structure, while (b) is for the *Cmce* structure. Note the bifurcated hydrogen bonding observed in the *Cmce* structure.

Table 4.7: Ca-X-Ca angles in $CaX_2(NH_3)_2$ phases. A smaller Ca-X-Ca angle can limit repulsion between $H^{\delta+}$ and Ca^{2+}.

Structure	Cl (°)	Br (°)
Cmmm	95.5	94.5
Cmce	125.7	124.8

4.26). The *Cmmm* structure, on the other hand, arranges anions 'in-line', leading to much higher anionic repulsions, thus controlling the interlayer spacings tightly (Figure 4.25). It should be noted that bromide ions are weaker hydrogen bond acceptors than chloride ions due to their larger size and weaker orbital overlap with the N-H σ^* orbital, and as such hydrogen bonding will have a smaller, but still very significant effect on the stability of bromide phases.

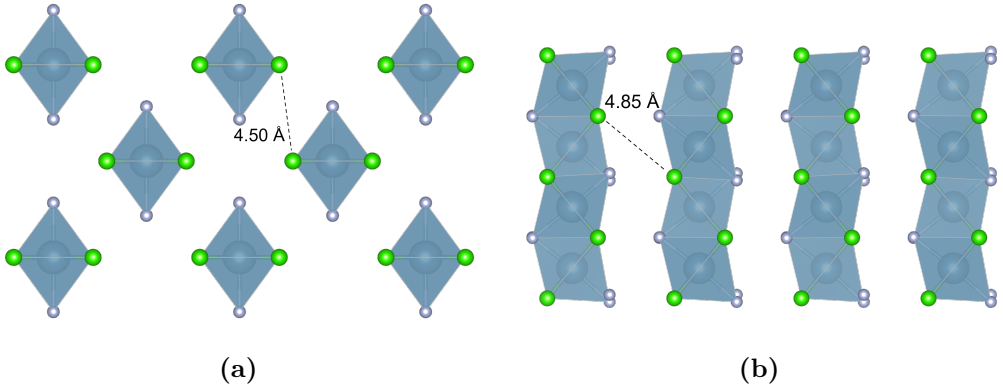


Figure 4.25: Interlayer nearest-neighbour distances for chloride anions in the (a) *Cmmm* and (b) *Cmce* di-ammoniate phases. The 'in-line' arrangement of anions in the *Cmmm* phase controls interlayer distances through anionic repulsion, while the staggered arrangement of anions in the *Cmce* phase allows hydrogen bonding to impact interlayer distances more significantly.

In order to learn more about hydrogen bonding within these structures, a singular ammonia molecule was rotated with constant N-H bond length (1.02 Å) and H-N-H angle (106°), with all other atoms/ions held in constant position. The energy of each of these structures was calculated in CASTEP, with results shown in Figures 4.27 and 4.30.

Unsurprisingly, rotation within the *Cmmm* structure shows greater energy changes for chloride anions, as would be expected from the greater hydrogen bond strength of the chloride ion. The *Cmmm* dataset shows two minima, at $\theta = 120\text{n}^\circ$ and $\theta = 120\text{n} + 60^\circ$, and maxima at $\theta = 120\text{n} \pm 28^\circ$. It should be noted that these structures were not geometry optimised, and as such the energy minima of NH_3 rotation

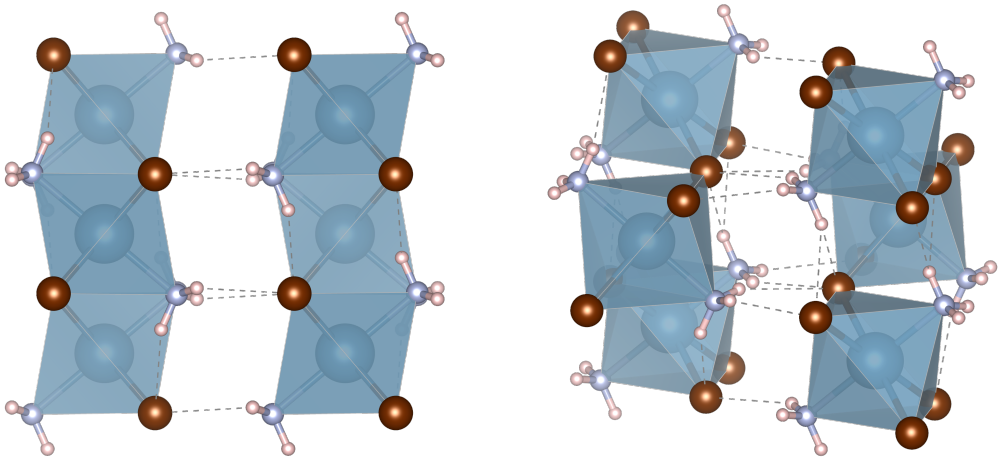


Figure 4.26: 'Between-layer' and 'in-layer' hydrogen bonding in the *Cmce* di-ammoniate phase, viewed down the *a* axis (left) and slightly offset from the *a* axis (right). CASTEP results show 'between-layer' bonding is significantly more favourable. This is likely on account of the favourable H···X−Ca angles (97° and 135° for 'between-layer' vs. 101° and 87° for 'in-layer' bonding), limiting repulsion between $H^{\delta+}$ and Ca^{2+}. Pink = H, Brown = Br, Blue = Ca, Grey = N.

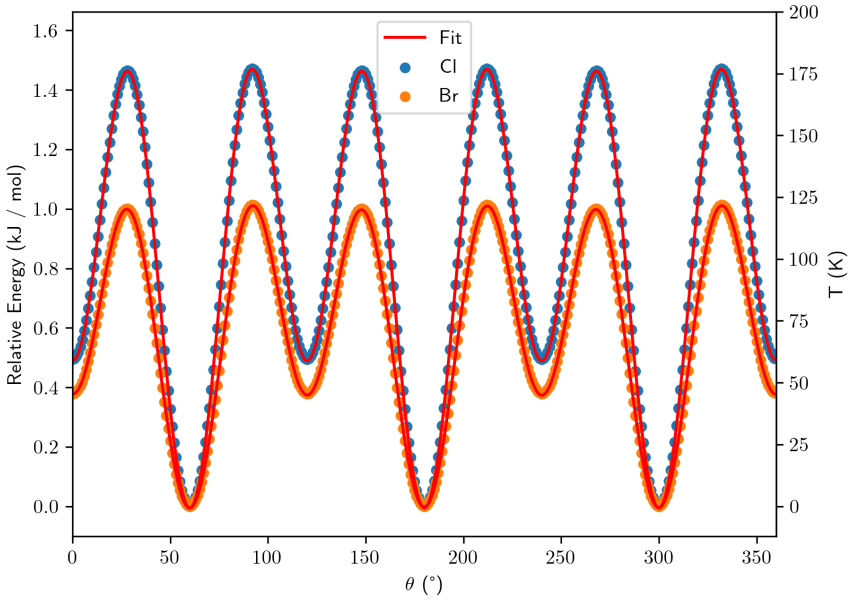
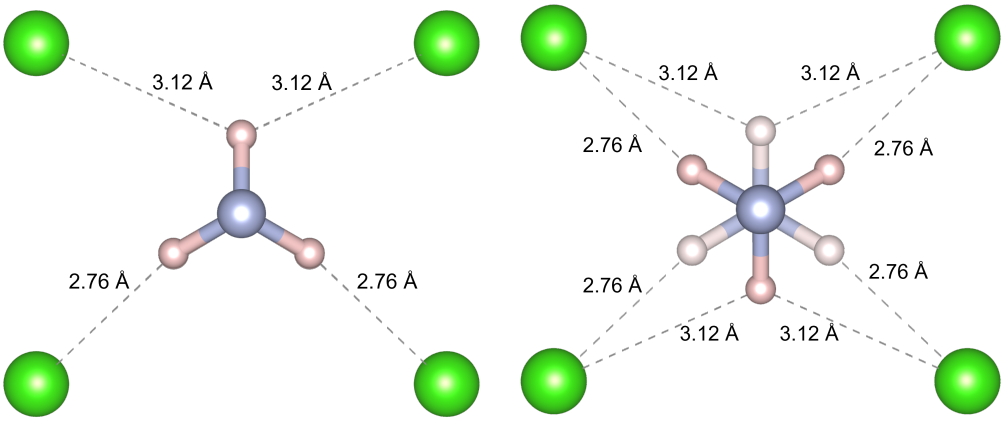


Figure 4.27: Energy changes upon rotation of one NH_3 molecule in the *Cmmm* structure for chloride and bromide anions. Fits to a sum of sine and cosine functions are shown.

correspond to the equivalent of the picture seen in Figure 4.24b rather than Figure 4.24a (i.e. minimum involves bifurcated hydrogen bonding). This implies that the ability of the anions to move significantly stabilises the arrangement seen in Figure 4.24a. The primary difference between minimum and maximum energies is which side of the anion rectangle is bifurcated hydrogen bonding. Bifurcated is used to refer to an N-H bond which splits its hydrogen bonding equally between two halide ions, while mono-furcated is used to describe an N-H bond which points towards, and bonds exclusively with, a singular anion. If the longer side (between octahedra) is bifurcated, this corresponds to a minimum (the mono-furcated hydrogen bonds have shorter H-X distances). If the shorter side (within octahedra) is bifurcated, this corresponds to an energy maximum. The difference between the local and global minima is the effect of other NH_3 molecules within the structure, one of which points directly at our rotating NH_3 molecule. Much like conformations in organic molecules, if the NH_3 molecules are eclipsed this raises the energy through repulsion of the $H^{\delta+}$ atoms. This effect also appears to a lesser degree in the maxima, slightly shifting them off the expected position of $\theta = 120\text{n} \pm 30^\circ$ to $\theta = 120\text{n} \pm 28^\circ$, as this corresponds to both unfavourable interactions with the anion rectangle and closer 'eclipsing' of $H^{\delta+}$ atoms (28° off a perfect eclipse rather than 30°). Figures 4.28 and 4.29 show the local structure around the rotating NH_3 molecule for $\theta = 0, 30, 60^\circ$ in the *Cmmm* structure.

Refinement of deuterium occupancies in the neutron diffraction data of the *Cmmm* di-ammoniate of $CaCl_2(NH_3)_2$ did not correlate with energy calculations performed in CASTEP. All deuterium scattering was refined onto the deuterium sites at $\theta = 60\text{n} + 30^\circ$ (occupancy = 0.5), which represent the energy maximum of the DFT calculations, while deuterium sites at $\theta = 60\text{n}^\circ$ had a refined occupancy value of 0 (this was not performed using circular harmonics as there are only two distinct sites, as shown in Figure A.1). While data quality was limited, it is important to recognise that there are deficiencies in the fit of this diffraction data (specifi-



(a) **(b)**

Figure 4.28: Local structure of energy minima for an ammonia molecule rotating in the *Cmmm* di-ammoniate phase, viewed down the Ca-N bond. Distances given are for chloride ions. The hydrogen atoms of the rotating ammonia molecule are pink, while those of the nearby stationary ammonia molecule are white. (a) shows the local structure for $\theta = 0°$ while (b) shows the local structure for $\theta = 60°$. These both correspond to energy minima due to the favourable hydrogen bonding. However, the eclipsing of ammonia molecules for $\theta = 0°$, and thus shorter $H^{\delta+}\cdots H^{\delta+}$ distances (3.09 vs. 3.23 Å), leads to an increase in the energy of the system.

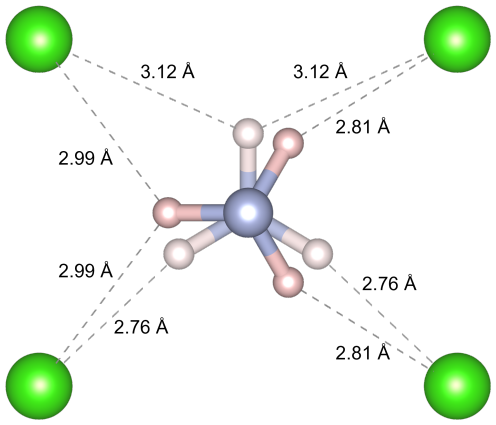


Figure 4.29: Local structure of energy maxima for an ammonia molecule rotating in the *Cmmm* di-ammoniate phase, viewed down the Ca-N bond. Distances given are for chloride ions. The hydrogen atoms of the rotating ammonia molecule are pink, while those of the nearby stationary ammonia molecule are white. The structure shown is for $\theta = 30, 90°$. However, energy maxima are actually observed at $\theta = 28, 92°$ as this corresponds to slightly closer $H^{\delta+}\cdots H^{\delta+}$ distances, raising the energy of the system.

cally peak intensities), and thus deficiencies in the model used. As shown by the CASTEP calculations above, 'eclipsing' of ammonia molecules which point towards one another in this structure has a significant effect on the energy of the system. As such, it is reasonable to expect the disorder associated with rotation of one ND_3 molecule to be correlated with the rotation of another nearby ND_3 molecule. This is not accounted for in the model used for Rietveld refinement of this data and may be the origin of the discrepancy between observed and calculated peak intensities.

For rotation of NH_3 in the *Cmce* structure, only global maxima, at $\theta = 120n + 60°$, and global minima, at $\theta = 120n°$, are observed. The subtleties of eclipsing are now absent, as NH_3 molecules in the *Cmce* structure do not point directly toward one another. However, it is notable that multiple minima are no longer observed within the 120° cycle. As such, this requires a move beyond the simple 'anion rectangle' depicted in Figure 4.24b. The minima correspond to two of the three hydrogens bonding to X ions in a different layer of the *Cmce* structure, while the maxima

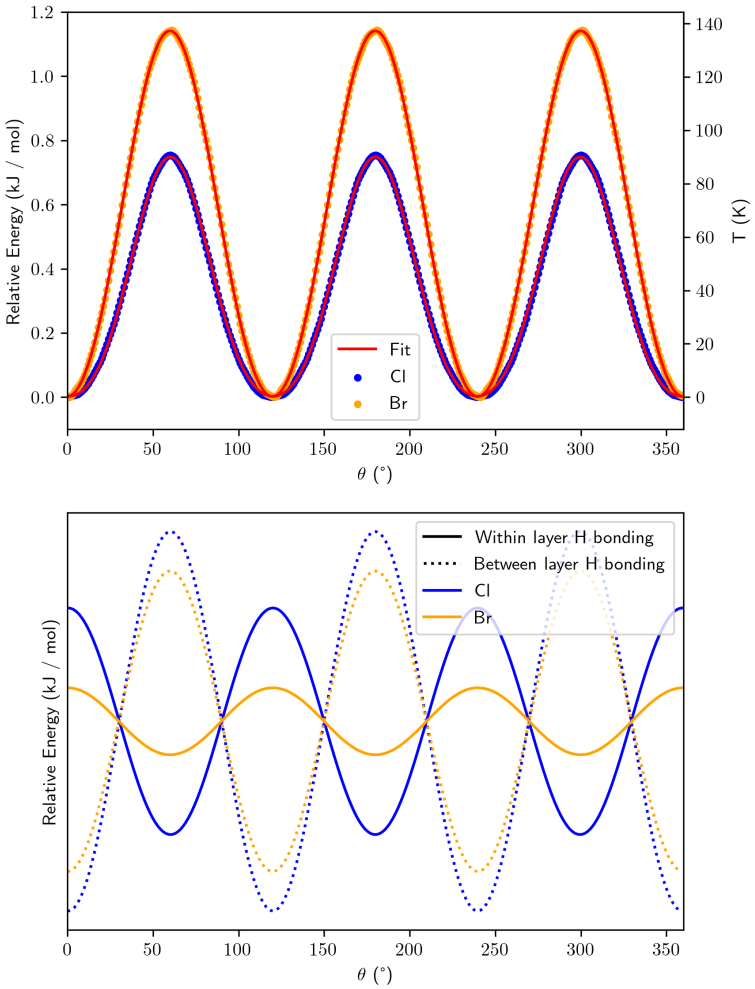


Figure 4.30: Energy changes upon rotation of one NH_3 molecule in the *Cmce* structure for chloride and bromide anions. Fits to sine functions are shown. While the bromide cells show larger energy changes, this does not explicitly mean that bromide forms stronger hydrogen bonds than chloride in the *Cmce* structure. The lower figure shows an example of deconvolution into two modes of hydrogen bonding in the *Cmce* structure, of which the overall energy change would be a sum of these bonding modes. This is purely a representation and is not data. If 'between layer' bonding is weakened less than 'in layer' bonding when moving to a larger halide, then the larger halide will show greater energy changes upon rotation.

correspond to strong hydrogen bonding with two X ions within the same layer of the *Cmce* structure. The 'anion rectangle' approach in the *Cmmm* structure is sufficient for an analysis of local bonding, as all anions in the rectangle are equivalent. However, in the *Cmce* structure this is not the case. The H···X−Ca angle for 'between-layer' hydrogen bonding is much more favourable (H atoms approach from further away from the Ca^{2+} ions) than the angle for 'in-layer' hydrogen bonding, leading to favourability towards maximising 'between-layer' bonding at the expense of other hydrogen bonding. This is shown in Figure 4.26.

It is slightly surprising to see larger energy changes for Br than for Cl, though this can be explained. Similar to the explanation given above for the reversal of the H-X distance trend, when the *Cmce* structure moves to a larger ion, the H-X distances for 'in-layer' hydrogen bonding are 'forced' to rise significantly by the anion repulsion and Ca-X bond distance. However, from an ionic repulsion perspective, the 'between-layer' distances are much more free to vary due to the staggered arrangement of anions. Nearest-neighbour bromide ions in the same layer have an interionic distance of 4.18 Å while nearest-neighbours in different layers show a distance of 4.85 Å. This is similar to the explanation given previously, explaining how significantly interlayer distances are controlled by anion-anion repulsions. As such, when changing the anion from chloride to bromide in the *Cmce* structure, the 'in-layer' hydrogen bonding is weakened significantly, while the 'between layer' bonding is only slightly weakened.

The lower figure in Figure 4.30 depicts how this can lead to larger overall energy changes for bromide ions, if the unfavourable bonding mode is weakened more than the favourable bonding mode. The larger energy change for bromide upon NH_3 rotation in the *Cmce* structure does not necessarily mean bromide forms stronger hydrogen bonds in this structure than chloride. However, the results to date suggest that chloride favours the *Cmmm* structure on a hydrogen bonding basis, while it appears the *Cmce* structure would provide stronger hydrogen bonding for bromide.

This is consistent with, though not a direct conclusion of, the maximum energy changes seen upon NH_3 rotation, which are ordered like so: Cl^- *Cmmm* > Br^- *Cmce* > Br^- *Cmmm* > Cl^- *Cmce*.

These results can be used to gauge the likelihood of free rotation of NH_3 molecules within these systems. RT = 2.479 kJ / mol at 298 K, well above the energy changes seen for rotation of these NH_3 ligands, and as such free rotation is highly likely at room temperature and above in the di-ammoniate systems. However, it should be noted that these energy calculations were performed by rotating one ammonia molecule in a static framework of atoms, and so the effects of spinning multiple ammonia molecules are not fully captured, though the effects of eclipsing, where relevant, are. It should be noted that the effects of subtle movements of X^- ions are also absent from this approach.

Figure 4.31 shows the occupancy of deuterium sites obtained from PND analysis plotted alongside the energy of the corresponding rotation calculated using DFT. Some correlation between the datasets is seen, with the maximum site occupancy corresponding to the minimum energy as expected. However, the minimum site occupancy does not correspond to the maximum energy values seen from DFT. The large uncertainties on the occupancy values indicate the low reliability of the occupancy values from the PND analysis. No clear correlational effects between rotating and static ammonia molecules were seen in the DFT calculations, which would cause local minima and maxima to appear, as seen for the *Cmmm* structure. However, only one ammonia molecule was rotated within a static framework of atoms. As such, subtler effects of ammonia correlation will have been missed in these CASTEP results. It is possible that correlation of ND_3 rotation is affecting peak intensities in the diffraction data, and this may be the origin of occupancy values inconsistent with CASTEP results and chemical intuition. It should be noted that limits were imposed on the circular harmonic function to ensure the occupancy of every position (including those between the modelled sites) was greater than

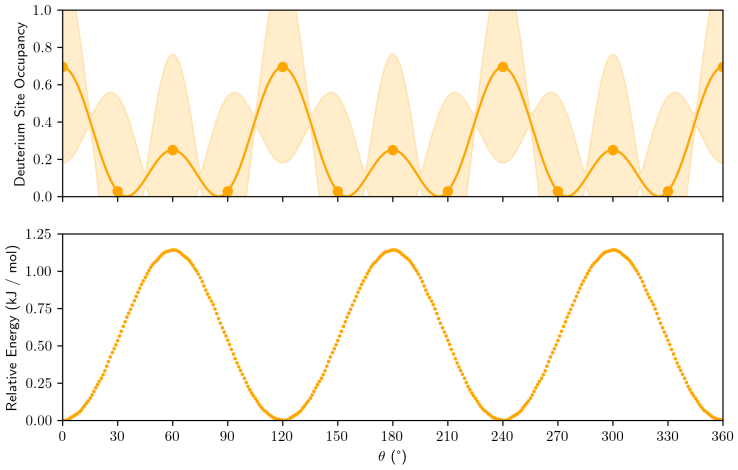


Figure 4.31: Refined deuterium site occupancies in the *Cmce* di-ammoniate structure ($CaBr_2(ND_3)_2$) plotted above corresponding energy changes according to DFT calculations. The site occupancies were fitted to a circular harmonic function of the form $\text{occ} = \frac{1}{6}\big(1.5 + \alpha_3 \cos(3\theta) + \alpha_6 \cos(6\theta)\big)$, which preserves the three-fold and mirror plane symmetry. $\alpha_3 = 1.3(4)$, $\alpha_6 = 1(3)$. θ is the angle of rotation of the ND_3 ligand (rotated around the Ca-N vector). Uncertainties on occupancy values are shown as a filled area. Deuterium sites used in refinement are shown as dots. Uncertainties are small at $\theta = 30$n +15° as the largest uncertainty is associated with α_6 and $\cos(6\theta) = 0$ at these points. The PND pattern was recorded from 141–223 °C with a temperature ramp rate of 2 K / min and is shown in Figure 4.20.

zero. When occupancies are refined individually (i.e. without the circular harmonic function), all deuterium occupancy is refined onto the $\theta = 120n°$ sites, with all other deuterium occupancies refined to zero.

4.1.5 $CaCl_2$ Tetra-ammoniate

In the available literature there is sparse information on $CaCl_2(NH_3)_4$. Its existence has been known since Hüttig's work in 1922[102]. However, no research has moved beyond this, presumably in part due to its limited stability (it is unstable at room temperature without an ammonia atmosphere present). The *in-situ* POLARIS experiment was the first opportunity to study this material crystallographically. Indexing of the PND pattern produced by $CaCl_2(NH_3)_4$ suggested one crystal structure, which could be represented as a trigonal $P3$ unit cell (a = 11.17, c = 5.88 Å) or the equivalent orthorhombic cell (lattice parameters of ($a\sqrt{3}$, a, c)). The volumes of formula units of other $CaCl_2(NH_3)_n$ ammoniate phases approximately follow a volume relationship equal to 84 + 31n Å^3. As the $P3$ cell has a volume of 635.4 Å^3, this unit cell likely contains three formula units (which may be anticipated with a threefold rotation axis as a symmetry element).

In order to determine the exact positioning of atoms within this unit cell, the relevant number of calcium atoms, ammonia molecules (with a random orientation) and chlorine atoms were placed in a $P3$ unit cell, at random positions, and refined against the data. This was repeated hundreds of times using TOPAS' batch refinement functionality. The crystal structures corresponding to the best fits (by analysis of R_{wp}) were then visually examined to ensure reasonable interatomic distances and overall structural motif. The output structure from the best fits consisted of isolated $CaCl_2(ND_3)_4$ octahedra stacked on top of one another in the c direction of the crystal (AAA stacking). It should be noted that indexing of peaks in TOPAS is biased towards smaller unit cells, as larger unit cells will produce peaks closer together in d spacing, which are therefore more likely to fit a given set of peaks, even if this is not the true unit cell. It should then be considered that multiples of the indexed unit cell are completely plausible crystal structures and can simply

be overlooked/downweighted in TOPAS' indexing program due to its (inherent and justified) bias. The same base octahedra were used to produce AB and ABC stacked cells, with the corresponding expansion of the c lattice parameter.

Figures 4.32 and 4.33 show fits of the PND data to the AA stacked cell and the AB stacked cell respectively. While an ABC stacking structure was refined also, no suitable fit could be found to the data with this stacking arrangement. Each of the structures output from structural refinement are shown in Figures 4.34 and 4.35.

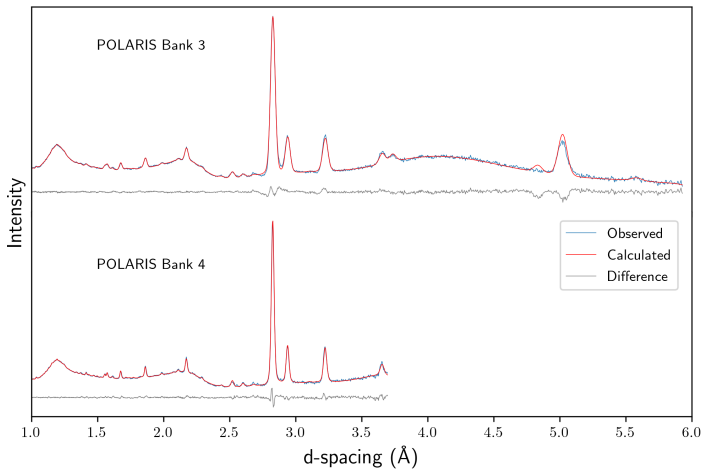


Figure 4.32: PND Data recorded for $CaCl_2(ND_3)_4$ on the POLARIS diffractometer, with fitting to the AA stacked cell shown in Figure 4.34. $\chi^2 = 1.52$.

The primary issue with the AA stacked fit is the calculated peak at 4.84 Å (the (200) reflection), which is clearly absent from the observed data. This could indicate the structure adopted is actually that of an orthorhombic cell with lattice parameters very close to, but slightly different from the aforementioned orthorhombic (a$\sqrt{3}$, a, c) cell, along with a space group which would cause a systematic absence in this position. However, if this were the case, subtle peak splitting is likely to appear. Bank 5 of POLARIS gives the highest resolution but still no peak splitting was evident. The origin of this discrepancy between calculated and observed data remains unclear.

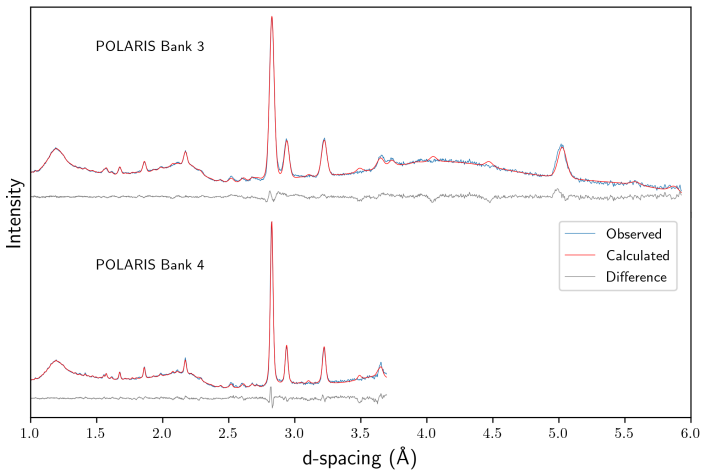


Figure 4.33: PND Data recorded for $CaCl_2(ND_3)_4$ on the POLARIS diffractometer, with fitting to the AB stacked cell shown in Figure 4.35. $\chi^2 = 1.76$.

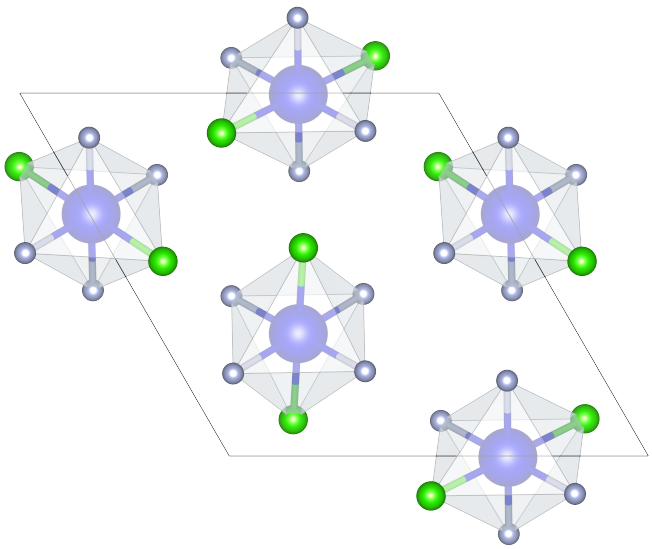


Figure 4.34: Crystal structure of AA stacked $CaCl_2(ND_3)_4$, viewed along the c axis. Cl = green, N = grey, Ca = dark blue. Deuterium atoms are omitted for clarity.

Table 4.8: Data output from the refinement of different $CaCl_2(ND_3)_4$ structures to PND data collected on the POLARIS diffractometer. The high uncertainty on the Ca-Cl bond length in the AA stacked structure is almost entirely due to high uncertainty in the c fractional coordinate of the Cl atoms.

Parameter	Value (AA Stacked)	Value (AB Stacked)
χ^2	1.52	1.76
R_{wp}	1.29	1.40
R_{exp}	0.85	0.79
a-lattice parameter (Å)	11.1732(3)	11.1740(3)
c-lattice parameter (Å)	5.8813(3)	11.7631(7)
N-D bond length (Å)	0.98(2)	0.99(1)
D-N-D bond angle (°)	105(1)	105(1)
Ca-N bond length (Å)	2.47(3)	2.57(1)
Ca-Cl bond length (Å)	2.73(83)	2.58(2)

Table 4.9: Data from CASTEP geometry optimisations of different $CaCl_2(NH_3)_4$ structures. Note the vastly different lattice parameters obtained for each structure.

	AA Stacked	AB Stacked
a-lattice parameter (Å)	11.54	13.13
c-lattice parameter (Å)	6.10	10.14
Volume (Å^3 per Ca^{2+})	234.6	252.5
Relative CASTEP Energy (kJ / mol Ca)	0	13.91

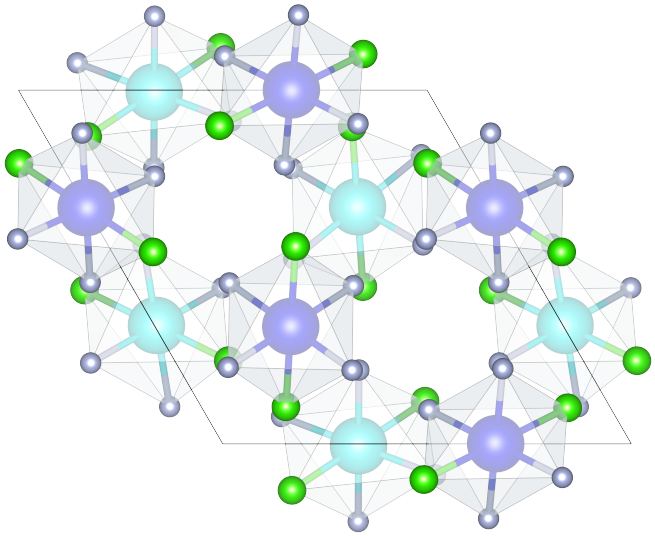


Figure 4.35: Crystal structure of AB stacked $CaCl_2(ND_3)_4$, viewed along the c axis. Cl = green, N = grey, Ca top layer = dark blue, Ca bottom layer = light blue. Deuterium atoms are omitted for clarity.

Table 4.8 shows some of the data output from refinement against the PND data for each of the structures. It should be noted that the AB stacked structure produces extremely similar Ca-N and Ca-Cl bond lengths. This is at odds with other $CaCl_2(NH_3)_n$ structures refined against PND datasets and CASTEP geometry optimisations, which both consistently give Ca-N bond lengths of around 2.45–2.55 Å and Ca-Cl bond lengths of around 2.7–2.8 Å. This does suggest that AB stacking may not be the motif adopted by $CaCl_2(NH_3)_2$, and the refined structure has contorted itself into an unrealistic position to best fit the data.

Given the structure consists of distinct octahedra, the possibility of disorder across the ammonia and chlorine sites should not be ruled out without further examination. However, this requires the removal of the threefold rotation axis to allow for sub-stoichiometric occupancies which produce fundamentally different structures (simply switching Cl and N positions leads to the same structure in a different basis set). AA and AB stacked cells were built in a P1 space group to allow for this disorder. 500 cells, with randomised starting occupancies, were refined using the

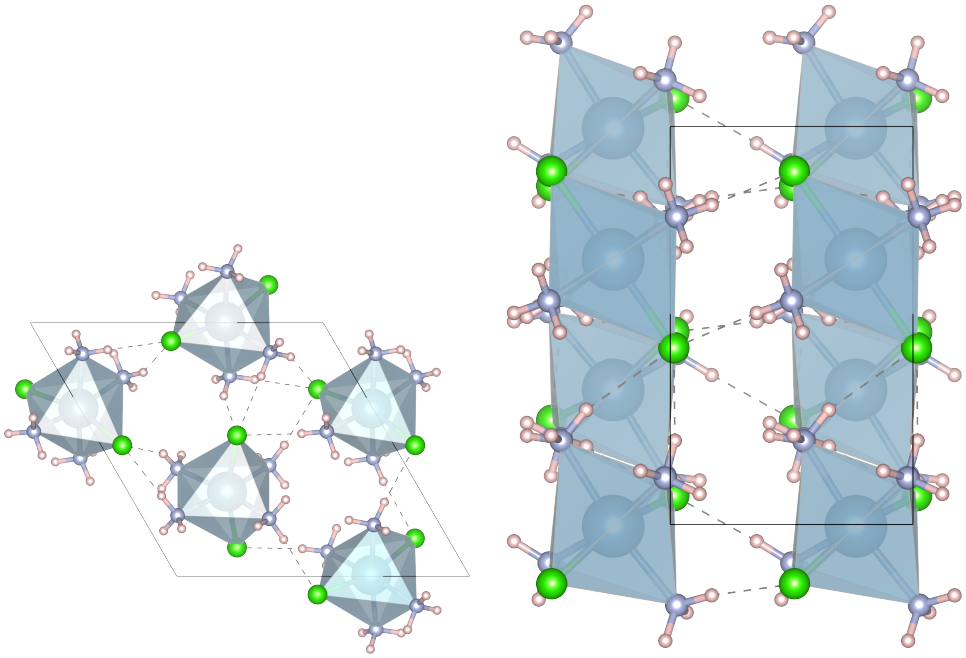
TOPAS batch refinement option. However, none of these cells were able to significantly improve the fit to the PND data. As such, significant disorder is unlikely to be present within the $CaCl_2(ND_3)_4$ structure.

An AA stacked structure does seem unlikely without a clear reason. The arrangement of octahedra can be viewed akin to the stacking of atoms in metals. It should be remembered that octahedra are stacked in $CaCl_2(ND_3)_4$, rather than spheres, but adopting a CCP (ABC stacking) or HCP (AB stacking) arrangement intuitively appears more likely, though evidence to the contrary is strong.

CASTEP geometry optimisations were run on the structures output from TOPAS refinement. Table 4.9 shows the lattice parameters, volumes, and CASTEP calculated energy of these structures after optimisation. It should be noted that the lattice parameters of these phases are extremely different. The AB stacked cell is effectively squashed in the *c* direction, with a corresponding significant expansion in the area of the *ab* plane. This appears to be related to the optimal 'tilt' of the octahedra within each structure. Tilt, as used here, is best defined as the angle between the Ca-Cl vector and the (001) vector (the *c* axis). Within the context of geometry optimisation searching for a local minimum, it is pertinent to point out that the tilt observed for the output AB stacked structure is significantly different to that inputted (the tilt in the input structure is much closer to the tilt observed for the output A stacked structure). Figures 4.36 and 4.37 show the output structures from the CASTEP geometry optimisations. It is clear to see why these structures have arisen as the local minima. The AB stacked structure maximises hydrogen bonding between and within the layers (between octahedra) by the Ca-Cl vector being perpendicular to the *c* axis (full tilt). The AA stacked structure however, due to the alignment of octahedra along the (001) vector, maximises hydrogen bonding between octahedra by reducing the angle between the Ca-Cl vector and the (001)

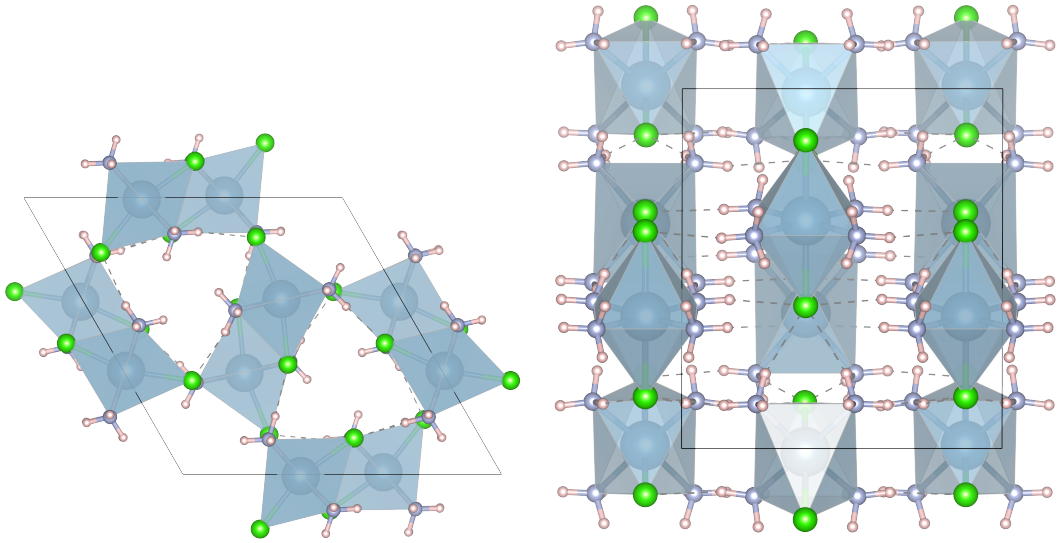
vector. It is clear to see how the hydrogen bonding between the layers of the AA stacked structure would be very weak if these octahedra were fully tilted (90° angle between Ca-Cl vector and (001)).

After appropriate tilting to maximise hydrogen bonding, this has a great effect on the lattice parameters and volume of the structure. With Ca-Cl bonds (which are longer than Ca-N bonds) oriented within the *ab* plane in the AB stacked structure, it is no surprise to see a contraction of the *c* lattice parameter and a corresponding expansion of the *ab* plane. With similar H-Cl distances in both structures, it appears that maximising hydrogen bonding strength in the AB structure leads to inefficient octahedral packing (larger volume) and is likely one of the reasons for the instability of the AB stacking motif.



(a) **(b)**

Figure 4.36: CASTEP geometry optimised AA stacked $CaCl_2(NH_3)_4$ structure viewed along (a) the *c* axis and (b) the *b* axis.



(a) **(b)**

Figure 4.37: CASTEP geometry optimised AB stacked $CaCl_2(NH_3)_4$ structure viewed along (a) the *c* axis and (b) the *b* axis.

It should be noted that the significantly modified lattice parameters of the geometry optimised AB stacked structure do not fit to the diffraction peaks observed in the PND pattern of the tetra-ammoniate, and forcing the AB stacked structure into the lattice parameters observed in the PND pattern will only raise the energy of this stacking motif higher. Considering all the evidence, the tetra-ammoniate is most likely to adopt the AA stacking motif.

For all four ND_3 moieties placed in the unit cell of AA-stacked $CaCl_2(ND_3)_4$, deuterium occupancy was spread between all twelve positions (occupancies all refined to values between 0.1 and 0.5). While data quality is limited, and accurate conclusions are difficult, this suggests free ammonia rotation is possible at the temperature studied (∼40 °C).

4.1.6 $CaBr_2$ Hexa-ammoniate

The crystal structure of the hexa-ammoniate phase of CaI_2 was first reported by Woidy *et al.*[122] after synthesis of the octa-ammoniate at −40 °C in liquid ammonia and subsequent decomposition upon warming to room temperature. PXRD analysis showed the hexa-ammoniate crystallises in the $Fm\bar{3}m$ space group and adopts the fluorite structure. It is also isostructural to all other known 2+ metal halide hexa-ammoniates ($MgX_2(NH_3)_6$, $MnX_2(NH_3)_6$ etc.). Figure 4.38 shows the crystal structure reported by Woidy *et al.*

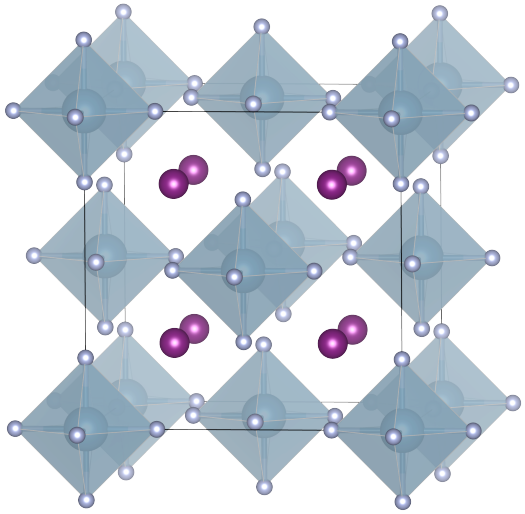


Figure 4.38: Crystal structure of $CaI_2(NH_3)_6$ ($Fm\bar{3}m$) as reported by Woidy *et al*[122]. Hydrogens are omitted due to uncertainty in their positions in PXRD experiments. Ca = blue, N = grey, I = purple.

Figure 4.39 shows the PND pattern of $CaBr_2(NH_3)_6$, fitted to the same $Fm\bar{3}m$ structure.

In order to understand the structure and bonding within the hexa-ammoniate phase better, a detailed study into its hydrogen bonding network was performed using CASTEP calculations. To achieve this, various methods of understanding the $CaX_2(NH_3)_6$ structure must be used. If the base structure is considered as $Ca(NH_3)_6{}^{2+}$ cations and X^- anions, then the structure is simply fluorite. Under

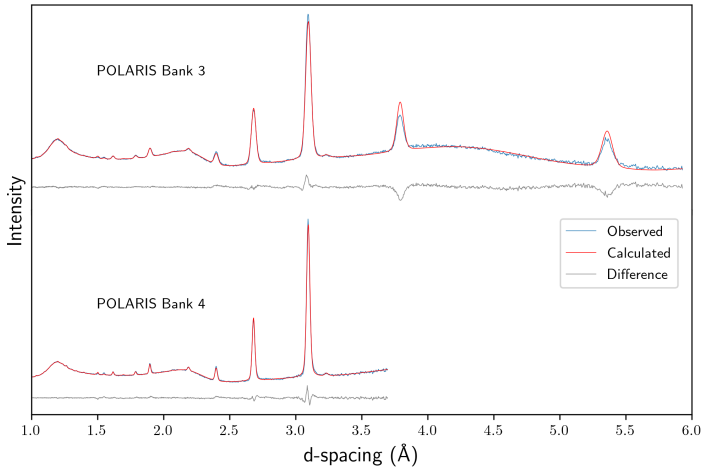


Figure 4.39: PND pattern of $CaBr_2(ND_3)_6$ recorded on the POLARIS diffractometer at ISIS Neutron and Muon Source. Data are fitted to the $Fm\bar{3}m$ structure shown in Figure 4.38. $\chi^2 = 1.83$.

Table 4.10: Data output from PND refinement of $CaBr_2(ND_3)_6$ in the $Fm\bar{3}m$ structure.

Parameter	Value
χ^2	1.83
R_{wp}	1.44
R_{exp}	0.79
a-lattice parameter (Å)	10.7303(2)
N-D bond length (Å)	0.980(5)
D-N-D bond angle (°)	105.0(5)
Ca-N bond length (Å)	2.429(8)
Space Group	$Fm\bar{3}m$
Br-fractional coordinates	(0.25, 0.25, 0.25)
Ca-fractional coordinates	(0, 0, 0)
N-fractional coordinates	(0.2263(7), 0, 0)

this approach, the X^- anions are in tetrahedral holes, with a coordination number of 4, while the $Ca(NH_3)_6{}^{2+}$ cations have a coordination number of 8, in a cubic arrangement. This corresponds to 12 ammonia molecules around each X^- anion and consists of 3 vertical layers of 4 nitrogen atoms. It is perhaps best described as a quadcapped cube. When centring the ammonia molecule, each Ca-N bond points towards the centre of a square of X^- anions (this square is one of the 6 faces of the cubic arrangement of X^- around $Ca(NH_3)_6{}^{2+}$). This means each ammonia molecule can strongly hydrogen bond to two X^- anions, in a situation somewhat similar to the 'anion rectangles' seen for the di-ammoniate phases. As such, it is presumed that the lowest energy hydrogen bonding motif is one in which each X^- anion forms 6 hydrogen bonds (such that the total hydrogen bonding is equally distributed).

Figure 4.40 shows data on the hydrogen bonding network within one example structure of $CaX_2(NH_3)_6$, after geometry optimisation of all atoms. It is clear to identify the strong mono-furcated hydrogen bonds (blue rectangle) and the weak bifurcated hydrogen bonds (red rectangle). This is a product of the 'anion square' described previously. Comparing H-X distances with the di-ammoniate structures, it is clear that hydrogen bonding is significantly more 'divided', with much shorter H-X distances for strong mono-furcated hydrogen bonding in the hexa-ammoniate, and much greater H-X distances for bifurcated hydrogen bonding.

To investigate the correlation between energy and hydrogen-bonding motifs, the structure was represented as a cube of X^- anions around the $Ca(NH_3)_6{}^{2+}$ cation. The six NH_3 molecules emanating from the centre of the cube, can then 'pick' two of the adjacent X^- anions at the corners of their face of the cube to bond to. The benefit of this approach is that when this 'ammonia cube' is repeated at each Ca^{2+} ion, it mandates each X^- anion to have 6 hydrogen bonds attached, due to the tetrahedral arrangement of 'ammonia cubes' around the X^- anions. As each ammonia molecule facing a square can adopt 4 different orientations, there are, at most, 4^6 possible 'ammonia cubes'. Applying the point group O_h (the point group

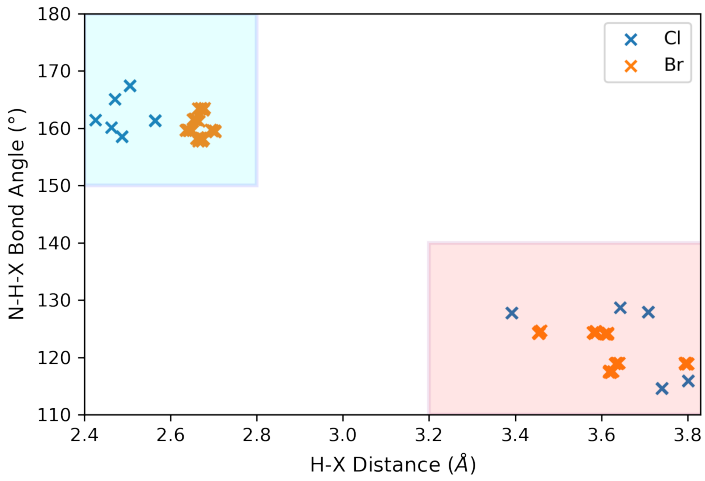


Figure 4.40: Data on hydrogen bonds formed in a geometry optimised structure of $CaX_2(NH_3)_6$. Data points in the blue rectangle are monofurcated hydrogen bonding, while those in the red rectangle are weaker, bifurcated hydrogen bonding.

of a cube) allows for the identification of identical cubes in a different orientation. In total, there are 102 distinct 'ammonia cubes'. An extension to this would involve examination of more than one cube. However, this problem becomes complicated very quickly as the number of free ammonia molecules are increased (it also allows for X^- anions to have different numbers of hydrogen bonds). Using two cubes gives 4^{12} possible arrangements, and a lower bound of $\frac{4^{12}}{8}$ (over 2 million) distinct cubes after consideration of the 8 symmetry elements in D_{2h} symmetry (the point group of two edge-sharing cubes).

Figure 4.41 shows the localised hydrogen bonding in an exemplar 'ammonia cube'. After construction of these 102 unit cells, single point energy calculations were performed, alongside separate geometry optimisations of the X^- positions in CASTEP. This was done to inform about the energetic effects of X^- ions moving off their 'ideal' site, which should be heavily influenced by the nature of the hydrogen bonding motif. Figure 4.42 shows the energies resulting from each of these motifs, before and after optimisation of the X^- position within the cell.

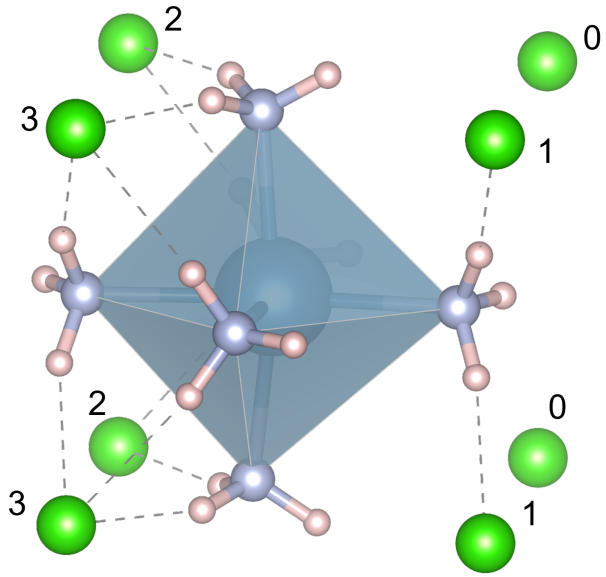
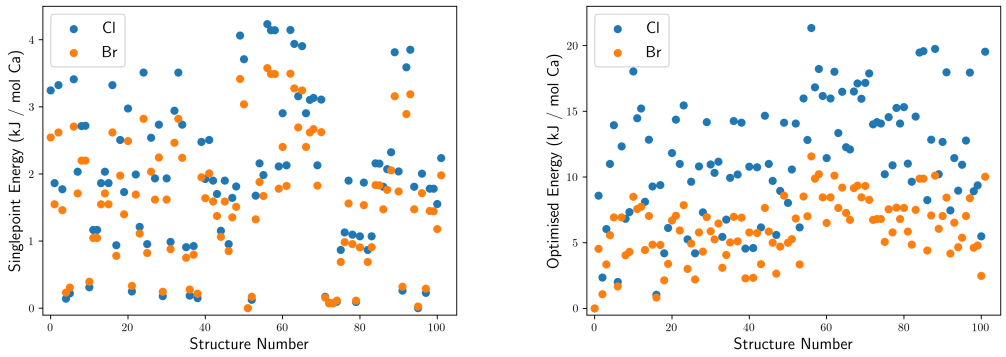


Figure 4.41: The 'ammonia cube' in the $CaX_2(NH_3)_6$ structure. The numbers depict the number of hydrogen bonds between the $Ca(NH_3)_6{}^{2+}$ octahedron and the X^- anion. Note how the ammonia molecules point towards the faces of the cube of X^- ions. Rotation of an NH_3 molecule affects the number of hydrogen bonds formed to each vertex (halide) of the cube. Ca = blue, Cl = green, N = grey, H = pink.



(a) **(b)**

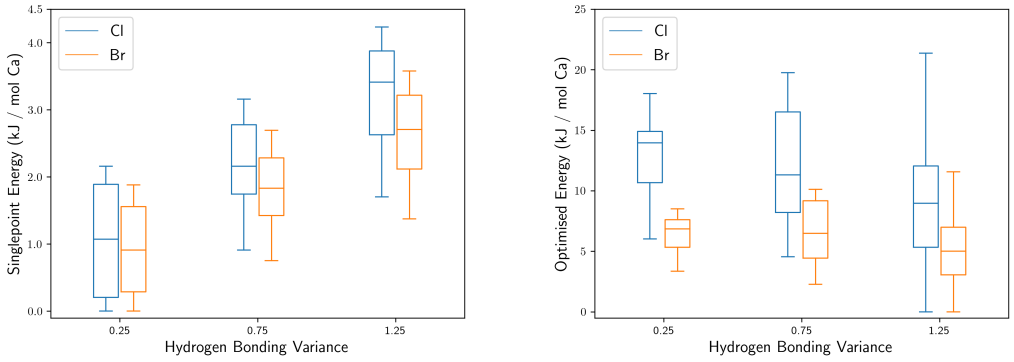
Figure 4.42: The energies of different hydrogen-bonding motifs in $CaX_2(NH_3)_6$. (a) shows the energies calculated for starting cells with X^- ions on the 'ideal' site (0.25, 0.25, 0.25), while (b) shows the energies when the X^- ions (and only the X^- ions) are allowed to optimise their position within CASTEP. 'Structure number' is simply an identifier and should have no direct bearing on the energy.

Unsurprisingly, bromide-containing cells show generally lower relative energies, as bromide forms weaker hydrogen bonds than chloride, so the effects are likely to be the same, only less exaggerated. It is clear that allowing movement of the X^- ion off the site greatly increases the energy differences, presumably as some cells are stabilised more than others by this movement. Applying 4096 possible combinations to Boltzmann's Equation (Equation 4.6) gives an entropy value of 69.16 J mol^{-1} K^{-1}. At 298 K, this equates to an energy of 20.61 kJ / mol, suggesting that these states are likely to all be occupied at room temperature for bromide. Only one optimised state is above this energy value for chloride, suggesting that the rest are likely to be occupied, but this high energy state may not be. However, it should be noted that free, rapid exchange between these states may not actually be feasible at 298 K, as there may be a significant activation energy barrier between them.

$$S = k_B \ln \omega \tag{4.6}$$

If cells are classified into groups based on the number of hydrogen bonds to each X^- ion (i.e. '0123' refers to zero hydrogen bonds between Ca1 and X1, two hydrogen bonds between Ca1 and X3 etc.), then there is a clear correlation between energy and the variance of the number of hydrogen bonds. Figure 4.43a shows the energy of cells plotted against the variance in hydrogen bonding number for single-point energy calculations and X^- optimised cells. When X^- occupies the ideal site, a higher hydrogen bonding variance leads to a higher energy. In simple terms, this means that 'spreading out' the hydrogen bonding across different directions leads to a lower energy, perhaps in part due to the minimisation of repulsions between hydrogen atoms, but also as this allows the full complement of valence electrons in X^- ions to participate in hydrogen bonding. However, when X^- ions are allowed to move off their 'ideal site', this correlation is reversed (Figure 4.43b). There is clearly a stabilisation effect associated with X^- ions moving towards the area with

strongest hydrogen bonding, leading to 'spread out' hydrogen bonded cells being unfavourable, and highly directional hydrogen bonding being lower energy in 'real cells'.



(a) **(b)**

Figure 4.43: The energy of $CaX_2(NH_3)_6$ cells compared with the 'hydrogen bond variance', presented as box and whisker plots. Cells are classified according to the number of hydrogen bonds between each $Ca(NH_3)_6{}^{2+}$ octahedron and the X atoms around it, and the variance is calculated (with a mean hydrogen bonding number of 1.5 hydrogen bonds per X atom). Adjacent box plots are centred at the same position, but are offset to clearly present the data. (a) shows this relationship for X atoms confined to the high symmetry site, while (b) shows this relationship when the positions of X atoms are optimised.

Figure 4.44 shows the Ca-X distance plotted against the number of hydrogen bonds formed between the Ca^{2+} and X^- ions. While confounding variables such as the exact arrangement of hydrogen bonds interfere slightly, it is clear that there is an attraction between X^- ions and the $Ca(NH_3)_6{}^{2+}$ octahedra with which they form the greatest number of hydrogen bonds.

Figure 4.45 shows the energy of optimised cells plotted against the distance of X^- ions from their 'ideal site'. This serves to confirm the hypothesis that movement off the site due to highly directional hydrogen bonding has a significant effect on the energy. Fits to an $a + be^{(-\frac{x^2}{2\sigma^2})}$ are shown.

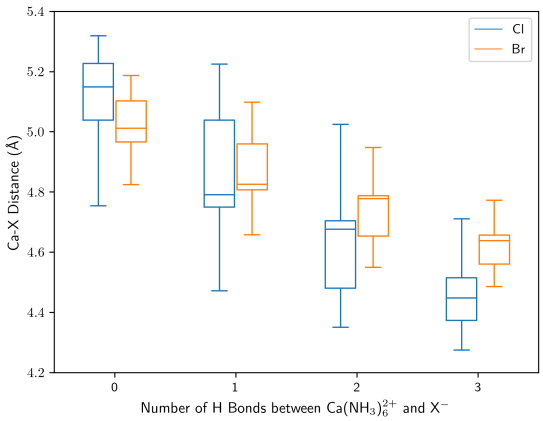


Figure 4.44: Ca-X distances plotted against the number of hydrogen bonds formed between $Ca(NH_3)_6{}^{2+}$ octahedra and X atoms. Data are presented as box and whisker plots. Adjacent box plots are centred at the same position, but are offset in order to clearly present the data.

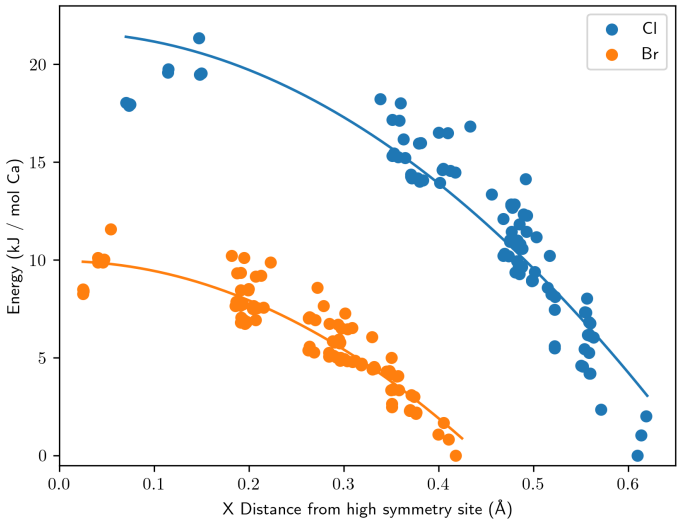


Figure 4.45: The energy of cells plotted against the distance of the X atom from its high symmetry site. The data are fitted to an $a + be^{(-\frac{x^2}{2\sigma^2})}$ function.

These CASTEP calculations paint a picture of $CaX_2(NH_3)_6$ structures with significant movement of X atoms away from their high symmetry position, towards areas of strong hydrogen bonding. If at a sufficiently high temperature to rotate freely, then it is likely that X atoms would show significant motion, effectively 'rattling' around as the directionality of hydrogen bonds continually changes. Strong hydrogen-bonding motifs appear to be largely based around the directionality of hydrogen bonding, which facilitates this off-site movement from X atoms. One of the recurrent results of hydrogen bonding analyses using CASTEP calculations, in both the hexa-ammoniate and di-ammoniate phases, is the importance of a favourable hydrogen bonding network. Hydrogen bonding clearly makes a sizeable contribution to the energy of the system, particularly for cells containing chloride ions.

4.1.7 $CaCl_2$ and $CaBr_2$ Octa-ammoniates

Westman *et al.*[95] first reported the crystal structure of $CaCl_2(NH_3)_8$ using X-ray powder diffraction, due to difficulty obtaining crystals large enough for single crystal X-ray diffraction. Their structure, crystallising in the *Pnma* space group, consisted of $Ca(NH_3)_6{}^{2+}$ trigonal prisms with two occluded NH_3 molecules (i.e. not bonded to a metal ion as one might expect), though the authors mentioned their uncertainty about the position of light atoms such as nitrogen due to the quality of the data used. In 2014, Woidy *et al.*[122] studied $CaBr_2(NH_3)_8$ and $CaI_2(NH_3)_8$ by single crystal X-ray diffraction, enabling the accurate location of nitrogen atoms. Their structures, which gave very similar lattice parameters and the same space group as Westman's structure, consisted of a bicapped trigonal prismatic arrangement of $Ca(NH_3)_8{}^{2+}$, with bromide/iodide ions between the polyhedra. This is in contrast to Westman's structure, which was best described as $Ca(NH_3)_6Cl_2{\cdot}2\,NH_3$. It should be noted that Westman was studying the calcium chloride octa-ammoniate, while

Woidy studied the calcium bromide/iodide octa-ammoniate. However, because of the uncertainty associated with Westman's data, it is likely that Woidy's structure applies to calcium chloride also.

Due to the instability of the octa-ammoniate at room temperature without ammonia pressure, *ex-situ* studies are difficult to perform. *In-situ* PND data (Figures 4.47 and 4.48) collected on the POLARIS diffractometer have confirmed Woidy's structure for $CaCl_2$ and $CaBr_2$. This structure is shown in Figure 4.46.

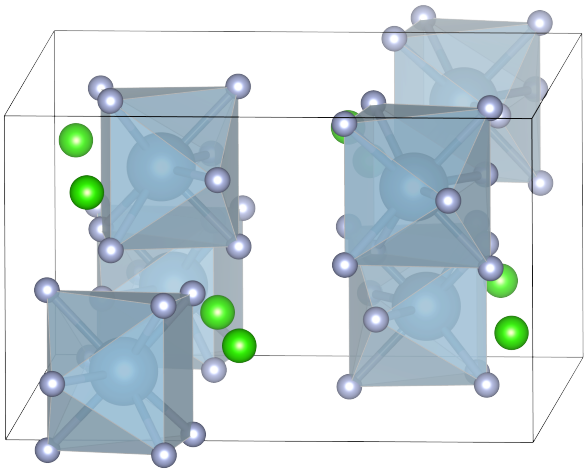


Figure 4.46: The crystal structure of $CaX_2(NH_3)_8$, as reported by Woidy *et al*[122]. and confirmed in this work by PND (Figures 4.47 and 4.48). Ca = blue, N = grey, Cl = green. Hydrogen atoms are omitted for clarity.

PND data is shown in Figures 4.47 and 4.48. It should be noted that data collected for chloride is a mixture of the tetra- and octa-ammoniates. This is due to the slow absorption of ammonia by $CaCl_2$ at atmospheric pressure and time constraints on the POLARIS diffractometer.

It is unusual to observe calcium ions with a coordination number of 8, given its small ionic radius compared with the size of an NH_3 molecule. However, a key feature of the octa-ammoniate structure, and a large reason for its stability, is the hydrogen bonding network. Rather than each NH_3 pointing towards an anion rectangle or square, as seen in di-ammoniate and hexa-ammoniate structures, each

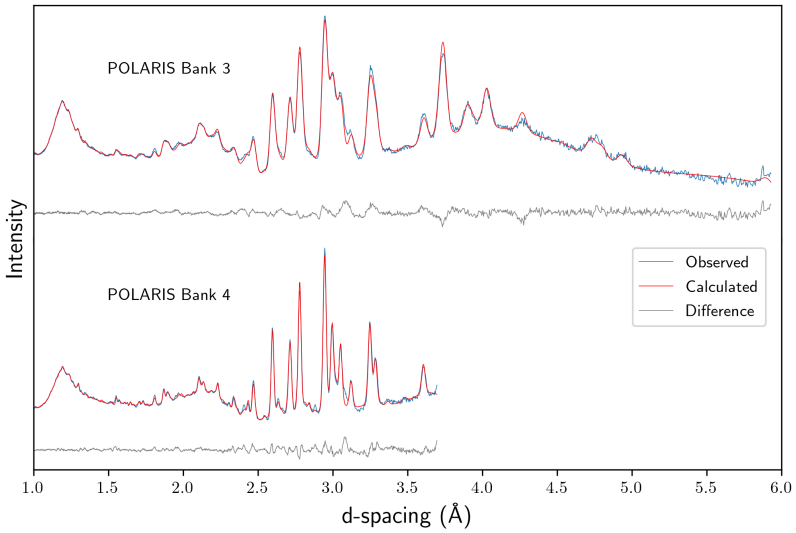


Figure 4.47: PND pattern of $CaBr_2(ND_3)_8$ recorded on the POLARIS diffractometer. The data is fitted to the bicapped trigonal prismatic structure of $CaBr_2(ND_3)_8$ (Figure 4.46). Blue = observed data, red = calculated data. $\chi^2 = 2.31$.

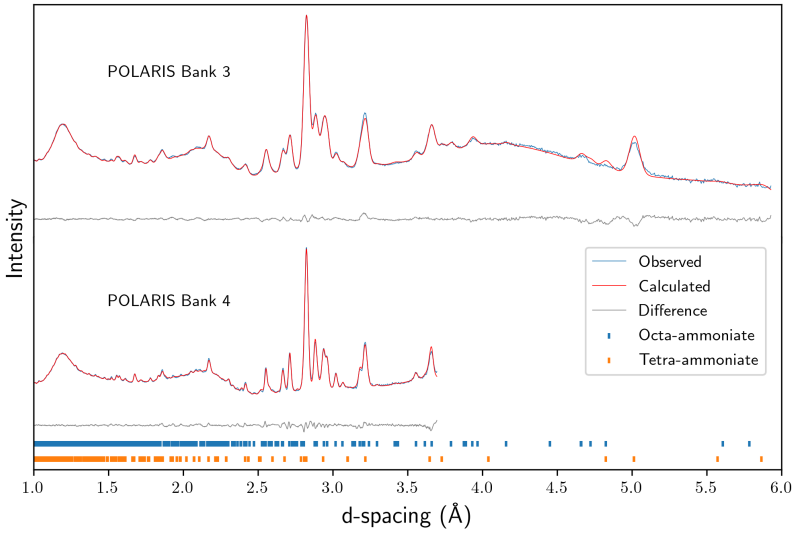


Figure 4.48: PND pattern of a mixture of $CaCl_2(ND_3)_8$ and $CaCl_2(ND_3)_4$ recorded on the POLARIS diffractometer. The data is fitted to the bicapped trigonal prismatic structure of $CaCl_2(ND_3)_8$ (Figure 4.46) and the AA stacked structure of $CaCl_2(ND_3)_4$ (Figure 4.34). TOPAS outputted weight percents of 45.3% octa-ammoniate and 54.7% tetra-ammoniate (mole percents of 36.9 and 63.1% respectively). $\chi^2 = 2.36$.

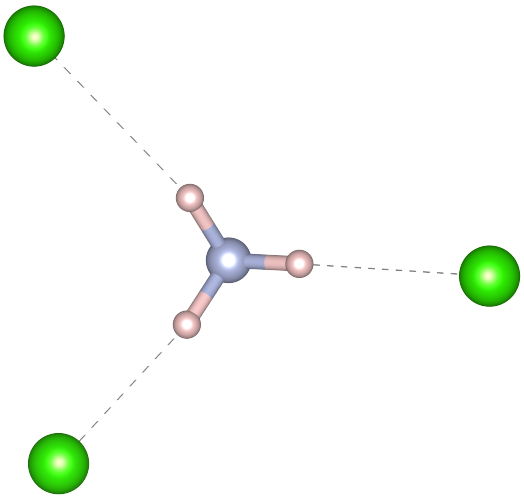


Figure 4.49: The hydrogen bonding between an NH_3 molecule in one of the trigonal prismatic sites and X^- ions in the $CaX_2(NH_3)_8$ structure. The Cl-N-Cl angle matches closely to the H-N-H angle, enabling strong hydrogen bonding within the structure. N = grey, H = pink, Cl = green.

trigonal prismatic NH_3 points towards an anion triangle, similar to that seen in the mono-ammoniate. Analysis of a CASTEP geometry optimised cell shows that Cl-N-Cl angles for trigonal prismatic NH_3 molecules range from 94.6–119.4° (with a mean value of 109.7°), close to the H-N-H bond angle, allowing for strong hydrogen bonding to all nearby X^- ions. Figure 4.49 shows one of these NH_3 molecules and its hydrogen bonding to adjacent X^- ions.

Similar to the tetra-ammoniate, all deuterium positions in the unit cell refined to occupancies greater than zero, suggesting free ammonia rotation is possible at the temperatures studied (25–50 °C). From analysis of PND and CASTEP data, it appears that only the mono-ammoniate is likely to not allow full rotation of ammonia moieties at standard temperatures. This is likely due to the ratio of N-H bonds to halide ions, which impacts hydrogen bond strength (the main interaction preventing free rotation). For n ammonia molecules in the crystal structure, the ratio of N-H

Table 4.11: Data output from PND refinements of $CaX_2(ND_3)_8$ in the *Pnma* structure.

Parameter	Value (Cl)	Value (Br)
χ^2	2.36	2.31
R_{wp}	0.86	1.35
R_{exp}	0.36	0.58
a-lattice parameter (Å)	12.1013(9)	12.2369(7)
b-lattice parameter (Å)	7.3354(5)	7.4901(4)
c-lattice parameter (Å)	15.1936(9)	15.6312(7)
N-D bond length (Å)	1.000(9)	1.005(6)
D-N-D bond angle (°)	105.0(7)	107.4(5)
Space Group	*Pnma*	*Pnma*
X1-coordinates	(0.365(2), 0.25, 0.443(2))	(0.365(2), 0.25, 0.450(1))
X2-coordinates	(0.922(2), 0.25, 0.685(2))	(0.924(2), 0.25, 0.652(2))
Ca-coordinates	(0.776(3), 0.25, 0.329(3))	(0.761(2), 0.25, 0.378(2))
N1-coordinates	(0.5906(9), 0.008(2), 0.3675(8))	(0.5956(7), 0.003(1), 0.3765(5))
N2-coordinates	(0.8071(9), 0.028(2), 0.2513(7))	(0.8143(6), 0.022(1), 0.2593(4))
N3-coordinates	(0.869(1), 0.023(2), 0.4566(8))	(0.8567(7), 0.021(1), 0.4552(5))
N4-coordinates	(0.649(1), 0.25, 0.525(1))	(0.658(1), 0.25, 0.5242(8))
N5-coordinates	(0.610(2), 0.25, 0.190(1))	(0.612(1), 0.25, 0.1993(7))

bonds to halide ions is $3n : 2$. As n increases, the hydrogen bond strength will weaken greatly as the halide interacts in multiple directions, allowing free rotation of ammonia molecules.

4.2 Ammonia Absorption Pathways and Energetics

STA was used to study the absorption-desorption cycles of $CaCl_2$ and $CaBr_2$. Figures 4.50–4.53 show the results from the temperature cycling of these samples under flowing NH_3-Ar mixtures.

As expected, the desorption events from each sample shift to lower temperature as pressure is reduced. The $CaCl_2$ 5:1 $NH_3 : Ar$ cycle shows four distinct desorption events, corresponding to the transitions expected ($8 \rightarrow 4 \rightarrow 2 \rightarrow 1 \rightarrow 0$), despite full absorption to 8 moles of NH_3 not occurring. The slow absorption of NH_3 by $CaCl_2$ samples was seen continuously throughout this work, and is repeated here, alongside being heavily dependent on ammonia partial pressure. As seen continuously also, it appears as though ammoniated phases tend to show faster absorption than pure $CaCl_2$. This is evidenced by the observation of significant octa-ammoniate desorption peaks from a sample that, on average, has only absorbed $\sim$3 moles of ammonia per Ca ion (the 4:2 $NH_3 : Ar$ cycle). If the opposite were true, a sample which has absorbed $\sim$3 moles of ammonia per Ca ion would primarily consist of a 1:1 mixture of tetra-ammoniate and di-ammoniate. However, this is clearly not the case.

A surprising observation is the double desorption peak seen at the beginning of the temperature ramp in the 4:2 $NH_3 : Ar$ cycle. The exact origin of this is unclear, though it could signify desorption from a hexa-ammoniate phase. It is unclear whether this possible hexa-ammoniate phase is seen as an intermediate during absorption or desorption or both. It could be an intermediate phase formed upon desorption, reducing the kinetic barriers in the $8 \rightarrow 4$ desorption, though as this has not been seen elsewhere it seems unlikely. Similarly, it could also be an intermediate metastable phase formed during absorption, again due to a reduced kinetic barrier through this pathway. A change of 4 moles of NH_3 in one step would likely induce a significant kinetic barrier (either energetically or due to the unlikelihood

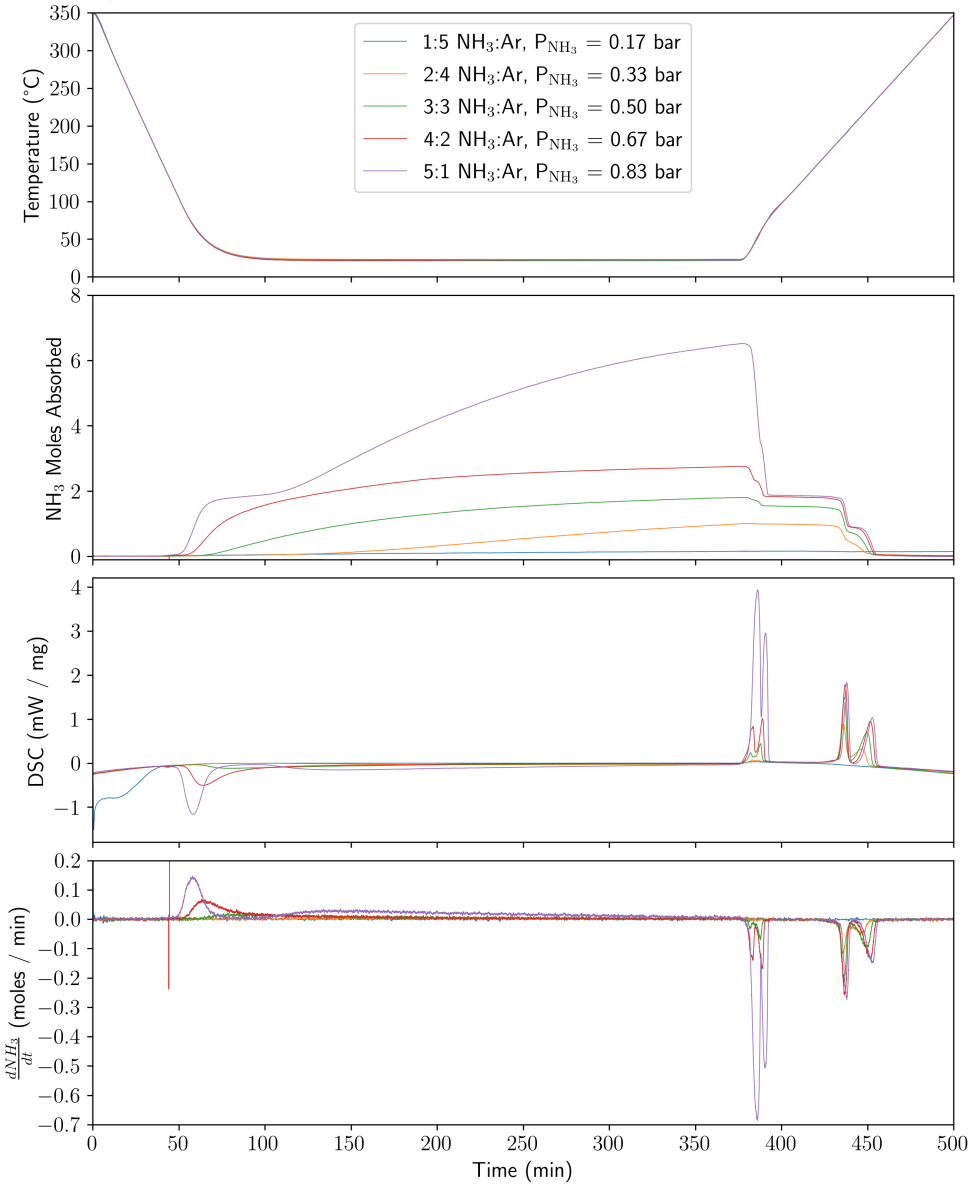


Figure 4.50: STA of $CaCl_2$ ammonia cycling under 60 sccm flowing gas. Pressure remained at atmospheric pressure i.e. 1:5 NH_3 : Ar corresponds to an ammonia partial pressure of 0.17 bar.

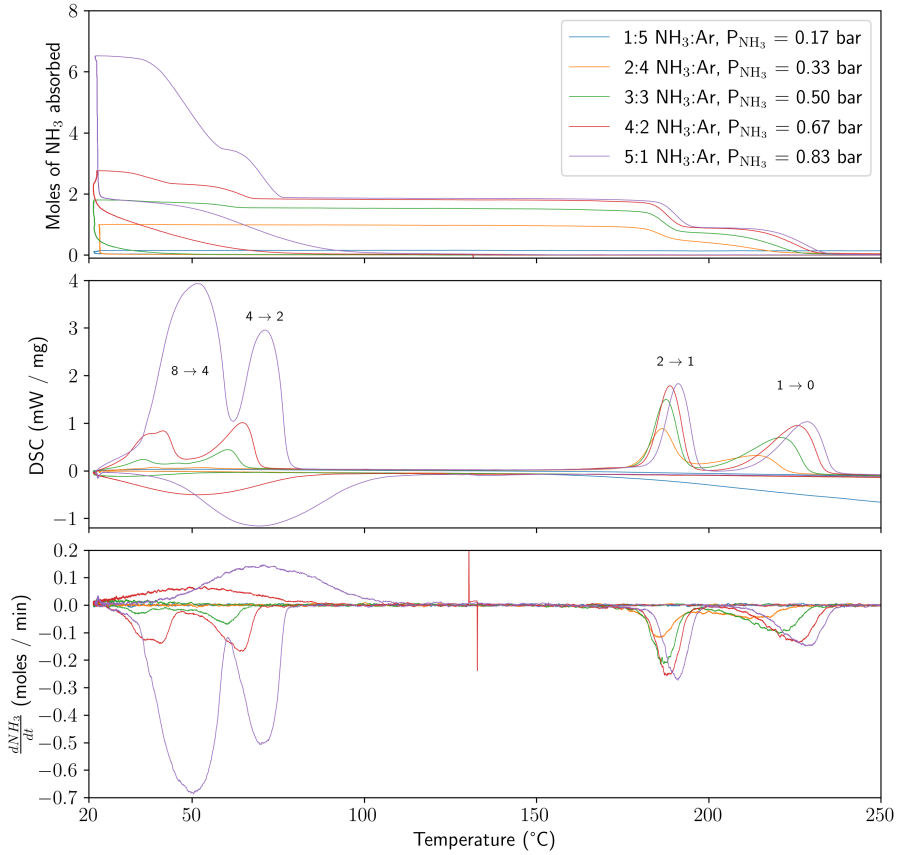


Figure 4.51: STA of $CaCl_2$ ammonia cycling under 60 sccm flowing gas. The expected desorption steps ($8 \rightarrow 4 \rightarrow 2 \rightarrow 1 \rightarrow 0$) are clear in the highest NH_3 pressure cycle. This data is the same as presented in Figure 4.50 with temperature on the horizontal axis to allow clear comparison of desorption steps.

of favourable collisions of such a large number of moieties). It is feasible that this ($4 \rightarrow 8$) absorption step happens in a two-step process; an initial slow step to form the hexa-ammoniate, followed by a rapid second step which is often not able to be separated, particularly in experiments searching for fully stable phases only (i.e. under thermodynamic control rather than kinetic control). The use of low ammonia pressure may be required in order to slow the second absorption step, allowing for observation of this metastable hexa-ammoniate. It is difficult to comment conclusively on whether it appears in cycles of even lower ammonia pressure given the limited absorption of NH_3.

The $CaBr_2$ sample (Figures 4.52 and 4.53) shows the expected desorption steps of $6 \rightarrow 2 \rightarrow 1 \rightarrow 0$ and none of the subtleties observed in the $CaCl_2$ sample. Much faster absorption is seen, with even the 1:5 NH_3 : Ar cycle showing over 4 moles of NH_3 per Ca ion. The 1:5 NH_3 : Ar cycle for $CaCl_2$ showed no discernible absorption, and 4 moles of NH_3 was only achieved for the 5:1 NH_3 : Ar cycle. This exemplifies the sizeable difference in absorption rates of the two materials. The octa-ammoniate is not observed as pressure slightly elevated above atmospheric is required for this phase to form at room temperature for $CaBr_2$.

In order to understand the energetics of ammonia absorption and desorption in these cycling experiments, variable NH_3 pressure experiments were performed using the high pressure gas rig described in Section 3.2.1. After loading of the powder, the system pressure was raised to 4.5 bar, and the inflow rates of ammonia and argon were set in order to adjust the partial pressure of ammonia in the system. One absorption-desorption cycle was performed at each pressure step, with the gas outflow monitored to detect absorption or release from the sample. Figure 4.54 shows the 4.5 bar cycle of this experiment for $CaBr_2$. Each increase in gas flow corresponds to a desorption event. From 780 minutes to 800 minutes corresponds to desorption from the mono-ammoniate, while 760 minutes to 775 minutes signifies

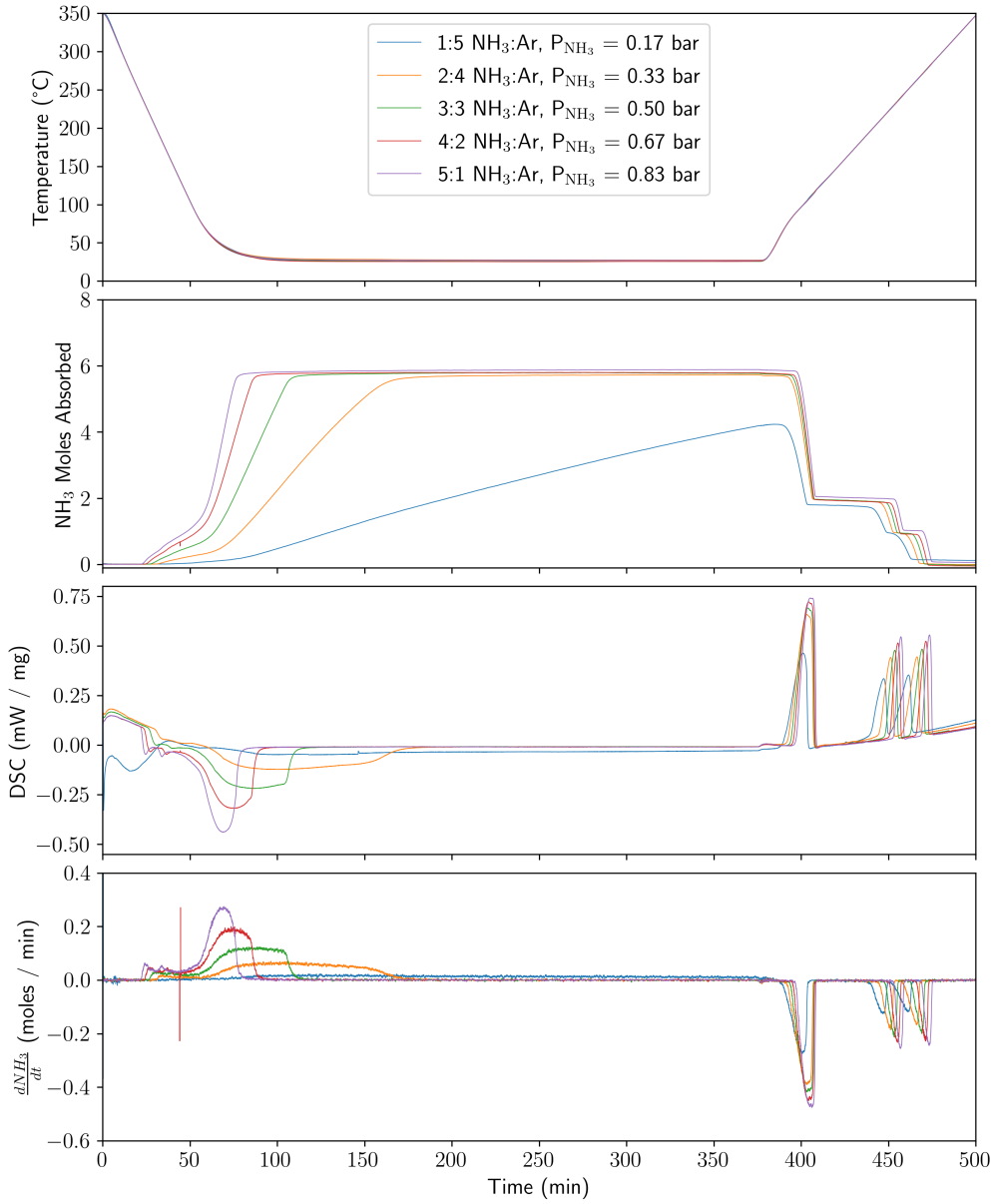


Figure 4.52: STA of $CaBr_2$ ammonia cycling under 60 sccm flowing gas. Pressure remained at atmospheric pressure i.e. 1:5 NH_3 : Ar corresponds to an ammonia partial pressure of 0.17 bar.

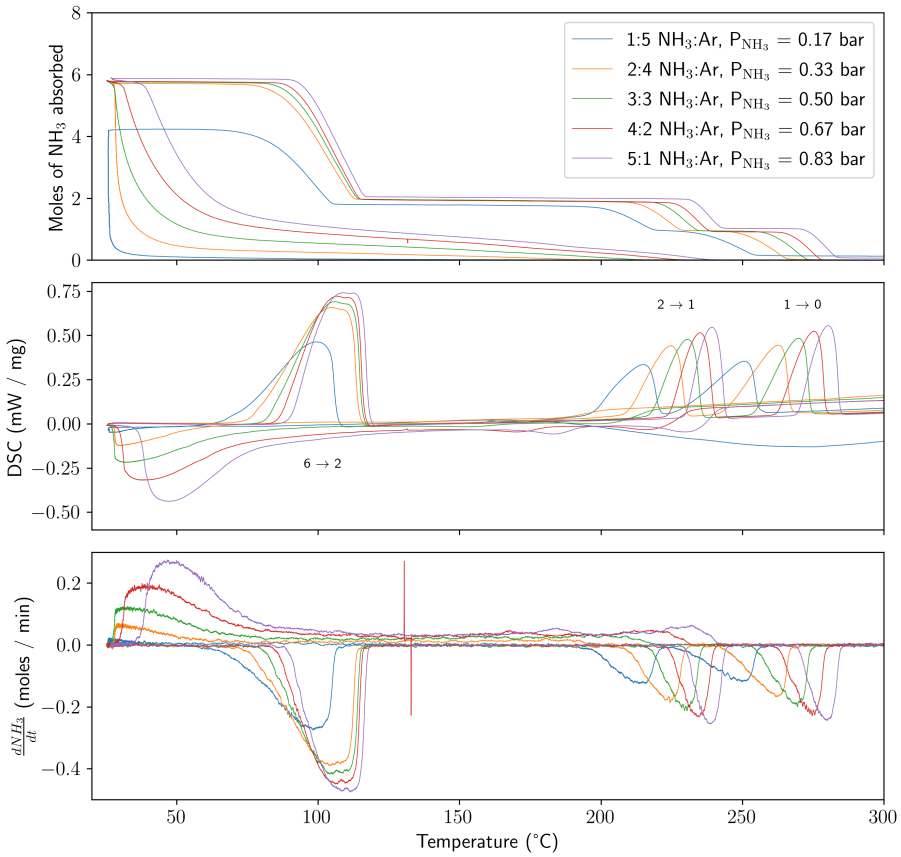


Figure 4.53: STA of $CaBr_2$ ammonia cycling under 60 sccm flowing gas. The expected desorption steps ($6 \rightarrow 2 \rightarrow 1 \rightarrow 0$) are clear in all cycles. This data is the same as presented in Figure 4.52 with temperature on the horizontal axis to allow clear comparison of desorption steps.

di-ammoniate desorption. The previous two steps, 685 to 705 minutes and 650 to 665 minutes, correspond to the $6 \rightarrow 2$ and $8 \rightarrow 6$ transitions respectively. There does appear to be an extra desorption event, rapidly occurring from 635 to 645 minutes.

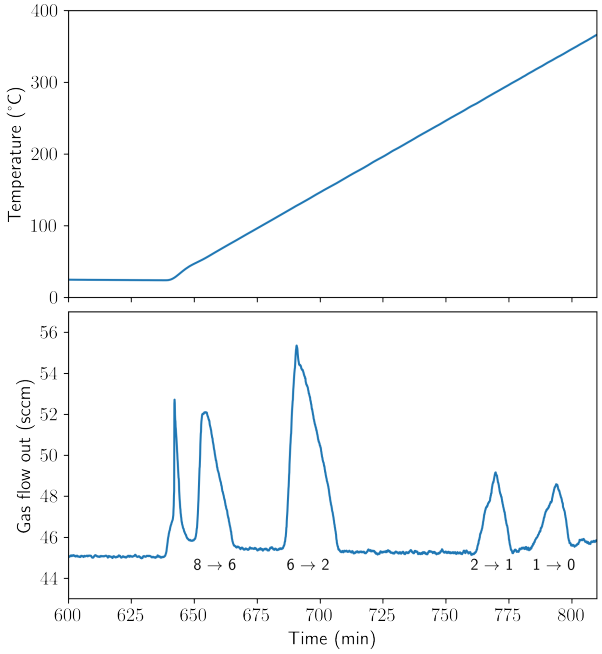


Figure 4.54: 4.5 bar NH_3 desorption cycle from $CaBr_2$. Phase transitions are seen as peaks in the gas flow. The expected transitions of $8 \rightarrow 6$, $6 \rightarrow 2$, $2 \rightarrow 1$ and $1 \rightarrow 0$ are seen. However, an initial extra transition is seen immediately after heating. This is understood to be desorption from a deliquesced phase of $CaBr_2(NH_3)_n$.

Integration of the desorption events shown in Figure 4.55 indicated that the unknown desorption event corresponded to release of 0.59 mol of NH_3. Given that this is not close to an integer value, it is unlikely that this desorption is from one solid phase to another. The most probable rationale is deliquescence of $CaBr_2$ (absorption to form a solution).

It has long been known of the effect that dissolved salts can have on the vapour pressure of water. The same is anticipated to hold for ammonia. At 25 °C, the vapour pressure of NH_3 is ~10 bar. With a dissolved salt, this would be lowered significantly.

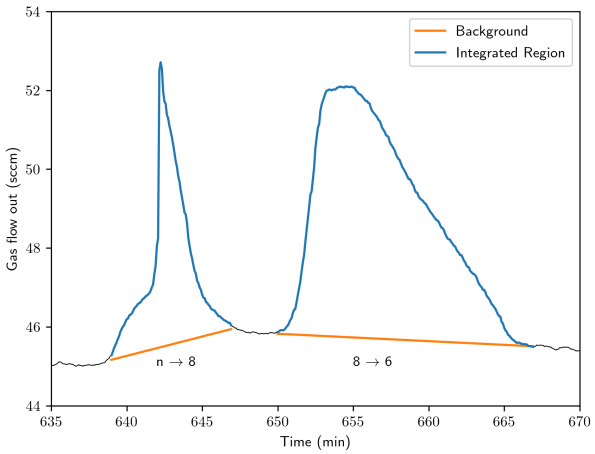


Figure 4.55: Integration of the extra peak in the 4.5 bar NH_3 desorption cycle of $CaBr_2$. The peak at 640–645 minutes corresponds to evaporation of ammonia from a $CaBr_2$-NH_3 solution, while the peak from 650–665 minutes corresponds to desorption from the octa-ammoniate phase. The area of the second desorption peak is 3.37× that of the first peak, suggesting the first peak corresponds to desorption from $n = 8.59$ to $n = 8$.

The additional transition was not observed for $CaCl_2$ at 4.5 bar. However, this is not surprising. The enthalpy of solution in water for calcium chloride is significantly less negative than that for calcium bromide, due to the stronger ionic bonding being disrupted in calcium chloride. This is akin to Jones *et al.*'s explanation for the trends seen in MgX_2 ammoniates[92], but here it is applied to liquids rather than solids. This trend in aqueous solution enthalpies would be expected to hold for dissolution into liquid ammonia also.

While not investigated further in this work, dissolved salts could be an alternative to cooling for vapour pressure reduction of liquid NH_3 (a key aspect to ensuring the safety of ammonia tanks). Fundamentally, this is similar to the use of solid MX_2 for vapour pressure reduction. However, the handling properties of liquids in industrial uses can be preferable as, for example, liquids allow pumping. One issue with coordinating salts (i.e. salts that form solid ammoniates) such as $CaBr_2$ is that large

quantities of ammonia become absorbed in the solid complex and require heating to be removed. If a non-coordinating salt is used, the benefits of liquid handling can be gained and all ammonia can be removed as gaseous without active heating.

$$\ln \frac{P}{P_0} = \frac{\Delta S}{R} - \frac{\Delta H}{RT} \tag{4.7}$$

By examination of the onset temperatures for ammonia desorption from each phase, fitting to the integrated form of the Clausius-Clapeyron equation (Equation 4.7) allowed for calculation of enthalpy and entropy change values, and the equivalent phase diagram, for different equilibria. The results from this analysis are shown in Table 4.12 and Figures 4.56 and 4.57. Desorption from the tetra-ammoniate phase was excluded from this analysis due to the significant overlap of desorption peaks, preventing accurate deduction of onset temperatures.

These results should be considered within the context that entropy changes are dominated by gas release, meaning that entropy changes are likely to be very similar for all processes. It is plausible that differences in hydrogen bonding between different halides allow for differences in the rotational and vibrational entropy of NH_3 molecules within the solid. However, this effect would not be significant in comparison to gas release.

Multiple linear regression was used to perform this analysis using a constant ΔS for all equilibria. Under the assumption of a constant ΔS, $CaBr_2$ shows significantly greater enthalpy changes for the mono-ammoniate and di-ammoniate desorption, while $CaCl_2$ shows a greater enthalpy change for desorption from the octa-ammoniate.

Comparison of enthalpy change values determined in this work with those present in the literature (Table 4.13) shows enthalpy values determined in this work as consistently larger by, on average, $\sim$10 kJ / mol. Given these enthalpy values were determined from desorption onset temperatures, it is possible that small amounts of hysteresis/slow kinetics may have led to greater onset temperatures observed.

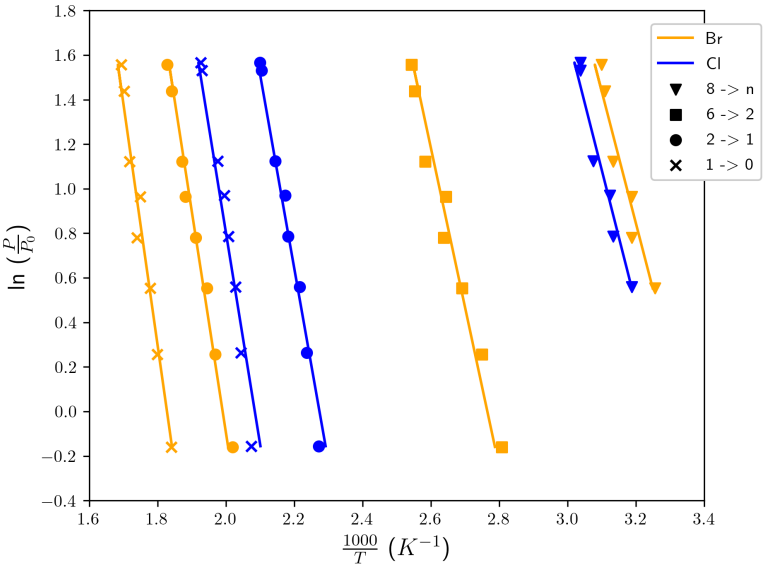
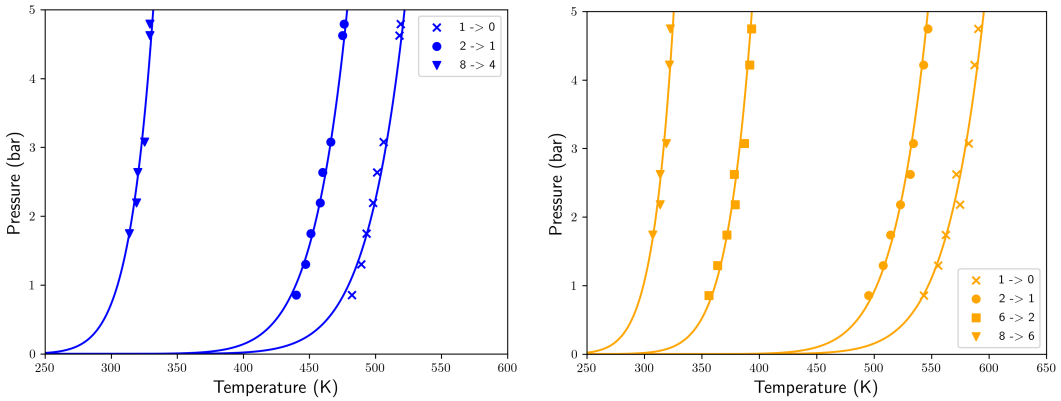


Figure 4.56: Clausius-Clapeyron fits for CaX_2 ammoniate phases calculated assuming a constant entropy change. It should be noted that the linear relationship shown relies on the value of ΔH being constant over the observed range. As such, extrapolation beyond these recorded datapoints should be treated with caution.



(a) **(b)**

Figure 4.57: CaX_2 ammoniate coexistence curves for (a) Cl and (b) Br assuming constant entropy changes, calculated using the Clausius-Clapeyron equation (Equation 4.7)

Table 4.12: Experimentally determined ammonia sorption enthalpy and entropy changes for CaX_2 when a constant ΔS is used. These values are determined using the variable NH_3 pressure experiments presented in Figures A.6 and A.7.

Desorption Step	Br	Cl
ΔS (J (mol NH_3)$^{-1}$ K^{-1})	165(5)	165(5)
$\Delta H_{8\rightarrow n}$ (kJ / mol NH_3)	49(1)	50(1)
$\Delta H_{6\rightarrow 2}$ (kJ / mol NH_3)	60(2)	
$\Delta H_{2\rightarrow 1}$ (kJ / mol NH_3)	83(2)	72(2)
$\Delta H_{1\rightarrow 0}$ (kJ / mol NH_3)	90(3)	79(2)

Table 4.13: Experimentally determined ammonia sorption enthalpy values for CaX_2 from the literature[108]. It should be noted that many literature sources use an incorrect version of the Clausius-Clapeyron equation, $\ln P = -\frac{\Delta H}{RT} + \frac{\Delta S}{R}$. The correct version is $\ln \frac{P}{P_0} = -\frac{\Delta H}{RT} + \frac{\Delta S}{R}$. Due to the properties of logarithms, fitting to the incorrect equation leads to a different ΔS value, but the same ΔH value. However, the use of an incorrect equation does call into question the accuracy of these results as a whole.

Desorption Step	Br	Cl
$\Delta H_{8\rightarrow 6}$ (kJ / mol NH_3)	41.65	
$\Delta H_{8\rightarrow 4}$ (kJ / mol NH_3)		41.01
$\Delta H_{6\rightarrow 2}$ (kJ / mol NH_3)	45.57	
$\Delta H_{4\rightarrow 2}$ (kJ / mol NH_3)		42.27
$\Delta H_{2\rightarrow 1}$ (kJ / mol NH_3)	79.04	63.19
$\Delta H_{1\rightarrow 0}$ (kJ / mol NH_3)	71.32	69.05

However, there are multiple issues with previous literature data which call it into question. Firstly, the use of an incorrect form of the Clausius-Clapeyron equation leads to incorrect entropy values. In theory, these values should all be offset by the same quantity. However, with a large range of ΔS values observed for different equilibria (e.g. 165.01 J mol^{-1} K^{-1} for $SrBr_2$ $1 \rightarrow 0$ and 340.78 J mol^{-1} K^{-1} for $SrBr_2$ $2 \rightarrow 1$) in these sources, the integrity of these values must be questioned. As explained above, gas releases dominate entropy changes in these reactions, and such a large variation in entropy values would not be explainable. The observation of a greater enthalpy of reaction for the $CaBr_2$ $2 \rightarrow 1$ reaction compared with the $CaBr_2$ $1 \rightarrow 0$ reaction also appears surprising, alongside being inconsistent with the results in this work.

Table 4.14: CASTEP calculated enthalpy changes for CaX_2 ammoniates. Sorption steps involving di-ammoniate phases include only the relevant di-ammoniate phase (i.e. *Cmmm* for Cl, *Cmce* for Br).

Desorption Step	Br	Cl
$\Delta H_{8\rightarrow6}$ (kJ / mol NH_3)	41.8	44.1
$\Delta H_{6\rightarrow4}$ (kJ / mol NH_3)	50.7	40.6
$\Delta H_{4\rightarrow2}$ (kJ / mol NH_3)	37.4	29.6
$\Delta H_{2\rightarrow1}$ (kJ / mol NH_3)	55.9	51.7
$\Delta H_{1\rightarrow0}$ (kJ / mol NH_3)	70.1	61.8

CASTEP geometry optimisations were performed on each phase in order to further understand the equilibria involved. It should be noted that geometry optimisations search for local minima, and as such can be heavily dependent on the starting position of atoms. This is not likely to cause issues for atoms such as Ca, N, Cl or Br, which have well-defined starting positions. However, the orientation of ammonia molecules and the starting position of hydrogen atoms can have a sizeable effect on the final energy and optimised cell configuration. Searching through all possible

ammonia orientations to locate a global minimum was considered to be too computationally expensive. Therefore, CASTEP energy results for NH_3-containing phases should be considered approximate, rather than exact. Madelung energy calculations were also performed on the optimised structures in order to inform about the 'ionic bonding strength' within these phases.

Table 4.14 and Figure 4.58 show the enthalpy changes between different ammoniate phases, calculated using CASTEP. Under the assumption of constant entropy changes, Figure 4.58 works akin to a Frost diagram, where phases at a higher energy than the average of the members either side are unstable with respect to disproportionation to the two adjacent phases. As seen in experiments, the tetra-ammoniate is considered unstable for $CaBr_2$, and the hexa-ammoniate is considered unstable for $CaCl_2$. However, it is surprising to see the tetra-ammoniate lie so clearly atop a peak for chloride ions. The tetra-ammoniate of calcium chloride has only been observed to be fleetingly stable in all experiments. However, CASTEP results suggests it should be unstable. It is possible that elements of these structures are missed in CASTEP calculations, which are effectively a snapshot of the real structure (T = 0 K). Vibration, rotation and any disorder of NH_3 molecules will adjust enthalpy and entropy values, which are not accounted for under this approach.

Taking these results into account, the tetra-ammoniate may be considered to be only kinetically stable, and more akin to an intermediate phase upon absorption or desorption between the octa-ammoniate and the di-ammoniate. However, this does not seem to be the case given the results recorded on POLARIS (Section 4.3), and Hüttig's original paper[102], which showed presence of the tetra-ammoniate for an extended period of time.

Overall, with the exception of the tetra-ammoniate of $CaCl_2$, these results are in agreement with experimental observations. As shown in Table 4.14, n = 1, 2, 6, 8 phases are stable with respect to disproportionation for $CaBr_2$, while n = 1, 2, 8 phases are stable with respect to disproportionation for $CaCl_2$. It should be noted

that the CASTEP calculated enthalpy changes are significantly below the experimentally determined enthalpy changes. A similar effect has been seen by Sørensen *et al.*[135], where experimentally determined enthalpy changes were consistently seen to be around 1.5× larger than the DFT calculated enthalpy changes for metal halide ammoniate formation. The cause of this is unclear, but may be related to either overestimating the enthalpy of gaseous NH_3 or underestimating the energy associated with hydrogen bonding in ammoniate phases.

Figure 4.59 shows the Madelung energy of each geometry optimised cell. Aside from small deviations, the most significant result is that the change in Madelung energy upon absorption is large if NH_3 replaces a halide in the first coordination sphere of calcium (all phases $n \leq 6$), and significantly smaller if no halide is replaced. This is instructive for understanding the stability of the different phases for different halides. As expected, greater changes in Madelung energy occur for chloride, due to its smaller size.

Having understood the structures in detail, and with the support of computational calculations, examination of the energetics of ammoniate phase formation is now possible. Upon absorption of each molecule of NH_3, there are three primary factors to consider: Ca-N bond formation, H-X hydrogen bonding, and the loss of ionic bonding (due to increased distance between Ca^{2+} and X^-). It is reasonable to expect Ca-N bonds to become weaker as more NH_3 molecules are introduced, due to the weaker donation of electrons from each N lone pair to the calcium ion. This is the principal reason why phases with high amounts of ammonia tend to have less favourable enthalpies of formation. This is also very unlikely to be significantly affected by which halide is present, as confirmed by Jones *et al.* for MgX_2 ammoniates using solid state NMR[92].

The loss of Madelung energy upon NH_3 absorption is a significant effect, and is the primary reason why bromide ammoniates tend to have greater enthalpies of formation than chloride ammoniates. As bromide is a larger anion, the increase in

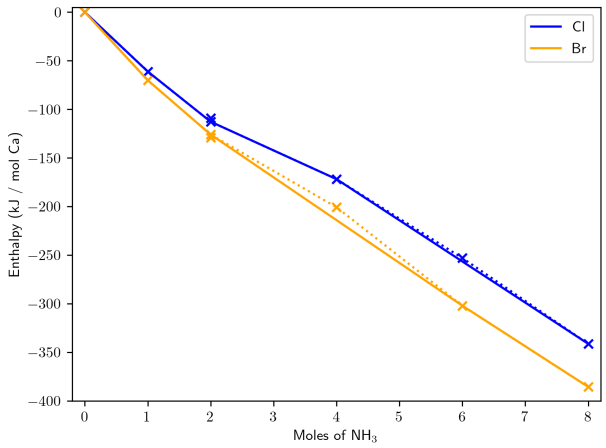


Figure 4.58: Energy changes relative to CaX_2 and gaseous NH_3 for ammoniate phases, calculated using CASTEP. The solid line goes through the stable phases for each halide, while the dotted line goes through all phases.

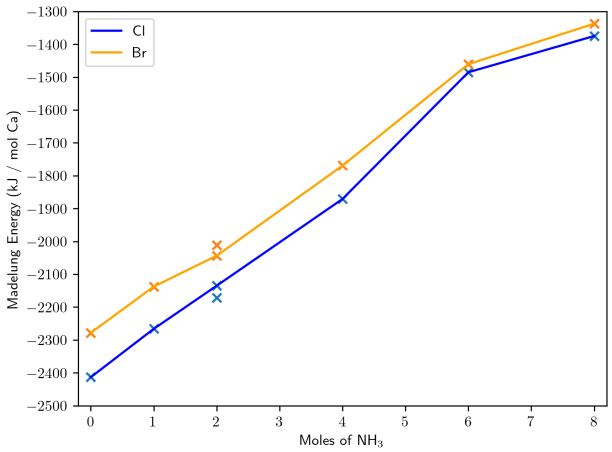


Figure 4.59: Madelung energies for CaX_2 ammoniates. Both *Cmmm* and *Cmce* di-ammoniate structures are shown. However, the line depicted only goes through the stable structure (i.e. *Cmmm* for Cl, *Cmce* for Br). The change in Madelung energy is large for any absorption processes involving replacement of a halide in the first coordination sphere of the metal. However, absorption to the octa-ammoniate shows a much smaller change in Madelung energy due to the expansion of the coordination environment to accommodate the extra NH_3 molecules.

distance from calcium ion to halide upon NH_3 absorption is not as consequential. As discussed previously (Section 4.1.6) when examining the structures of ammoniates, hydrogen bonding generally has a significant effect on the energy of a structure. As stated previously, hydrogen bonding will be stronger for chloride, due to its smaller size. When looking at ammoniate phases that form for one halide but not another, this is almost certainly due to a competition between hydrogen bonding (stronger for Cl) and ionic bonding (stronger for Cl). This also means that the relative loss of ionic bonding is greater for Cl.

The octa-ammoniate of chloride is therefore of higher stability than the bromide octa-ammoniate due to the reduced Madelung energy change when absorbing beyond 6 moles of NH_3, and the strong hydrogen bonding in the octa-ammoniate phase. This, in turn, is likely a reason for the relative instability of the hexa- and tetra-ammoniates of chloride. The Madelung energy penalty associated with removing chloride from the first coordination sphere of calcium is so high that after absorption of the first 2 moles of NH_3, the strength of new Ca-N bonds formed is not high enough to overcome the energetic effects of displacing Cl from the first coordination sphere until the temperature is low.

However, due to the low Madelung energy penalty associated with absorption of the final two moles of NH_3, and the strong hydrogen bonding observed in $CaCl_2(NH_3)_8$, then once this 'barrier' is overcome, it is likely to be thermodynamically favourable to avoid these intermediate phases, and absorb all the way to the octa-ammoniate. Bromide, on the other hand, has weaker hydrogen bonding, which reduces the stability of the octa-ammoniate relative to the hexa-ammoniate, and Madelung energy changes are of lower magnitude, leading to further increased stability of the hexa-ammoniate. This is also likely the origin of the fleeting stability of the tetra-ammoniate for $CaCl_2$. The hexa-ammoniate is unstable for the reasons laid out above. These reasons also apply to the tetra-ammoniate. However, Ca-N bond strength is not so significantly reduced when $n = 4$, and the Madelung energy

change from tetra- to octa-ammoniate still involves displacement of two chloride ions from the first coordination sphere, leading to a narrow temperature window of stability for the tetra-ammoniate.

This form of analysis of phase stability is further discussed in Chapter 7, where the energetics and structures of ammoniate phases across the range of metal halides will be examined.

4.3 *In-Situ* Powder Neutron Diffraction

Samples of $CaCl_2$ and $CaBr_2$, mixed with amorphous silica, were examined on the POLARIS diffractometer at ISIS Neutron and Muon Source under flowing ND_3 gas, in order to understand the sorption pathways followed. Discussion of powder neutron diffraction patterns of pure $CaCl_2(NH_3)_n$ and $CaBr_2(NH_3)_n$ phases was presented in Section 4.1.

4.3.1 $CaCl_2$

Figure 4.60 shows the complete set of *in-situ* powder neutron diffraction data for the $CaCl_2$ sample from POLARIS banks 3 and 4. Upon heating, the phase transitions are clear to see, as the powder releases integer amounts of ammonia. Heating was paused whenever the beam was off, but also around 50 °C, in order to collect PND data of pure tetra-ammoniate for later structure solution. After structure solution of unknown crystal structures, batch refinements were performed to determine the weight, and subsequently molar, percentage of each phase.

Figures A.8 and 4.61 show the weight percent and mole percent of each phase during the experiment, determined through Rietveld analysis. Initial absorption at room temperature appears to primarily produce the di-ammoniate phase, though small amounts of mono-ammoniate are observed. This is likely due to absorption from the mono-ammoniate being much more rapid than absorption from the anhy-

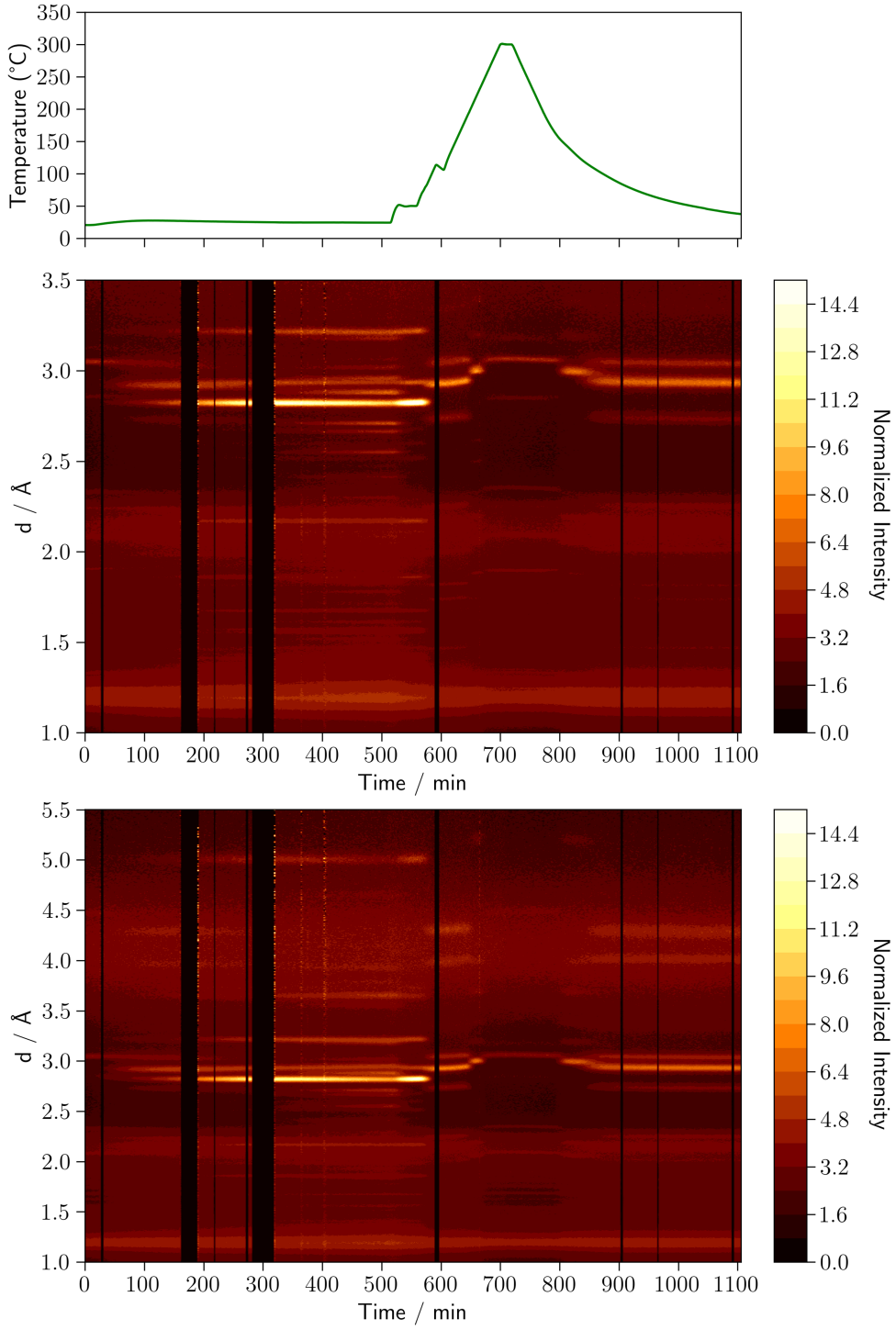


Figure 4.60: A contour plot of all PND data for $CaCl_2$ from POLARIS bank 3 (bottom) and bank 4 (middle). The top plot shows the corresponding temperature. It is clear to see the phase transitions upon heating to 300 °C. Black sections correspond to periods where the beam was down.

drous phase, leading to the mono-ammoniate present only at low concentrations. As discussed in Section 4.1.4 this may be related to the heat release associated with the initial absorption process, leading to rapid absorption of the second mole of ammonia. This is also consistent with previous results seen from STA data, where di-ammoniate and mono-ammoniate desorption peaks would typically be the same size, even when limited absorption had occurred, as, at the end of the absorption phase, all mono-ammoniate was converted to higher ammoniate phases.

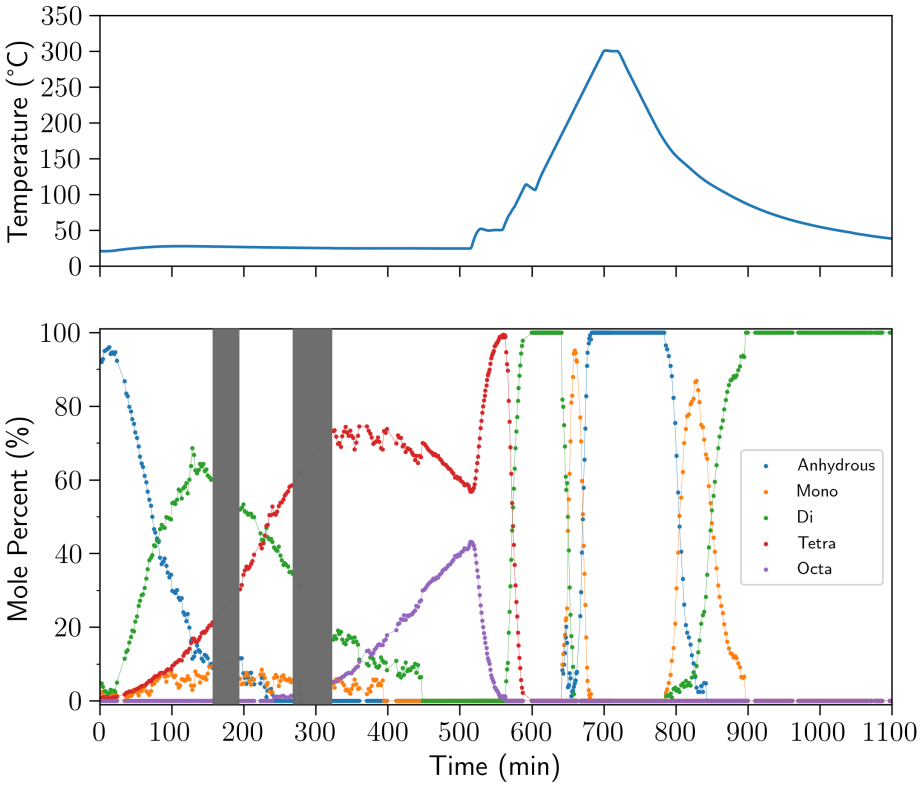


Figure 4.61: Mole percent of phases in $CaCl_2$ PND data calculated through Rietveld analysis. Phase transitions are clear to see.

Absorption to the tetra-ammoniate occurs almost immediately after the increase in di-ammoniate mole percent, suggesting that absorption to this phase is rapid. The tetra-ammoniate reaches around 30 mol % of sample before the anhydrous phase has effectively disappeared around 200 minutes. The high mole percent of tetra-

ammoniate shows that absorption is not a clear cut process, with regions of the sample absorbing well beyond the average molar amount of ND_3. This exemplifies the faster absorption observed for ammoniate phases when compared with their corresponding anhydrous phases.

Absorption to the octa-ammoniate does not appear significant until around 300 minutes, as absorption from the tetra-ammoniate to the octa-ammoniate is slowed significantly by the four-mole jump in ND_3 quantity. The data presented in Figure 4.61 exemplify the slow absorption shown by $CaCl_2$ at room temperature and pressure, requiring over 8 hours for the sample to be constituted of 40 mol % octa-ammoniate. Due to time constraints within the experiment, full absorption to the octa-ammoniate phase was not achieved.

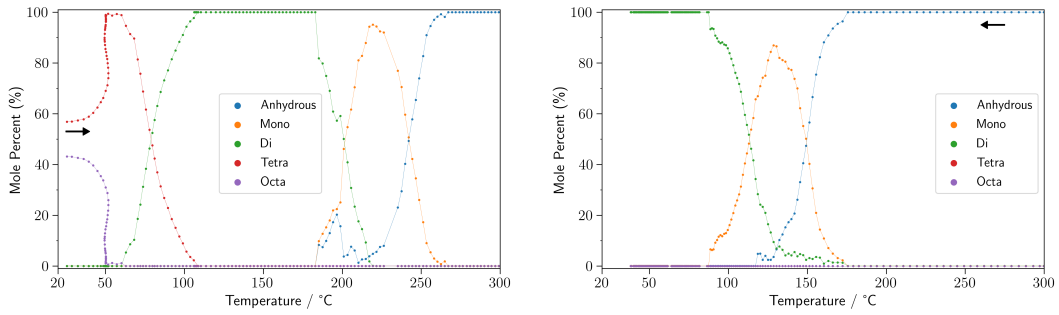


Figure 4.62: Mole percent of phases in $CaCl_2$ PND data during the (a) temperature ramp and (b) cooldown. The temperature was held at 50 °C briefly during the temperature ramp to allow for collection of a pure tetra-ammoniate pattern.

Figure 4.62 shows the mole percents of each phase during the temperature ramp and cooldown. The onset temperatures of each desorption (and absorption) event are shown in Table 4.15. These values show good agreement with desorption events observed on gas rigs at similar pressures. It should be noted that the large amount of sample used here (1.0319 g total, of which 0.7770 g was $CaCl_2$) led to prolonged desorption events, and hence significant overlap when temperature ramping was continuous (such as the di-ammoniate and mono-ammoniate desorption events).

Table 4.15: $CaCl_2(NH_3)_n$ desorption onset temperatures based on change in mole percentage from PND data. Absorption onset temperatures are also given for the cooldown. Significant hysteresis (>50 °C) is observed between desorption and absorption temperatures.

Event	Onset Temperature (°C)
$8 \rightarrow 4$	42(1)
$4 \rightarrow 2$	66(1)
$2 \rightarrow 1$	187(1)
$1 \rightarrow 0$	226(1)
$0 \rightarrow 1$	169(1)
$1 \rightarrow 2$	134(1)

Upon cooldown from 300 °C, absorption to the mono-ammoniate and di-ammoniate occurred once the temperature was low enough. It appears that there is significant hysteresis, with absorption only becoming noticeable in the diffraction data at temperatures > 50 °C below the corresponding desorption event. While absorption at room temperature showed limited mono-ammoniate stability (due to further absorption to the di-ammoniate), this was not seen on cooling, with nearer stoichiometric conversion to the mono-ammoniate phase before further absorption to the di-ammoniate phase. This is likely in part due to the temperature being too high initially for absorption to the di-ammoniate. However, formation of the mono-ammoniate at temperature is significantly more rapid than formation of the di-ammoniate was at room temperature (at the beginning of the experiment). As with almost all reactions, a higher temperature usually indicates a faster reaction rate. Prior to the temperature ramp, gas flow through the sample proved tricky, with the gas inflow requiring monitoring in order to prevent overpressurisation of the sample cell. This was particularly observed during the latter stages of the room temperature absorption, due to the large volume expansion associated with ND_3

absorption. After desorption from the tetra-ammoniate phase, it was noticed that gas flowed freely, as a much more porous sample was left behind. Expansion initially will have caused the sample to close any spaces in the powder and then subsequently expand up the sample cell. During desorption, it appears that sample contraction was localised, leaving a much more porous material. Upon cooldown, all areas of this porous sample will have been much more accessible by ND_3 gas, leading to much more rapid absorption. This effect of increased porosity was observed for all three samples measured on POLARIS.

4.3.2 $CaBr_2$

Figure 4.63 shows all *in-situ* powder neutron diffraction data for the $CaBr_2$ sample from POLARIS banks 3 and 4. Similar to the $CaCl_2$ sample, phase transitions are clear in the heating stage. Unfortunately, the neutron beam was down for long periods of time, leading to interrupted datasets. During the first long outage, gas inflow was switched to argon, to ensure absorption processes halted. During the second long outage, the sample had absorbed ammonia beyond a stable amount when under an argon atmosphere at room temperature i.e. if the gas inflow was switched to argon, desorption from any octa-ammoniate present to the hexa-ammoniate would have occurred. As such, during the second significant outage, gas inflow and outflow were closed, keeping the sample under a static ND_3 atmosphere. It should be noted that limited absorption would have been possible under these conditions, as was seen in the molar percentages output from batch refinement (Figure 4.64).

Figures A.9 and 4.64 show the weight percent and mole percent of each phase throughout the experiment, as determined by Rietveld analysis. Limited absorption was observed before the first outage, which occurred only 35 minutes after ND_3 flow was introduced to the sample. After ND_3 flow returned, around 1100 minutes into the experiment, absorption proceeded to the hexa-ammoniate, with no observed presence of mono- or di-ammoniate phases. This is consistent with previous results

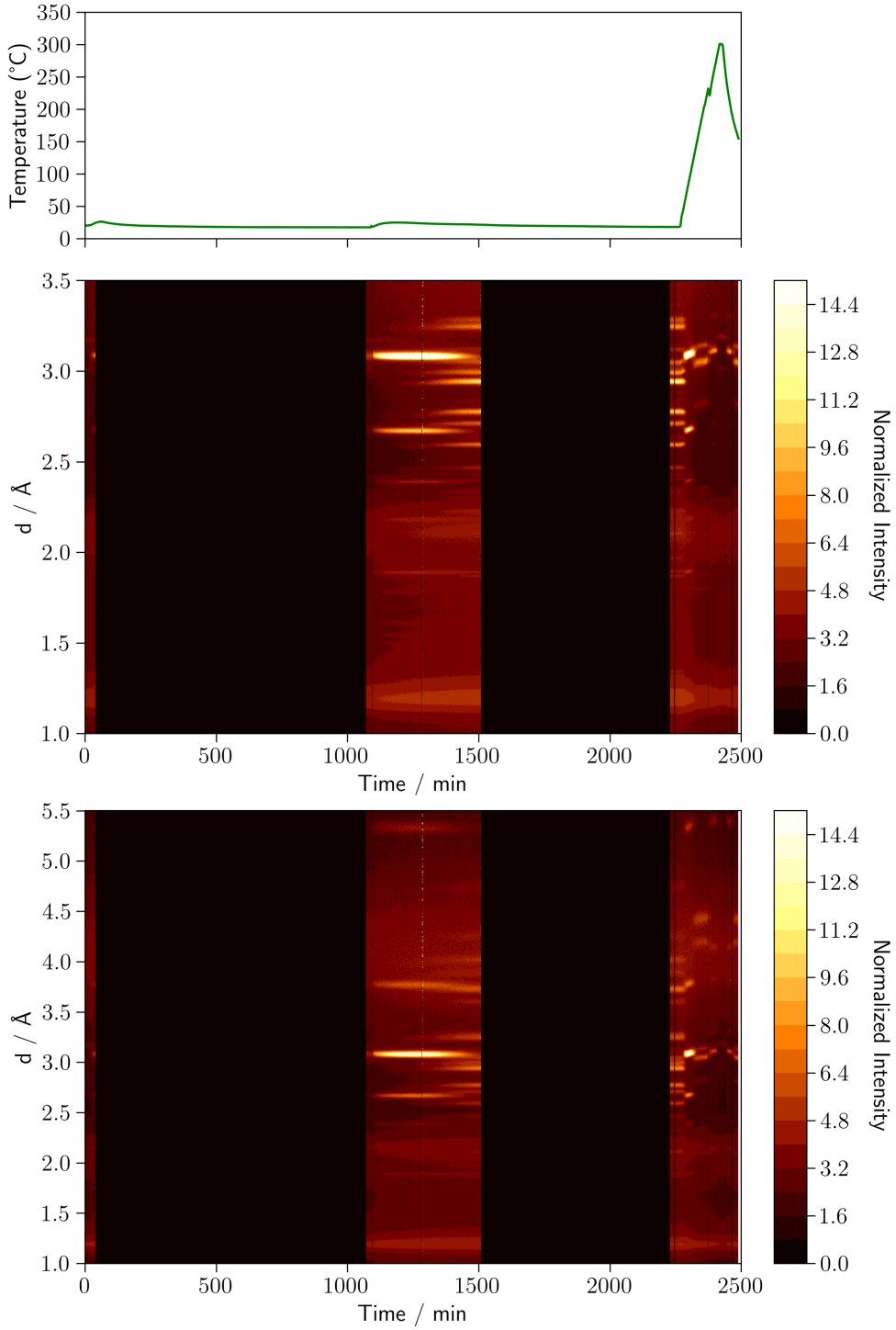


Figure 4.63: A contour plot of all PND data for $CaBr_2$ from POLARIS bank 3 (bottom) and bank 4 (middle). The top plot shows the corresponding temperature. It is clear to see the phase transitions upon heating to 300 °C. Black sections correspond to periods where the beam was down.

suggesting that absorption proceeds rapidly once it has begun (likely related to heat release upon absorption of the first mole of NH_3). Once the mono-ammoniate has formed, it quickly absorbs further to the hexa-ammoniate. It should also be noted that small increases in the mole percentage of the octa-ammoniate phase are noticeable immediately after the ND_3 was returned.

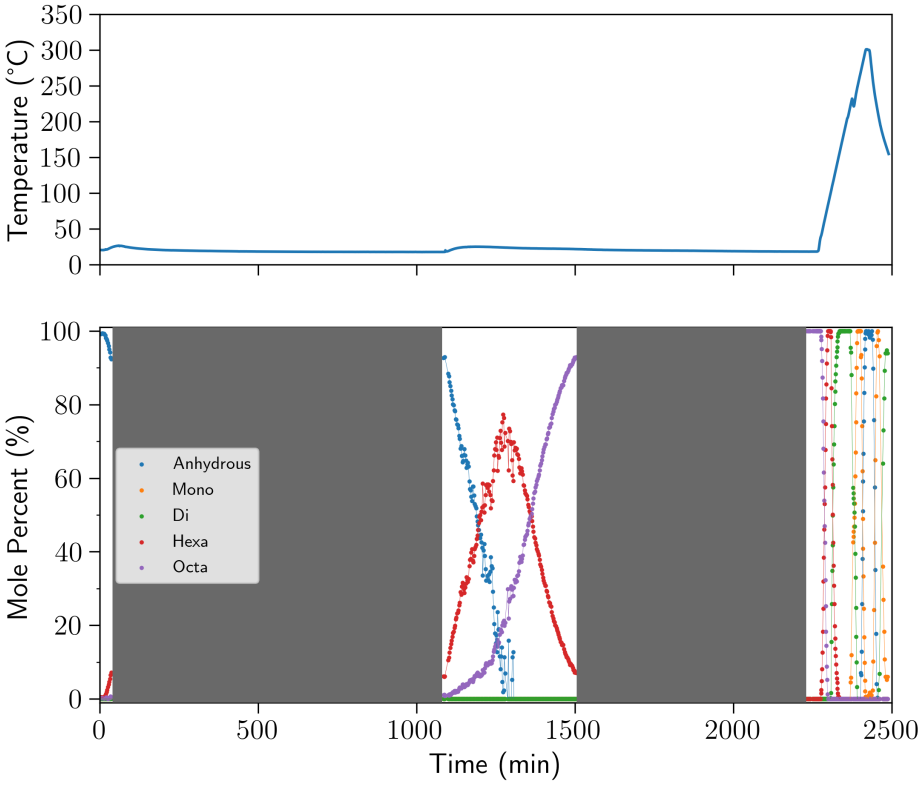


Figure 4.64: Mole percent of phases in $CaBr_2$ PND data calculated through Rietveld analysis.

Figure 4.65 shows the mole percent of each phase during the temperature ramp and cooldown period. It is clear to see the faster room temperature absorption exhibited by $CaBr_2$, where absorption rates were consistently around 1.5–2.5 mol/hr, when compared with $CaCl_2$, where absorption rates never rose significantly above 1 mol/hr. In both samples, absorption during cooldown (i.e. at elevated temperature) was significantly faster than at room temperature.

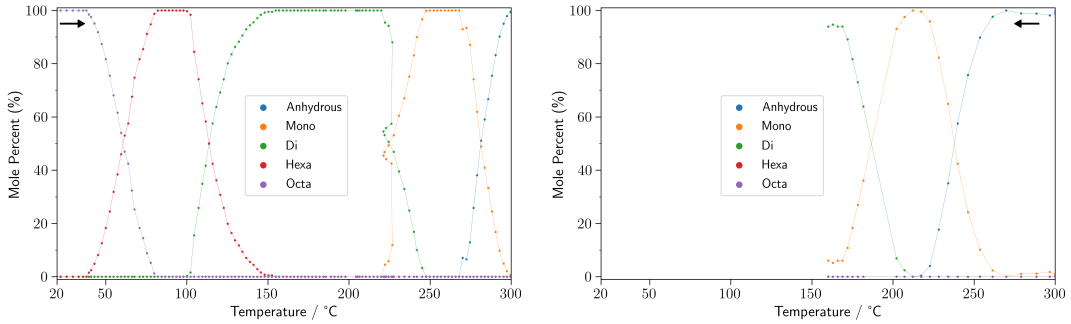


Figure 4.65: Mole percent of phases in $CaBr_2$ PND data during the (a) temperature ramp and (b) cooldown.

Table 4.16 shows the onset temperatures of different events during the experiment. While hysteresis is observed, as was the case for $CaCl_2$, the observed temperature difference between the $2 \rightarrow 1 \rightarrow 0$ absorption and equivalent desorption events is significantly diminished for $CaBr_2$ (23–25 °C compared with 53–57 °C for $CaCl_2$). This may be related to a greater diffusion rate of ND_3 in $CaBr_2$.

Table 4.16: $CaBr_2(NH_3)_n$ desorption onset temperatures based on change in mole percentage from PND data. Absorption onset temperatures are also given for the cooldown. Hysteresis is seen (∼20 °C), though this is much less significant than observed for $CaCl_2$ (Table 4.15).

Event	Onset Temperature (°C)
$8 \rightarrow 6$	40(1)
$6 \rightarrow 2$	104(1)
$2 \rightarrow 1$	227(1)
$1 \rightarrow 0$	277(1)
$0 \rightarrow 1$	254(1)
$1 \rightarrow 2$	202(1)

4.4 Conclusions and Future Work

Detailed studies into the structures of ammoniate phases have been performed through the use of PXRD and PND, enabling the solution of the previously unknown structures of $CaX_2(NH_3)$ and $CaCl_2(NH_3)_4$. Somewhat surprisingly, the mono-ammoniate appears to crystallise in a polar space group ($Cmc2_1$), though questions remain about non-Bragg features in PXRD data, suggesting the possibility of defects in the structure. DFT calculations have been used to study the dynamics of hydrogen bonding in these phases, demonstrating the importance of this bonding mode in stabilising the crystal structures. Despite the importance of hydrogen bonding, the decomposition temperatures of ammoniate phases, with the exception of the octa-ammoniate, are generally modified according to the increased ionic bonding strength upon loss of NH_3, leading to greater desorption temperatures for $CaBr_2$ ammoniates.

$CaCl_2$ and $CaBr_2$ show significantly different ammonia absorption pathways, with $CaCl_2$ forming stable phases at n = 0, 1, 2, 4, 8 and $CaBr_2$ forming stable phases at n = 0, 1, 2, 6, 8. The reduced temperature stability of $n < 6$ phases for $CaCl_2$ was shown to relate to the large Madelung energy change upon absorption of NH_3. The octa-ammoniate phase was shown to have a slightly greater temperature stability for $CaCl_2$ due to the expansion of the metal coordination sphere in this phase, thus limiting the Madelung energy change upon loss of NH_3.

Alongside allowing for elucidation of unknown crystal structures, *in-situ* neutron diffraction experiments confirmed the absorption processes of $CaCl_2$ and $CaBr_2$ do not proceed stepwise, with intermediate phases rapidly bypassed by a portion of the material, if the thermodynamic conditions allow. This is likely related to local heating upon absorption of ammonia, leading to rapid further absorption. This experiment also revealed significant hysteresis for sorption equilibria, with a $\sim$55 K difference in absorption and desorption onset temperatures for $CaCl_2$, and a $\sim$25 K difference in onset temperatures for $CaBr_2$.

Further work could investigate the origin of non-Bragg features in the PXRD pattern of the $CaBr_2$ mono-ammoniate, which may be related to defects in this structure. While the tetra-ammoniate phase of $CaCl_2$ is unstable at room temperature without an ammonia atmosphere present, *in-situ* PXRD could be used to confirm the stacking motif observed in the crystal structure of the tetra-ammoniate of $CaCl_2$.

5

Ammonia Absorption of $CaCl_xBr_{2-x}$ Solid Solutions

Alongside analysis of the phases formed by calcium halides under an ammonia atmosphere, extensive work was performed on the ammonia absorption properties of $CaCl_xBr_{2-x}$ materials. CASTEP was used to determine the likelihood of stability of solid solutions of $CaCl_xBr_{2-x}(NH_3)_n$, followed by temperature cycling experiments to determine the ammonia absorption pathways undertaken by these materials. *In-situ* PND results are used to gain a detailed understanding of the changes undergone by a CaClBr sample during these cycles.

5.1 Stability of Solid Solution Phases

CASTEP contains an option for use of the 'virtual crystal approximation', in which virtual atoms placed on anion sites would be an interpolation of chloride and bromide (their potentials), weighted appropriately according to their user defined occupancies. However, this approach is unable to reproduce the short range order that would be observed in truly disordered materials, and as such can give unrealistic energies when atoms are sufficiently different in size or nature. This approach was tested, but gave very poor estimates of the energy values for mixture atoms of chloride and bromide, in main part because of their significantly different size. Instead, a series of cells were run with halides randomly dispersed across the 32 available anion sites in a 2×2×2 unit cell.

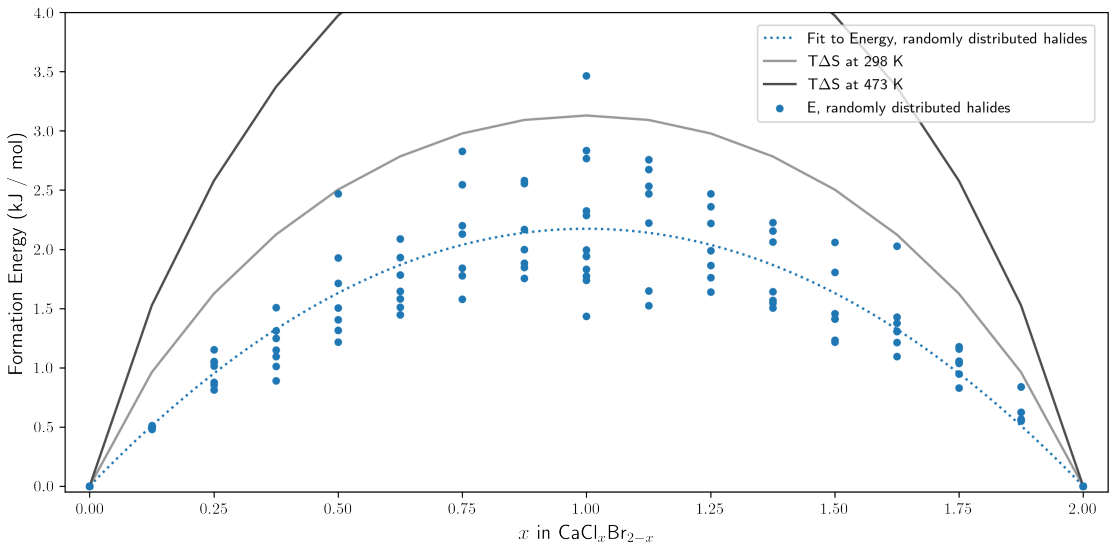


Figure 5.1: CASTEP calculated energies of $CaCl_xBr_{2-x}$ cells, relative to the weighted average of $CaCl_2$ and $CaBr_2$. The energies of individual cells are shown, with fitting to a parabolic function anchored at (0,0) and (2,0) (i.e. $E = ax(x-2)$). $a = -2.17(1)$. Solid solution formation energies are typically well below the entropic term at room temperature, indicating stability.

Figure 5.1 shows the energies calculated for each of these cells, relative to the corresponding quantities of $CaCl_2$ and $CaBr_2$. Also shown is the entropy associated with the disorder across the available anion sites at two different temperatures, calculated using Boltzmann's entropy formula (Equation 4.6). The mean enthalpy change associated with solid solution formation is well below $T\Delta S$ at room temperature, and as such it is expected that solid solution formation is thermodynamically facile at all temperatures.

Figure 5.2 shows the energies of these cells plotted against the 'deviation parameter'. The 'deviation parameter' is defined as:

$$D = \frac{1}{N}\sum_{i=1}^{N}\frac{|r_i - r_0|}{r_0} \tag{5.1}$$

where r_0 is the 'ideal' bond length (calculated as the mean bond length in the pure chloride and bromide cells), and r_i is the i^{th} bond length (between Ca and X ions). This sum is performed for both Ca-Cl and Ca-Br distances, with r_0 representing the relevant ideal bond length. The correlation between sub-optimal bond lengths and energy is driven by the asymmetric bonding environments when differently sized anions are dispersed at random across the available sites. When this idea is extended to the ammoniate phases however, the enthalpies of mixing are reduced.

Figure 5.3 shows the energies of individual cells, and the mean formation energies of mixed ammoniate phases based on CASTEP geometry optimisations. The di-ammoniate phases show a slightly reduced enthalpy of mixing, as some of their close Ca-X contacts are replaced by hydrogen bonding, which is likely less sensitive to variations in interatomic distance. This is further exemplified by the hexa- and octa-ammoniate phases, as the Ca-X distances become significantly less important. This is corroborated by the correlation between energy and the deviation parameter, a correlation which is largely broken for higher ammoniate phases (see Figure 5.4). It should be noted that there is a large variation in the energies of individual octa-ammoniate cells. The high energy variation is related to the strong hydrogen

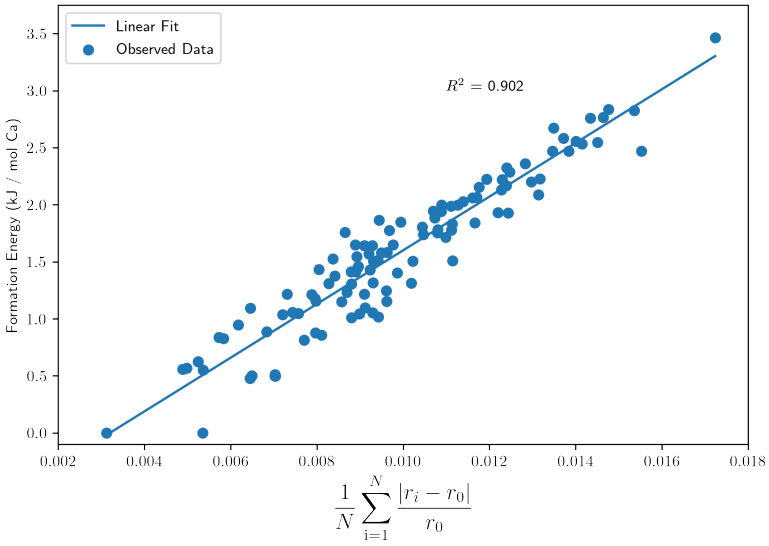


Figure 5.2: CASTEP calculated energies of $CaCl_xBr_{2-x}$ cells plotted against the deviation in ideal bond lengths. The ideal bond length is defined as the mean bond length observed in pure $CaCl_2$ and $CaBr_2$ cells. The formation energy appears directly related to the unfavourable bond lengths observed in $CaCl_xBr_{2-x}$ cells.

bonding in the octa-ammoniate structure (see Section 4.1.7), which allows for specific cells to be significantly lower or higher in energy based on which anion sites are occupied by which halide ion. Overall, the average mixing enthalpies for higher ammoniate phases appear to be reduced to around 0 kJ / mol Ca for higher ammoniate phases (n $\geq$ 6), and reduced slightly to $<$ 1 kJ / mol Ca for di-ammoniate phases. Mono-ammoniate and tetra-ammoniate phases were excluded as their structures were not known at the time of this work.

Figure 5.4 shows the energy of CASTEP geometry optimised cells against the deviation parameter (Equation 5.1). It is clear to see the correlation between energy and bond length deviation break down for higher ammoniate phases, as hydrogen bonding becomes the dominant short range bonding interaction between anions and cations. The correlation is observed to be slightly reversed for the hexa-ammoniate phase which is a consequence of the anions leaving the high symmetry site to maximise the hydrogen bonding interactions (see Section 4.1.6). These CASTEP calcu-

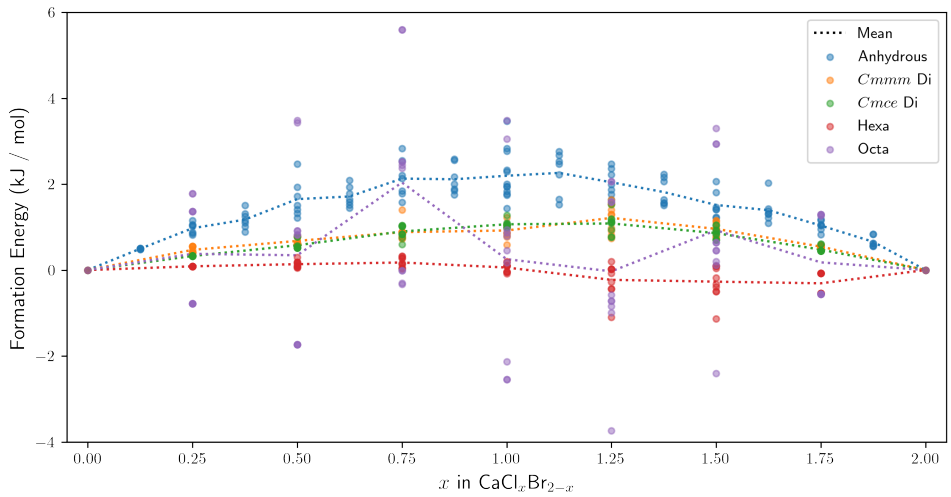
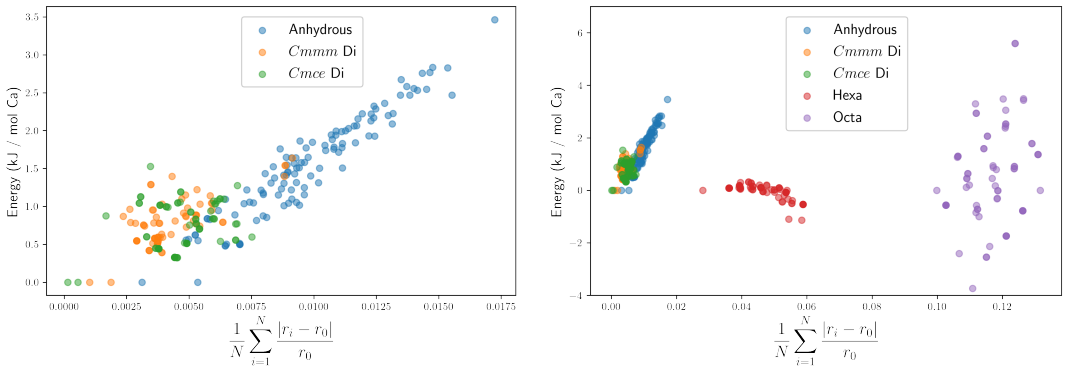


Figure 5.3: CASTEP calculated energies of $CaCl_xBr_{2-x}(NH_3)_n$ cells with halide ions randomly dispersed across the available sites. Solid solution formation energies typically reduce as the ammoniation number of the phase increases.

lations suggest that mixed ammoniate phases will be stable for ammoniate phases adopted by both $CaBr_2$ and $CaCl_2$. Ammoniate phases such as the di-ammoniate or hexa-ammoniate may have low mixing enthalpies, but there will also be an energy barrier associated with the change of structure, which may or may not be possible to overcome.

Figure 5.5 shows the PXRD patterns resulting from attempted synthesis of solid solution phases. The tube furnace setup used for these syntheses involved flowing argon gas, but was subsequently discovered to not be fully airtight, leading to hydrate formation for many samples. The $x = 0.2$ sample was synthesised using a fully airtight setup once this issue was discovered.

Importantly, the PXRD patterns show successful mixed phase formation for all samples. This is best evidenced by the variation in lattice parameters of CaX_2 and $CaX_2(H_2O)_2$ across the series of samples (Figure 5.6), which roughly follow Vegard's Law.



(a) **(b)**

Figure 5.4: CASTEP calculated energies of $CaCl_xBr_{2-x}(NH_3)_n$ cells plotted against the deviation in 'ideal' Ca-X bond lengths. While a strong relationship was seen between the deviation parameter and cell energy for anhydrous solid solutions, this relationship is weakened for the di-ammoniate phases, and broken for the hexa-ammoniate and octa-ammoniate cells (when halides are no longer part of the first coordination sphere).

However, unfitted peaks were seen in the $x = 0.2$ and $x = 0.4$ samples. The $x = 0.4$ sample was re-synthesised in an airtight environment in order to help understand the origin of these unfitted peaks.

Figure 5.7 shows the diffraction patterns of these two samples clearly. The previously unfitted peaks were indexed and fitted to an orthorhombic cell with lattice parameters $a \approx 15.20\,\text{Å}$, $b \approx 5.61\,\text{Å}$, $c \approx 6.71\,\text{Å}$ and space group *Pnna*. However, it should be noted that exact identification of the space group is not possible as (i) powder diffraction patterns are inherently centrosymmetric and (ii) some peaks may be hidden in the noise. Indexing of all peaks in the pattern was attempted using the indexing functionality in TOPAS, in order to determine whether these peaks might represent a supercell of the usual *Pnnm* structure. However, no suitable fit could be found. This suggests that these peaks originate from a new phase altogether, though the relative peak size between these two phases is very similar across both samples, suggesting it may be originating from the same phase (i.e. a superstructure). The presence of these peaks in the airtight samples rules out the

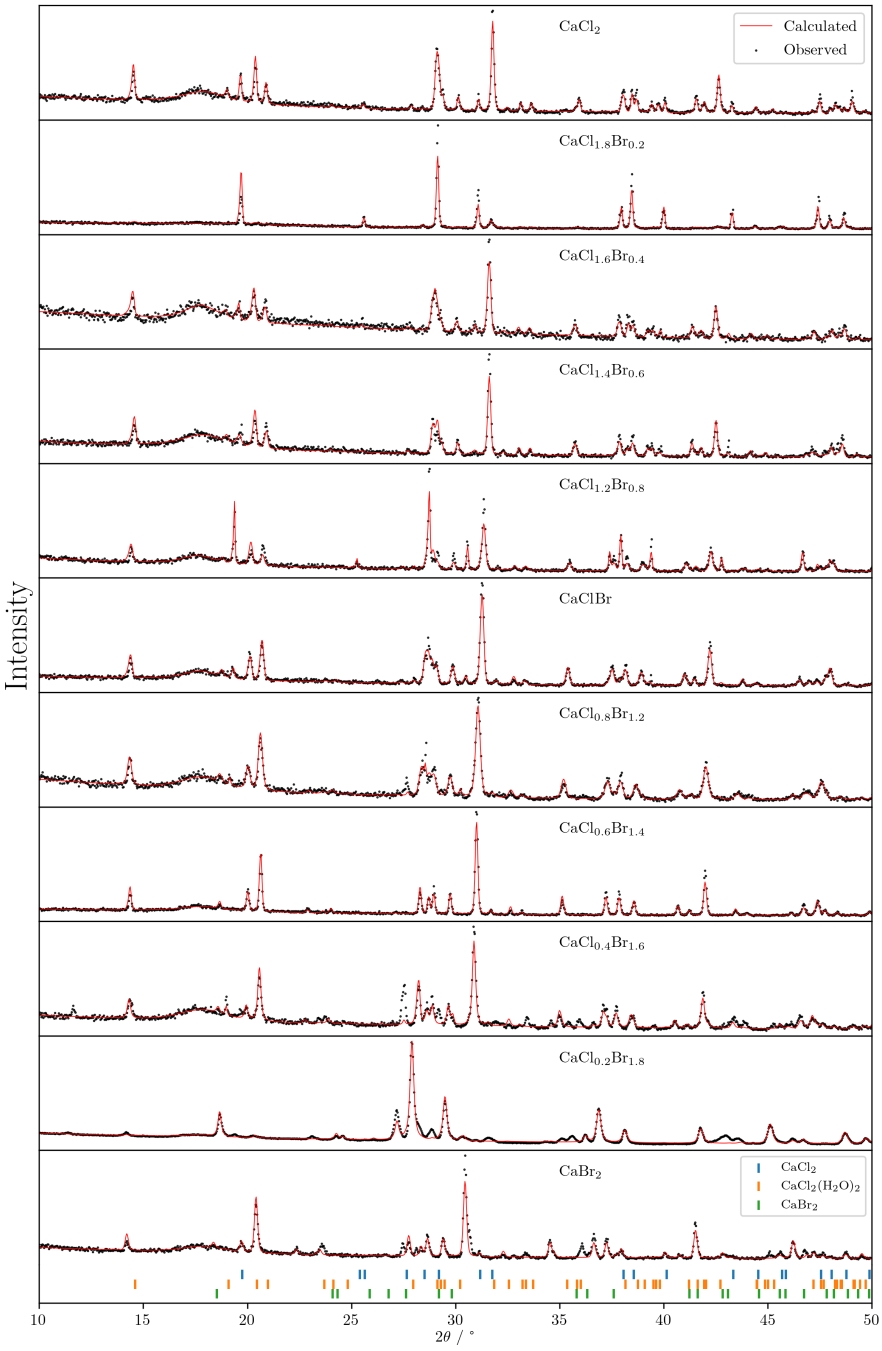
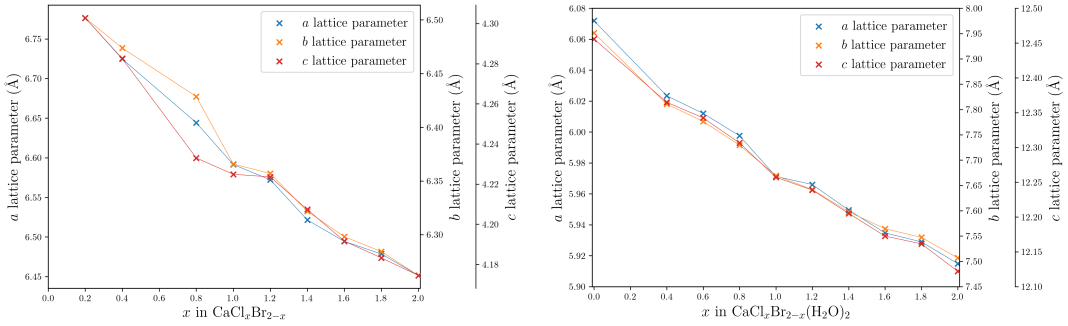


Figure 5.5: PXRD patterns of $CaCl_xBr_{2-x}$ syntheses. Samples were ground before heating to 550 °C for 40 hours. The tube furnace used for these syntheses was subsequently discovered to not be fully airtight, and as such many samples showed hydrate formation upon cooling.



(a) **(b)**

Figure 5.6: Lattice parameters of (a) $CaCl_xBr_{2-x}$ and (b) $CaCl_xBr_{2-x}(H_2O)_2$ phases, as determined by PXRD. Deviations from Vegard's Law are observed, though lattice parameters are approximately interpolations of the end members.

possibility of an undetermined hydrated phase. Overall, it is unclear whether this is a new halide phase, or a superstructure originating from halide ordering. It is clear however, that the origin of these peaks is related to a halide phase, due to the shift in peak position upon changing the x value (i.e. changing the halide ratio), indicating an associated lattice parameter change. This new phase or superstructure appears not to have affected the ammonia absorption properties of the materials, with a single di-ammoniate phase being formed after exposure to ammonia (see x = 0.2 PXRD in Figure 5.9). The disappearance of these peaks further suggests that they originate from a halide phase.

The peaks are not apparent for the $x = 0$ or $x = 0.6$ phases, suggesting this new phase is only stable for small amounts of chloride dissolved into $CaBr_2$. There are small unfitted peaks in the $x = 0$ sample, with unknown origin. These were deemed to be an impurity, as they were not observed in subsequently synthesised samples, and remained present at identical d spacing (Figure 5.9) after exposure to ammonia and heat ($< 300\,^{\circ}C$).

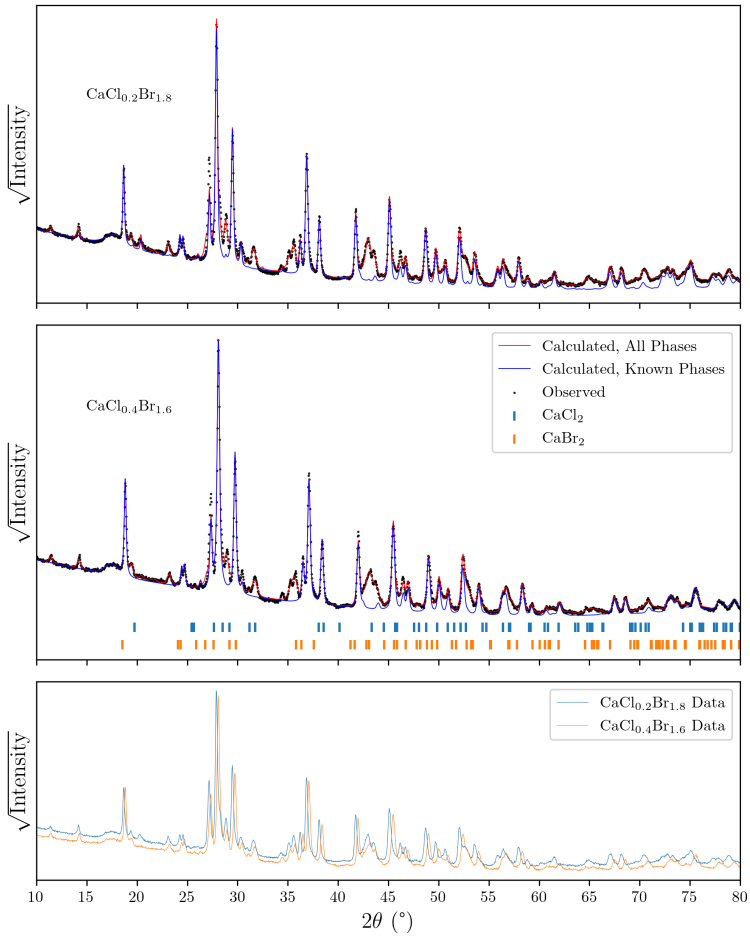


Figure 5.7: PXRD patterns of $CaCl_{0.4}Br_{1.6}$ and $CaCl_{0.2}Br_{1.8}$. The square root of intensity is plotted in order for the small, unknown peaks to show up clearly. The peak at $2\theta = 20.25°$ in the $x = 0.2$ sample fits to the dihydrate structure, and is not part of the set of unfitted peaks. The red line shows the calculated pattern including a Pawley fit (using the space group *Pnna*) to the peaks of unknown origin, while the blue line is a fit to only known phases (almost entirely the anhydrous *Pnnm* phase). The bottom plot shows the observed data for the two samples, to clearly show the shift in peaks as a result of changing the halide composition.

5.2 Interactions of $CaCl_xBr_{2-x}$ Solid Solutions with NH_3

Each of the synthesised powders was loaded into a crucible on the low pressure gas rig described in Section 3.2.1, before exposure to flowing ammonia at atmospheric pressure and temperature cycling from room temperature to 300 °C. All recorded gas flow and temperature data are presented in Figures B.1–B.11. Peak and onset desorption temperatures were recorded from this data for di-ammoniate and mono-ammoniate desorption events. Onset temperatures for desorptions from the mono-ammoniate phase are best estimates for high x value samples, due to the slight overlap of desorption peaks. For higher n transitions, the desorption peaks are of much more complex shape, with significant amounts of overlap, and as such are not so easily condensed to a few numbers describing them. Some samples also showed limited desorption from higher n transitions. Slow cooling of the reactor may have limited octa-ammoniate formation for some samples as the reactor never quite fully cooled, even after 20 hours of passive cooling.

A consistent trend observed is the more rapid absorption of ammonia by low x (primarily bromide) samples. Upon cooldown, no significant deviation in gas outflow is seen for high x samples, suggesting very slow absorption. In contrast, low x samples show clear reductions in gas outflow once temperature has dropped below that of a phase transition.

For samples with $x < 1.4$, it is clear to see the relative peak size between the first two desorption events shift slowly as x is changed, as would be expected from the known desorption pathways of $CaCl_2$ ($8 \rightarrow 4 \rightarrow 2$) and $CaBr_2$ ($8 \rightarrow 6 \rightarrow 2$). For $x > 1.6$ however, this trend is no longer clear. This could be related to slow absorption by high x samples i.e. the ammonia desorption pathway is still $8 \rightarrow 4 \rightarrow$

2, but absorption past the tetra-ammoniate is limited, leading to the relative peak sizes appearing to show otherwise. Due to the heavily overlapped peaks, calculation of individual peak area was considered to be unachievable.

It may be reasonable to expect three peaks in the low temperature regime, corresponding to octa-ammoniate, hexa-ammoniate and tetra-ammoniate desorption. However, this is only visible for the $x = 1.4$ sample. This is likely due to a combination of the limited temporal resolution of this experiment and the possibility of small desorption events being hidden beneath other peaks. It is plausible that solid solutions of these ammoniate phases are stable, though data here are insufficient to confidently comment on this, and as such it will be examined in more detail in further experiments.

Figure 5.8 shows the onset and peak desorption temperatures of the di-ammoniate and mono-ammoniate desorptions across the series of samples. From this data, it appears that solid solutions of the mono-ammoniate are stable, with interpolation between the extremes visible for both onset and peak desorption temperatures. The di-ammoniate desorption behaviour is significantly more complex. The peak desorption temperature could easily be due to the overlap of desorption peaks from two separate di-ammoniate phases, while the onset temperature likely informs about the first desorption peak observed. However, no significant peak splitting was observed for the di-ammoniate desorptions. These data appear consistent with formation of solid solutions at high and low x values, while separation into the two di-ammoniate phases occurs around $x = 1$. At high x values, small amounts of bromide dissolving into the *Cmmm* phase does not affect the peak or onset desorption temperature significantly due to the importance of hydrogen bonding in this phase. At low x values, the change of bromide to chloride in the *Cmce* structure significantly affects the onset and peak desorption temperatures. At intermediate x values, onset temperatures are low, due to the presence of the *Cmmm* structure (the first desorption to occur), while peak desorption temperatures likely vary due to the changing ra-

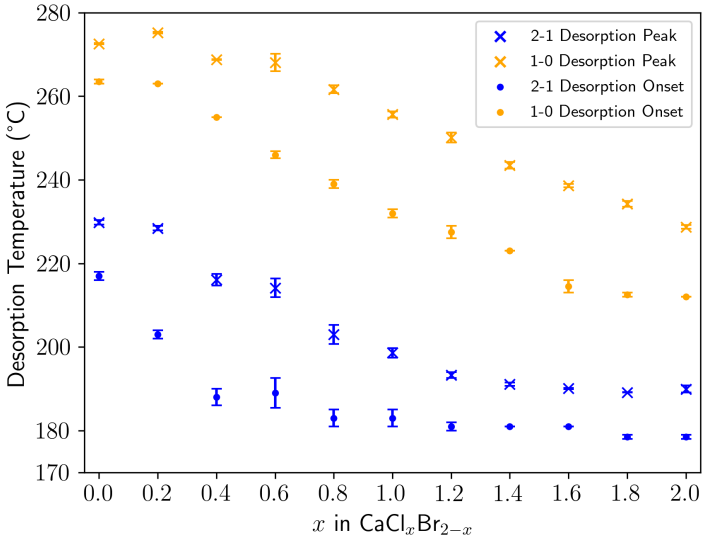


Figure 5.8: Onset and peak desorption temperatures for di-ammoniate and mono-ammoniate desorptions across the x series. Two cycles were performed for each sample. Data points are thus presented as the mean and uncertainty of the recorded data. It should be noted that insulation around the reactor was absent for the $x = 0$ and $x = 0.4$ samples, which appears to have slightly affected the accuracy of the temperature measurement. The mono-ammoniate desorption approximately follows a linear interpolation of the end members, while much more complex behaviour is seen for desorption from the di-ammoniate phase. Original cycling data is presented in Figures B.1–B.11. These experiments were conducted under pure ammonia flow (20 sccm) at atmospheric pressure.

tio of $Cmmm : Cmce$ structures i.e. the single peak is simply two overlapping broad peaks, and the observed maximum depends on the size of these two peaks. It should be noted that the limited temporal resolution of the gas flow data recorded makes accurate conclusions tricky.

Ex-situ PXRD recorded on the I11 beamline of samples after these experiments help to explain these results. Figures 5.9 and 5.10 show the PXRD patterns of samples after exposure to NH_3 and temperature cycling. One of the significant observations of this is the (partial) decomposition of hydrated samples into CaXOH and NH_4X upon exposure to ammonia.

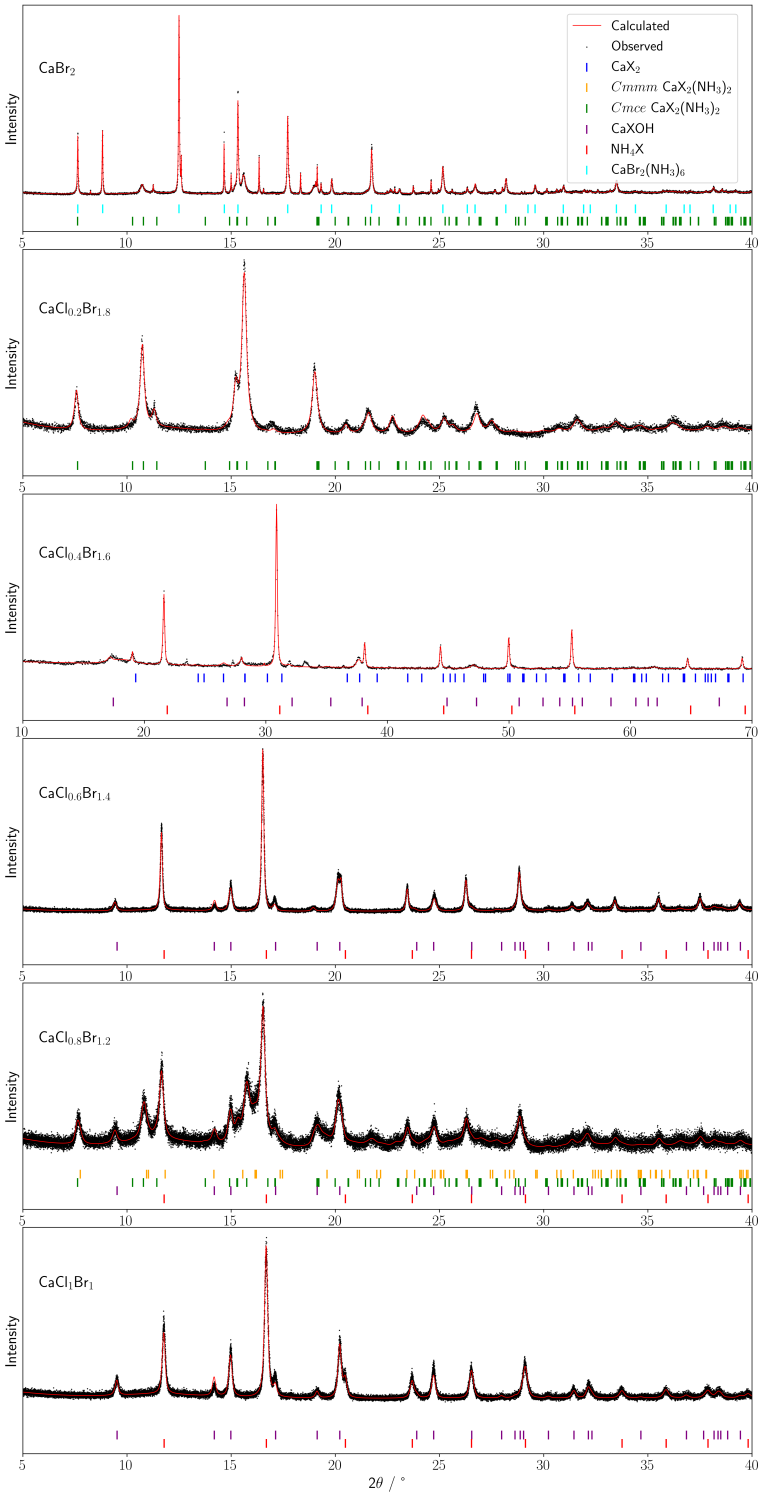


Figure 5.9: PXRD patterns of $CaCl_xBr_{2-x}$ samples after exposure to ammonia. Tick marks within each plot are shown only for phases deemed to be present. The $x = 0.4$ sample was recorded on the PANalytical X'Pert Diffractometer at the Inorganic Chemistry Laboratory in Oxford ($\lambda = 1.5406\,\text{Å}$). All other samples were recorded on the I11 diffractometer at Diamond Light Source ($\lambda = 0.826\,833\,\text{Å}$).

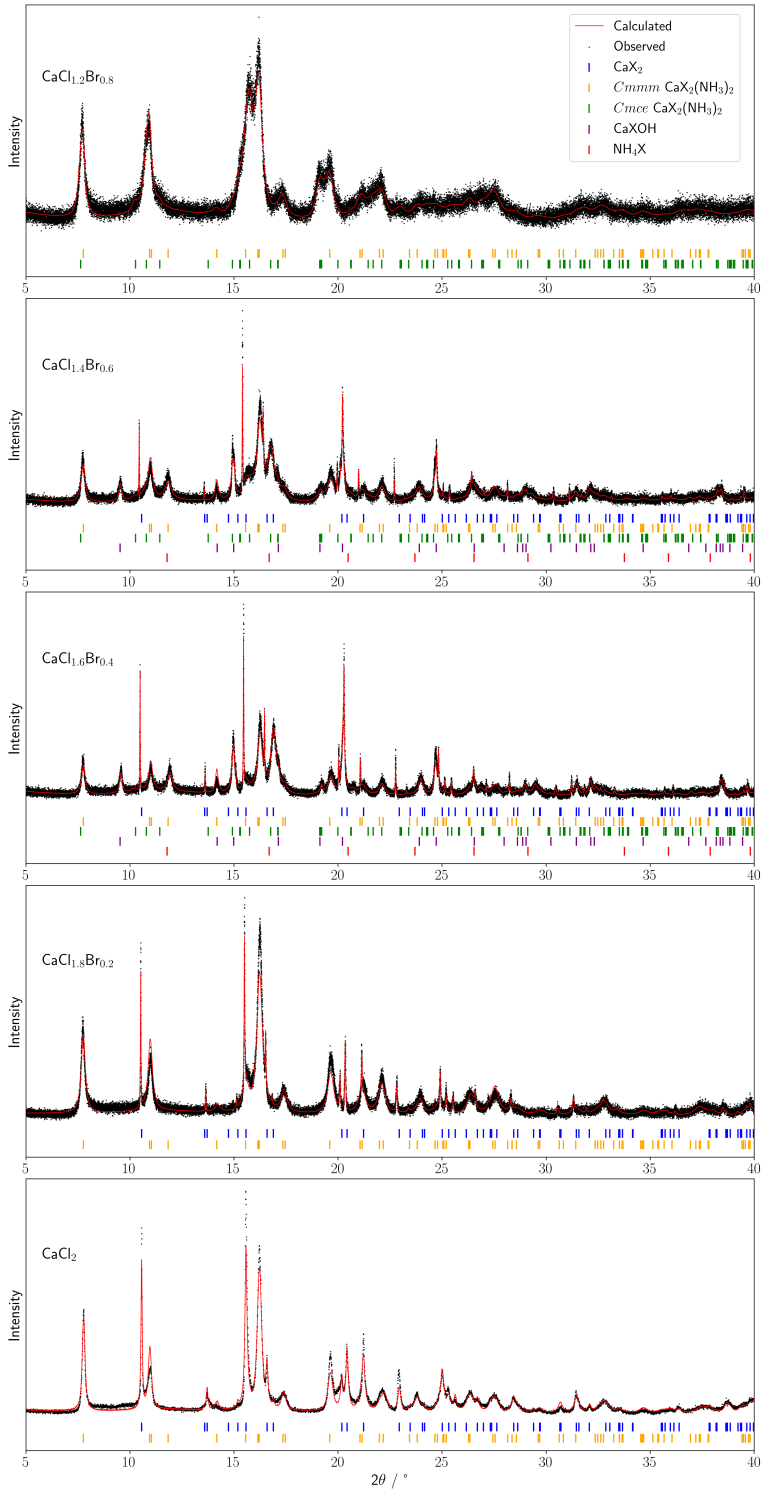


Figure 5.10: PXRD patterns of $CaCl_xBr_{2-x}$ samples after exposure to ammonia. Tick marks within each plot are shown only for phases deemed to be present. All samples were recorded on the I11 diffractometer at Diamond Light Source ($\lambda = 0.826\,833$ Å).

Equation 5.2 shows the presumed stoichiometry of this decomposition reaction. However, Rietveld analysis of PXRD patterns consistently assigned a significantly higher weight percent to NH_4X than to CaXOH, despite the lower molar mass of NH_4X. This implies the stoichiometry of this decomposition reaction is not obeyed. However, it is unclear how another decomposition is possible without the formation of extremely unstable species or CaO, neither of which was observed. The possible reaction to form CaO and NH_4X is shown in Equation 5.3, though no evidence of CaO formation was ever seen.

$$CaX_2 + H_2O + NH_3 \longrightarrow CaXOH + NH_4X \tag{5.2}$$

$$CaX_2 + H_2O + 2\,NH_3 \longrightarrow CaO + 2\,NH_4X \tag{5.3}$$

Despite some samples showing only NH_4X and CaXOH diffraction peaks (x = 0.6, 1.0), desorptions as expected were still observed during the temperature cycling experiment. As such, there must be some small amount of remaining CaX_2 or $CaX_2(NH_3)_n$ present in the sample. It is possible that this did not show up clearly in the diffraction data due to it constituting a small percentage of sample, the low crystallinity of the di-ammoniate phases, and the poor quality of the data. All subsequent experiments were performed with a pre-analysis dehydration step to ensure the prevention of decomposition in the presence of both water and ammonia.

An important result from these PXRD patterns is the presence of both *Cmmm* and *Cmce* di-ammoniate phases for $0.8 \leq x \leq 1.6$. This is consistent with the suggestion from the temperature cycling data (Figure 5.8), whereby halide separation occurs at intermediate x values. There are two main caveats to this. Firstly, the $x = 0.4$ and $x = 0.6$ data did not show di-ammoniate phases, so the stability of a mixed di-ammoniate phase at these compositions is unknown. Secondly, PXRD patterns shown here were recorded at room temperature, and mixed phases are likely to become more stable as the temperature increases (due to the entropic

gain associated with mixing halides). As established above, small quantities of a di-ammoniate phase may not appear in these diffraction data due to the poor data quality and relatively low crystallinity of these phases. While single di-ammoniate phases were observed for $x = 0.2$ and $x = 1.8$ samples, supporting the conclusion that mixed phases are stable at high and low x values, this evidence should not be considered definitive.

Figure 5.11 shows the volumes of di-ammoniate phases observed in PXRD patterns. It is clear to see the change in volumes of di-ammoniate phases as more chloride/bromide is incorporated into the sample. This strongly suggests that small amounts of chloride can dissolve into the *Cmce* structure, and small amounts of bromide can dissolve into the *Cmmm* structure, even at room temperature. There is a clear limiting value for chloride dissolution into the *Cmce* structure, corresponding to a volume of $\sim 160\,\text{Å}^3$. A clear limiting value is not obviously apparent for bromide incorporation into the *Cmmm* structure. However, a value of $151.9\,\text{Å}^3$ is observed in the $x = 0.8$ sample.

In order to obtain data with significantly better time resolution, STA was used to further study the absorption-desorption cycles of the CaClBr sample. The small mass of sample used ($\sim$10 mg) in STA will also reduce the occurrence of temperature gradients through the sample, leading to better temperature resolution for desorption events. Figures 5.12 and 5.13 show the results from the temperature cycling of this sample under flowing NH_3-Ar mixtures. Similar experiments performed on pure $CaCl_2$ and $CaBr_2$ samples are presented in Figures 4.50–4.53.

The CaClBr ammoniation properties appear significantly more complicated than those exhibited by either $CaCl_2$ or $CaBr_2$. Desorption from the octa-ammoniate phase is clear for the higher ammonia pressure cycles. However, above the temperature of the octa-ammoniate desorption peak appears to be a 'flat' region of desorption (i.e. constant desorption rate) before another desorption double peak. CASTEP results (Figure 5.3) suggest it is likely that the octa-ammoniate consists of a solid

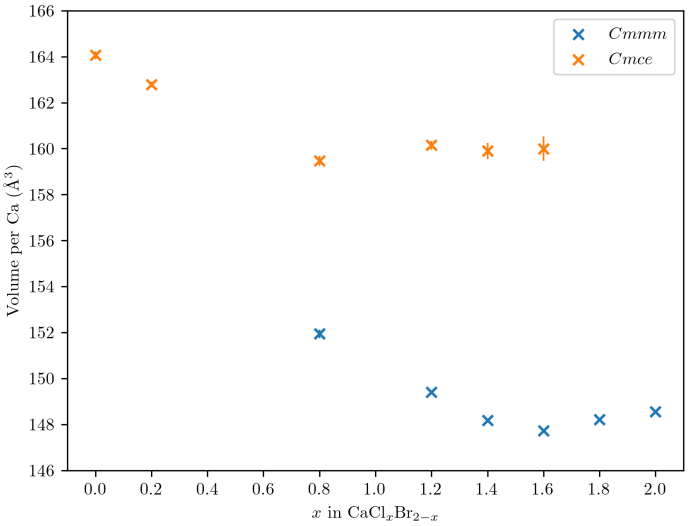


Figure 5.11: Volumes of $CaX_2(NH_3)_2$ cells in Rietveld analyses of I11 PXRD patterns. Uncertainties are plotted also, but are too small to be visible for many datapoints. Volumes are clearly affected by the halide ratio, indicating that some quantity of chloride can dissolve into the bromide di-ammoniate phase (and vice versa).

solution, due to the small mixing enthalpy associated with this phase. Desorption from this phase will likely produce an unstable solid solution hexa-ammoniate phase (unstable with respect to separation of halide ions). 'Halide separation' is likely to occur in this region. This 'halide separation' appears to be the cause of this 'flat' desorption event in Figure 5.13, occurring between the octa- and hexa-ammoniate desorptions (from ∼50 °C to ∼100 °C). As the halides separate, $n > 2$ is unstable for chloride phases at these temperatures, and so NH_3 loss is a consequence of the halide separation. The desorption of NH_3 in this flat region could therefore be limited by the diffusion rate of X^- ions in the material, perhaps explaining why this is not typically seen as a peak but instead a long, slow desorption process.

If this flat region is related to phase separation, phase separation is incomplete before the temperature is sufficient for a desorption peak. The double peak (∼ 100 °C in Figure 5.13) after this may then be made up of an initial desorption from the halide mixed phase (which has not yet sufficiently phase separated), and desorption

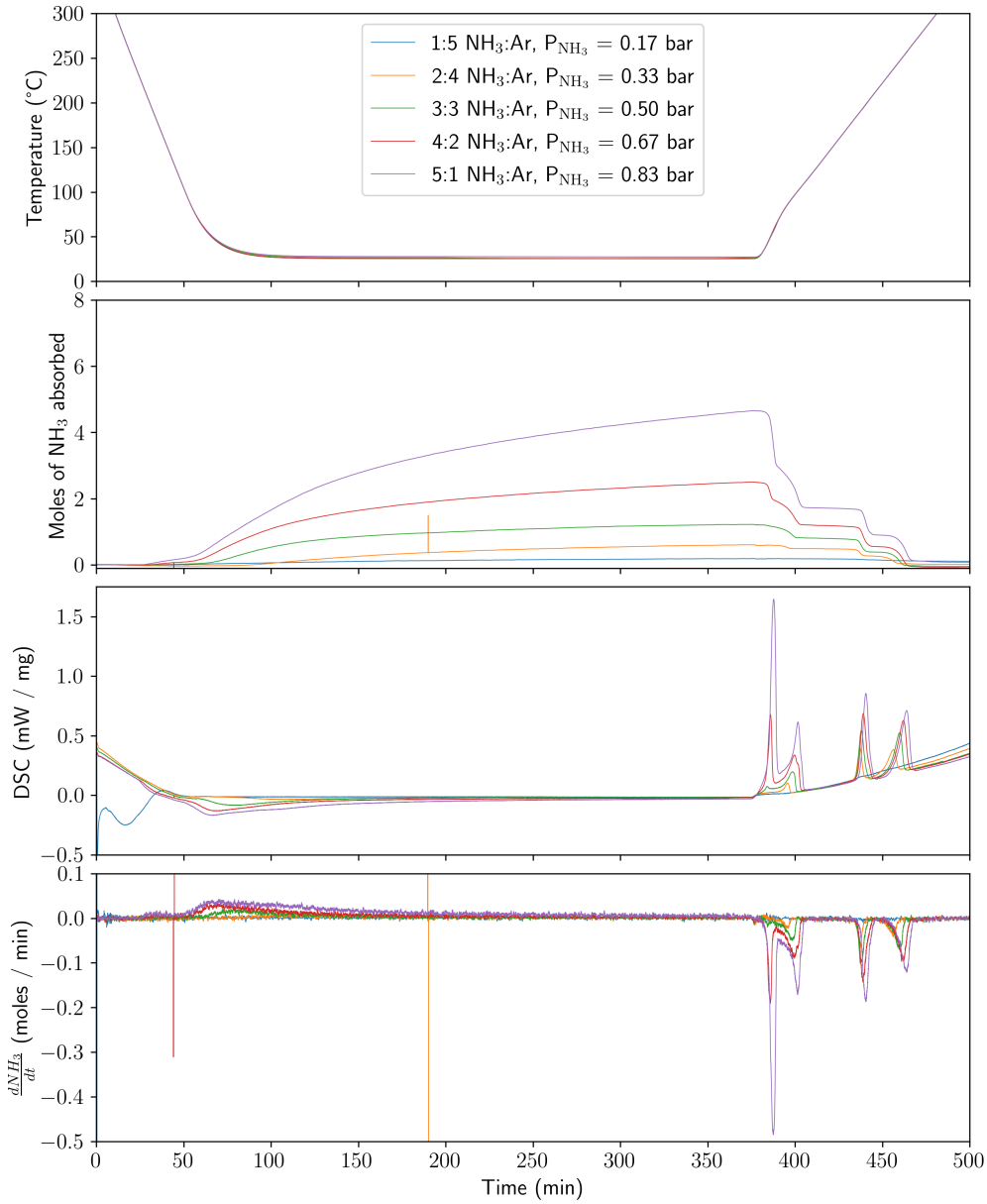


Figure 5.12: STA of CaClBr ammonia cycling under 60 sccm flowing gas. Pressure remained at atmospheric pressure i.e. 1:5 NH_3:Ar corresponds to an ammonia partial pressure of 0.17 bar.

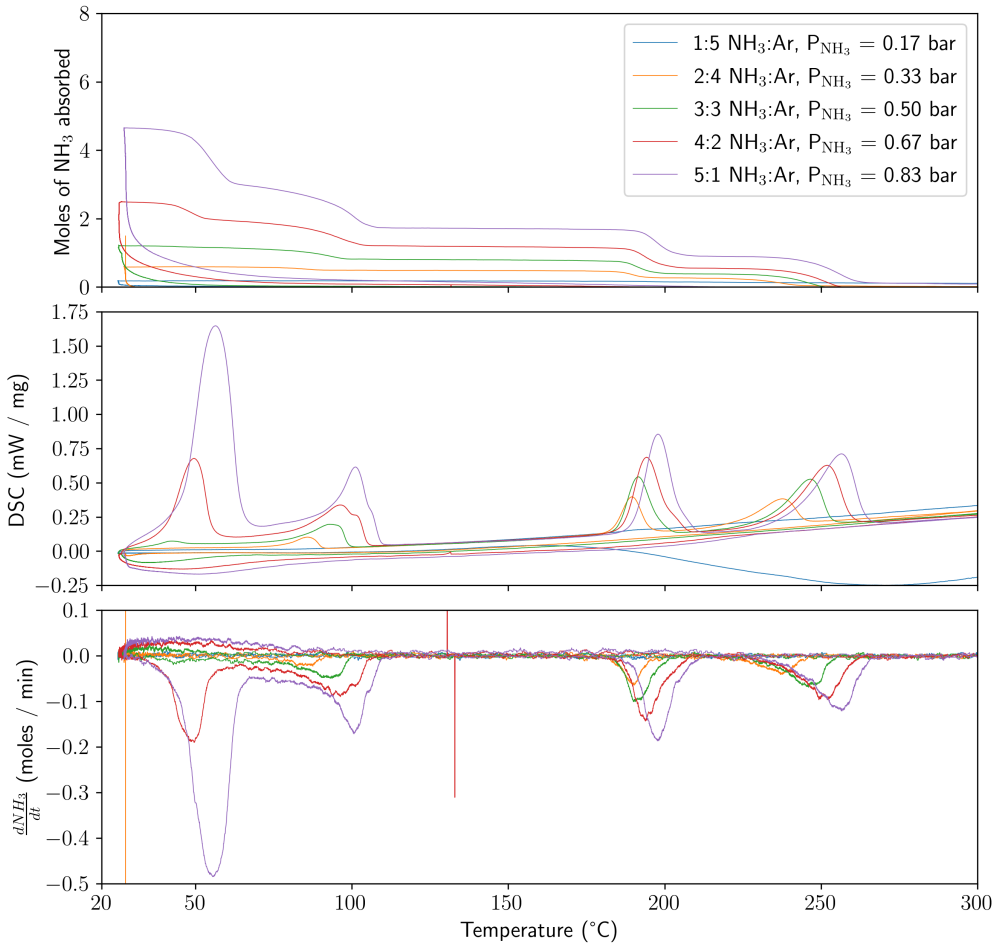
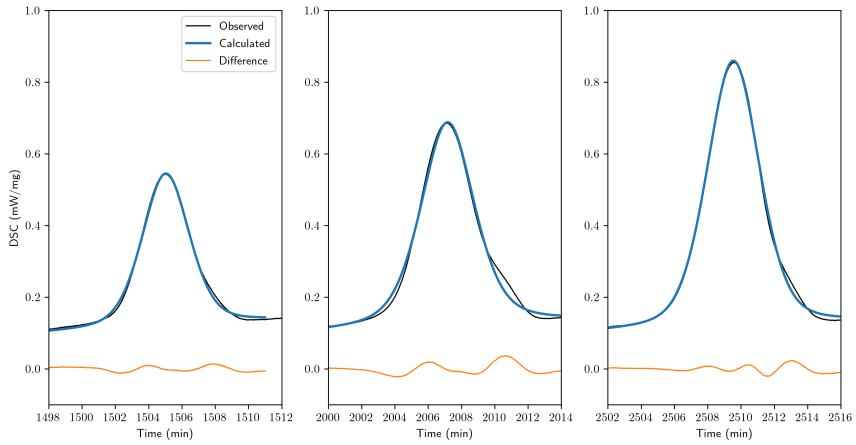


Figure 5.13: STA of CaClBr ammonia cycling under 60 sccm flowing gas. This data is the same as presented in Figure 5.12 with temperature on the horizontal axis to allow clear comparison of desorption steps.

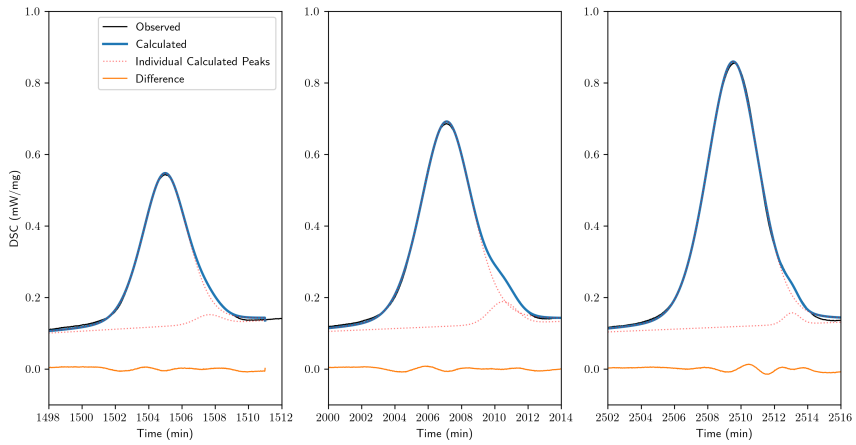
from a calcium bromide hexa-ammoniate phase. The temperature of this second peak/shoulder matches well with the hexa-ammoniate desorptions seen in the $CaBr_2$ sample. It is important to note that a 'mixed phase' is more likely to crystallise into an array of many different local compositions around a mean composition.

The $1 \rightarrow 0$ desorption step appears as a single peak, with the temperature of this step simply an average of the $1 \rightarrow 0$ steps for $CaCl_2$ and $CaBr_2$, suggesting solid solution formation for the mono-ammoniate phase (as expected from DFT calculations). However, the $2 \rightarrow 1$ desorption step appears more complex, with a clear shoulder appearing on the peaks for the 5:1, 4:2 and 3:3 NH_3:Ar cycles.

Figure 5.14 shows fits of the $2 \rightarrow 1$ desorption; the empirical model chosen was based on the pseudo-Voigt function. It is clear to see the presence of a second peak in this step, though it is surprising to see such a small peak. From PXRD data (Figure 5.11) it is known that halides can dissolve into the other di-ammoniate structure, up to a limit. However, it should be noted that those results were from patterns recorded at room temperature, and the limit of dissolution may be different at ∼200 °C. Nonetheless it is clear that this is two overlapping desorption events, likely related to the presence of both di-ammoniate structures. The relative peak size and peak positions still remain a question however, as the higher temperature peak is centred well below that which might be expected for the *Cmce* di-ammoniate structure of $CaBr_2$ (∼205 vs ∼240 °C). Even when considering the presence of chloride in this structure, it still appears to be shifted to a much lower temperature than might be expected. This may be related to the stability of the solid solution phase for the mono-ammoniate. The entropy associated with mixing halides in the mono-ammoniate phase could lead to its preferential formation, and thus lower decomposition temperature of the bromide di-ammoniate phase. Formation of the mono-ammoniate phase from the chloride di-ammoniate phase might trigger desorption of the bromide di-ammoniate, due to the increased stability associated with halide mixing in the mono-ammoniate phase.



(a)



(b)

Figure 5.14: Peak fitting for the 2 → 1 desorption in the CaClBr STA. (a) shows fits to one pseudo-Voigt function while (b) shows fits to two pseudo-Voigt functions. This is presented as evidence of the presence of two di-ammoniate phases. Left = 3:3, middle = 4:2 and right = 5:1 NH_3:Ar cycles.

Figures 5.15–5.18 show the desorption events from $x = 0.4$, 0.8, 1.2 and 1.6 samples after absorption of NH_3. All samples show the desorption region around 65–90 °C hypothesised as related to phase separation after desorption from the octa-ammoniate. This supports the conclusion that this is related to phase separation, as this is only ever observed for mixed halide samples. However, the $x = 1.6$ sample shows a distinct peak in this region. This is likely desorption from a tetra-ammoniate phase, as this sample is 80% chloride.

A clear trend in these data is the correlation between the x value and the temperature of the octa-ammoniate desorption. As expected, a higher x value gives greater desorption temperatures for the octa-ammoniate phase. Similarly, a greater x value gives lower desorption temperatures for the mono-ammoniate desorption, as would be expected. A similar trend is observed for the di-ammoniate desorption. However, the presence of double peaks is not clear, as might be expected after analysis of Figure 5.14. The $x = 0.4$ sample does appear to show a shoulder at low temperature, likely due to desorption from the *Cmmm* phase. It is currently unclear why double peaks/shoulders are not always clearly present in the di-ammoniate desorptions of these samples. It is possible that the peaks overlap to the extent that they are not clearly separable, though this would also be expected to appear in Figure 5.13.

The desorption at ∼100 °C (the exact temperature depends on sample composition) is another area of complexity, which does not show clear correlations with the halide ratio. Two distinct peaks are observed in the $x = 0.8$ sample, while only one is observed for other samples. This double peak appears at almost identical temperature to that seen in the CaClBr STA and again may be related to incomplete phase separation.

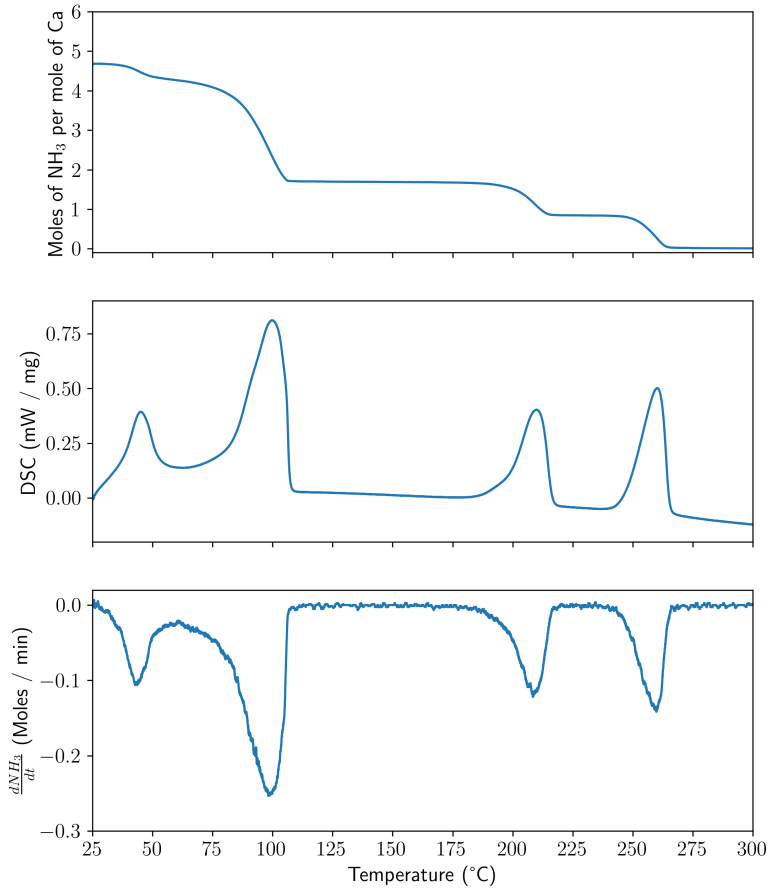


Figure 5.15: STA of $CaCl_{0.4}Br_{1.6}$ ammonia desorption. From 60–80 °C a region of constant ammonia desorption is seen, as was commonly (and only) observed for mixed samples. Ramp rate = 2 K / min. Gas flow = 40 sccm NH_3, 20 sccm Ar (i.e. P_{NH_3} = 0.67 bar).

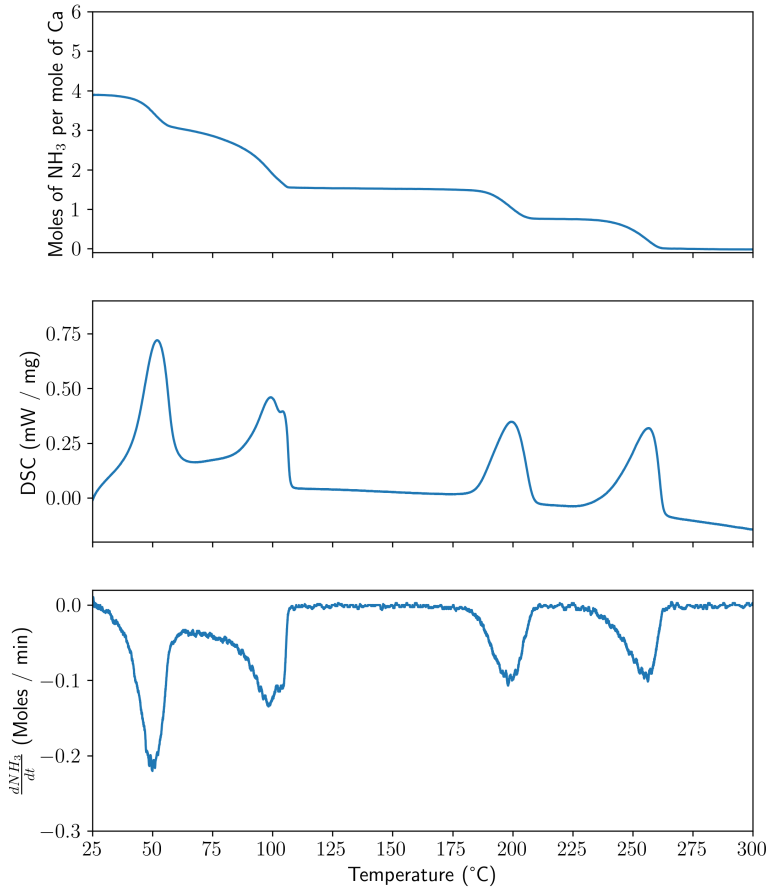


Figure 5.16: STA of $CaCl_{0.8}Br_{1.2}$ ammonia desorption. From 60–80 °C a region of constant ammonia desorption is seen, as was commonly (and only) observed for mixed samples. Ramp rate = 2 K / min. Gas flow = 40 sccm NH_3, 20 sccm Ar (i.e. P_{NH_3} = 0.67 bar).

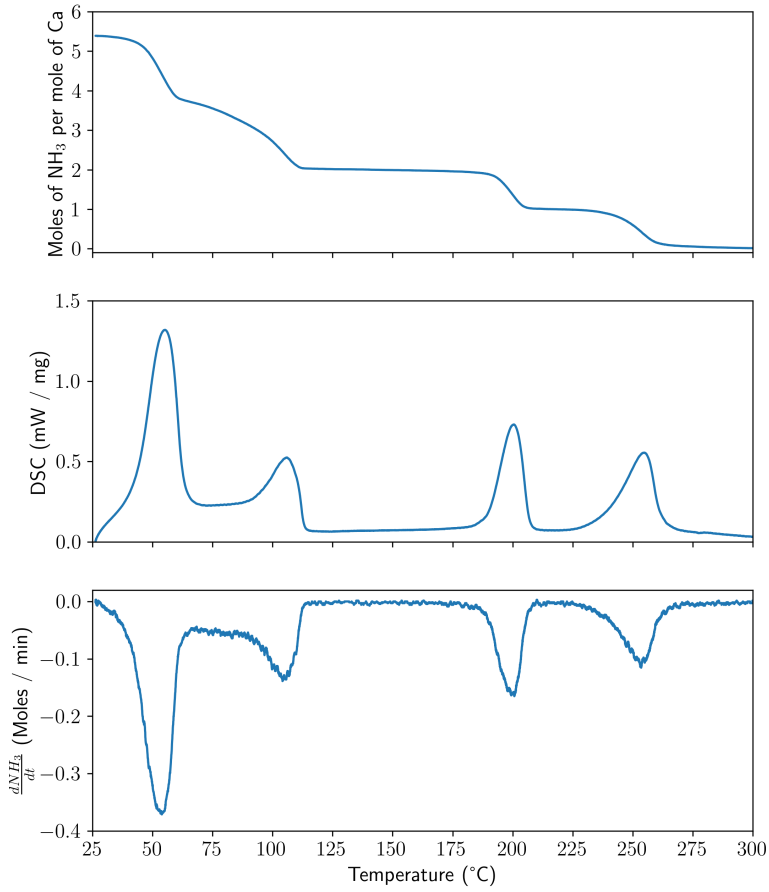


Figure 5.17: STA of $CaCl_{1.2}Br_{0.8}$ ammonia desorption. From 60–80 °C a region of constant ammonia desorption is seen, as was commonly (and only) observed for mixed samples. Ramp rate = 2 K / min. Gas flow = 40 sccm NH_3, 20 sccm Ar (i.e. P_{NH_3} = 0.67 bar).

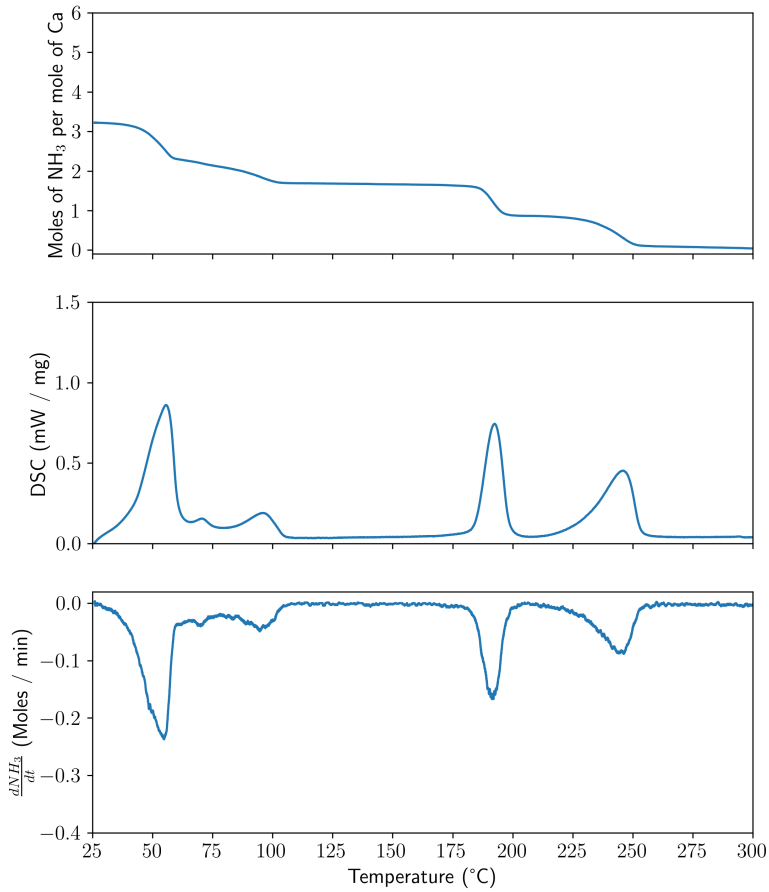


Figure 5.18: STA of $CaCl_{1.6}Br_{0.4}$ ammonia desorption. Ramp rate = 2 K / min. Gas flow = 40 sccm NH_3, 20 sccm Ar (i.e. P_{NH_3} = 0.67 bar).

It is likely that the desorption events observed are very sensitive to the amount of ammonia in the sample and also the morphology of the sample. This, in turn, makes it difficult to deduce the exact nature of these desorptions. Figure 5.19 shows these mixed halide STAs plotted on the same graph in order to assist with visual analysis.

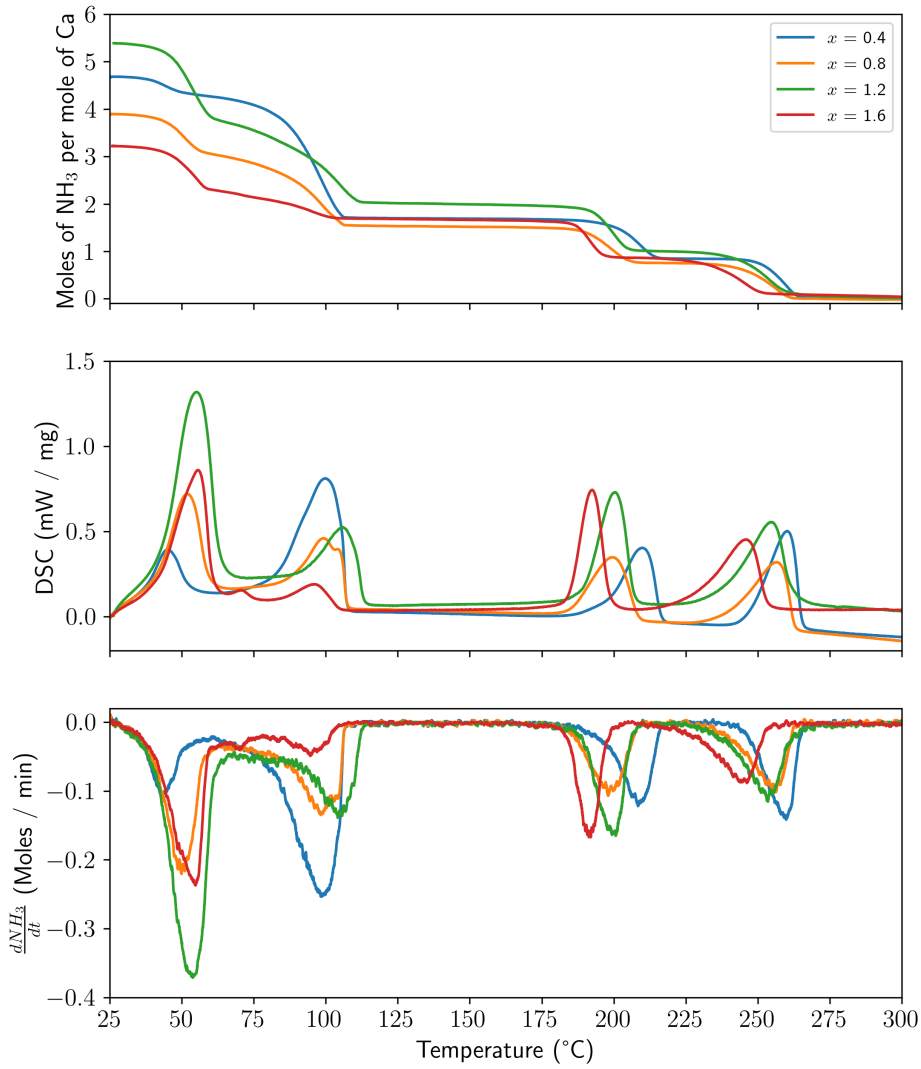


Figure 5.19: Ammonia desorption STAs of $x = 0.4$, 0.8, 1.2 and 1.6 samples. Ramp rate = 2 K / min. Gas flow = 40 sccm NH_3, 20 sccm Ar (i.e. $P_{NH_3} = 0.67$ bar).

5.3 *In-Situ* Powder Neutron Diffraction

Alongside pure $CaCl_2$ and $CaBr_2$ (Section 4.3), a sample of CaClBr (i.e. $x = 1$ in $CaCl_xBr_{2-x}$) was also examined on the POLARIS diffractometer at ISIS Neutron and Muon Source under flowing ND_3 gas, in order to understand the sorption pathways followed.

Figure 5.20 shows all *in-situ* powder neutron diffraction data for the CaClBr sample from POLARIS banks 3 and 4.

Figures B.12 and 5.21 show the weight and mole percent of each phase throughout the experiment. Weight and mole percents were calculated assuming a 1:1 ratio of chloride to bromide in all ammoniate phases, though it is important to recognise this will not be perfectly accurate. Unfortunately, data quality was not sufficient to refine occupancies of halides (which show low coherent neutron scattering factors) accurately.

Initial absorption at room temperature shows the presence of only small amounts of hexa-ammoniate on the path to the octa-ammoniate. The mono-ammoniate and octa-ammoniate are the only ammoniate structures adopted by both $CaCl_2$ and $CaBr_2$, and as such it is not surprising to see intermediate phases bypassed. If intermediate phases such as the di- or hexa-ammoniates form briefly, the instability associated with the presence of both chloride and bromide ions in these phases would likely lower the activation energy to further absorption, explaining why these phases are never observed in great quantities in the data for the absorption period.

During the experiment, no tetra-ammoniate phase was observed, with desorption from the octa-ammoniate phase forming the hexa-ammoniate and the *Cmmm* di-ammoniate. While the octa-ammoniate was considered single phase with mixed halides, rapid halide separation must occur during the desorption process in order to effectively phase separate.

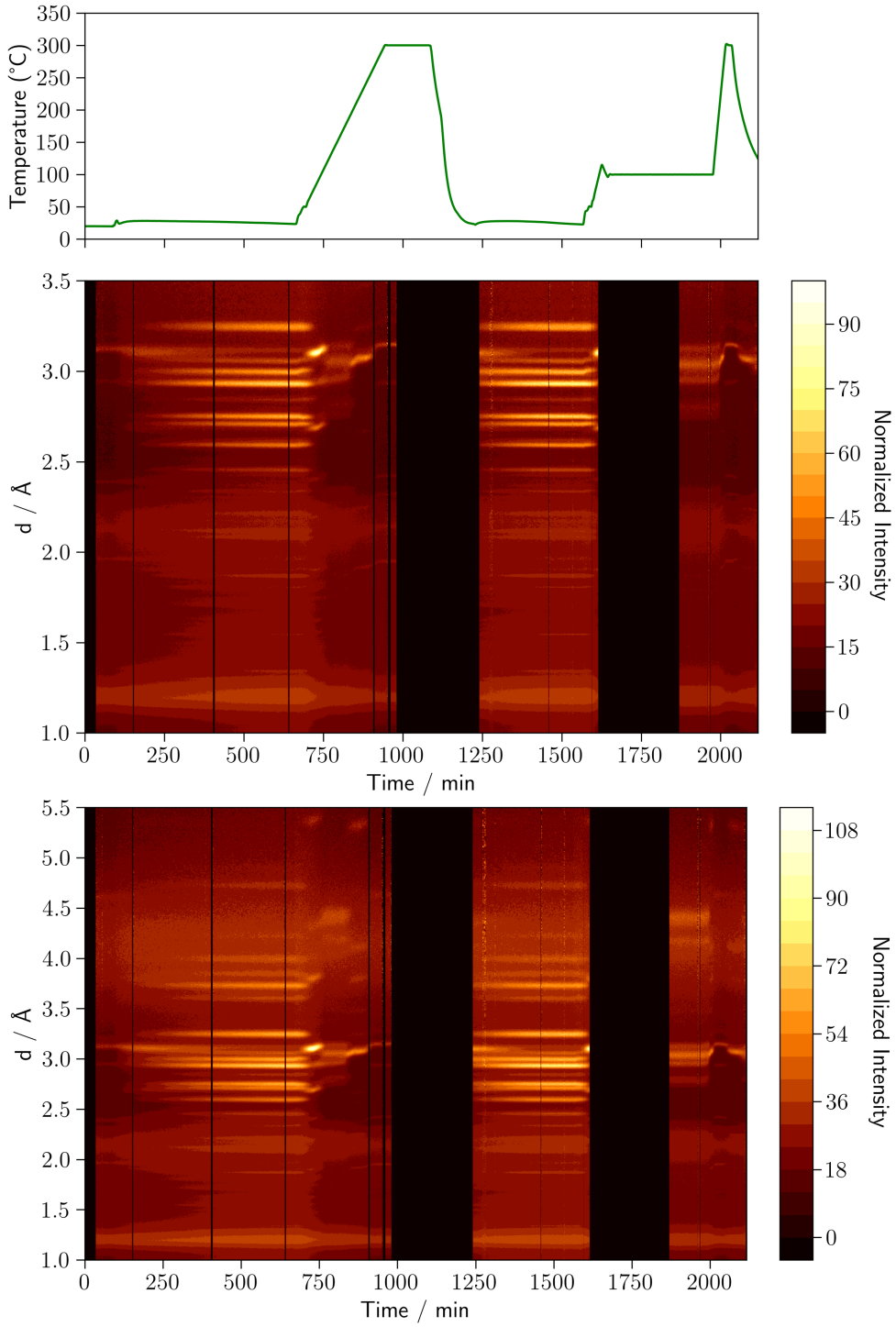


Figure 5.20: A contour plot of all PND data for CaClBr from POLARIS bank 3 (bottom) and bank 4 (middle). The top plot shows the corresponding temperature. It is clear to see the phase transitions upon heating to 300 °C. Black sections correspond to periods where the beam was down.

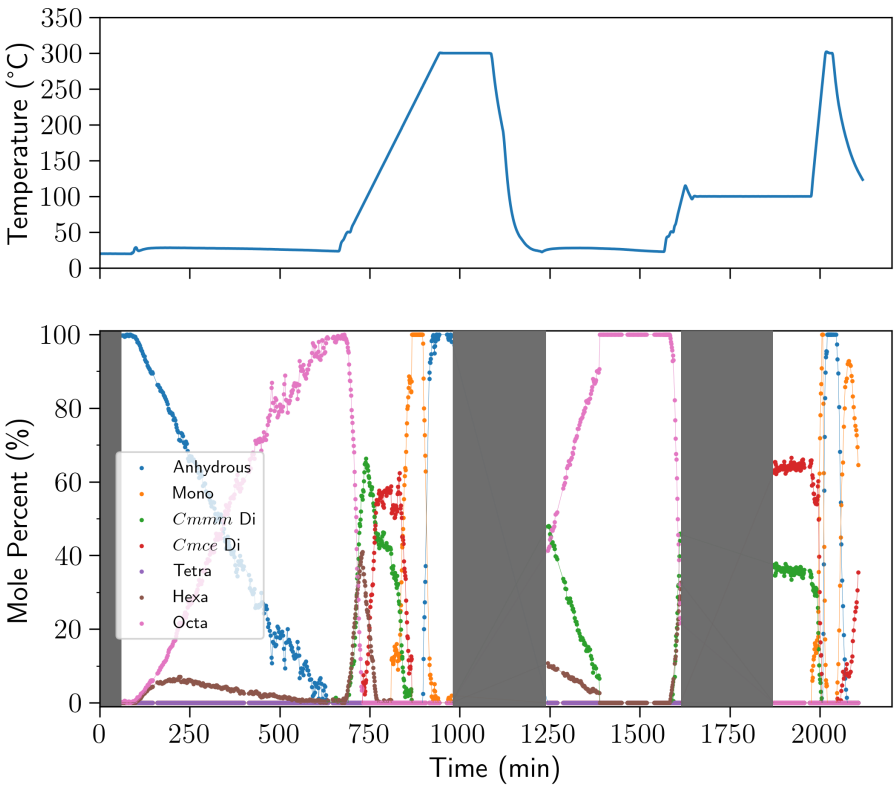


Figure 5.21: Mole percent of phases in CaClBr PND data calculated through Rietveld analysis. Note the presence of both di-ammoniate phases, suggesting decomposition of the solid solution and separation of chloride and bromide ions.

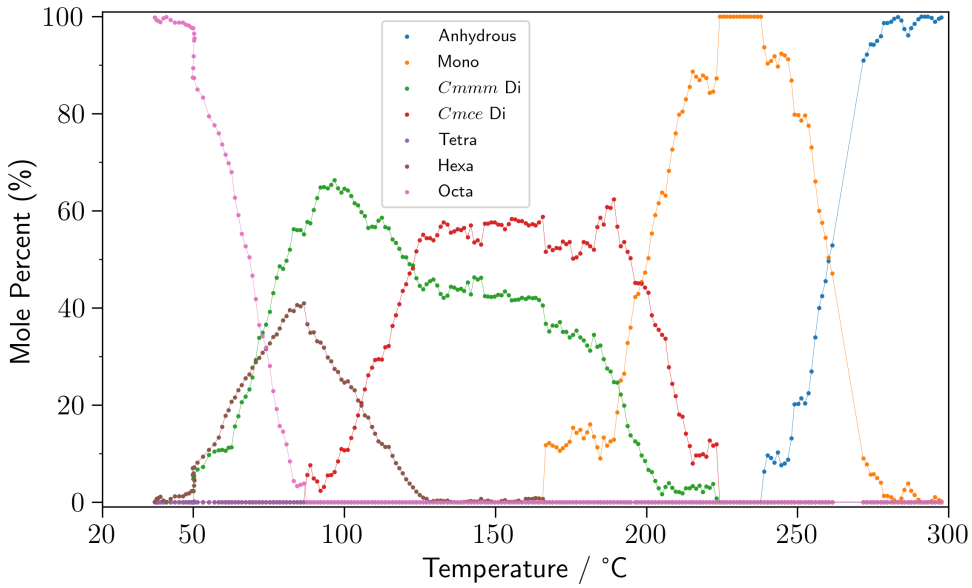


Figure 5.22: Mole percent of phases in the CaClBr PND data during the first temperature ramp. Note the presence of the hexa-ammoniate phase and the *Cmmm* di-ammoniate phase simultaneously from 50–100 °C, and the presence of the *Cmce* di-ammoniate phase and *Cmmm* di-ammoniate phase from 100–200 °C. Given that the octa-ammoniate and mono-ammoniate phases were only ever observed to be single phase, this shows the rapid destruction and formation of solid solutions by this system.

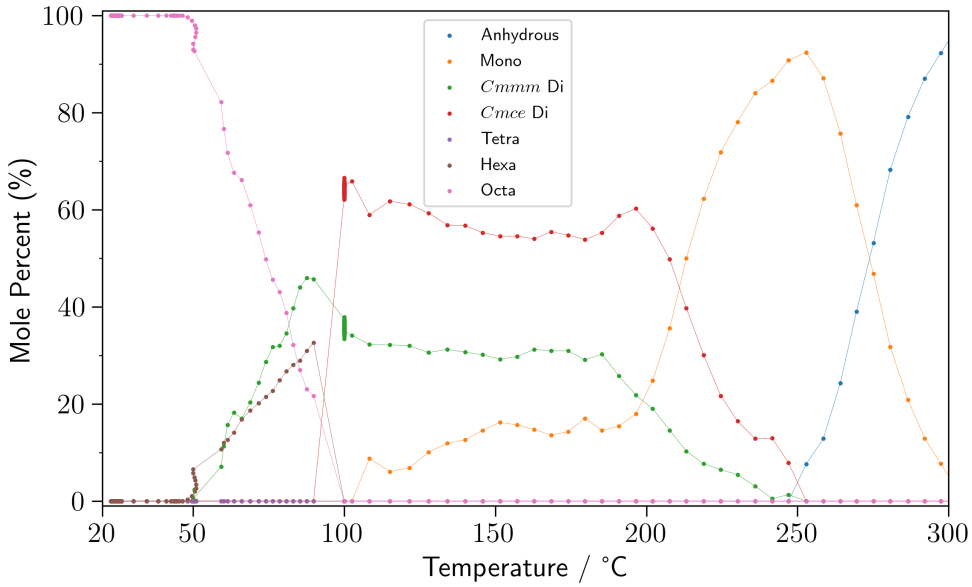


Figure 5.23: Mole percent of phases in the CaClBr PND data during the second temperature ramp. A 3 hour 'beam down' period interrupted this temperature ramp. During this time, the temperature was dwelled at 100 °C before continuing. Note the presence of the hexa-ammoniate phase and the *Cmmm* di-ammoniate phase simultaneously from 50–100 °C, and the presence of the *Cmce* di-ammoniate phase and *Cmmm* di-ammoniate phase from 100–200 °C. Given that the octa-ammoniate and mono-ammoniate phases were only ever observed to be single phase, this shows the rapid destruction and formation of solid solutions by this system.

Desorption of the di-ammoniate phases consists of inital desorption from the *Cmmm* di-ammoniate phase, which will be a majority chloride phase, followed by desorption of the *Cmce* di-ammoniate phase, a majority bromide phase. This leads to rapid expansion of the mono-ammoniate phase, as shown by the (131) reflection in Figure 5.24. Expansion is primarily due to the changing halide ratio prior to 860 minutes, and once all *Cmce* di-ammoniate has vanished, remaining expansion is simply thermal (shown by the change in gradient of the maximum intensity). It should be noted that the onset temperature of the *Cmce* $2 \rightarrow 1$ transition is significantly lower than observed for the pure $CaBr_2$ sample. As established from the mono-ammoniate expansion and volumes of each di-ammoniate phase, this *Cmce* phase is primarily bromide. As the mono-ammoniate allows for favourable mixing of halide ions, the increased stability of this phase appears to be the origin of the reduction in onset temperature. This is consistent with the results observed from STA data in Section 5.2. A similar magnitude of volume expansion was seen in the second temperature cycle. However, the greater ramp rate led to the lack of a clear separation between thermal and halide-related expansion, with the mono-ammoniate phase beginning decomposition before all di-ammoniate phase had decomposed, preventing effective separation of the two expansion effects.

It should be noted that at no time were two distinct mono-ammoniate phases observed in the PND patterns. Alongside the observation of a lower desorption temperature for the *Cmce* di-ammoniate phase, believed to be driven by the possibility of solid solution formation in the mono-ammoniate, this suggests that halide migration to form and destroy solid solutions is extremely rapid.

A similar stability effect is seen for the octa-ammoniate of CaClBr. Significant desorption is not seen until around 50 °C for the CaClBr octa-ammoniate, noticeably higher than observed for either $CaCl_2$ or $CaBr_2$ (42 and 40 °C respectively). This is likely due to an increased stability of the mixed phase, based on the greater entropy of disordering halides.

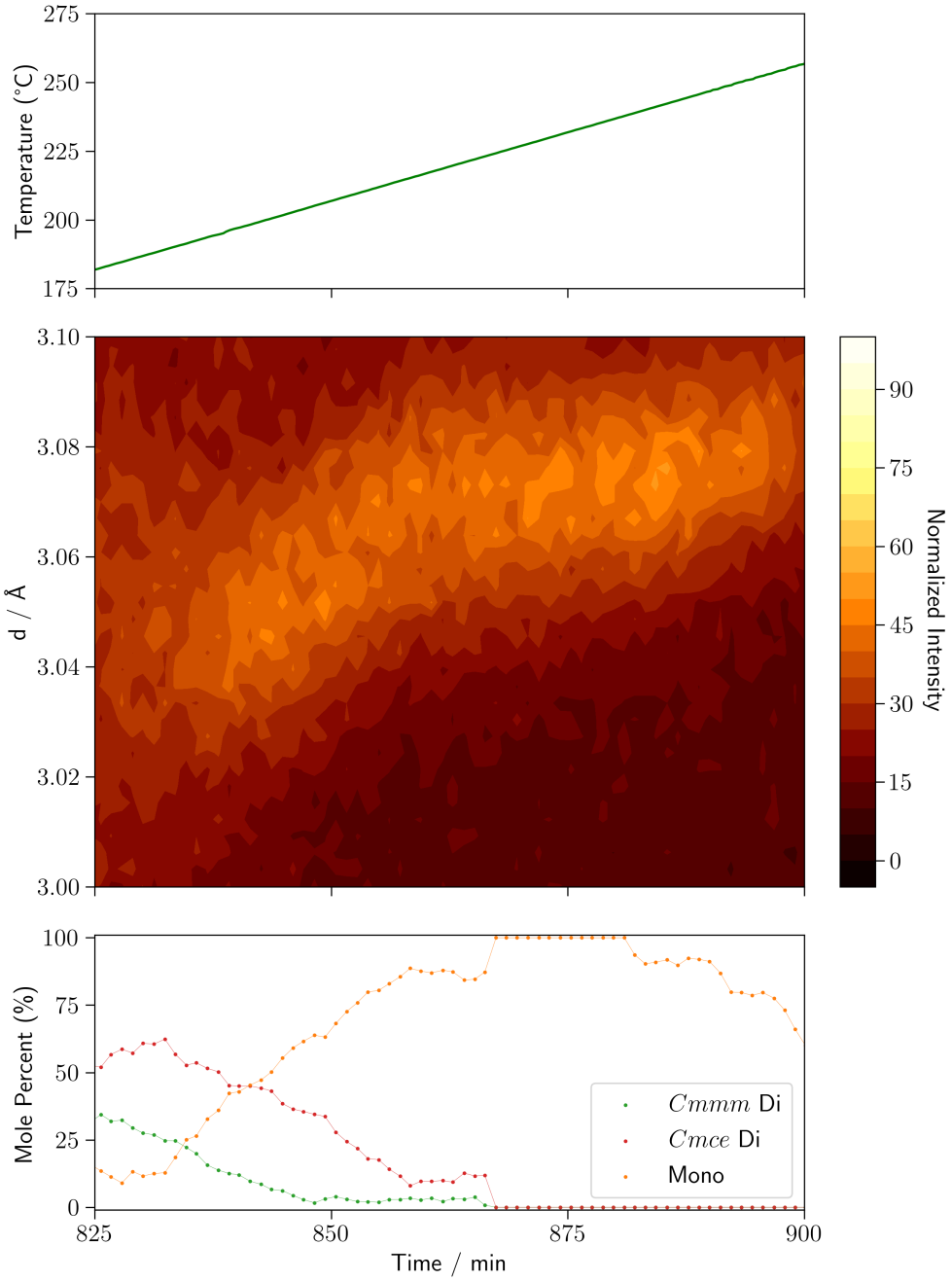


Figure 5.24: Expansion of the CaClBr mono-ammoniate during di-ammoniate desorption in the first temperature cycle. The reflection depicted is the (131) reflection (the most intense reflection) of the mono-ammoniate phase. Initial expansion is due to incorporation of bromide ions into the phase (as the *Cmce* di-ammoniate desorbs), while subsequent expansion (860 minutes onwards) is simply thermal.

Desorption from the CaClBr mono-ammoniate phase is approximately a linear interpolation of the desorption from the $CaCl_2$ and $CaBr_2$ mono-ammoniate. The results seen here for di-ammoniate and mono-ammoniate desorption map well onto those observed previously for gas flow and STA data in Section 5.1. In particular, this explains the intricate nature of Figure 5.8. Desorption onset temperatures largely remain unchanged across the series, as the value recorded was representing the desorption from the *Cmmm* di-ammoniate (when it was present). After the *Cmmm* di-ammoniate phase desorbs, the *Cmce* di-ammoniate becomes unstable with respect to the formation of a mixed halide mono-ammoniate phase. The exact peak desorption temperature in this figure is a function of desorption from both phases, but remains largely unchanged at high and middle x values as the *Cmce* di-ammoniate phase favours desorption at a lower temperature when in the presence of chloride ions (due to the possibility of formation of a mixed mono-ammoniate phase).

Desorption from the mono-ammoniate phase represents a linear interpolation as both mono-ammoniate and anhydrous phases are mixed, and hence the mono-ammoniate phase gains no clear extra stability as a result of mixing halides. The usual effects discussed in Section 4.2 are then observed.

STA data presented in Figure 5.19 shows desorption occurring continuously from 40 °C through to over 100 °C. This was previously hypothesised as related to the presence of chloride in a hexa-ammoniate phase, which subsequently shows desorption equivalent to the rate at which the halides can separate in this phase. This appears consistent with the PND data of CaClBr, which shows desorption from the hexa-ammoniate phase immediately after the octa-ammoniate has fully decomposed. Similarly, the onset temperature for the hexa-ammoniate desorption is recorded as 89 °C for CaClBr, significantly lower than the 104 °C observed for $CaBr_2$. It is likely this is an effect of hysteresis, where the material has not yet sufficiently 'halide-

Table 5.1: $CaClBr(NH_3)_n$ desorption onset temperatures based on change in mole percentage from PND data. Absorption onset temperatures are also given for the cooldown observed. The ramp rate for cycle 1 was 1 °C per minute, while that of cycle 2 was 5 °C per minute (due to time constraints). This is reflected in the greater observed desorption temperatures of cycle 2.

Event	Onset Temperature 1 (°C)	Onset Temperature 2 (°C)
$8 \rightarrow 6/2$	49(1)	50(1)
$6 \rightarrow Cmce$ 2	89(1)	
$Cmmm$ 2 $\rightarrow$ 1	183(1)	188(1)
$Cmce$ 2 $\rightarrow$ 1	191(1)	199(1)
$1 \rightarrow 0$	249(1)	256(1)
$0 \rightarrow 1$		236(1)
$1 \rightarrow Cmce$ 2		158(1)

separated' after desorption from the halide-mixed octa-ammoniate, and as such, chloride ions remain 'trapped' in the hexa-ammoniate phase. The presence of these chloride ions then lower the temperature stability of the hexa-ammoniate phase.

Figure 5.25 shows the (222) reflection as the hexa-ammoniate desorbs. Initial expansion as the hexa-ammoniate phase forms is likely thermal. However, while subtle, the gradient of the maximum intensity against time slightly changes as the hexa-ammoniate begins to lose ND_3 (∼730 mins). Formation of the *Cmce* di-ammoniate phase is also occurring in this region. This is hypothesised to be related to desorption initially occurring from regions of the hexa-ammoniate phase with a chloride proportion above that which is stable. However, the chloride proportion which is stable will change with temperature, explaining the long, slow desorption from 50–100 °C seen in this experiment and Figure 5.13. This would explain both the expansion

of the hexa-ammoniate, and the formation of the *Cmce* phase. The separation of halides immediately after octa-ammoniate desorption is clearly not sufficient to prevent early decomposition of bromide-containing hexa-ammoniate phases.

Figures 5.26 and 5.27 show the PND data and fits for the CaClBr octa- and mono-ammoniate phases respectively. Both patterns showed good fitting ($\chi^2 = 2.39$ and 1.20 respectively) to single phases with chloride and bromide occupancies of 0.5 on each site. While the coherent scattering cross sections of chloride and bromide are not large, the observation of satisfactory fitting to a single set of lattice parameters and space group suggests successful formation of solid solutions for both phases.

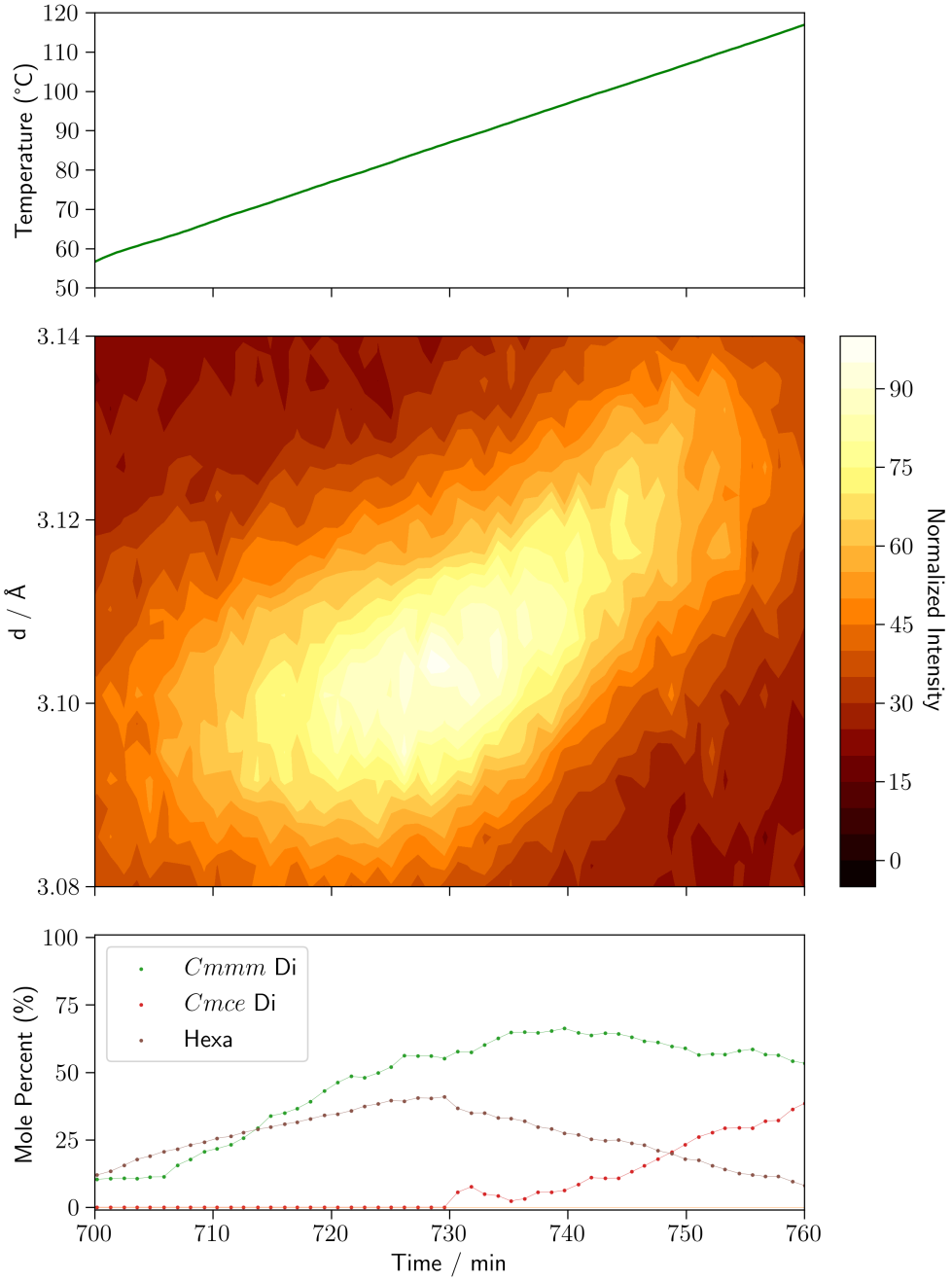


Figure 5.25: Expansion of the CaClBr hexa-ammoniate phase during desorption in the first temperature cycle. The reflection depicted is the (222) reflection (the most intense reflection) of the hexa-ammoniate. Similar to Figure 5.24, the change in the gradient of expansion could indicate switches between thermal expansion and halide-induced expansion.

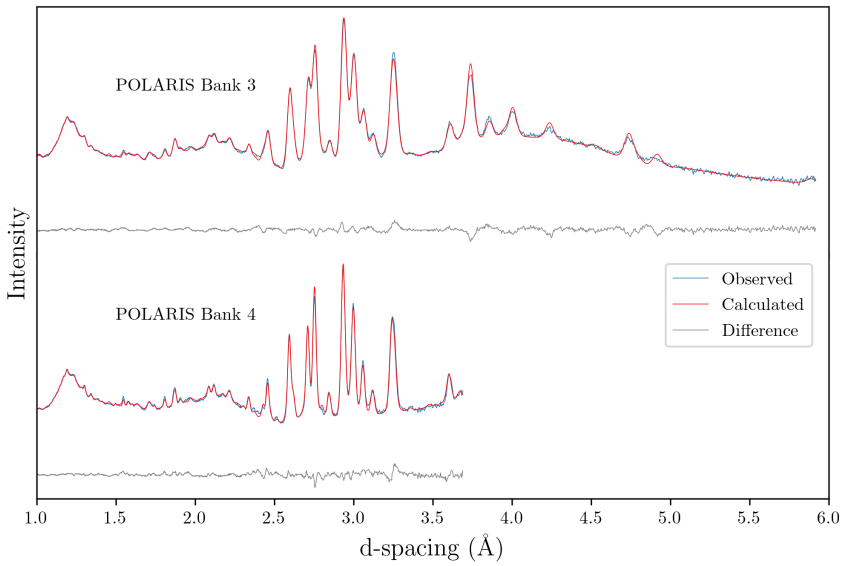


Figure 5.26: PND data of $CaClBr(ND_3)_8$ fitted to a single *Pnma* octa-ammoniate phase, indicating stable solid solution formation. $\chi^2 = 2.39$.

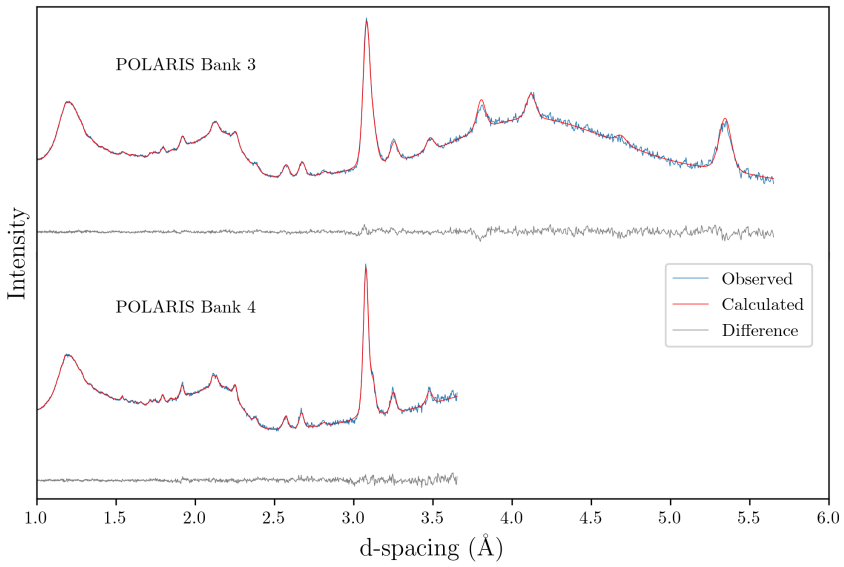


Figure 5.27: PND data of $CaClBr(ND_3)$ fitted to a single $Cmc2_1$ mono-ammoniate phase, indicating stable solid solution formation. $\chi^2 = 1.20$.

5.4 Conclusions and Future Work

$CaCl_xBr_{2-x}$ phases show complex ammonia absorption properties, studied primarily by *in-situ* PND and STA. Computational evidence suggests that mixing enthalpies of individual phases are minimal, particularly for ammoniate phases. As such, solid solutions are stable for mono-ammoniate and octa-ammoniate phases across the full compositional range, but unstable for large regions of the compositional spectrum when solid solution formation would entail a change in crystal structure or ammoniation number. The increased entropy associated with halide mixing in solid solutions of octa- or mono-ammoniate leads to phase stability over a wider temperature range than might be expected. Alongside this, the decomposition temperature of the mono-ammoniate can be controlled effectively via a change in halide composition as both the mono-ammoniate and anhydrous phase comfortably form solid solutions.

Phase separation is observed for the mixed phases between the regions of mono- and octa-ammoniate stability. Evidence suggests that all ammoniate phases may be stable at high and low x values, allowing for slight modification of desorption temperatures, enthalpy changes and absorption rates. Importantly, mixed halide samples did not appear to suffer from stability issues as a result of halide mixing, with facile separation and recombination of halides depending on the current ammoniation number of the sample.

It is important to note that there was no particular evidence that the mixed calcium halide systems were unique. While no work was carried out on mixed-halide systems of other metal halide ammoniates, the results suggest that halide-based solid solutions of metal halide ammoniate phases will be stable if the individual metal halide ammoniates adopt the same crystal structure. As such, further work could be undertaken to examine the mixing of metal halides which show the same phase transitions in a desired pressure-temperature region. For example, many metal halides (such as MgX_2 and MnX_2) form a hexa-ammoniate as their highest

ammoniate phase, and, based on the evidence here, halide-based mixtures of these metal halides would likely form a hexa-ammoniate solid solution. The opportunity to control the onset temperature and enthalpy change of the hexa-ammoniate desorption via a change in halide composition could have a significant impact on the use of these ammoniate materials for thermal energy storage.

6

Eutectic Mixtures

Ammonia, as the feedstock for inorganic fertilisers, is of prime global importance in providing food worldwide. Despite recognition of its potential to be the carbon-free replacement for fossil fuels, future ammonia synthesis on a global scale must be provided by intermittent renewable energy. Among the principal technical challenges, the synthesis of ammonia at lower temperatures and pressure is at the forefront. Ammonia sorbents can have a key role in achieving this challenge.

Ammonia sorbents can be used in the Haber-Bosch process to separate ammonia from unreacted nitrogen and hydrogen. The use of a sorbent allows this separation process to occur at higher temperature than separation by condensation, reducing the energy usage for cooling and subsequent heating of recycled gases. Metal halide salts such as $MgCl_2$, $CaCl_2$ and $MnCl_2$ have been candidates for study[60,104,64]. The

commonly suggested approach is to use a batch process, consisting of two sorbent chambers operating in opposite modes; chamber 1 is receiving gas from the reactor (on-line mode) while chamber 2 is releasing pure ammonia (regen mode). The two chambers then switch modes at an appropriate time, with gas flow from the reactor directed to chamber 2. This is illustrated in Figure 6.1 (from Smith *et al.*[63]).

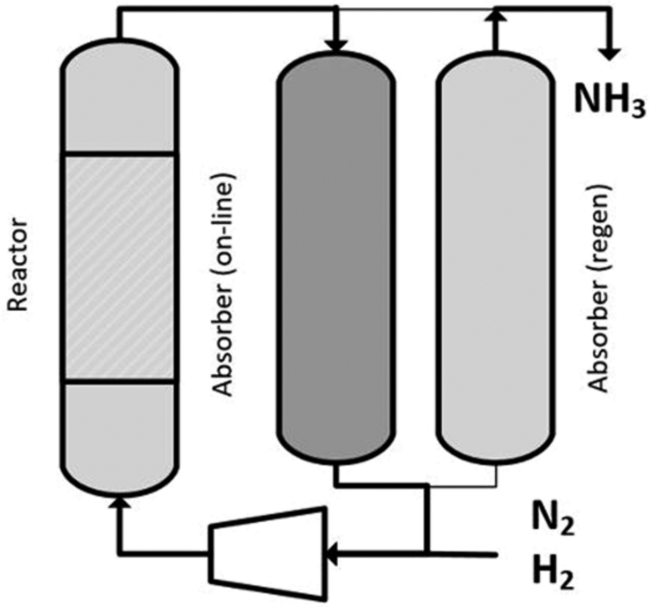


Figure 6.1: The suggested ammonia separation procedure using ammonia sorbents. One absorber is on-line while the other is undergoing regeneration. After this process is complete, the processes are switched. Figure adapted from Smith *et al.*[63]

Liquid[79,80,81,82,83,84,85] and slurry based[136] ammonia sorbents have been studied also for ammonia absorption at low temperature, commonly showing vastly improved rates of absorption when compared with solids due to faster diffusion coefficients and better thermal conductivity. Unfortunately, these are not suitable for ammonia absorption from the Haber process due to the low boiling points of the solvents used.

Mixing metal halide salts results in a significant reduction in melting point, taking advantage of the properties of eutectic mixtures. While liquid metal halides will be viscous at low temperatures, this opens up the possibility of the sorbent being pumped, potentially turning a batch absorption process into a continuous one,

without the requirement of recycling gases. However, for gas recycling to be fully retired, the absorption process would be required to occur at the same temperature and pressure as the reaction (∼400 °C and ∼20 bar P_{NH_3}). A suggestion for how this process might look is shown in Figure 6.2. If the molten salt used does not work sufficiently at Haber process conditions then a secondary chamber for absorption could be used. This would still be a continuous process, but would require gas recycling.

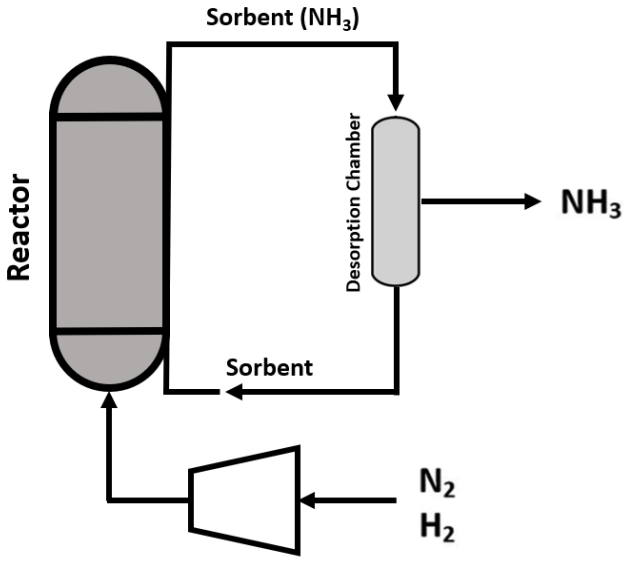


Figure 6.2: The suggested ammonia separation procedure using liquid ammonia sorbents. Sorbent is recycled continuously. This enables a continuous process, as opposed to the batch process depicted in Figure 6.1.

While molten metal halide mixtures have been well studied for other applications, such as latent heat storage in concentrated solar power (CSP) plants, there has been no investigation into their use for ammonia absorption applications at high temperature. This chapter examines the possibility of molten metal halide salts for ammonia separation from the Haber process.

6.1 Thermodynamics of Molten Salt Ammonia Absorption

Figure 6.2 shows a Hess cycle for absorption into a molten metal halide salt. It should be noted that this Hess cycle accounts only for a single metal. The Hess cycle for a eutectic mixture requires the addition of mixing enthalpies and entropies for both the anhydrous molten salts and the ammoniated molten salts. However, the mixing enthalpies and entropies are likely to be of little relevance compared with melting and gas releases, and thus can be considered as a small perturbation. It is also important to recognise that a liquid sorbent no longer requires integer amounts of ammonia, and so the Hess cycle (in which integer amounts of ammonia are depicted) should be understood to be a guide to the ammonia absorption abilities of molten salts.

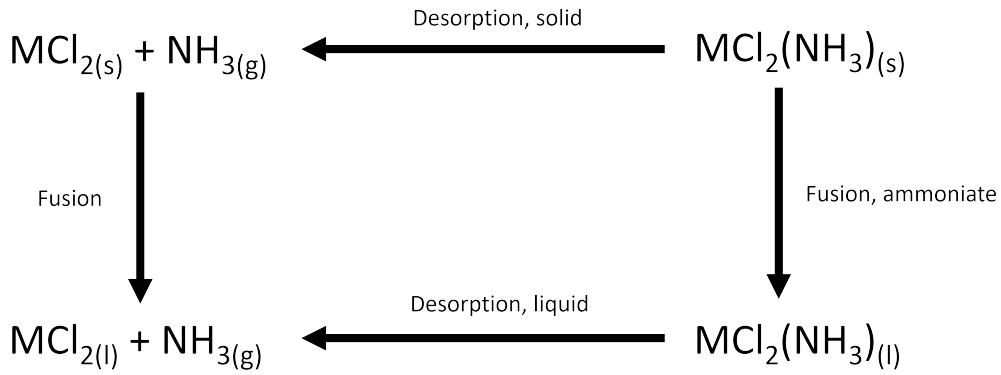


Figure 6.3: Hess cycle showing absorption into a molten metal halide salt.

Starting from the Hess cycle in Figure 6.3:

$$\Delta H_{\text{des, l}} = \Delta H_{\text{des, s}} + \Delta H_{\text{fus}} - \Delta H_{\text{fus, amm}} \tag{6.1}$$

$$\Delta S_{\text{des, l}} = \Delta S_{\text{des, s}} + \Delta S_{\text{fus}} - \Delta S_{\text{fus, amm}} \tag{6.2}$$

It should be noted that all ΔS and ΔH values are positive.

Using $\Delta G = \Delta H - T\Delta S = 0$ at the point of equilibrium:

$$T_{\text{des, l}} = \frac{\Delta H_{\text{des, s}} + \Delta H_{\text{fus}} - \Delta H_{\text{fus, amm}}}{\Delta S_{\text{des, s}} + \Delta S_{\text{fus}} - \Delta S_{\text{fus, amm}}} \tag{6.3}$$

Division through by ΔS_{fus} gives:

$$T_{\text{des, l}} = \frac{\frac{\Delta H_{\text{des, s}}}{\Delta S_{\text{fus}}} + T_{\text{fus}} - \frac{\Delta H_{\text{fus, amm}}}{\Delta S_{\text{fus}}}}{\frac{\Delta S_{\text{des, s}}}{\Delta S_{\text{fus}}} + 1 - \frac{\Delta S_{\text{fus, amm}}}{\Delta S_{\text{fus}}}} \tag{6.4}$$

If γ_1 is defined as $\frac{\Delta H_{\text{des, s}}}{\Delta H_{\text{fus}}}$ and γ_2 is defined as $\frac{\Delta H_{\text{fus, amm}}}{\Delta H_{\text{fus}}}$, then using fraction multiplication:

$$\frac{\Delta H_{\text{des, s}}}{\Delta S_{\text{fus}}} = \frac{\Delta H_{\text{des, s}}}{\Delta H_{\text{fus}}} \frac{\Delta H_{\text{fus}}}{\Delta S_{\text{fus}}} = T_{\text{fus}}\gamma_1 \tag{6.5}$$

$$\frac{\Delta S_{\text{fus, amm}}}{\Delta S_{\text{fus}}} = \frac{\Delta S_{\text{fus, amm}}}{\Delta H_{\text{fus, amm}}} \frac{\Delta H_{\text{fus}}}{\Delta S_{\text{fus}}} \frac{\Delta H_{\text{fus, amm}}}{\Delta H_{\text{fus}}} = \frac{T_{\text{fus}}\gamma_2}{T_{\text{fus, amm}}} \tag{6.6}$$

Applying these fraction multiplications throughout yields:

$$T_{\text{des, l}} = \frac{T_{\text{fus}}(1 + \gamma_1 - \gamma_2)}{1 + \frac{T_{\text{fus}}}{T_{\text{des, s}}}\gamma_1 - \frac{T_{\text{fus}}}{T_{\text{fus, amm}}}\gamma_2} \tag{6.7}$$

This equation enables the calculation of the temperature of desorption from the molten salt in terms of other parameters. Assumptions should be made to simplify the exploration of the parameter space. Firstly, even for a high melting point salt such as $CaCl_2$, the enthalpy of fusion does not reach values shown by the first absorption enthalpies (typically around 80 kJ/mol). As such, it can be assumed that $\gamma_1 > 1$. The value of γ_2 is, however, less clear. It should be noted that the enthalpy of fusion of the monohydrate of calcium chloride has been reported as significantly lower than the enthalpy of fusion of the pure salts (17.3 vs 28.6 kJ/mol)[137].

However, while hydrates and ammoniates have many similarities in their bonding, they are by no means identical. Given the significantly lower melting temperature of ammonia compared to water (-78 vs. 0 °C), it may appear likely that

ammoniates have even lower melting points than hydrates. However, it should be noted that the melting point of $CaCl_2(H_2O)_6$ is reported as 24–30 °C[137,138,139], and 45.3 °C for $CaCl_2(H_2O)_4$[137]. Given that desorption temperatures for $CaCl_2(NH_3)_8$ and $CaCl_2(NH_3)_4$ were observed to be 42 °C and 66 °C respectively at 1 bar in the *in-situ* PND experiments (Table 4.15) and melting of the material was not observed, it is likely that ammoniates typically show slightly greater melting points than hydrates. Generalisation is difficult without melting point data of a range of metal halide ammoniates. However, this may relate to the use of water's second lone pair in hydrogen bonding upon melting, while ammonia does not gain this extra hydrogen bond upon a melting transition.

A conservative approach is thus to assume that $0.5 < \gamma_2 < 1.2$. It is also reasonable to assume that $T_{\text{fus, amm}} < T_{\text{fus}}$, as is supported by chemical intuition and experimental observations[140,137], including the observation in this work of deliquescence at 4.5 bar ammonia pressure for $CaBr_2$.

Figure 6.4 shows a colour map of $T_{\text{des, l}}$ for parameters chosen to be reasonable for $ZnCl_2$. The primary takeaway from this data is that for all reasonable values of each parameter, $T_{\text{des, l}} > T_{\text{des, s}}$. This was seen throughout various iterations. Further exploration of the parameter space showed that $T_{\text{des, l}} > T_{\text{des, s}}$ when $T_{\text{fus, amm}} < T_{\text{fus}}$. If $T_{\text{fus, amm}} > T_{\text{fus}}$ then $T_{\text{des, l}} < T_{\text{des, s}}$, though it should again be noted that the melting point of ammoniates is known to be lower than that of the anhydrous salt. Figures 6.4, C.1 and C.2 illustrate these points. In simple terms, $T_{\text{fus, amm}} < T_{\text{fus}}$ indicates greater stability of the liquid phase for the ammoniate, which in turn indicates an increased favourability for ammonia to absorb into a liquid phase. The reverse is true when $T_{\text{fus, amm}} > T_{\text{fus}}$.

While integer amounts of ammonia are not required in a liquid phase, this is instructive in informing about the likelihood of observing ammonia absorption at Haber process conditions. Molten salts indicate one mechanism by which to raise the

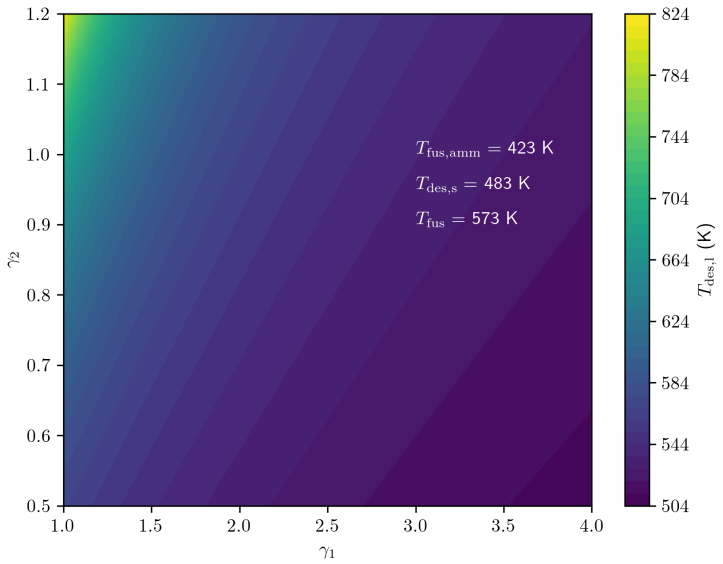


Figure 6.4: Colour map showing $T_{\mathrm{des,\,l}}$ values as a function of γ_1 and γ_2 for selected $T_{\mathrm{des,\,s}}$, $T_{\mathrm{fus,\,amm}}$ and T_{fus} values. Values were chosen to be approximately correct for $ZnCl_2$, which has a known liquid ammoniate phase[140], at 1 bar ammonia pressure.

temperature at which significant absorption is observed, both through the thermodynamic preference for ammonia to absorb into a liquid phase, and by the possibility of sub-stoichiometric absorption.

6.2 Ammonia Absorption into Molten Salt Mixtures

There are a number of aspects to consider in the production of a molten salt which absorbs ammonia at elevated temperatures. The temperature of the desired application must be above the melting point of the sample to ensure that the sample remains molten throughout usage. However, a very high temperature could lead to a significant vapour pressure and evaporation from the sample. As such, it is ideal for the application temperature to be slightly above that of the melting point of the mixture. As mentioned in Section 2.5, materials must be affordable, abundant and easily accessible if they are to be used widely. A final consideration is the possibility that the materials may nitride. Many group II and transition metals nitride. However, this usually only occurs at high temperature ($> 600\,^{\circ}\mathrm{C}$) when reacting with the pure metal, rather than the metal chloride. Table 6.1 shows the elemental abundances, melting points, boiling points, ammonia absorption ability and possibility of nitridation for various metal chlorides that were considered for this work.

Any metal chlorides that would almost certainly nitride during usage (Fe, Co, Ni) were avoided, alongside those with insufficient boiling points such as Al or Ga. While many elements in the table do form stable nitrides, these are commonly synthesised from the pure metal at high temperatures. It is unlikely that nitridation would occur for most of these metal chlorides as no evidence has previously suggested decomposition of the ammoniates into the nitride phase (except for Cr, Fe, Co, Ni). Initially, zinc chloride was used, despite its low elemental abundance, as the only metal chloride with both a low melting point and a high boiling point. Magnesium, calcium and manganese chlorides were also identified as viable, though would require modification of melting points via the use of eutectic mixtures. Sodium and potassium chloride, while not ammonia absorbers, were viewed as potential additives to adjust the melting point of metal chloride mixtures. It should be noted that the

Table 6.1: Only lighter metals (period 4 or higher) were considered in order to limit the mass required for subsequent applications. $CuCl_2$ is not included in this table due to its propensity to decompose into CuCl and Cl_2 at 400 °C[141]. While many pure metals are known to nitride, few are known to nitride from the metal halides.

Metal Chloride	Earth Abundance of Metal[132] (ppm)	Melting Point (°C)	Boiling Point (°C)	Ammonia Sorbent	Nitridation
LiCl	20	605	1,382	Yes[91]	Easily formed from pure metal at elevated temperatures[142]
NaCl	23,600	801	1,465	No[91]	Not formed without extreme synthesis methods, unstable under standard conditions[143]
KCl	20,900	770	1,420	No	Not formed without extreme synthesis methods, unstable under standard conditions[144]
$BeCl_2$	2.8	415	520	Yes[145]	Synthesis from pure metal at high temperatures (> 700 °C)[146]
$MgCl_2$	23,300	714	1,412	Yes[97]	Synthesis from pure metal at high temperatures (> 600 °C)[147]
$CaCl_2$	41,500	772	1,935	Yes[91,97]	Synthesis from pure metal at elevated temperatures[148]
$CrCl_2$	102	824	1,302	Unclear	$CrCl_2$ known to form CrN when heated to 500 °C under NH_3[149]
$MnCl_2$	950	654	1,225	Yes[97]	Synthesis from pure metal at elevated temperatures[150]
$FeCl_2$	56,300	677	1,023	Yes[110]	Ammoniate phases can decompose into nitride phase[110]
$CoCl_2$	25	735	1,049	Yes[151]	Ammoniate phases can decompose into nitride phase[112]
$NiCl_2$	84	N/A	973 (Sublimes)	Yes[91,97]	Ammoniate phases can decompose into nitride phase[111]
$ZnCl_2$	70	290	732	Yes[97]	Synthesis from pure metal at high temperatures (> 500 °C)[152]
$AlCl_3$	82,300	N/A	180 (Sublimes)	Yes[153]	Synthesis from pure metal at high temperatures (> 500 °C)[154]
$GaCl_3$	19	78	201	Yes[155]	Synthesis from pure metal at high temperatures (> 800 °C)[156]

basis of melting point reduction in eutectic mixtures is due to the entropic gain upon melting, which enables mixing of different metals. Manganese and magnesium chlorides are predicted to form solid solutions, due to their identical crystal structures and similar cationic radius[157]. As such, a significant eutectic effect is not predicted for mixtures of manganese and magnesium chloride (the entropic gain occurs in the solid state too). As a result, manganese and magnesium were not used in the same mixture, as no significant gain in melting point properties would be likely to occur. Given the constraints listed above, all samples studied for ammonia absorption at high temperatures consist of some combination of zinc, sodium, potassium, manganese and calcium chlorides. Magnesium was excluded due to potential issues with decomposition of the hydrates, which can lead to MgClOH and MgO formation.

6.2.1 Pure Salt Ammonia Absorption

Figures C.3 and 6.5 show the ammonia absorption and desorption properties of pure $ZnCl_2$, recorded via STA data. Prior to desorption, a small mass loss was observed through loss of water from the sample, leading to a final mass of 99.0 % prior to the presence of ammonia. Mass plateaus at 125.9 % and 112.3 % during the initial temperature ramp to 130 °C correspond to a di-ammoniate and mono-ammoniate respectively (each ammonia molecule has a mass of 17 g/mol, around 12.5 % of the molar mass of $ZnCl_2$). Initial desorption occurs from a mass of 139.4 %. However, absorption has clearly not finished at this point (Figure C.3). This is likely to be an incomplete absorption to a tetra-ammoniate phase, as reported previously by Biltz[158]. This is notably different to that seen for calcium halide phases, where absorption typically 'skipped' stable ammoniate phases, and some of the sample remained anhydrous metal halide. For $ZnCl_2$, it appears that absorption likely proceeds stepwise, with the sample fully forming the di-ammoniate phase prior to formation of the tetra-ammoniate.

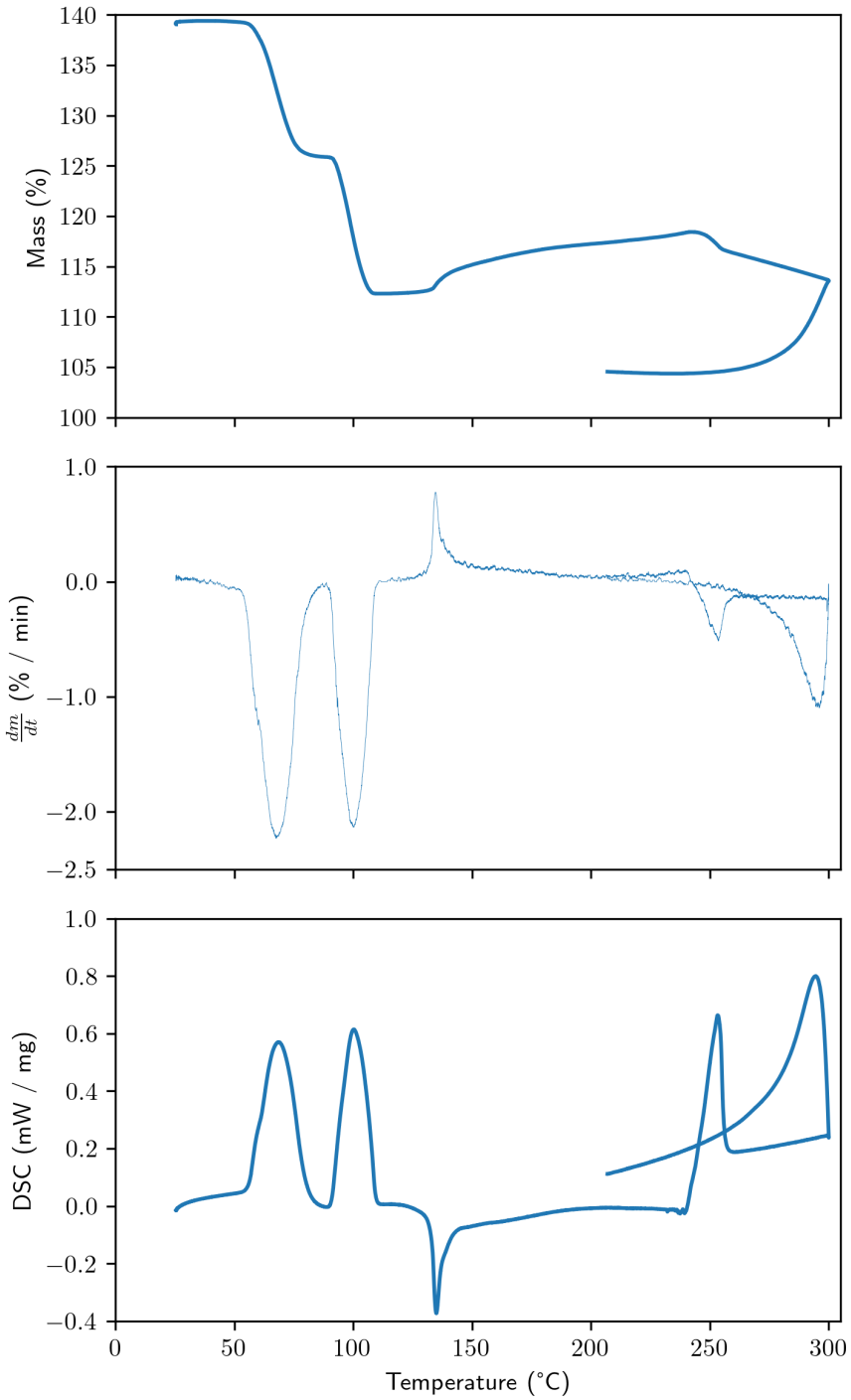


Figure 6.5: Ammonia desorption of $ZnCl_2$ after absorption at room temperature, recorded through STA data at an ammonia pressure of 0.83 bar. The exothermic peak at 130 °C is understood to be a simultaneous absorption-melting process.

It is surprising to see an exothermic event and increase in mass percent during the temperature ramp (∼135 °C), though this is likely explained by the simultaneous absorption and melting of the ammoniate phase (consistent with the results of Pang[140], which showed melting of $ZnCl_2(NH_3)$ from 140–148 °C). Melting and ammonia absorption occurring separately would show up as two separate DSC peaks, but it appears these events are happening concomitantly. The increase in mass percent is likely due to the ability of liquids to have non-integer amounts of ammonia absorbed and the thermodynamic effects described in Section 6.1, though this impact is of unclear magnitude without further thermodynamic data. Absorption into this liquid phase continues until around 240 °C. This is likely an effect of hysteresis, and the thermodynamic limit of ammonia absorption at 150 °C is likely to be much higher than observed in the data. The nature of the desorption event at ∼250 °C is unclear. Assuming this phase is liquid, ammonia loss would typically be a smooth function of temperature. However, a clear DSC peak and sudden mass loss occurs at this temperature. After this peak, the expected smooth ammonia loss occurs until 300 °C, at which point the NH_3 atmosphere is removed and cooldown begins, leading to significant desorption from the sample. This shows the strength of ammonia absorption into $ZnCl_2$ compared with $CaCl_2$, which loses all ammonia by 230 °C at the same pressure.

Figures C.4 and 6.6 show the ammonia absorption and desorption properties of pure $MnCl_2$. Clear desorption is observed from the hexa-ammoniate (theoretically 181.2 %, 181.1 % measured) to the di-ammoniate (theoretically 127.1 %, 127.0 % measured) and mono-ammoniate (theoretically 113.5 %, 113.3 % measured). As observed for $ZnCl_2$, the last significant desorption event occurs after the ammonia atmosphere is removed, signifying the strength of binding between ammonia and $MnCl_2$. However, the initial hydrate desorption and ammonia absorption (Figure C.4) is of interest. The temperature of the initial dehydration step was not high enough to remove all waters of crystallisation, with a final mass of around 113.1 %,

even under an argon atmosphere. Upon exposure to ammonia, the mass rapidly increases, before a small, slow decrease to the expected mass of ∼181 %, as would be expected for a hexa-ammoniate phase. This slow decrease in mass may be related to exchange of residual water for ammonia in the crystal structure of the material. It is clear from the mass plateaus of (as explained above) the temperature ramp (Figure 6.6) that decomposition of the material to NH_4Cl and MnClOH does not occur, as was seen for $CaCl_2$ when exposed to both ammonia and water, and as such some exchange must occur between water and ammonia in the sample.

The ammonia absorption properties of pure $CaCl_2$ are discussed extensively in Chapter 4. Figures C.5 and C.6 show the STA data for samples of NaCl and KCl under the same procedure as samples of $MnCl_2$ and $ZnCl_2$. No evidence of any reaction or significant change in mass was seen, as would be expected for materials reported not to absorb ammonia.

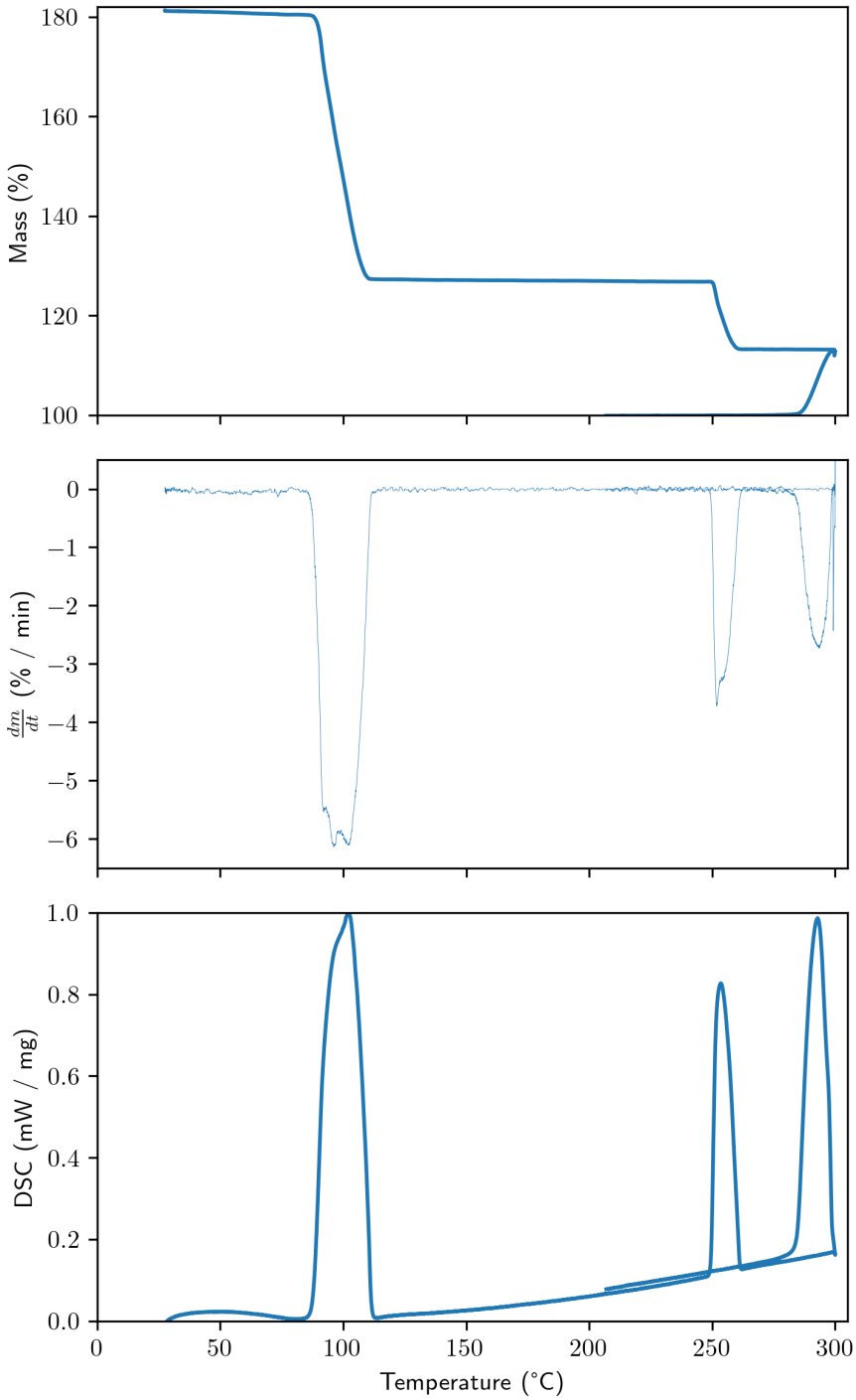


Figure 6.6: Ammonia desorption of $MnCl_2$ after absorption at room temperature, recorded through STA data at an ammonia pressure of 0.83 bar. The expected phase transitions from $n = 6 \rightarrow 2 \rightarrow 1 \rightarrow 0$ are clear.

6.2.2 Mixed Molten Salts Containing Zinc Chloride

Table 6.2 shows the liquidus temperatures (the temperature at which the sample is fully molten i.e. after all melting processes have occurred) of all zinc-containing samples studied for ammonia absorption at high temperatures. Due to significant hysteresis in the melting and solidification processes of these materials, the liquidus temperatures reported in Table 6.2 are calculated as the midpoint between the final melting process and the first solidification process on cooldown. It is presumed this more accurately represents the temperature at which the melting process is thermodynamically favourable. Figures C.7–C.12 show the STA data from which the liquidus temperatures are calculated.

Table 6.2: Liquidus temperatures of zinc-containing eutectic samples used in this work. Liquidus temperatures are calculated as the midpoint between melting and solidification, due to the large amount of hysteresis observed for these samples. The large uncertainty is a result of the large difference in melting and solidification temperatures (up to 80 °C for some samples).

$ZnCl_2$ Mol %	NaCl Mol %	KCl Mol %	Liquidus Temperature (°C)
60	40	0	223(27)
60	0	40	174(42)
60	20	20	189(25)
70	15	15	203(10)
80	10	10	241(27)
100	0	0	278(27)

These samples were chosen to allow for analysis of the effects of increased/reduced zinc content on ammonia absorption, and also study the effect of changing the ratio of the supposedly inert salts (KCl and NaCl).

In order to understand the thermodynamics of ammonia absorption into these molten salt mixtures, the samples were placed on the STA and heated to 240 °C followed by exposure to ammonia. The STA cannot operate above atmospheric

pressure, and Netzsch recommend running an inert carrier gas alongside NH_3 to prevent damage to sensitive components. As such, the ammonia pressure was 0.83 bar (50 sccm NH_3 and 10 sccm Ar). The temperature was then raised in 5 K increments up to 300 °C, allowing for the calculation of the ammonia absorption limit for each sample at each temperature. A dwell was performed at each temperature for 30 minutes to allow equilibration. Figures C.13–C.17 show the raw data from these experiments, while Figure 6.7 shows the combined results of these experiments.

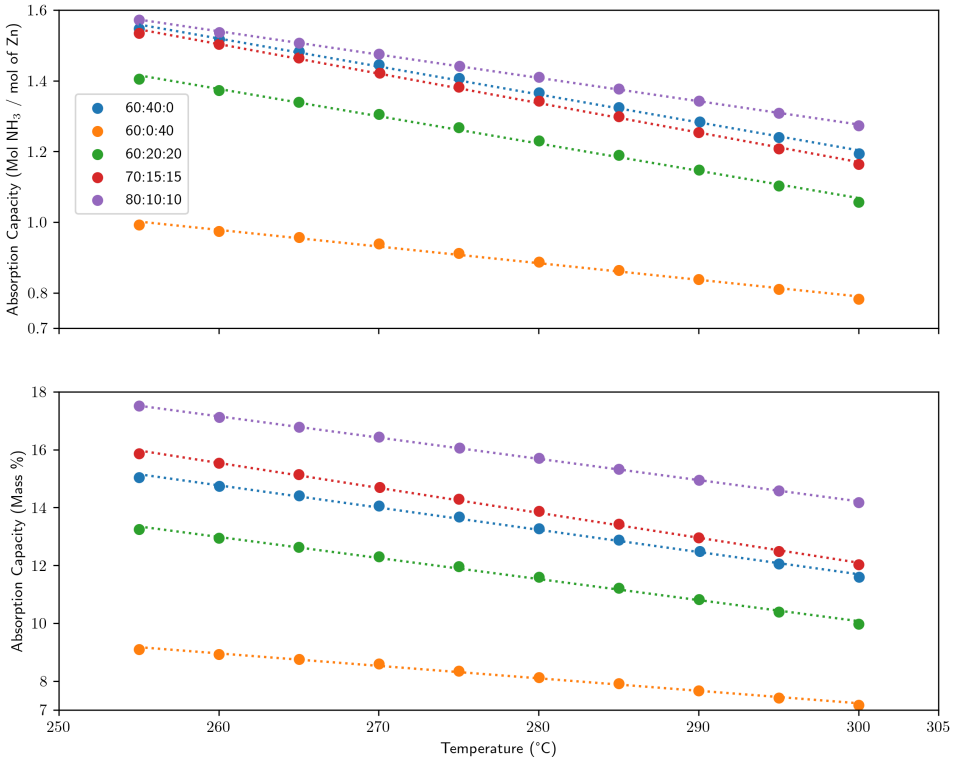


Figure 6.7: NH_3 absorption capacity as a function of temperature for all mixed molten salt samples at an ammonia partial pressure of 0.83 bar. Molar ratios are given as the Zn : Na : K ratio. Fits to linear functions are shown as dotted lines.

Using the series of samples containing 60 % $ZnCl_2$, it appears as though a greater sodium content also leads to greater ammonia absorption capacity on a mass percent basis. This, again, would be expected as Na has a lower mass than K. However,

this trend is also present when examined on a molar basis (top of Figure 6.7). It is reasonable to expect that the lone pair of ammonia only bonds to Zn^{2+}, as might be expected from previous experimental observations that group I metal halides heavier than lithium do not absorb ammonia under ambient conditions. However, the difference in the moles of NH_3 per mole of Zn between the 60:40:0 and 60:0:40 sample is so significant that it does raise questions about the assumption these cations are inert to ammonia in these melts. There does not appear a clear reason why changing the identity of a supposedly inert cation would lead to such large changes in the molar quantity of NH_3 in the sample (over 1.5×). This inevitably leads to the conclusion that this cation may not be completely inert, and ammonia molecules may be rapidly forming and breaking bonds between all cations (though it is likely each ammonia molecule would spend more time bonded to Zn^{2+}).

Unsurprisingly, absorption capacity in terms of mass percent is strongly correlated with the mole percent of $ZnCl_2$ in the sample, with the 80:10:10 and 70:15:15 samples showing the greatest amount of ammonia absorbed at all temperatures. The correlation with mass percent is unsurprising. However, even when considered in terms of the moles of NH_3 per mole of $ZnCl_2$, this correlation holds.

The exact origin of this is unclear, but may be related to hydrogen bonding. It is unlikely that the local Zn-N bonding will be significantly changed by small changes in the ratio of nearby cations. However, in changing the ratio of $2+:1+$ cations, the ratio of cations to anions has also been changed. This will impact the hydrogen bonding network that can be formed by ammonia molecules absorbed into the molten sample. It should be noted that small quantities of NH_3 bonding to sodium and potassium cations (as discussed above) would increase the moles of NH_3 per mole of Zn^{2+}, which works in the opposite direction of the trend observed. This trend is likely to be a play-off between the favourable hydrogen bonding network

of di-cationic salts and the weak bonding possible between ammonia and group I cations in these melts. In the region studied, the effects of hydrogen bonding appear to comfortably dominate.

No data directly aimed at the causal nature of these hypotheses can be easily collected. However, molecular dynamics calculations may inform about the nature of bonding in these melts on the atomic level.

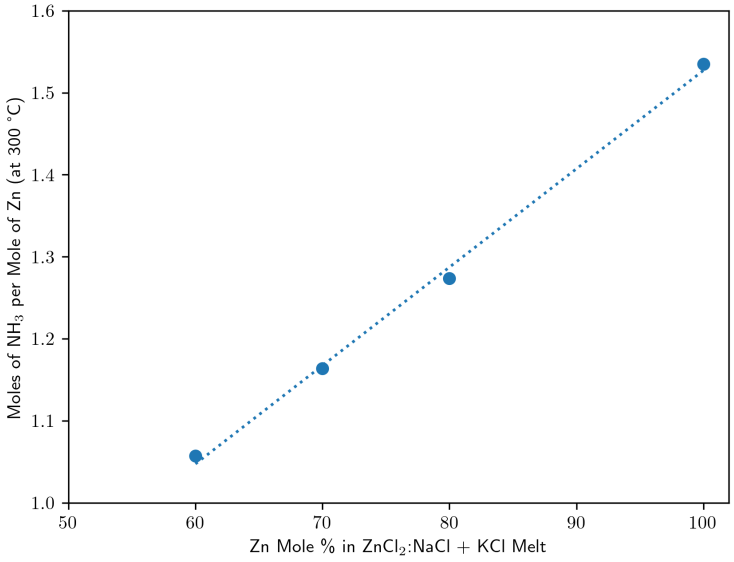


Figure 6.8: NH_3 absorption capacity at 300 °C and 0.83 bar NH_3 for different Zn mole percentages in $ZnCl_2$: NaCl + KCl melts. The mole percent of NaCl and KCl was equal. The datapoint for pure $ZnCl_2$ is calculated using the PSA experiment shown in Figure 6.15. A fit to a linear function is shown as a dotted line.

6.2.3 Pressure Swing Absorption

Pressure swing absorption of ammonia in an industrial context is typically performed between atmospheric and elevated pressure. However, the use of the STA for data collection prevented pressure above atmospheric. As such, pressure swing absorption experiments presented here involved pressure swings between ammonia

partial pressures of 0.83 bar and 0 bar. Pressure swing absorption experiments were performed at 300 °C, ensuring all examined samples were molten (with the exception of $MnCl_2$) but evaporation was limited.

Figure 6.9 shows a pressure swing absorption experiment of $MnCl_2$ (a commonly studied ammonia sorbent in the literature[97,60,135]) at 300 °C and 0.83 bar NH_3. Ammonia absorption occurs slowly at this temperature and pressure, with limited uptake observed in 30 minutes. Desorption also occurs slowly, with insufficient desorption of absorbed NH_3 within 30 minutes, leading to a slow accumulation of NH_3 over many cycles. Full formation of the mono-ammoniate of $MnCl_2$ would correspond to a mass of 113.5 %; this is not reached.

Figures 6.9–6.15 show the data from the pressure swing absorption experiments. Table 6.3 presents some key data from the pressure swing absorption experiments on molten salts, with $MnCl_2$ as a comparison. Ammonia sorption capacities from Table 6.3 appear to be consistently lower when compared with the NH_3 content of samples at 300 °C in Figure 6.7. This is a result of the method used and insufficient desorption after 30 minutes. In all experiments, 30 minutes under argon was insufficient to fully remove all ammonia from the sample, and as such this then limits the ammonia uptake in the following absorption cycle. The low ammonia sorption capacity seen for $MnCl_2$ is due to the slow rate of absorption. Assuming formation of the mono-ammoniate, absolute sorption capacity would be 135.3 gNH_3 / kg over a long enough time period.

The maximum masses observed after the first cycle are approximately consistent with those seen in Figure 6.7. It is possible that the small sample size of the STA ($\sim$13 mg) and insufficient mixing of samples has led to some slight variation in molar ratio in the actual sample used (thus leading to slightly variable maximum mass/NH_3 uptake).

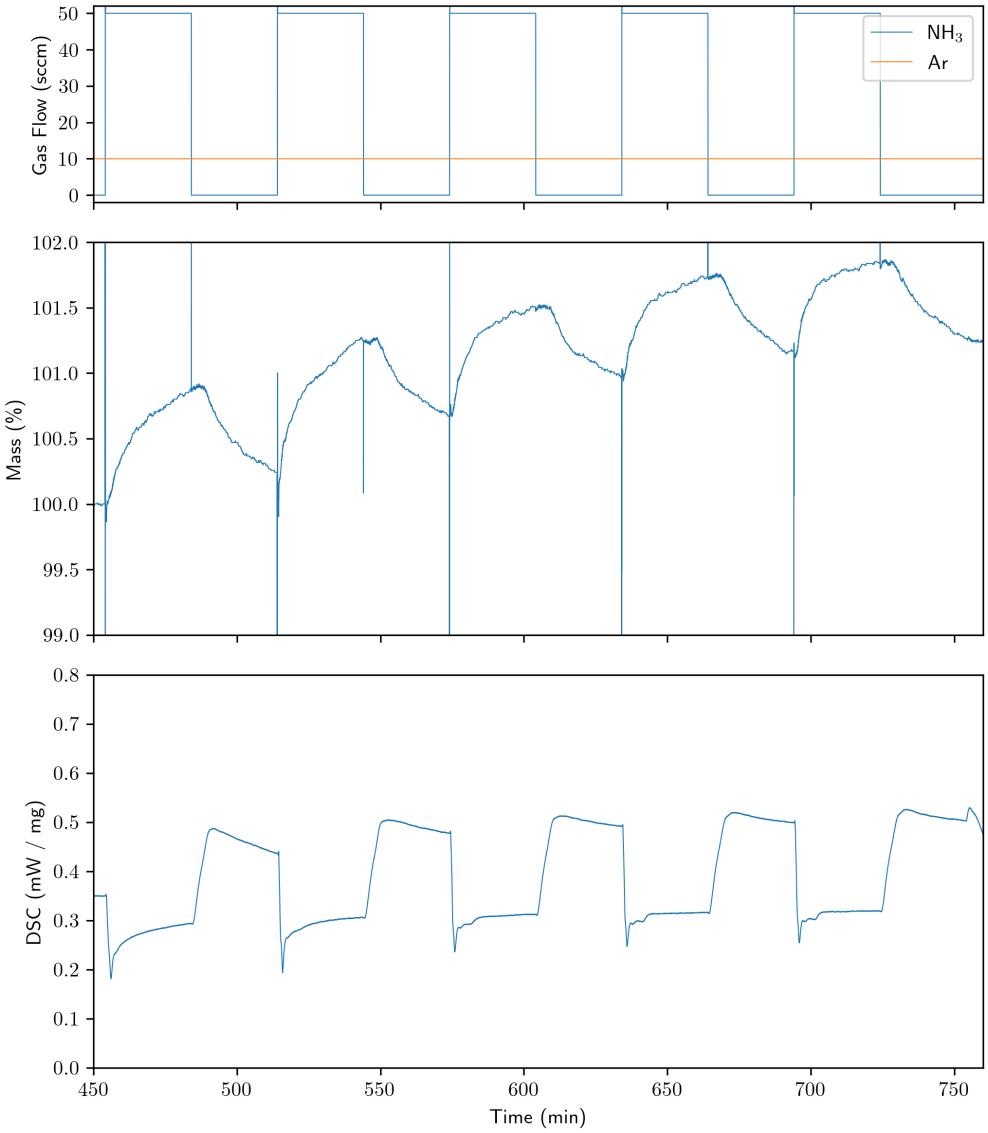


Figure 6.9: 300 °C PSA (0–0.83 bar) experiment for a $MnCl_2$ sample. The $MnCl_2$ sample was hand-ground in a pestle and mortar for 5 minutes prior to loading.

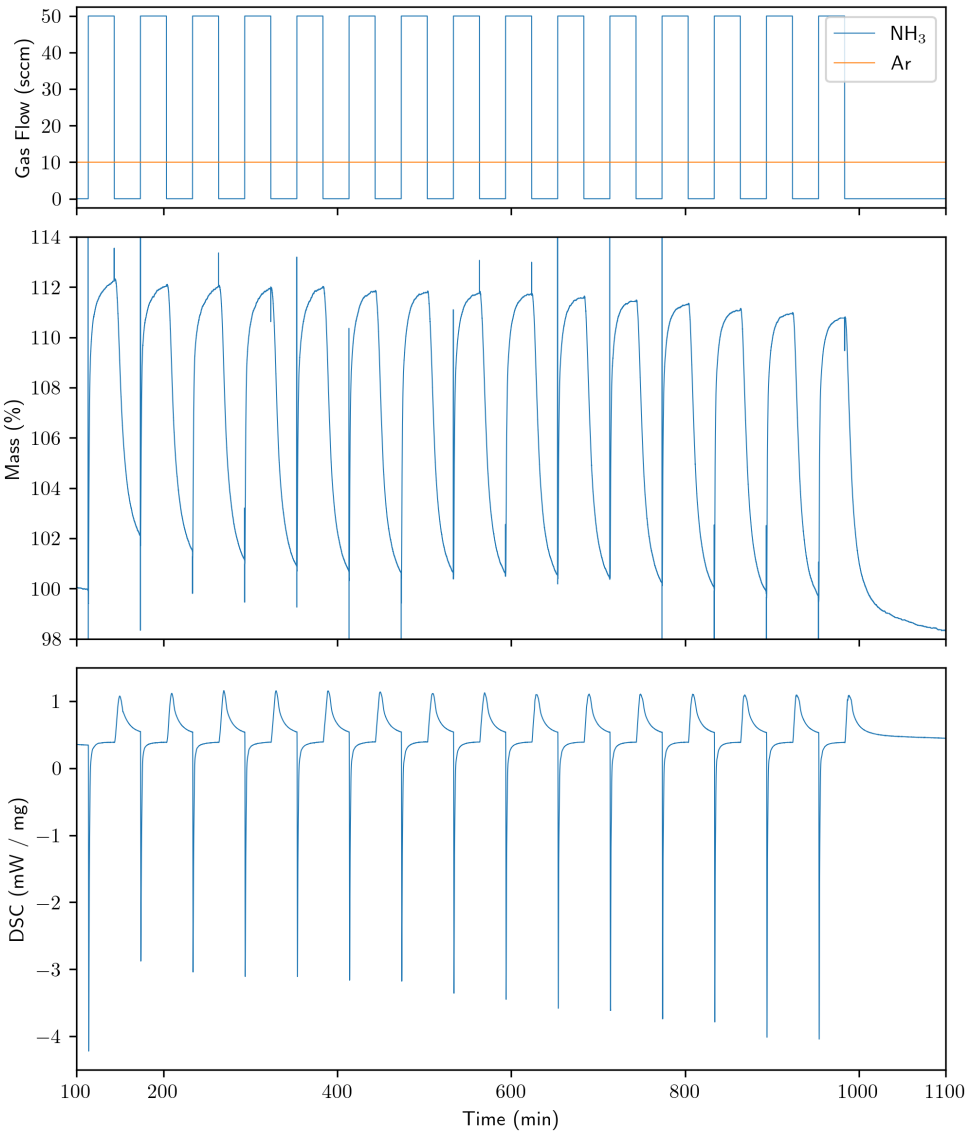


Figure 6.10: 300 °C PSA (0–0.83 bar) experiment for the 60:40 Zn : Na chloride sample.

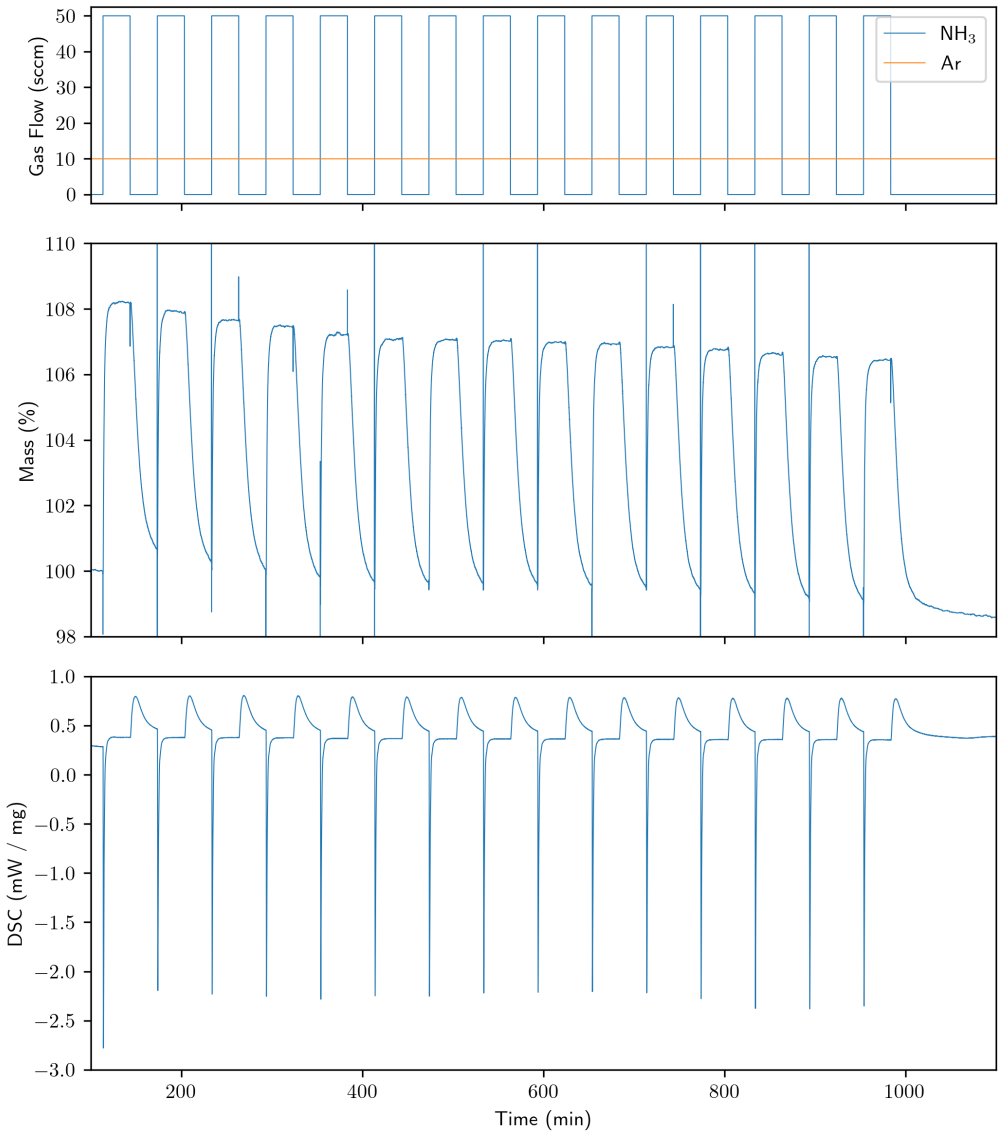


Figure 6.11: 300 °C PSA (0–0.83 bar) experiment for the 60:40 Zn : K chloride sample.

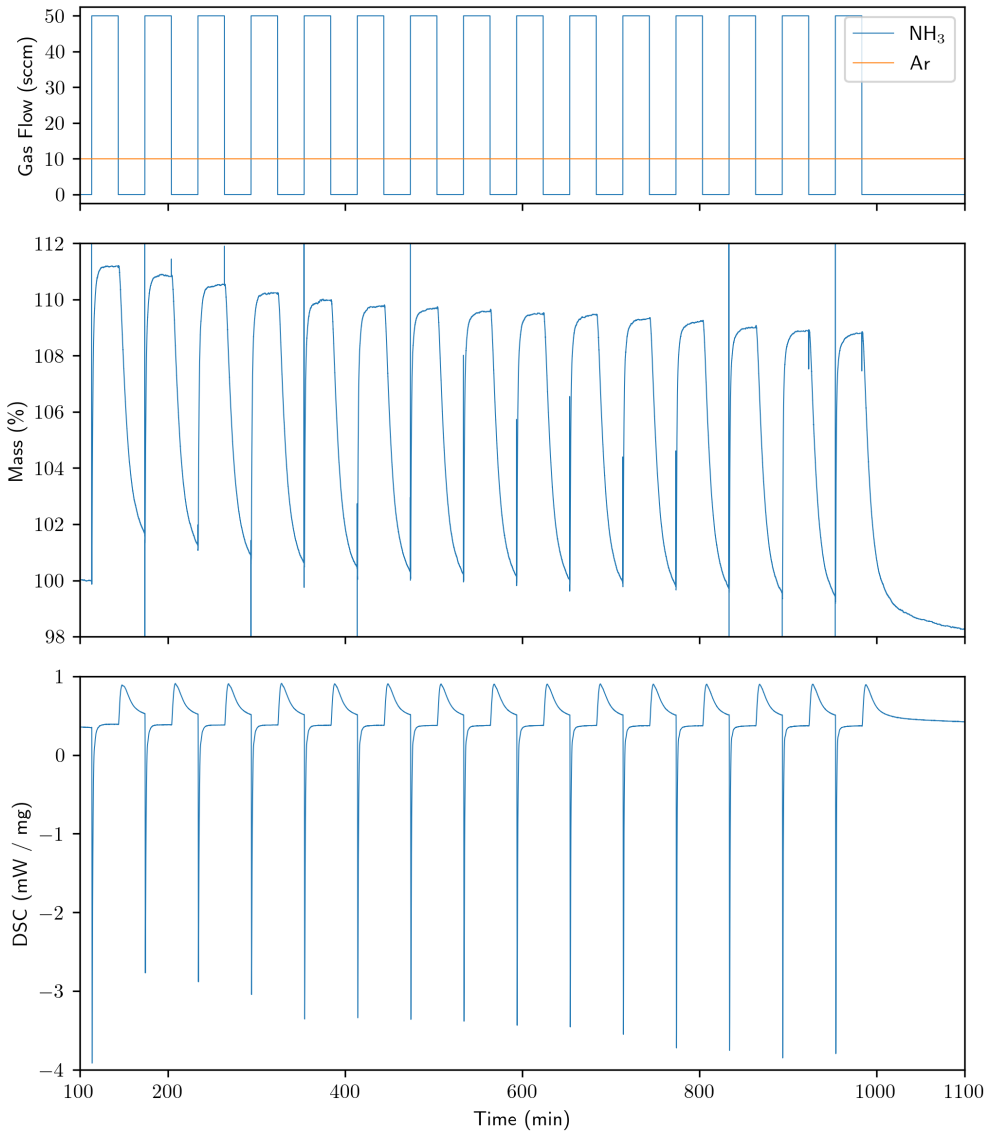


Figure 6.12: 300 °C PSA (0–0.83 bar) experiment for the 60:20:20 Zn : Na : K chloride sample.

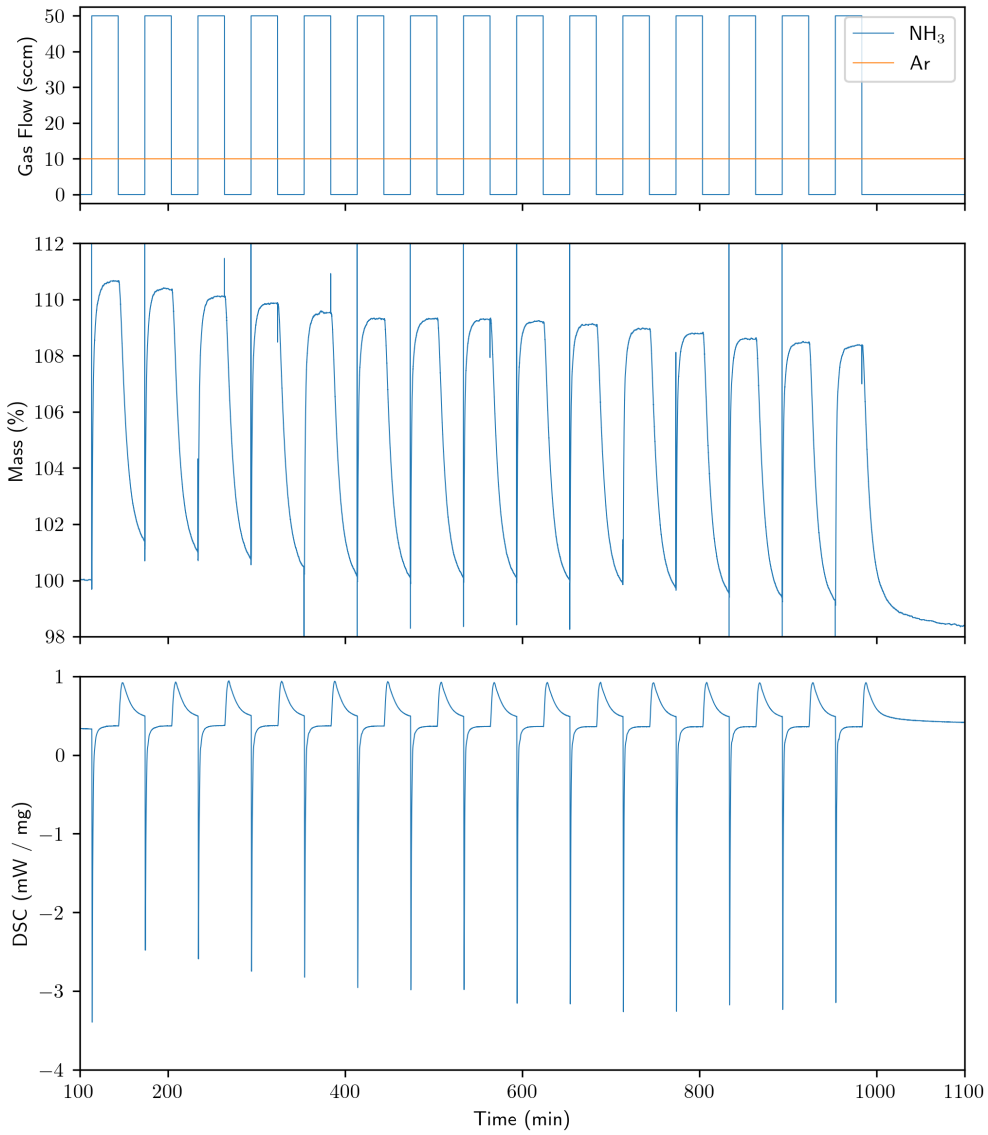


Figure 6.13: 300 °C PSA (0–0.83 bar) experiment for the 70:15:15 Zn : Na : K chloride sample.

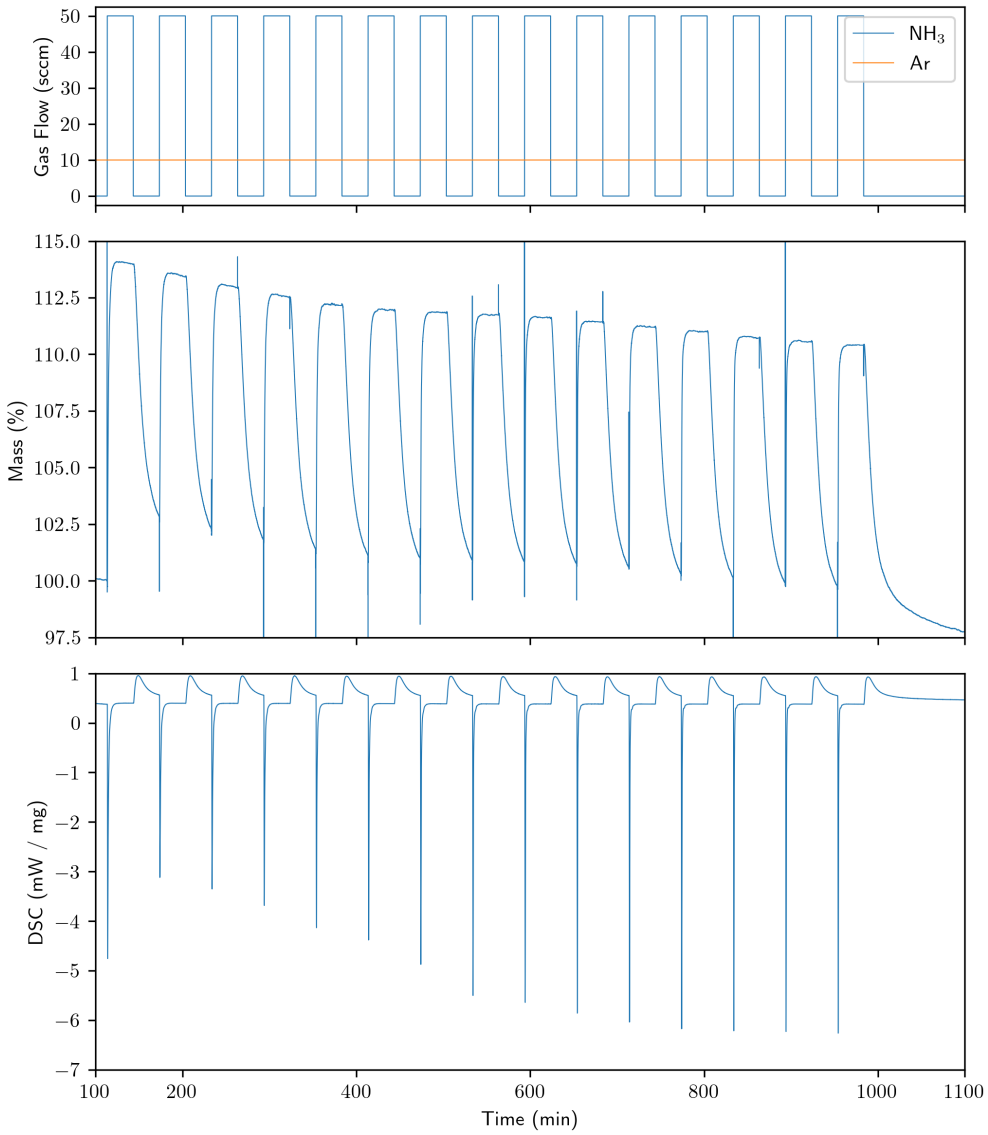


Figure 6.14: 300 °C PSA (0–0.83 bar) experiment for the 80:10:10 Zn : Na : K chloride sample.

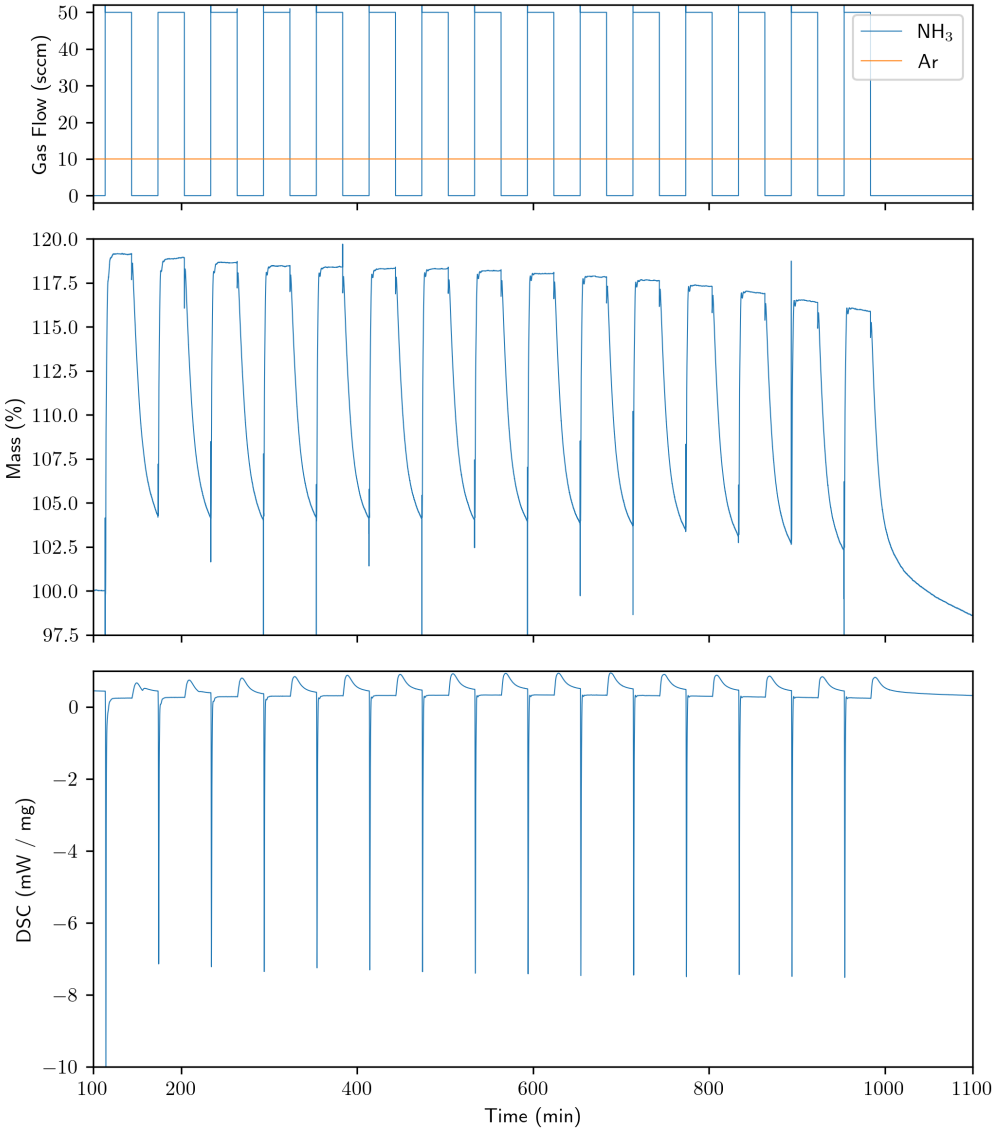


Figure 6.15: 300 °C PSA (0–0.83 bar) experiment for a $ZnCl_2$ sample.

When both datasets are taken into account, the two trends identified from Figure 6.7 hold when considering maximum NH_3 uptake (i.e. the only data independent of the slow desorption process). Pure $ZnCl_2$ shows the strongest performance across the metrics used. However, the 80:10:10 and 60:40:0 samples also show strong performance. Alongside this, the price and environmental cost of the elements should be considered, which will heavily favour a sample containing less zinc.

It should be noted that these PSA experiments were performed at sub-atmospheric pressure, and further study should be done to examine similar metrics at elevated pressures. Desorption from the molten salt mixtures is consistently a much slower process than absorption. While matching the rate of each process would be optimal for the batch process described in Figure 6.1, a continuous process such as that shown in Figure 6.2 would easily allow for the time spent under absorption and desorption conditions to differ (simply maintain constant flow rate but use a larger desorption chamber/loop).

Figures C.18–C.24 show the sorption quantity and sorption rates of the PSA cycling experiments for all of the samples studied. Good agreement is observed between cycles for molten samples, with consistent absorption and desorption rates and capacities.

Table 6.3: Output data from PSA (0–0.83 bar) experiments at 300 °C. Mass retention is the mass % of the sample after the experiment was completed. Sorption capacity is calculated as the average mass change after 30 minutes of absorption/desorption. Absorption (2 min) is the average mass change two minutes after ammonia gas flow is turned on, while Desorption (5 min) is the average mass change five minutes after ammonia gas flow is turned off.

Sample ($ZnCl_2$: NaCl : KCl)	Maximum Mass (PSA, 300 °C, %)	Mass at 300 °C (Figure 6.7, %)	Mass Retention (%)	Sorption Capacity (30 min, gNH_3 / kg)	Absorption (2 min, gNH_3 / kg)	Desorption (5 min, gNH_3 / kg)
60:40:0	112.3	111.6	98.8	110.1	70.82	27.20
60:0:40	108.2	107.2	99.0	74.1	52.46	20.92
60:20:20	111.2	110.0	98.8	94.1	68.16	27.27
70:15:15	110.7	112.0	98.9	91.7	61.90	28.63
80:10:10	114.1	114.2	98.3	108.3	86.13	30.46
100:0:0	119.2	N/A	98.5	138.3	103.96	46.39
$MnCl_2$	101.8	N/A	N/A	7.0	1.51	0.05

6.2.4 Mixed Molten Salts Without Zinc Chloride

While the low melting point and strong ammonia bonding of zinc chloride provides a useful starting point for ammonia absorption into molten salts at ∼300 °C, the lower boiling point of zinc chloride could lead to significant evaporation of the molten salt at higher temperatures. This was seen during the melting point testing of $ZnCl_2$, with significant evaporation (∼1 % loss every 30 minutes) above 350 °C. As the Haber-Bosch process is commonly performed at temperatures > 400 °C, *in-situ* absorption using $ZnCl_2$ could lead to significant evaporation of the molten salt. In order to reduce the use of zinc, and possibly enable higher temperature ammonia sorption, a sample of 40:40:10:10 Mn : Ca : Na : K chloride was made. As previously, the sodium and potassium chloride were primarily used to lower the liquidus temperature of the mixture. Calcium chloride does absorb ammonia but typically at lower temperatures than required here. However, as seen in Section 6.2.2, the ammonia absorption ability of a molten salt mixture is not equivalent to the sum of its parts under the same conditions, and as such calcium, sodium and potassium may all impact the ammonia absorption of this mixture in the liquid phase.

Figure 6.16 shows temperature cycling of this sample to 500 °C. The exothermic peak at ∼260 °C is likely due to reaction between powders, likely forming $M_x^{1+}M_y^{2+}Cl_{x\,+\,2y}$ materials. The large peaks slightly below 400 °C are likely melting transitions. However, a further, smaller peak appears to occur around 450–470 °C, which is likely another melting/dissolution transition. The exact proportion of the sample which is liquid at any given point is difficult to ascertain. However, given the relative peak sizes, it is likely that the sample consists of a mostly liquid slurry at 400 °C.

Figure 6.17 shows the PSA cycling experiment at 400 °C for the 40:40:10:10 Mn : Ca : Na : K chloride sample, while Figure 6.18 shows the absorption-desorption cycles plotted on the same axes.

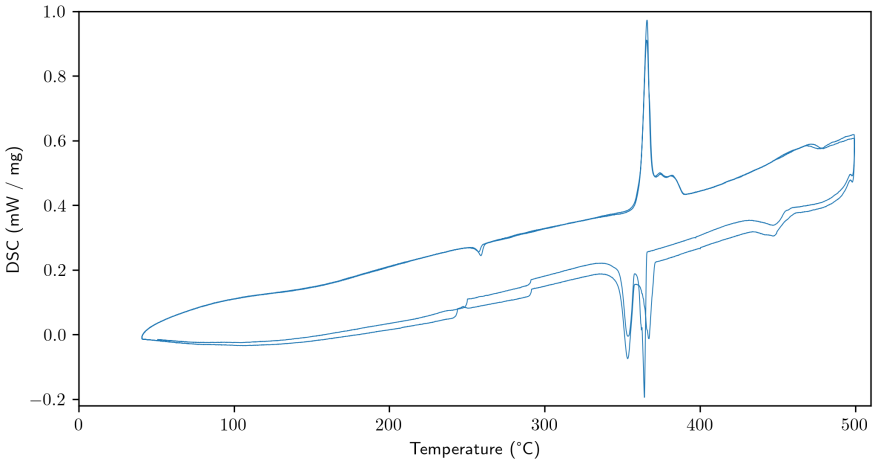


Figure 6.16: Melting point test for the 40:40:10:10 Mn : Ca : Na : K chloride sample. While the most significant peaks in heat flow occur below 400 °C, small peaks are seen around 450–470 °C which could signify a final melting event.

As was seen for zinc-based samples, consistency is observed between cycles. A significantly lowered ammonia absorption capacity (average of 9.27 gNH_3 / kg) is seen compared to the zinc-based samples at 300 °C, though this is unsurprising for a temperature 100 °C greater. Virtually no absorption or desorption is seen past 15 minutes. Unlike the zinc-based samples at 300 °C, absorption and desorption rates of this sample at 400 °C are very similar. While the sample may not be fully molten, this illustrates the possibility of using salt mixtures for *in-situ* absorption from the Haber-Bosch process.

Figure 6.19 shows a PSA experiment at 400 °C for pure $MnCl_2$. While small mass changes (0.2 %) do occur upon the switch between NH_3 and argon, the immediate change in mass, coupled with the lack of smooth DSC features suggests that these mass changes are likely an effect of the change in the environment surrounding the sample (gas flow rate and buoyancy of the gas atmosphere), rather than actual mass changes. It is thus considered that the ammonia absorption capacity of $MnCl_2$ at this temperature and pressure is functionally zero. This is unsurprising, as solid $MnCl_2$ is not expected to retain any ammonia in the solid state at 400 °C and 0.83 bar NH_3.

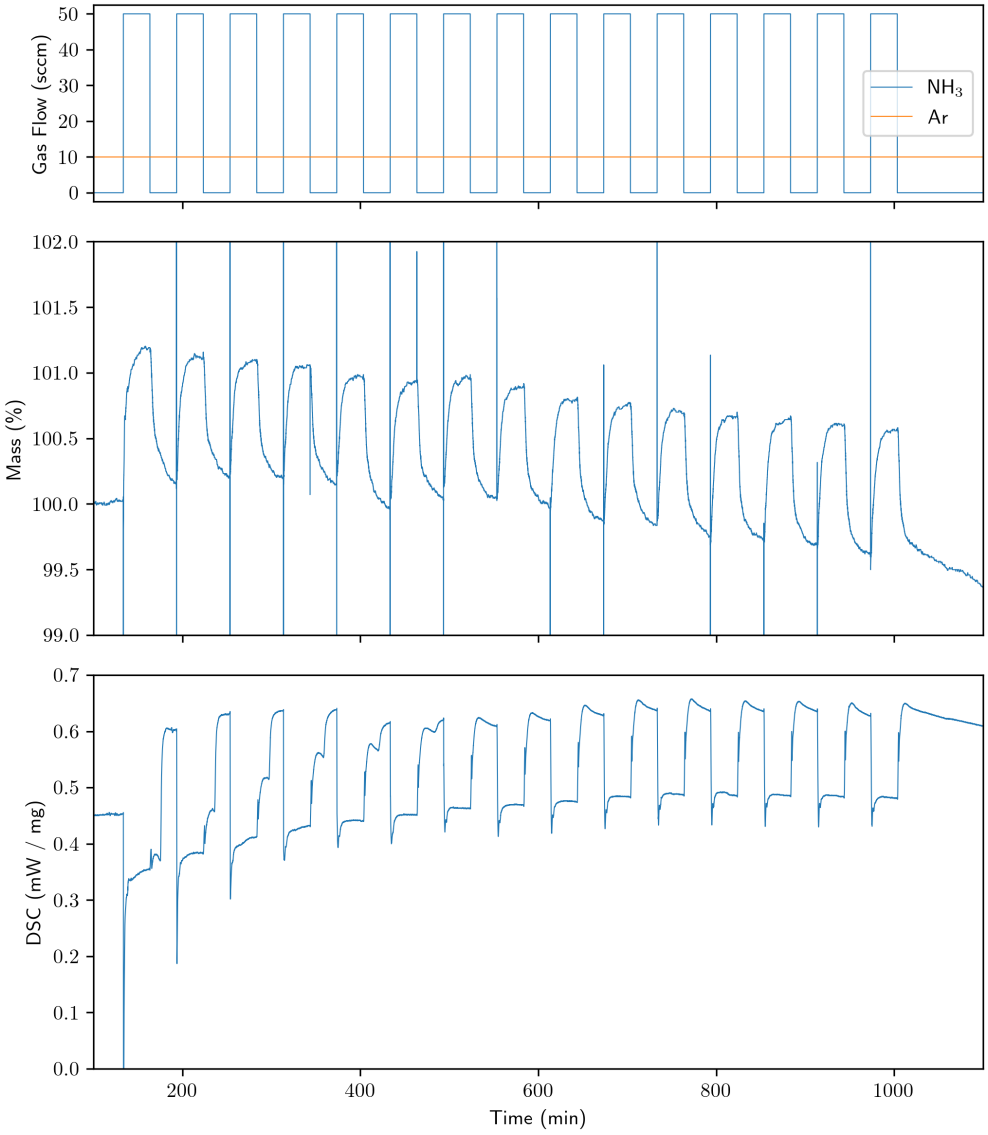


Figure 6.17: PSA (0–0.83 bar) cycling data for the 40:40:10:10 Mn : Ca : Na : K chloride sample. t = 0 refers to the switching on/off of ammonia gas flow. There is a slight delay before significant absorption/desorption occurs as the atmosphere is not immediately replaced. The mass recorded at the end of the experiment was 99.2 % of that recorded at the start of the experiment.

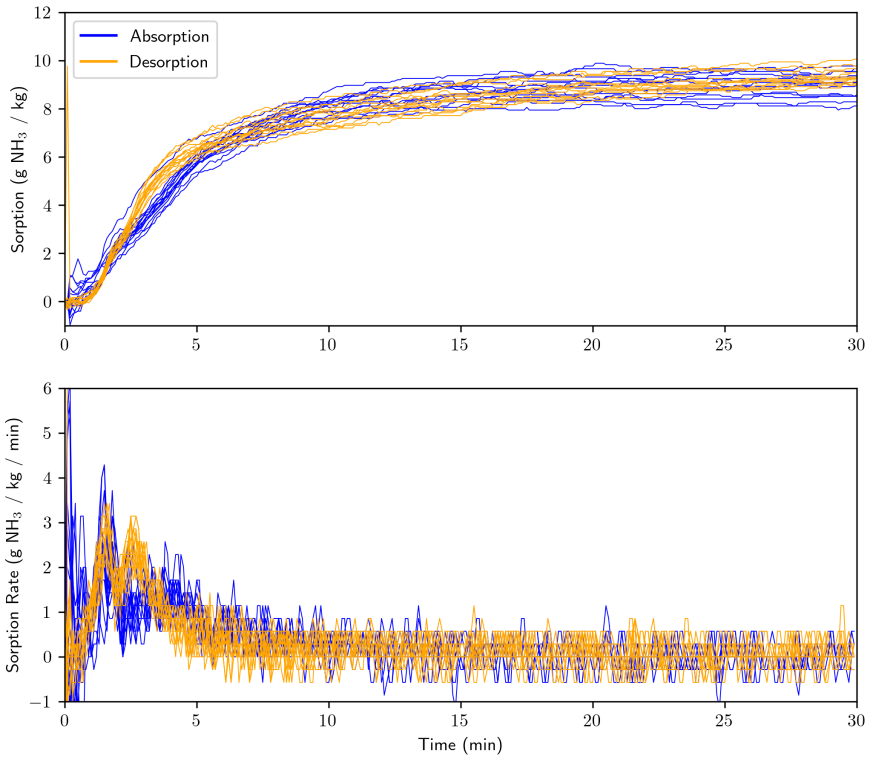


Figure 6.18: PSA cycling at 400 °C and 0–0.83 bar NH_3 for the 40:40:10:10 Mn : Ca : Na : K chloride sample.

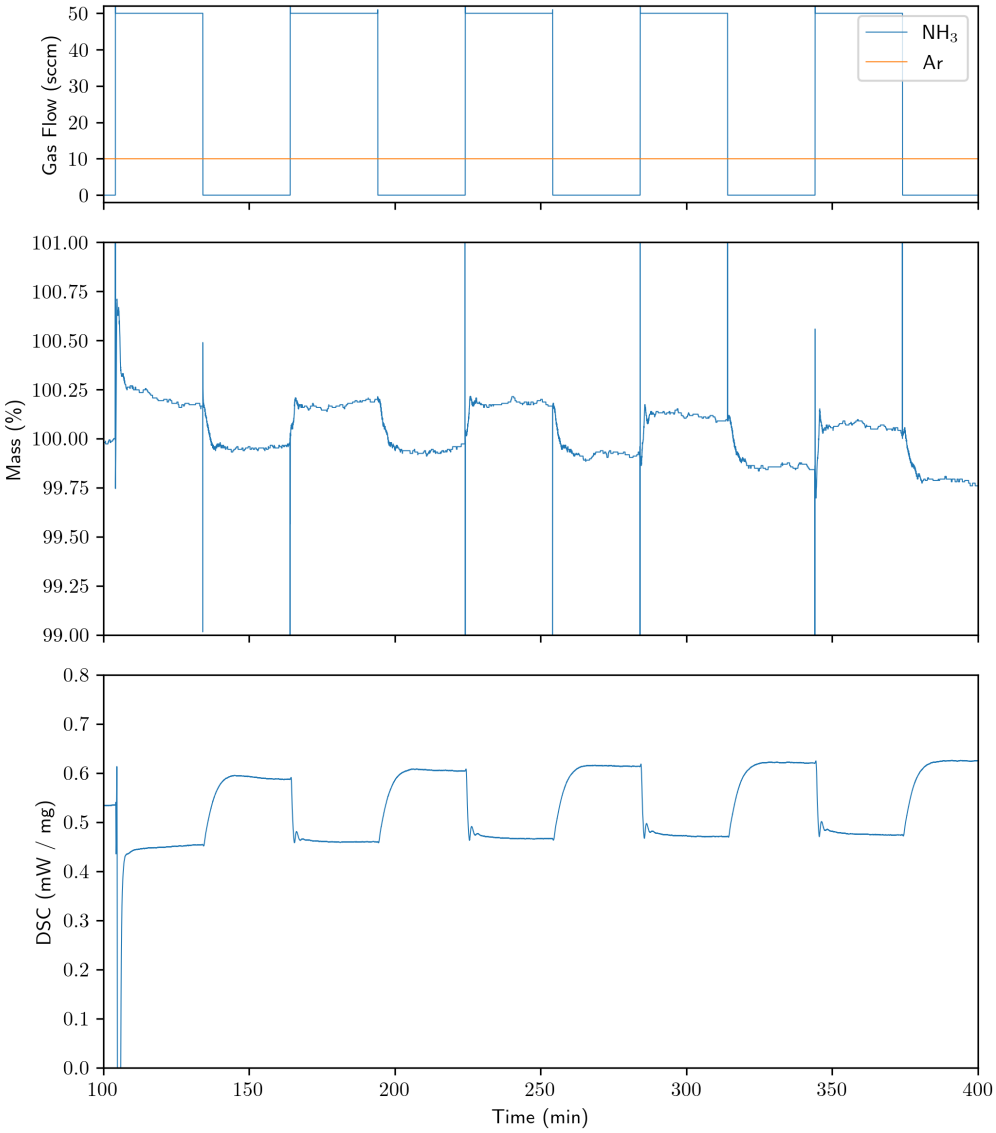


Figure 6.19: PSA cycling at 400 °C and 0–0.83 bar NH_3 for a $MnCl_2$ sample. The $MnCl_2$ sample was hand-ground in a pestle and mortar for 5 minutes prior to loading.

The two experiments studying absorption at 400 °C show how molten salt mixtures can be used to increase the temperature at which significant ammonia absorption is seen. It is unclear the extent to which this is affected by the thermodynamic considerations laid out in Section 6.1, as the ability of liquids to absorb sub-stoichiometric quantities of NH_3 also enables this increase in operation temperature. Time constraints have prevented further development of this branch of zinc-less eutectics, though the initial iteration suggests these may be a promising area of research for *in-situ* ammonia absorption, particularly considering that the NH_3 partial pressure in a Haber-Bosch reactor is significantly higher than 0.83 bar.

6.3 Conclusions and Future Work

A study into the possibility of using mixed molten salts as ammonia absorbers at high temperature has been performed. While the ammonia pressure was limited to ≤ 0.83 bar, results appeared promising, showing rapid absorption of high amounts of NH_3 at 300 °C, and small amounts of NH_3 at 400 °C using a sample absent of zinc.

Despite the limited number of samples studied, trends were identified. Initially, it was expected that the molten salts would consist of an ammonia absorbing component and an inert component (used to lower the melting point). This was shown not to be the case, with the ratio of mono-cationic to di-cationic salts proving important in ammonia absorption on a di-cationic molar basis. This is understood to be an effect of the ratio of anions to cations, affecting the hydrogen bonding network formed by NH_3 molecules in the melt.

Alongside this, it was observed that replacement of potassium with sodium in the eutectic mixtures also had a significant effect on the absorption capacity of the mixture. This implies that there may be exchange of NH_3 molecules in the melt between the absorbing component (Zn) and the previously considered non-absorbing component (Na/K); the identity of the mono-cationic salt can have a large effect on ammonia absorption.

Molten samples consistently showed greater performance at 300 °C than $MnCl_2$, with pure $ZnCl_2$ showing the greatest absorption rate and capacity. However, it should be noted that $ZnCl_2$ melts at ∼280 °C and as such is not suitable for applications below this temperature. Similarly, the 40:40:10:10 Mn : Ca : Na : K sample tested at 400 °C showed significant absorption, while pure $MnCl_2$ showed no absorption.

Two primary strands of work are suggested to take this concept forward. It was shown how the identity and charge of all metals in the melt can affect ammonia absorption, and thus further examination of the compositional space should be undertaken. This should focus on the study of liquidus temperatures and ammonia absorption rates as Zn, Na, K are replaced with di-cationic absorbing salts such as $CaCl_2$, $MgCl_2$ and $MnCl_2$ (among others). Mixing $ZnCl_2$ with other di-cationic salts allows for the removal of (some of the) expensive zinc while maintaining the low melting point and high ammonia absorption ability.

Alternatively, variation of anions, such as incorporating bromide and iodide can further depress melting points and give greater ammonia absorption performance, as might be expected from the results of Chapters 4 and 7 (though these focus on absorption into solids). Given the limited ammonia absorption seen for the 40:40:10:10 Mn : Ca : Na : K chloride sample at 400 °C, this should particularly be considered for eutectic mixtures absent of zinc, with the aim of *in-situ* Haber-Bosch ammonia absorption. However, it should be noted that the pressure of a Haber-Bosch reactor is significantly higher than that used in this work (0.83 bar), and as such greater absorption of ammonia would be expected regardless of a change in composition.

7

Periodic Trends in Ammoniate Formation of Metal Halides

Group I metal halides are understood to show significantly weaker binding with ammonia when compared with group II or group III metal halides. Lithium chloride is the only solid group I metal chloride to absorb ammonia under ambient conditions. However, its limited binding strength leads to loss of all ammonia by 100 °C at ambient ammonia pressure[94]. While the effect of changing halides was discussed in the context of calcium halides in Chapter 4, this chapter seeks to use computational data to develop an understanding of trends in ammoniate formation across the periodic table.

7.1 Scope of the Work

Appropriate metals from groups I, II (and XII), III (and XIII) and IV were chosen for study. This was in part to avoid obscuring effects such as ligand field stabilisation energy for transition metals, and attempt to understand the fundamental interactions of ammoniate formation in metal halides. Similarly, non-metals, or elements which do not comfortably form 3+ or 4+ cations, were excluded, as the ammoniate structures studied here are inappropriate for covalently bonded elements. This includes all group XIII elements except aluminium, and all group XIV elements.

All ammoniate crystal structures reported on the ICSD (Inorganic Crystal Structure Database)[159], and those derived in this thesis for calcium halides were included, with the exception of a small number which exhibited occluded NH_3 (NH_3 moieties in which the N lone pair is not bonded to a metal ion). All combination of metals and halides which could reasonably be considered to adopt each structure were geometry optimised in CASTEP. The ratio of metals to halides needs to be correct, but also the coordination environment shown by the metal must be reasonable. For example, beryllium and magnesium halides were not geometry optimised in the $CaCl_2(NH_3)_8$ structure, as these metals are too small to accommodate 8 NH_3 molecules in their coordination sphere. All CASTEP geometry optimisations were performed with a cutoff energy of 950 eV and a Monkhorst-Pack spacing of 0.02 $Å^{-1}$.

It should be noted that the ICSD contains experimentally reported structures. This means that, as NaCl has not been reported to absorb ammonia, no NaCl ammoniate structures are present on the ICSD. Hypothetically, NaBr or NaI *might* adopt the same structure as the LiCl ammoniates, though this seems unlikely given the tetrahedral coordination environment of these ammoniates. However, sodium and bromide/iodide were geometry optimised in these structures. This is useful for understanding the trends in ammoniate formation, but the energy values obtained

should not be considered the true enthalpy of formation of a NaX ammoniate phase, which would likely adopt a different structure. Heavier group I metals were not used, as a tetrahedral coordination environment was considered not to be appropriate.

Another consideration is the effect that rotation of NH_3 molecules can have on the energy of the system. Furthermore, many ammoniate crystal structures arise from X-ray diffraction results and are reported without hydrogen positions. Full study of local and global minima in the rotation of NH_3 molecules was not possible for each structure, as this would be too computationally expensive. As such, NH_3 molecules in each structure were assigned a random rotation prior to optimisation of the NH_3 moieties only. The hydrogen positions obtained as the local minimum for each structure were then used as the starting position for all optimisations involving this structure, ensuring consistency upon the exchange of metals and halides.

The base salts were also geometry optimised to enable calculation of ammonia absorption enthalpies. Across all feasible structures, all metals (16), and all halides (4), 475 geometry optimisations were performed in CASTEP. For each ammoniation number, the lowest energy structure was taken as the datapoint for formation enthalpy and Madelung energy calculations.

Tables D.1–D.4 show the ammoniate structures run for each cation and anion combination. The coordination numbers of the cation in each structure are also shown, as these were used to inform about the structures which may give a reasonable energy value. As mentioned above, the energy results presented below are for the lowest energy structure at each ammoniation number, and so the optimisation of unsuitable structures should not impact the results. However, certain combinations of structures and cations which would clearly be unfavourable were skipped to save on computational time.

In group II, only beryllium and zinc commonly adopt tetrahedral coordination, and so only these metals were geometry optimised in structures with a coordination number of four. Similarly, beryllium, magnesium and zinc are too small to adopt

a structure with eight-fold coordination, and so these cations were not used in the structure of the octa-ammoniate. This similar logic was applied throughout other groups.

There are a number of 3+ cations that may form ammoniates experimentally (given the large number of lanthanides). However, it is likely that many have not been studied. No experimental structures are reported on the ICSD for most lanthanide halides. While commonly an ongoing debate about which element formally belongs in group III[160], it was decided that lutetium was more appropriate in the context of this work, due to lutetium commonly forming octahedral coordination environments. Lanthanum, on the other hand, often adopts nine-fold coordination spheres, and it was not clear that results would be appropriate if a lanthanum cation was forced into an octahedrally coordinated ammoniate phase. For the same reason hafnium was used, as opposed to cerium, for the study of group IV cations.

The bonding changes within a crystal upon absorption can be understood as the loss of ionic bonding upon an increase in cation-anion separation, with replacement of this by an M-N bond and hydrogen bonding between NH_3 and halide ions. As seen extensively for calcium halide ammoniates in Chapter 4, heavier halides reduce the loss of ionic bonding strength, but also form weaker hydrogen bonds. This will be studied further in this chapter. However, the focus is shifted to study the effect of exchanging metals also. It should be noted that the identity of the metal is not the only effect here, with the charge on the metal also controlling the number of anions in the crystal structure, affecting the hydrogen bonding network formed.

7.2 Trends in Ammoniate Stability Within Metal Groups

7.2.1 Group I

Figure 7.1 shows the absorption enthalpies of group I metal halides. For Li and Na halides, the expected trend of formation enthalpies for halides is seen (I > Br > Cl > F), explained simply as the domination of Madelung energy effects over hydrogen bonding effects. For hydrogen halides, the trend observed is actually Cl > Br > I >> F. Fluoride is often seen as a special case in the results in this chapter, due to the huge Madelung energy change seen upon interruption of the ionic bonds formed. The reversal of the trend for heavier halides is simply due to the importance of hydrogen bonding in NH_4X phases. Rather than the usual consideration of a metal ion bonded to a NH_3 moiety, which often struggles to perfectly orient its hydrogen atoms at halide ions, these phases consist of ammonium cations (which are highly symmetric), allowing for the hydrogen atoms to perfectly point at halide ions. As such, hydrogen bonding is extremely important in this structure. The 'metal' charge will be effectively spread over all hydrogen atoms, whereas in other metal halide ammoniates, the charge is localised on the metal ion.

There is also a general trend showing that smaller cations lead to greater absorption enthalpies. This is not surprising, as smaller cations would be expected to show a greater M-N bond strength. This can be explained in various ways, such as a lower energy LUMO for receipt of donated electrons, or on a charge to size basis, but fundamentally this is not unexpected. It should be noted that smaller cations also show a greater change in Madelung energy upon ammonia absorption, due to the greater proportional change in distance between cation and anion. However, the greater M-N bond strength is clearly significant enough to overcome this.

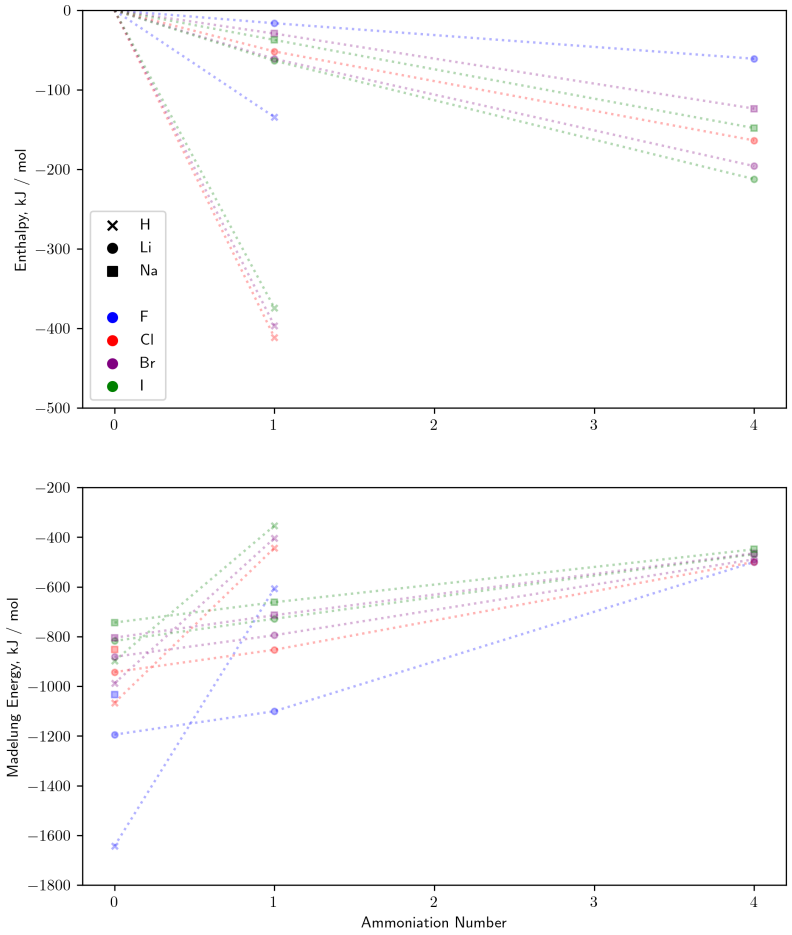


Figure 7.1: Formation enthalpies (relative to MX + nNH$_3$) and Madelung energies of group I metal halide ammoniates calculated using CASTEP. NaCl, NaF, KX, RbX and CsX were not optimised in any structures due to the inappropriate coordination environments of all experimental ammoniate structures. All HX materials were optimised in the rocksalt structure (the structure adopted upon solidification) in order to maintain consistency.

Hydrogen halides would not be expected to show absorption beyond one mole of NH_3 due to the small size of hydrogen and covalency of bonding in NH_4^+ ions. Lithium halides would not be expected to show absorption beyond four moles of NH_3 (without occluded NH_3) due to the small size of the ion preventing an octahedral coordination environment for ligands as large as NH_3.

7.2.2 Group II/XII

Figure 7.2 shows the formation enthalpies of ammoniate phases for beryllium, magnesium and zinc halides. The usual trend for halides is followed for Be and Mg, and the extremely low (in comparison to other halides) absorption enthalpies are seen for fluoride as was observed for group I. However, for zinc, this trend is not so clear. For the early ammoniate phases, the trend seen is Cl > Br > I > F. The exact origin of this is unclear, but might be related to the transition metal contraction. While zinc has a similar ionic radius to magnesium (very slightly larger in most measures)[134], many of its compounds are often considered to have a significant degree of covalency, commonly leading to tetrahedral coordination environments (as is seen in all 4 polymorphs of $ZnCl_2$ reported on the ICSD[161,162,163]). This covalency might be the origin of unexpectedly high absorption enthalpies for fluoride, and the reversal of the expected trend for the heavier halides. It is likely the significant degree of covalency leads to a reduced dependence of Zn-X bond strength on the ionic radius of the halides, allowing hydrogen bonding to become significant in comparison to the effect of Madelung energy changes (or, more formally, the reduced Madelung energy changes combined with the additional loss of Zn-X covalent bonding), thus reversing the trend for Cl, Br, I. This trend is effectively eliminated for the tetra-ammoniates and as expected for the hexa-ammoniates. As described in Section 7.2.1, the effect of changing halide ions is a playoff between increased hydrogen bonding and loss of M-X bonding upon ammonia absorption. As such, this may be a result of weakening hydrogen bonding (on a per ammonia/halide basis) as the number of am-

monia ligands increases (effectively saturating the halides), leading to slow recovery of the originally expected trend. Table 7.1 shows the formation enthalpies of each ammoniate phase for zinc chloride, bromide and iodide.

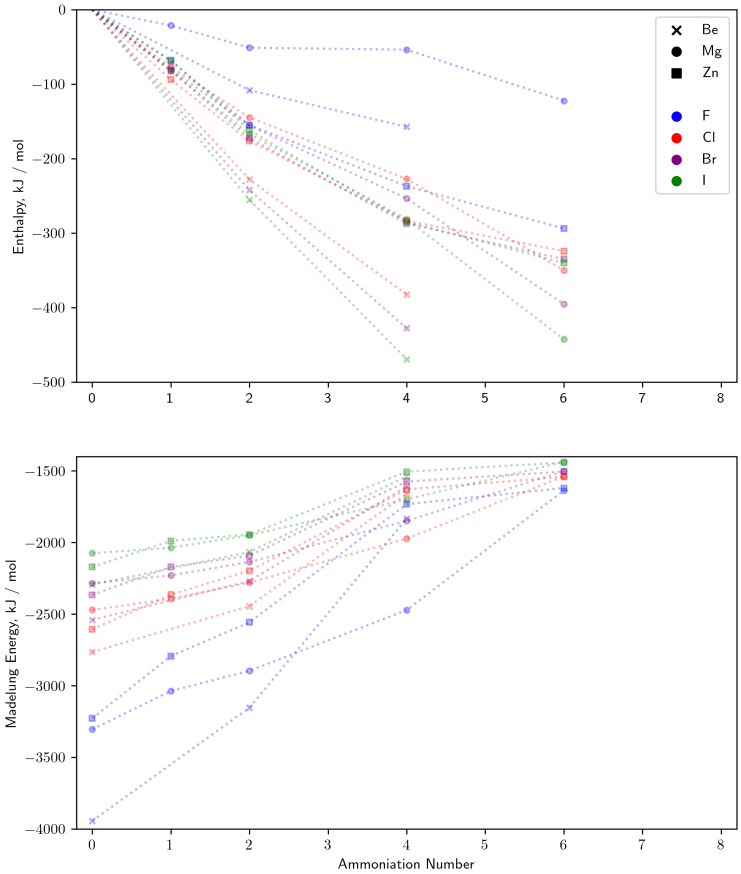


Figure 7.2: Formation enthalpies (relative to MX_2 + $n NH_3$) and Madelung energies of group II/XII metal halides (Be, Mg, Zn) calculated using CASTEP.

It should be noted that these results predict $MgX_2(NH_3)_4$ phases to be unstable (under the assumption of constant entropy changes), as is expected from previous experimental results in the literature[92]. Beryllium shows significantly greater absorption enthalpies for all halides except fluoride, due to the greater M-N bond strength. Zinc halides typically show similar/slightly larger absorption enthalpies

Table 7.1: Formation enthalpies of zinc halide ammoniates calculated using CASTEP. All values are given as kJ / mol Zn. Note the reversal and recovery of the expected trend for Madelung energy changes for low and high ammoniation numbers respectively.

	$n = 1$	$n = 2$	$n = 4$	$n = 6$
Cl	-93.8	-176.4	-283.4	-324.1
Br	-82.4	-172.3	-287.0	-334.9
I	-67.6	-161.9	-284.7	-340.1

when compared with magnesium halides, with the exception of the hexa-ammoniate phase for Cl, Br, I. This is likely a result of the covalency of bonding (stabilising ammoniate phases generally) and greater preference for tetrahedral environments for zinc (destabilising the hexa-ammoniate).

Madelung energy calculations show significantly larger changes upon absorption for beryllium, due to its smaller size. Zinc also shows larger Madelung energy changes than magnesium for absorption to low ammoniation numbers, most probably due to the preference of zinc for tetrahedral coordination environments. Each mole of NH_3 absorbed would lead to a greater reduction in Madelung energy as one of four halides is removed from the first coordination sphere, as opposed to one of six halides for magnesium. This can also be seen in the minimal change in Madelung energy from $n = 4$ to $n = 6$ for zinc halides, where halides are not removed from the first coordination sphere, but the coordination sphere is expanded to accommodate the extra NH_3 ligands. It should be remembered that Madelung energy calculations are performed using point charges on metal and halide, and, due to the covalency of Zn, Madelung energy should not be considered as important as for beryllium or magnesium.

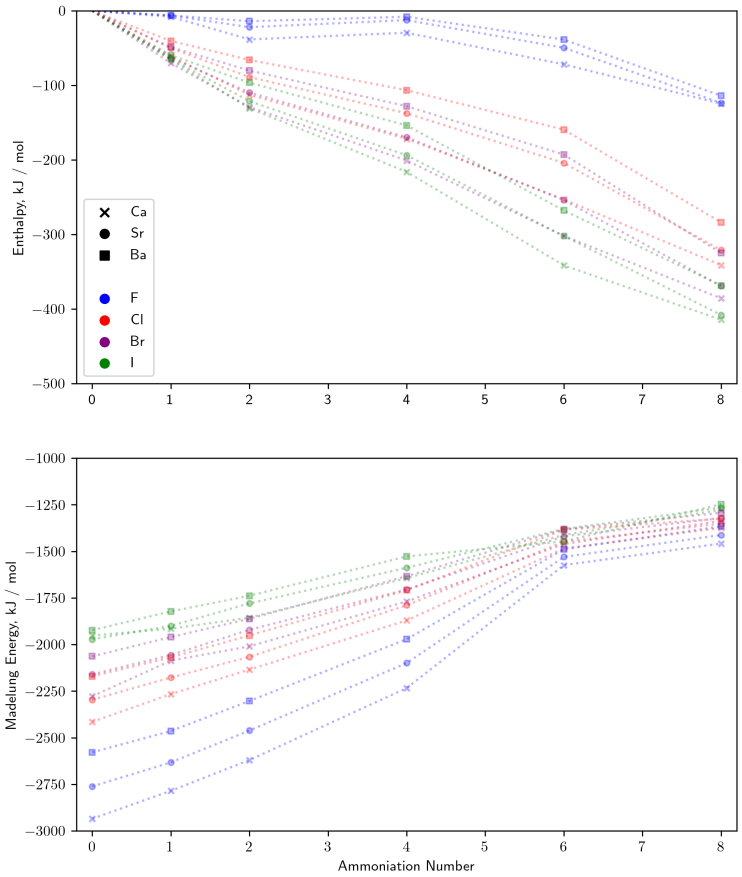


Figure 7.3: Formation enthalpies (relative to MX_2 + $n NH_3$) and Madelung energies of group II metal halides (Ca, Sr, Ba) calculated using CASTEP.

Figure 7.3 shows the formation enthalpies of ammoniate phases for calcium, strontium and barium halides. Comparison of hexa-ammoniate formation enthalpies with Figure 7.2 shows the expected trend that larger group II cations show lower formation enthalpies. As expected also, the standard trend for halides is observed, with no confounding effects such as significant covalency in bonding.

The main other consideration seen here is in the interplay between 'intermediate' ammoniate phases (n $\leq$ 6) and the octa-ammoniate phase. This is best observed by studying the formation enthalpies of the hexa-ammoniate and octa-ammoniate

phases (Table 7.2). Discussed briefly in Chapter 4, data on other metals and halides allows further examination. Increased stability of the octa-ammoniate is explained as the reduction in the effect of Madelung energy upon absorption from $n = 6$ to $n = 8$, due to the expansion of the coordination sphere, as opposed to removal of halides from the first coordination sphere. As Madelung energy is more important for lighter halides, this stabilises the octa-ammoniate relative to the hexa-ammoniate more for lighter halides. Similar trends are observed within data for strontium and barium halides.

Table 7.2: Hexa- and octa-ammoniate formation enthalpies for calcium, strontium and barium halides. Note how the difference in hexa- and octa-ammoniate formation enthalpies becomes more negative (i.e. stabilising the octa-ammoniate) as the cation is increased in size, and the halide is decreased in size.

Salt		Hexa-ammoniate Formation (kJ / mol NH_3)	Octa-ammoniate Formation (kJ / mol NH_3)	Difference (kJ / mol NH_3)
Ca	F	-12.0	-15.6	-3.6
	Cl	-42.2	-42.7	-0.5
	Br	-50.4	-48.2	2.2
	I	-56.9	-51.8	5.1
Sr	F	-8.3	-15.4	-7.1
	Cl	-34.0	-40.1	-6.1
	Br	-42.3	-46.1	-3.8
	I	-50.4	-51.0	0.6
Ba	F	-6.4	-14.2	-7.8
	Cl	-26.6	-35.5	-8.9
	Br	-32.1	-40.6	-8.5
	I	-44.6	-46.1	-1.5

Table 7.3: Ammoniation numbers of various group II metal halides, $MX_2(NH_3)_n$ [95,96].

	Be	Mg	Ca	Sr	Ba
Cl	2, 4	1, 2, 6	1, 2, 4, 8	1, 2, 8	8
Br	2, 4	1, 2, 6	1, 2, 6, 8	1, 2, 8	1, 2, 4, 8
I	2, 4	2, 6	1, 2, 6, 8	1, 2, 6, 8	2, 4, 6, 8, 9, 10

For strontium and barium, the octa-ammoniate is further stabilised relative to the hexa-ammoniate due to the greater size of the cation. Calcium typically forms octahedral complexes, rarely showing eight-fold coordination. However, a coordination number of 8 is readily accessible for strontium and barium. Table 7.3 shows data from Westman *et al.*[95] on the phases observed to be stable for each combination of group II metal and halide. For Ca, Sr and Ba, heavier metals tend to reduce the stability of intermediate ammoniate phases (by relative stabilisation of the octa-ammoniate). Lighter halides also stabilise the octa-ammoniate relative to intermediate phases due to the increased importance of the Madelung energy changes in destabilisation of these intermediate phases ($n \leq 6$). The effects discussed here are observed experimentally by the instability of 'intermediate' ammoniate phases for $CaCl_2$ ($n = 1$, 2 stable; $n = 4$ stable only over a small temperature range), $SrCl_2$ ($n = 1$, 2, 8 stable) and $BaCl_2$ ($n = 8$ stable)[95]. Similarly, $SrBr_2$ and $BaBr_2$ do not form a hexa-ammoniate, while $CaBr_2$ does[95].

7.2.3 Group III/XIII

Figure 7.4 shows the formation enthalpies of ammoniate phases for aluminium, scandium, yttrium and lutetium halides. For Al, Sc and Y, the previously observed trend showing smaller cations returning larger formation enthalpies is held. Lutetium may appear an outlier, slotting in between scandium and yttrium. However, this is an effect of the lanthanide contraction, due to the poor shielding of the 4f electrons, which do not compensate for the increase in the proton number across the lanthanide series. The expected trend for halides is also followed.

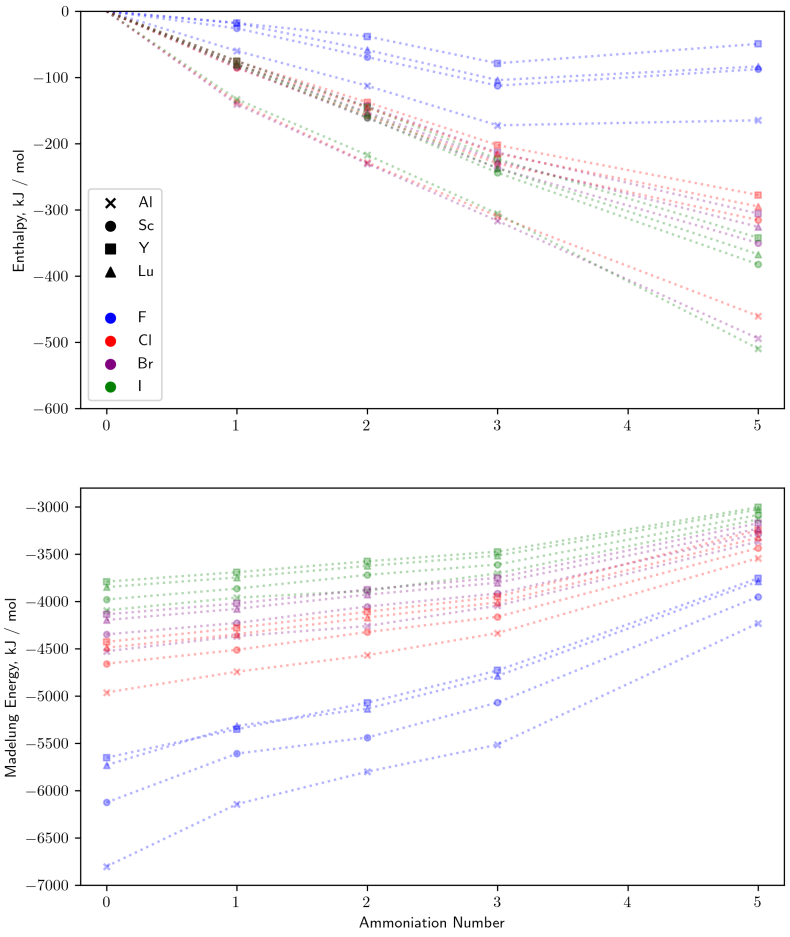


Figure 7.4: Formation enthalpies (relative to MX_3 + $n NH_3$) and Madelung energies of group III/XIII metal halides (Al, Sc, Y, Lu) calculated using CASTEP.

7.2.4 Group IV

Figure 7.5 shows the formation enthalpies of ammoniate phases for titanium, zirconium and hafnium halides. The expected trend is held for Ti and Zr, with Hf showing greater formation enthalpies, again due to the lanthanide contraction. The expected trend is held for halides also. The fluorides of the mono-ammoniate show surprisingly high formation enthalpies. This is likely a result of the eight-fold coordination environment for $ZrF_4(NH_3)$, minimising the change in Madelung energy upon absorption (only 1/8 of the halides removed from the first coordination sphere), coupled with the strong hydrogen bonding in this phase. This will be discussed further in Section 7.3, but it is reasonable to expect hydrogen bonding to become a more significant effect as the anion : cation ratio increases.

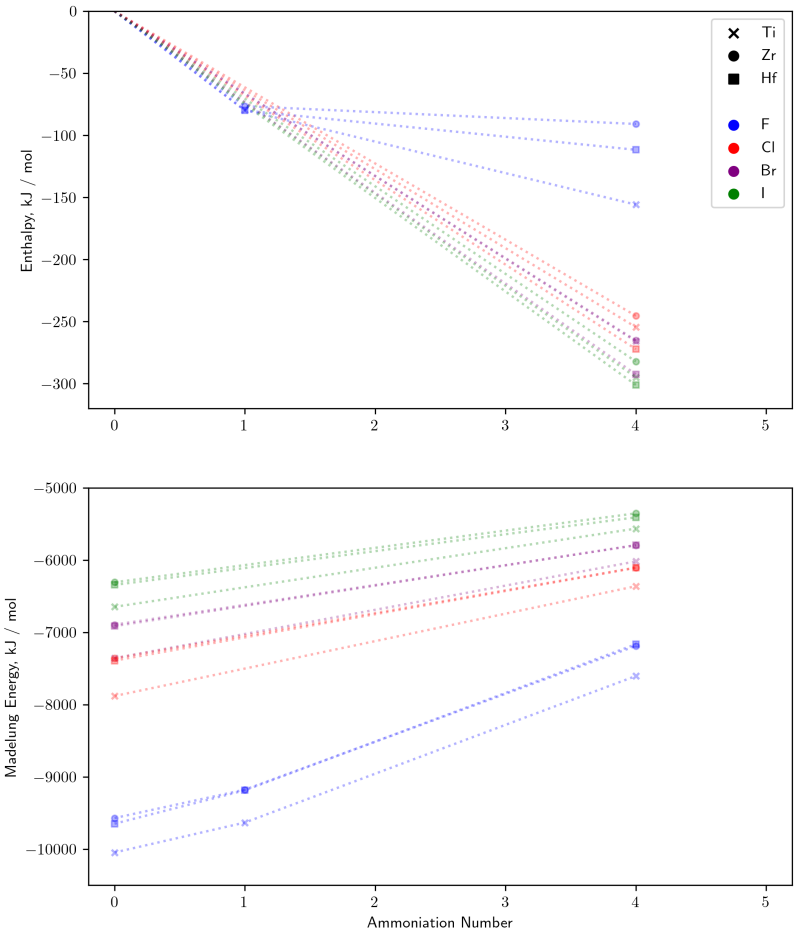


Figure 7.5: Formation enthalpies (relative to MX_4 + $n NH_3$) and Madelung energies of group IV metal halides (Ti, Zr, Hf) calculated using CASTEP.

7.3 Trends in Ammoniate Stability Within Periods

There are three main differences in the driving forces for ammoniate formation as the cation is exchanged across a period:

1. The anion : cation ratio: A greater number of anions per cation will positively impact the hydrogen bonding network formed in ammoniate phases.

2. The M-N bond strength: A cation with a greater charge will lead to a stronger M-N bond.

3. Diminishing Madelung energy: Separating an anion from a cation incurs a greater energy penalty for higher charged cations.

While distinguishing between these effects can be tricky, computational analyses provide insight into distinguishing the impact of these three trends.

Figure 7.6 shows the absorption enthalpies and relative Madelung energy changes across period 3 metal halides. It is evident that the higher the charge on the cation, the greater the absorption enthalpy. In the context of the three changes listed above, this can be explained as a result of the greater M-N bond strength, and the greater hydrogen bonding possible when more anions are present. There would be a greater reduction in Madelung energy expected for tricationic salts upon absorption. However, when considered as a proportion (bottom of Figure 7.6), this trend is reversed.

By analysing Madelung energy as a proportion of the base salt, this allows approximate comparison of the relative strength of effects 2 and 3 (assuming the M-X ionic bond and M-N covalent bond strength both scale similarly with cationic charge). It is clear from Figure 7.6 that lesser charged cations have their propor-

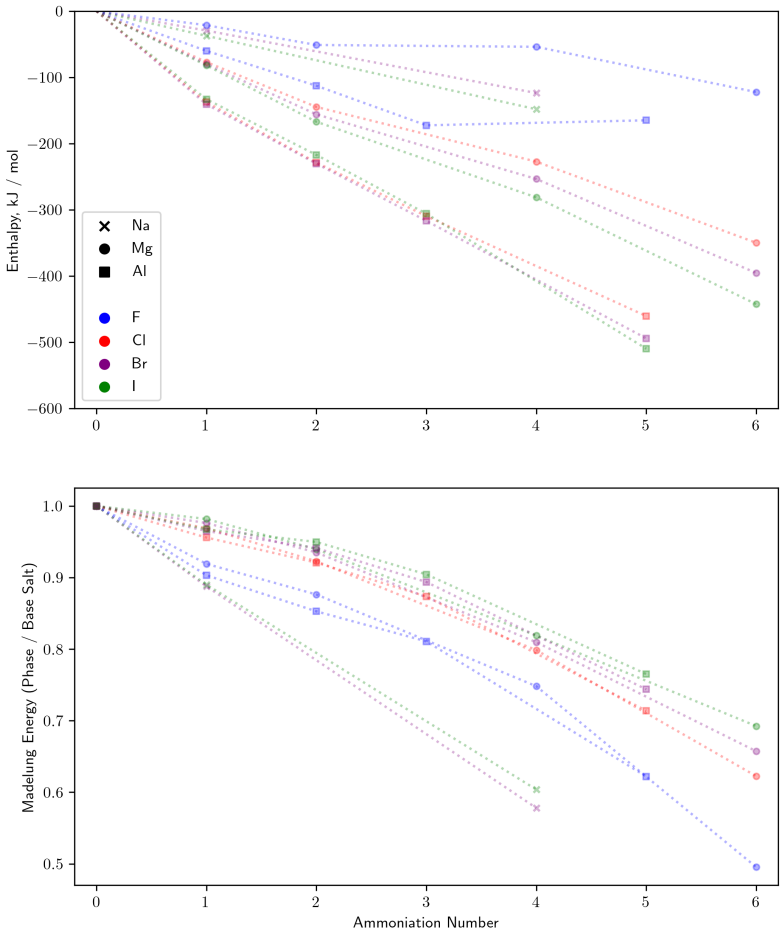


Figure 7.6: Formation enthalpies (relative to $MX_y + nNH_3$) and Madelung energies of period 3 metal halides (Na, Mg, Al) calculated using CASTEP. The Madelung energies of ammoniate phases are represented as a fraction of the Madelung energy of the base salt.

tional Madelung energy diminished more upon absorption. Due to the repulsion from like-charge ions, any deviation from a 1:1 cation : anion ratio results in a reduced scaled Madelung energy. Scaled Madelung energy is defined here as:

$$\text{Scaled Madelung Energy} = \frac{E(r_+ + r_-)}{z^+ \text{v}} \tag{7.1}$$

where $r_+ + r_-$ is the interionic distance (in Å), z^+ is the cationic charge number, and v is the number of ions in the empirical formula. Table 7.4 shows scaled Madelung energies for chlorides of all metals studied in this work. The scaled Madelung energy reduces as the cationic charge increases. This is essentially the same as originally noticed by Kapustinskii[164], where the Madelung constant for a structure is approximately 0.88v[164]. This shows that the effect of Madelung energy changes, while smaller in absolute magnitude for low charge cations, is larger in relative magnitude for low charge cations. In simple terms, the inherently higher ionic stability of 1:1 salts is a significant barrier to their absorption of small molecules. This can also be viewed as a reduction in the stability of 2:1, 3:1 and 4:1 salts, through the increased repulsion of like-charge ions.

The effect of the anion : cation ratio on hydrogen bonding can be difficult to fully ascertain the impact of as the cation increases in charge. In Section 6.2.2, it was shown that this was likely a reason for the greater absorption capacity (on a molar basis) of high zinc percentage eutectic mixtures. While the absorption enthalpies for fluoride and chloride salts could be studied across a period, these will also be impacted by the effect of Madelung energy changes, and so are not exclusively a measure of the impact of hydrogen bonding in each structure.

Figure 7.7 shows the absorption enthalpies for the metal halides studied in period 4. The trend of absorption enthalpies typically follows I > Br > Cl, due to the effect of Madelung energy changes upon absorption. However, for low ammoniation numbers and 3+ cations, this trend is loosened or reversed. It is only with the greater ammoniation numbers, whereby anions become more saturated with hydro-

Table 7.4: Scaled Madelung energy for various chloride salts studied in this work. Madelung energy is scaled according to Equation 7.1. Note how cations which are unlikely to be considered perfectly ionic (Be, Mg, Zn, Al, Ti) adopt structures with lower scaled Madelung energies than those within their group.

Salt	Scaled Madelung Energy (kJ Å mol^{-1})
HCl	-2428
LiCl	-2428
NaCl	-2428
$BeCl_2$	-1408
$MgCl_2$	-1560
$CaCl_2$	-1670
$SrCl_2$	-1750
$BaCl_2$	-1725
$ZnCl_2$	-1500
$AlCl_3$	-1293
$ScCl_3$	-1297
YCl_3	-1308
$LuCl_3$	-1301
$TiCl_4$	-1075
$ZrCl_4$	-1114
$HfCl_4$	-1113

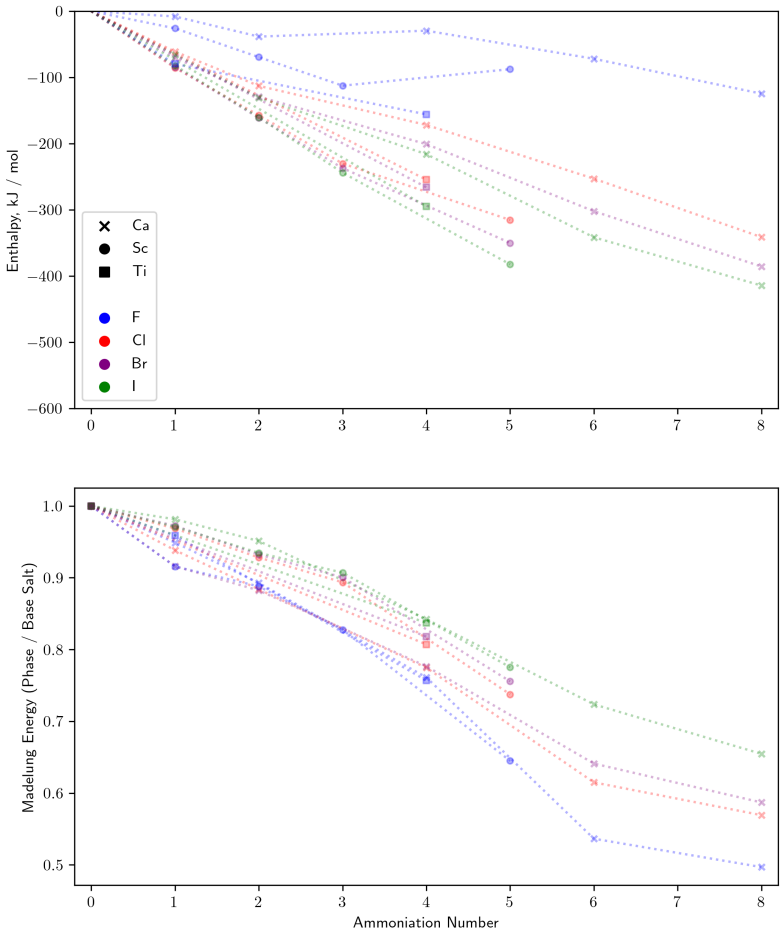


Figure 7.7: Formation enthalpies (relative to $MX_y + nNH_3$) and Madelung energies of period 4 metal halides (Ca, Sc, Ti) calculated using CASTEP. The Madelung energies of ammoniate phases are represented as a fraction of the Madelung energy of the base salt.

gen bonding, that the expected trend of the (usually dominant) effect of Madelung energy changes returns. Table 7.5 shows the formation enthalpies for various group II and III salt ammoniates. Note how, even for low ammoniation numbers, the expected trend from Madelung energy changes holds for all group II salt ammoniates (with the exception of $CaI_2(NH_3)$). In contrast, this trend is relaxed for low ammoniation numbers of group III cations. This is exemplified further by the Cl : Br : I ratio for formation enthalpies for group II and III halides. Similarly, as the ammoniation number increases, the chloride ratio generally decreases while the iodide ratio generally increases, denoting a shift towards a greater impact of Madelung energy changes and a reduced impact of hydrogen bonding.

This behaviour was also seen for zinc halides (as discussed in Section 7.2.2), and may actually be a combination of the hydrogen bonding effect and increased covalency in bonding for high (formal) charge cations.

With only two experimentally determined ammoniate structures in group IV, further analysis of this trend is difficult. However, the large absorption enthalpy of $TiF_4(NH_3)$ in Figure 7.7 may indicate further accuracy of this theory.

Hydrogen bonding appears to play an increasingly significant role as the anion : cation ratio is increased. This leads to the stabilisation of ammoniates involving high-charge cations, in particular phases with low ammoniation numbers (prior to approaching saturation of halides), and light halides, such as F and Cl, which show strong hydrogen bonding.

Table 7.5: Formation enthalpies of selected group II and III halide ammoniates calculated using CASTEP. All values are given as kJ / mol metal. Note how group II metal halides always follow the trend expected from Madelung energy changes, except for $CaI_2(NH_3)$, while group III metal halides only follow this trend for higher ammoniation numbers. The ratios of formation enthalpies for halides is also given. In both groups II and III, the trend expected from Madelung energy changes appears diminished or reversed (high Cl ratio, low I ratio) for low ammoniation numbers (due to the greater influence of hydrogen bonding prior to saturation of the halides).

		$n = 1$	$n = 2$	$n = 3$	$n = 4$	$n = 5$	$n = 6$
Mg	Cl	-76.9	-144.6		-227.2		-349.8
	Br	-79.9	-155.8		-253.4		-395.4
	I	-81.8	-167.0		-281.2		-442.5
	Ratio (Cl : Br : I)	0.96 : 1 : 1.02	0.93 : 1 : 1.07		0.90 : 1 : 1.11		0.88 : 1 : 1.12
Ca	Cl	-61.0	-112.8		-171.8		-253.0
	Br	-70.2	-129.1		-200.8		-302.1
	I	-65.6	-130.7		-216.0		-341.5
	Ratio (Cl : Br : I)	0.87 : 1 : 0.93	0.87 : 1 : 1.01		0.86 : 1 : 1.08		0.84 : 1 : 1.13
Sr	Cl	-50.1	-88.9		-137.5		-204.1
	Br	-63.0	-109.7		-169.6		-254.0
	I	-64.8	-121.2		-193.8		-302.1
	Ratio (Cl : Br : I)	0.80 : 1 : 1.03	0.81 : 1 : 1.10		0.81 : 1 : 1.14		0.80 : 1 : 1.19
Al	Cl	-137.3	-228.6	-309.5		-460.5	
	Br	-140.6	-230.3	-316.7		-494.2	
	I	-133.0	-217.1	-305.9		-509.8	
	Ratio (Cl : Br : I)	0.98 : 1 : 0.95	0.99 : 1 : 0.94	0.98 : 1 : 0.97		0.93 : 1 : 1.03	
Sc	Cl	-85.7	-157.2	-230.1		-315.4	
	Br	-84.4	-161.2	-237.0		-350.1	
	I	-82.1	-160.3	-244.0		-382.3	
	Ratio (Cl : Br : I)	1.02 : 1 : 0.97	0.98 : 1 : 0.99	0.97 : 1 : 1.03		0.90 : 1 : 1.09	
Y	Cl	-75.5	-137.5	-202.3		-277.6	
	Br	-75.8	-143.5	-213.1		-305.7	
	I	-75.2	-144.9	-223.2		-342.1	
	Ratio (Cl : Br : I)	1.00 : 1 : 0.99	0.96 : 1 : 1.01	0.95 : 1 : 1.05		0.91 : 1 : 1.12	

7.4 Conclusions and Future Work

A broad view of metal halide ammoniates, through the use of DFT calculations in CASTEP, has enabled a greater understanding of the driving forces behind ammoniate formation. Lighter metals lead to greater absorption enthalpies on account of their greater M-N bond strength, despite the greater Madelung energy change that results from the use of a smaller cation. Heavier halides tend to lead to greater absorption enthalpies for group I and II cations, and high ammoniation number phases of group III and IV. This was rationalised as a consequence of greater Madelung energy changes upon absorption for smaller halides. The exception to this trend for the low ammoniation number phases of group III and IV is seen as a result of the greater importance of hydrogen bonding in these materials (due to the higher anion : cation ratio). Prior to approaching saturation of the halides, the strong hydrogen bonding of these phases enables reversal of this trend. However, this was also seen for zinc halides and thus may also result from an increase in the covalency of M-X bonding.

Much of the reasoning applied in this chapter also applies to hydrate formation. However, due to the replacement of a hydrogen atom with a lone pair upon exchange of ammonia for water, the hydrogen bonding network in hydrates can often involve O···H hydrogen bonding, rather than exclusively hydrogen-halide bonding as observed in ammoniates. This would diminish the effect that halide substitution has on hydrogen bonding and thus hydrate stability.

Previous experimental work has generally focused on group II metal halides for ammoniate formation, likely due to the lower number of anions and thus generally greater ammonia density (volumetrically or gravimetrically). However, the significantly increased absorption enthalpies of group III metal halides, coupled with partial reversal of the trend expected from Madelung energy changes alone, indicate that further detailed experimental study of group III metal halides may be promising for high temperature ammonia absorption, such as from the Haber-Bosch process.

As discussed in Section 1.4.3, efficient thermal energy storage solutions involving NH_3 sorbents requires storage of NH_3 as a liquid. Vaporisation of liquid NH_3 thus reduces the effective energy density of these systems. As a result, while the ratio of absorption enthalpies for $ScCl_3(NH_3)$ and $CaCl_2(NH_3)$ is 1.40, it is increased to 1.66 when the enthalpy of vaporisation of NH_3 is accounted for (23.4 kJ/mol[165]). This is even more dramatic for $AlCl_3(NH_3)$ and $MgCl_2(NH_3)$ (1.79 to 2.13), though applications of $AlCl_3$ may be limited by its volatility.

Extensions of this work include the study of a greater range of cations, such as transition metals, and also further study of metals showing significant covalency, such as the heavier metals of groups XIII (Ga, In, Tl) and XIV (Sn, Pb). While contributing to a greater understanding, metal halides with high degrees of covalency tend to give very low melting and boiling points, limiting their use in applications.

8

Conclusion

Metal halide ammoniates have a role to play in enabling the storage of energy directly (e.g. thermal energy storage) or indirectly through the use of ammonia as a synthetic fuel (e.g. as ammonia storage systems or for separation of ammonia from the Haber-Bosch process). This thesis explores these materials in depth with a view to the applications in a zero-carbon future.

The $^{1}H/^{2}D$ positions of any rotating ammonia molecule in 3D space were derived using only the Ca-N bond vector, the H-N-H bond angle and the N-H bond length, enabling solution of all ammoniate structures of $CaCl_2$ and $CaBr_2$ through *in-situ* PND. Many of these were confirmed via PXRD also, though phases which are unstable at room temperature without ammonia pressure could only be studied via PND. The previously unknown mono-ammoniate phase of $CaCl_2$ and $CaBr_2$ crys-

tallises in a layered, polar $Cmc2_1$ structure, with strong hydrogen bonding holding the layers together. The previously unknown $CaCl_2(NH_3)_4$ structure crystallises in an AAA-stacked P3 unit cell, with octahedra of $CaCl_2(NH_3)_4$ stacked perfectly on top of one another, enabling optimal hydrogen bonding. Other stacking motifs were checked but did not give adequate fits to the data.

Through detailed STA experiments and CASTEP calculations, it was shown that the temperature stability of calcium halide ammoniate phases is primarily modified according to the anionic size, with hydrogen bond strength only becoming a deciding factor once the first coordination sphere of the metal is saturated. As such, $CaCl_2$ ammoniate phases decompose at lower temperatures than their equivalent $CaBr_2$ ammoniate phases, with the exception of $CaCl_2(NH_3)_8$.

Solid solutions of calcium chloride-bromide were synthesised, before analysis of their ammonia absorption properties. Through analysis of *in-situ* PND patterns, solid solutions of the anhydrous phase, the mono-ammoniate and the octa-ammoniate phase were stable, while phase separation occurred for intermediate phases (the di-ammoniate and hexa-ammoniate). However, this phase separation and recombination occurred rapidly, proceeding even at room temperature for the octa-ammoniate phase.

The absorption pathways observed at room temperature for $CaCl_2$, $CaBr_2$ and CaClBr exhibited very different behaviour. $CaCl_2$ would typically absorb to form the di-ammoniate phase, then proceed stepwise to the octa-ammoniate via the tetra-ammoniate. $CaBr_2$ would typically absorb to form the hexa-ammoniate phase, then proceed to the octa-ammoniate phase. However, during the absorption period at room temperature, CaClBr always consisted of $> 90\%$ anhydrous and octa-ammoniate phase. It appears that the presence of both halide ions leads to rapid absorption from the unstable intermediate phases (the di- and hexa-ammoniate), potentially enabling faster ammonia absorption kinetics for CaClBr.

The possibility of ammonia separation from the Haber-Bosch process using metal halide eutectics was demonstrated. While the development is in an early stage, the presence of dicationic salts is crucial in absorption capacity, due to the greater number of anions and hence hydrogen bonds formed with absorbed ammonia molecules. Through compositional variation, it was also shown that the identity of supposedly non-absorbing salts is crucial, with replacement of potassium by sodium revealing a $> 1.5\times$ ammonia absorption capacity (comparison of 60:40 $ZnCl_2$:MCl samples). While not initially expected, there is clearly significant interaction between the group I metal salts and the absorbed ammonia molecules in these melts.

Extended beyond calcium halides, CASTEP and Madelung energy calculations revealed trends in ammoniate phase formation among different metal halide salts. While Madelung energy has been described as a factor in ammonia absorption previously[92], the extent and limitations of this approach were discovered in Chapter 7. Madelung energy is a decisive factor in determining the ammonia absorption strength for ammoniate phases of group I and II metal salts. However, for group III and IV salts, when there is greater anionic repulsion and more halide ions are available for hydrogen bonding, it was shown that this trend is reversed for low ammoniation number phases. As such, the greatest absorption enthalpies were seen for light tri- and tetra-cationic metal chloride salts, such as $AlCl_3$ and $TiCl_4$.

Combining the results of Chapters 6 and 7, future work on high temperature ammonia absorption into metal halide eutectics should look to study the effect of 3+ cation salts in these systems, particularly those with not excessive melting points such as YCl_3 (721 °C). These salts can form part of a eutectic melt enabling high ammonia absorption capacities at Haber-Bosch temperatures.

The thermodynamic, crystallographic and computational measurements given in this thesis provide a detailed understanding of the calcium halide-ammonia systems, with extension to metal halide systems as a whole. Alongside the chemical under-

standing gained, a novel approach to high temperature ammonia separation using molten metal chloride salts opens a new area of research in the goal of improving the efficiency of ammonia synthesis.

Bibliography

[1] John van Zalk and Paul Behrens. The spatial extent of renewable and non-renewable power generation: A review and meta-analysis of power densities and their application in the U.S. *Energy Policy*, 123(2018):83–91, 2018.

[2] The Paris Agreement. https://unfccc.int/process-and-meetings/the-paris-agreement.

[3] Analysis: Global CO2 emissions from fossil fuels hit record high in 2022. https://www.carbonbrief.org/analysis-global-co2-emissions-from-fossil-fuels-hit-record-high-in-2022/, 2022.

[4] Climate change: No 'credible pathway' to 1.5C limit, UNEP warns. https://www.un.org/sustainabledevelopment/blog/2022/10/climate-change-no-credible-pathway-to-1-5c-limit-unep-warns/, 2022.

[5] Climate change and health. https://www.who.int/news-room/fact-sheets/detail/climate-change-and-health, 2021.

[6] Global Wind Atlas. https://globalwindatlas.info/en/.

[7] Extreme heat: Preparing for the heat waves of the future. https://www.ifrc.org/document/extreme-heat-preparing-heat-waves-future, 2022.

[8] Analysis: Which countries are historically responsible for climate change? https://www.carbonbrief.org/analysis-which-countries-are-historically-responsible-for-climate-change/, 2021.

[9] Global Solar Atlas. https://globalsolaratlas.info/map.

[10] Solar (photovoltaic) panel prices. https://ourworldindata.org/grapher/solar-pv-prices.

[11] With 2,245 MW of Commissioned Solar Projects, World's Largest Solar Park is Now at Bhadla. https://mercomindia.com/world-largest-solar-park-bhadla/, 2020.

[12] Vincent K.M. Cheng and Geoffrey P. Hammond. Life-cycle energy densities and land-take requirements of various power generators: A UK perspective. *Journal of the Energy Institute*, 90:201–213, 2017.

[13] We Could Power The Entire World By Harnessing Solar Energy From 1% Of The Sahara. https://www.forbes.com/sites/quora/2016/09/22/we-could-power-the-entire-world-by-harnessing-solar-energy-from-1-of-the-sahara/?sh=71a03ae8d440, 2016.

[14] Hornsea 2, the world's largest windfarm, enters full operation. https://orsted.com/en/media/newsroom/news/2022/08/20220831559011, 2022.

[15] Nuclear Energy. https://ourworldindata.org/nuclear-energy, 2022.

[16] Storage and Disposal of Radioactive Waste. https://world-nuclear.org/information-library/nuclear-fuel-cycle/nuclear-waste/storage-and-disposal-of-radioactive-waste.aspx, 2023.

[17] List of small modular reactor designs. https://en.wikipedia.org/wiki/List_of_small_modular_reactor_designs.

[18] Global number of small modular reactor (SMR) projects in 2022, by power generation capacity and development status. https://www.statista.com/statistics/1334632/number-of-small-modular-reactor-projects-worldwide/, 2023.

[19] Rolls Royce Reveals 440 MW Commercial Reactor Design. https://neutronbytes.com/2019/11/09/rolls-royce-reveals-440-mw-commecial-reactor-design/, 2019.

[20] Sizewell C nuclear power station. https://en.wikipedia.org/wiki/Sizewell_C_nuclear_power_station.

[21] Hydropower Special Market Report. https://www.iea.org/reports/hydropower-special-market-report/executive-summary, 2021.

[22] Three Gorges project operates at full capacity. https://www.waterpowermagazine.com/news/newsthree-gorges-project-operates-at-full-capacity-9074272, 2021.

[23] PPA Insights: Solar radiation and wind speed data. https://www.kyos.com/ppa-insight-on-solar-radiation-and-wind-speed-data/, 2020.

[24] DESERTEC. www.desertec.org.

[25] Arturs Purvins, Luigi Sereno, Mircea Ardelean, Catalin Felix Covrig, Tilemahos Efthimiadis, and Philip Minnebo. Submarine power cable between Europe and North America: A techno-economic analysis. *Journal of Cleaner Production*, 186:131–145, 2018.

[26] Total final consumption by sector, OECD, 1971-2019. https://www.iea.org/data-and-statistics/charts/total-final-consumption-by-sector-oecd-1971-2019.

[27] Energy consumption in transport by fuel in the Net Zero Scenario, 2000-2030. https://www.iea.org/data-and-statistics/charts/energy-consumption-in-transport-by-fuel-in-the-net-zero-scenario-2000-2030.

[28] Cars, planes, trains: where do CO2 emissions from transport come from? https://ourworldindata.org/co2-emissions-from-transport.

[29] World's first net zero transatlantic flight to fly from London in 2023. https://www.gov.uk/government/news/worlds-first-net-zero-transatlantic-flight-to-fly-from-london-in-2023.

[30] The role of renewables in decarbonising the aviation sector. https://www.icao.int/environmental-protection/Documents/EnvironmentalReports/2022/ENVReport2022_Art47.pdf, 2022.

[31] Global Freight Demand to Triple by 2050. https://www.maritime-executive.com/article/global-freight-demand-to-triple-by-2050.

[32] Digest of UK Energy Statistics (DUKES): energy. https://www.gov.uk/government/statistics/energy-chapter-1-digest-of-united-kingdom-energy-statistics-dukes.

[33] Scaling Up Retrofit 2050. https://www.theiet.org/impact-society/factfiles/built-environment-factfiles/retrofit-2050/.

[34] Shares of residential energy consumption by end use in selected IEA countries, 2019. https://www.iea.org/data-and-statistics/charts/shares-of-residential-energy-consumption-by-end-use-in-selected-iea-countries-2019.

[35] T. Pauschinger. *Advanced District Heating and Cooling (DHC) Systems*, chapter 5 - Solar thermal energy for district heating. Woodhead Publishing Series in Energy, 2016.

[36] Michael Papapetrou, George Kosmadakis, Andrea Cipollina, Umberto La Commare, and Giorgio Micale. Industrial waste heat: Estimation of the technically available resource in the EU per industrial sector, temperature level and country. *Applied Thermal Engineering*, 138(April):207–216, 2018.

[37] Alberto Benato and Anna Stoppato. Pumped Thermal Electricity Storage: A technology overview. *Thermal Science and Engineering Progress*, 6:301–315, 2018.

[38] L. I.M. Asri, W. N.S.F.W. Ariffin, A. S.M. Zain, J. Nordin, and N. S. Saad. Comparative Study of Energy Storage Systems (ESSs). *Journal of Physics: Conference Series*, 1962(012035), 2021.

[39] Felix Leach, Gautam Kalghatgi, Richard Stone, and Paul Miles. The scope for improving the efficiency and environmental impact of internal combustion engines. *Transportation Engineering*, 1(April), 2020.

[40] Beate Baensch-Baltruschat, Birgit Kocher, Friederike Stock, and Georg Reifferscheid. Tyre and road wear particles (TRWP) - A review of generation, properties, emissions, human health risk, ecotoxicity, and fate in the environment. *Science of the Total Environment*, 733:137823, 2020.

[41] New rapid, wireless bus charging technology introduced as part of the capital's journey to zero emission. https://tfl.gov.uk/info-for/media/press-releases/2022/october/new-rapid-wireless-bus-charging-technology-introduced-as-part-of-the-capital-s-journey-to-zero-emission.

[42] China takes the lead in adopting the all-electric bus equipped with supercapacitors. https://www.escomponents.com/blog/2017/10/11/china-takes-the-lead-in-adopting-the-all-electric-bus-equipped-with-supercapacitors.

[43] The Tesla 4680: Does Size Matter? https://www.aboutenergy.io/post/the-tesla-4680-does-size-matter.

[44] Alexander Bills, Shashank Sripad, William Leif Fredericks, Madalsa Singh, and Venkatasubramanian Viswanathan. Performance Metrics Required of Next-Generation Batteries to Electrify Commercial Aircraft. *ACS Energy Letters*, 5:663–668, 2020.

[45] ARENA backs eight big batteries to bolster grid. https://arena.gov.au/blog/arena-backs-eight-big-batteries-to-bolster-grid/.

[46] Energy consumption in Australia. https://www.worlddata.info/oceania/australia/energy-consumption.php.

[47] Commodities at a Glance: Special issue on strategic battery raw materials. https://unctad.org/publication/commodities-glance-special-issue-strategic-battery-raw-materials.

[48] Davide Castelvecchi. Electric cars and batteries: how will the world produce enough? *Nature*, 596:336–339, 2021.

[49] Mineral Commodity Summaries 2022. https://pubs.usgs.gov/publication/mcs2022.

[50] How many cars are there in the world? https://www.whichcar.com.au/news/how-many-cars-are-there-in-the-world.

[51] K. M. Abraham. How Comparable Are Sodium-Ion Batteries to Lithium-Ion Counterparts? *ACS Energy Letters*, 5:3544–3547, 2020.

[52] Methane Pyrolysis for Hydrogen– Opportunities and Challenges. https://www.energy.gov/sites/default/files/2021-09/h2-shot-summit-panel2-methane-pyrolysis.pdf.

[53] Bernard Chukwudi Tashie-Lewis and Somtochukwu Godfrey Nnabuife. Hydrogen Production, Distribution, Storage and Power Conversion in a Hydrogen Economy - A Technology Review. *Chemical Engineering Journal Advances*, 8:100172, 2021.

[54] Specific Energy and Energy Density of Fuels. https://neutrium.net/properties/specific-energy-and-energy-density-of-fuels/.

[55] A. Valera-Medina, H. Xiao, M. Owen-Jones, W. I.F. David, and P. J. Bowen. Ammonia for power. *Progress in Energy and Combustion Science*, 69:63–102, 2018.

[56] Materials-Based Hydrogen Storage. https://www.energy.gov/eere/fuelcells/materials-based-hydrogen-storage.

[57] Hydrogen refuelling stations worldwide. https://www.h2stations.org/.

[58] ZEROe: Towards the world's first hydrogen-powered commercial aircraft. https://www.airbus.com/en/innovation/low-carbon-aviation/hydrogen/zeroe, 2020.

[59] Konstantin Räuchle, Ludolf Plass, Hans Jürgen Wernicke, and Martin Bertau. Methanol for Renewable Energy Storage and Utilization. *Energy Technology*, 4:193–200, 2016.

[60] Collin Smith and Laura Torrente-Murciano. Exceeding Single-Pass Equilibrium with Integrated Absorption Separation for Ammonia Synthesis Using Renewable Energy—Redefining the Haber-Bosch Loop. *Advanced Energy Materials*, 11, 2021.

[61] Matthew J. Kale, Deepak K. Ojha, Sayandeep Biswas, Joshua I. Militti, Alon V. Mccormick, Jeffrey H. Schott, Paul J. Dauenhauer, and E. L. Cussler. Optimizing Ammonia Separation via Reactive Absorption for Sustainable Ammonia Synthesis. *ACS Applied Energy Materials*, 3(3):2576–2584, 2020.

[62] Mahdi Malmali, Michael Reese, Alon V. McCormick, and E. L. Cussler. Converting Wind Energy to Ammonia at Lower Pressure. *ACS Sustainable Chemistry and Engineering*, 6(1):827–834, 2018.

[63] Collin Smith, Alon V. McCormick, and E. L. Cussler. Optimizing the Conditions for Ammonia Production Using Absorption. *ACS Sustainable Chemistry and Engineering*, 7(4):4019–4029, 2019.

[64] Collin Smith, Mahdi Malmali, Chen Yu Liu, Alon V. McCormick, and E. L. Cussler. Rates of Ammonia Absorption and Release in Calcium Chloride. *ACS Sustainable Chemistry and Engineering*, 6(9):11827–11835, 2018.

[65] Lingting Ye, Hao Li, and Kui Xie. Sustainable ammonia production enabled by membrane reactor. *Nature Sustainability*, 5:787–794, 2022.

[66] Tingting Wu, Wenjun Fan, Yang Zhang, and Fuxiang Zhang. Electrochemical synthesis of ammonia: Progress and challenges. *Materials Today Physics*, 16:100310, 2021.

[67] Hiroki Miyaoka, Hikaru Miyaoka, Tomoyuki Ichikawa, Takayuki Ichikawa, and Yoshitsugu Kojima. Highly purified hydrogen production from ammonia for PEM fuel cell. *International Journal of Hydrogen Energy*, 43:14486–14492, 2018.

[68] Mandeep Singh, Dario Zappa, and Elisabetta Comini. Solid oxide fuel cell: Decade of progress, future perspectives and challenges. *International Journal of Hydrogen Energy*, 46:27643–27674, 2021.

[69] Ayman M. Elbaz, Shixing Wang, Thibault F. Guiberti, and William L. Roberts. Review on the recent advances on ammonia combustion from the fundamentals to the applications. *Fuel Communications*, 10:100053, 2022.

[70] Lupeng Han, Sixiang Cai, Min Gao, Jun Ya Hasegawa, Penglu Wang, Jianping Zhang, Liyi Shi, and Dengsong Zhang. Selective Catalytic Reduction of NOx with NH3 by Using Novel Catalysts: State of the Art and Future Prospects. *Chemical Reviews*, 119:10916–10976, 2019.

[71] World first: Siemens Gamesa begins operation of its innovative electrothermal energy storage system. `https://www.siemensgamesa.com/newsroom/2019/06/190612-siemens-gamesa-inauguration-energy-system-thermal`, 2020.

[72] John Allison, Keith Bell, Joe Clarke, Andrew Cowie, Ahmed Elsayed, Graeme Flett, Gbemi Oluleye, Adam Hawkes, Graeme Hawker, Nick Kelly, Maria Manuela Marinho de Castro, Tim Sharpe, Andy Shea, Paul Strachan, and Paul Tuohy. Assessing domestic heat storage requirements for energy flexibility over varying timescales. *Applied Thermal Engineering*, 136:602–616, 2018.

[73] Xin Xiao, Hongwei Jia, Dongsheng Wen, Yousef Golizadeh Akhlaghi, and Ali Badiei. Experimental investigation of a latent heat thermal energy storage unit encapsulated with molten salt/metal foam composite seeded with nanoparticles. *Energy and Built Environment*, 4:74–85, 2023.

[74] Tina Block and Martin Schmücker. Metal oxides for thermochemical energy storage: A comparison of several metal oxide systems. *Solar Energy*, 126:195–207, 2016.

[75] P. A.J. Donkers, L. C. Sögütoglu, H. P. Huinink, H. R. Fischer, and O. C.G. Adan. A review of salt hydrates for seasonal heat storage in domestic applications. *Applied Energy*, 199:45–68, 2017.

[76] Andrew K. Galwey and Geneviève M. Laverty. The thermal decomposition of magnesium chloride dihydrate. *Thermochimica Acta*, 138:115–127, 1989.

[77] Na Gao, Lisheng Deng, Jun Li, Hongyu Huang, Bin Zhou, and You Zhou. Multiform heat storage performance of expanded graphite based CaCl2 composites for low-grade heat source. *Energy Reports*, 8:12117–12125, 2022.

[78] B. Shabani, M. Hafttananian, Sh Khamani, A. Ramiar, and A. A. Ranjbar. Poisoning of proton exchange membrane fuel cells by contaminants and impurities: Review of mechanisms, effects, and mitigation strategies. *Journal of Power Sources*, 427:21–48, 2019.

[79] Wen Jing Jiang, Fu Yu Zhong, Yong Liu, and Kuan Huang. Effective and Reversible Capture of NH3 by Ethylamine Hydrochloride Plus Glycerol Deep Eutectic Solvents. *ACS Sustainable Chemistry and Engineering*, 7:10552–10560, 2019.

[80] Lu Zhang, Haifeng Dong, Shaojuan Zeng, Zongyuan Hu, Shahid Hussain, and Xiangping Zhang. An Overview of Ammonia Separation by Ionic Liquids. *Industrial and Engineering Chemistry Research*, 60:6908–6924, 2021.

[81] Dawei Shang, Xiangping Zhang, Shaojun Zeng, Kun Jiang, Hongshuai Gao, Haifeng Dong, Qingyuan Yang, and Suojiang Zhang. Protic ionic liquid [Bim][NTf2] with strong hydrogen bond donating ability for highly efficient ammonia absorption. *Green Chemistry*, 19:937, 2017.

[82] Wei Chen, Shiqiang Liang, Yongxian Guo, Xiaohong Gui, and Dawei Tang. Investigation on vapor – liquid equilibria for binary systems of metal ion-containing ionic liquid [bmim] Zn 2 Cl 5 / NH 3 by experiment and modified UNIFAC model. *Fluid Phase Equilibria*, 360:1–6, 2013.

[83] Junli Wang, Shaojuan Zeng, Feng Huo, Dawei Shang, Hongyan He, Lu Bai, Xiangping Zhang, and Jianwei Li. Metal chloride anion-based ionic liquids for efficient separation of NH3. *Journal of Cleaner Production*, 206:661–669, 2019.

[84] Fu Yu Zhong, Hai Long Peng, Duan Jian Tao, Ping Keng Wu, Jie Ping Fan, and Kuan Huang. Phenol-Based Ternary Deep Eutectic Solvents for Highly Efficient and Reversible Absorption of NH3. *ACS Sustainable Chemistry and Engineering*, 7:3258–3266, 2019.

[85] Xiaoxue Sun, Qinghua Wang, Shenghan Wu, Xinyu Zhao, Ligang Wei, Kunlan Li, Jingai Hao, Li Wei, Shangru Zhai, and Qingda An. Metal chlorides-promoted ammonia absorption of deep eutectic solvent. *International Journal of Hydrogen Energy*, 47:16121–16131, 2022.

[86] Adam J. Rieth, Yuri Tulchinsky, and Mircea Dincã. High and Reversible Ammonia Uptake in Mesoporous Azolate Metal-Organic Frameworks with Open Mn, Co, and Ni Sites. *Journal of the American Chemical Society*, 138:9401–9404, 2016.

[87] Yang Chen, Yadan Du, Puxu Liu, Jiangfeng Yang, Libo Li, and Jinping Li. Removal of Ammonia Emissions via Reversible Structural Transformation in M(BDC) (M = Cu, Zn, Cd) Metal-Organic Frameworks. *Environmental Science and Technology*, 54:3636–3642, 2020.

[88] Xue Han, Wanpeng Lu, Yinlin Chen, Ivan Da Silva, Jiangnan Li, Longfei Lin, Weiyao Li, Alena M. Sheveleva, Harry G.W. Godfrey, Zhenzhong Lu, Floriana Tuna, Eric J.L. McInnes, Yongqiang Cheng, Luke L. Daemen, Laura J.Mc Cormick Mcpherson, Simon J. Teat, Mark D. Frogley, Svemir Rudić, Pascal Manuel, Anibal J. Ramirez-Cuesta, Sihai Yang, and Martin Schröder. High Ammonia Adsorption in MFM-300 Materials: Dynamics and Charge Transfer in Host-Guest Binding. *Journal of the American Chemical Society*, 143:3153–3161, 2021.

[89] Benjamin E.R. Snyder, Ari B. Turkiewicz, Hiroyasu Furukawa, Maria V. Paley, Ever O. Velasquez, Matthew N. Dods, and Jeffrey R. Long. A ligand insertion mechanism for cooperative NH3 capture in metal-organic frameworks. *Nature*, 613:287–291, 2023.

[90] Lars H. Jepsen, Young Su Lee, Radovan Černý, Ram S. Sarusie, Young Whan Cho, Flemming Besenbacher, and Torben R. Jensen. Ammine Calcium and Strontium Borohydrides: Syntheses, Structures, and Properties. *ChemSusChem*, 8(20):3472–3482, 2015.

[91] Taihei Aoki, Takayuki Ichikawa, Hiroki Miyaoka, and Yoshitsugu Kojima. Thermodynamics on ammonia absorption of metal halides and borohydrides. *Journal of Physical Chemistry C*, 118(32):18412–18416, 2014.

[92] Martin Owen Jones, David M. Royse, Peter P. Edwards, and William I.F. David. The structure and desorption properties of the ammines of the group II halides. *Chemical Physics*, 427:38–43, 2013.

[93] A. Kapustinsky. Allgemeine formel für die gitterenergie von kristallen beliebiger struktur. *Zeitschrift für Physikalische Chemie*, 22B(1):257–260, 1933.

[94] E. R.T. Bevers, P. J. Van Ekeren, W. G. Haije, and H. A.J. Oonk. Thermodynamic properties of lithium chloride ammonia complexes for application in a high-lift high temperature chemical heat pump. *Journal of Thermal Analysis and Calorimetry*, 86(3):825–832, 2006.

[95] Sven Westman, Per-Erik Werner, Thomas Schuler, and Wiktor Raldow. X-Ray Investigations of Ammines of Alkaline Earth Metal Halides. I. The Structures of CaCl2(NH3)8, CaCl2(NH3)2 and the Decomposition Product CaClOH. *Acta Chemica Scandinavica*, 35a:467–472, 1981.

[96] Matthias Müller and Magnus R. Buchner. Preparation and crystal structures of the beryllium ammines [Be(NH3)4]X2 (X = Br, I, CN, SCN, N3) and Be(NH3)2X'2 (X' = Cl, Br, I). *Chemical Communications*, 55:13649–13652, 2019.

[97] Mitsuhiro Kubota, Keiichi Matsuo, Ryo Yamanouchi, and Hitoki Matsuda. Absorption and desorption characteristics of NH3 with metal chlorides for ammonia storage. *Journal of Chemical Engineering of Japan*, 47(7):542–548, 2014.

[98] Linus Pauling. The nature of the chemical bond. IV. The energy of single bonds and the relative electronegativity of atoms. *Journal of the American Chemical Society*, 54(9):3570–3582, 1932.

[99] Douglas R. Ketchum, George L. Schimek, William T. Pennington, and Joseph W. Kolis. Synthesis of new Group III fluoride-ammonia adducts in supercritical ammonia: Structures of AlF3(NH3)2 and InF2(NH2)(NH3). *Inorganica Chimica Acta*, 294:200–206, 1999.

[100] Christian Plitzko, Michael Strecker, and Gerd Meyer. Synthese und kristallstruktur der "fluorid-ammoniakate" Zr(NH3)F4 und Hf(NH3)F4. *Zeitschrift fur Anorganische und Allgemeine Chemie*, 623:79–83, 1997.

[101] A. Leineweber, M. W. Friedriszik, and H. Jacobs. Preparation and Crystal Structures of Mg(NH3)2Cl2, Mg(NH3)2Br2 and Mg(NH3)2I2. *Journal of Solid State Chemistry*, 147:229–234, 1999.

[102] Gustav F. Hüttig. Uber die Ammoniakate der Calciumhalogenide. 1922.

[103] T. Yan, R. Z. Wang, and T. X. Li. Experimental investigation on thermochemical heat storage using manganese chloride / ammonia. *Energy*, 143:562–574, 2018.

[104] Mark S. Huberty, Andrew L. Wagner, Alon McCormick, and Edward Cussler. Ammonia absorption at Haber Process Conditions. *AIChE Journal*, 58(11):3526–3532, 2012.

[105] Heath H. Himstedt, Mark S. Huberty, Alon McCormick, Lanny D. Schmidt, and Edward Cussler. Ammonia synthesis enhanced by magnesium chloride absorption. *AIChE Journal*, 61(4):1364–1371, 2015.

[106] Chun Yi Liu and Ken Ichi Aika. Absorption and desorption behavior of ammonia with alkali earth halide and mixed halide. *Chemistry Letters*, 2(8):798–799, 2002.

[107] Chun Yi Liu and Ken Ichi Aika. Effect of the Cl/Br molar ratio of a CaCl2-CaBr2 mixture used as an ammonia storage material. *Industrial and Engineering Chemistry Research*, 43(22):6994–7000, 2004.

[108] Chun Yi Liu and Ken Ichi Aika. Ammonia Absorption on Alkaline Earth Halides as Ammonia Separation and Storage Procedure. *Bulletin of the Chemical Society of Japan*, 77:123–131, 2004.

[109] Chun Yi Liu and Ken Ichi Aika. Ammonia absorption into alkaline earth metal halide mixtures as an ammonia storage material. *Industrial and Engineering Chemistry Research*, 43(23):7484–7491, 2004.

[110] Marc Widenmeyer, Thomas C. Hansen, Elke Meissner, and Rainer Niewa. Formation and decomposition of iron nitrides observed by in situ powder neutron diffraction and thermal analysis. *Zeitschrift fur Anorganische und Allgemeine Chemie*, 640(7):1265–1274, 2014.

[111] Robert Juza and Werner Sachsze. Zur kenntnis des systems nickel/stickstoff. metallamide und metallnitride. *Zeitschrift für anorganische und allgemeine Chemie*, 251(2):201–212, 1943.

[112] Robert Juza and Werner Sachsze. Über das system kobalt/stickstoff. metallamide und metallnitride. *Zeitschrift für anorganische Chemie*, 253(1-2):95–108, 1945.

[113] Joshua W Makepeace, Thomas J Wood, Hazel M A Hunter, O Jones, and William I F David. Ammonia decomposition catalysis using non-stoichiometric lithium imide. *Chemical Science*, 6:3805–3815, 2015.

[114] Simultaneous Thermal Analyzer – STA 449 F3 Jupiter. `https://analyzing-testing.netzsch.com/_Resources/Persistent/6/b/7/4/6b74b138b6dc4aee6d104a4f385a1ba8638e124f/STA_449_F3_Jupiter_en_web.pdf`, 2024.

[115] W. Friedrich, P. Knipping, and M. Laue. Interferenzerscheinungen bei röntgenstrahlen. *Annalen der Physik*, 346(10):971–988, 1913.

[116] William Henry Bragg and William Lawrence Bragg. The reflection of x-rays by crystals. *Proc. R. Soc. Lond. A*, 88:428–438, 1913.

[117] NIST Centre for Neutron Research. `https://www.ncnr.nist.gov/resources/n-lengths/`, 2021.

[118] Isotopes of Hydrogen. `https://www.britannica.com/science/hydrogen/Isotopes-of-hydrogen`.

[119] Y. Kume, Y. Miyazaki, T. Matsuo, H. Suga, W. I.F. David, and R. M. Ibberson. A strong isotope effect in the low-temperature property of ammonium hexachlorotellurate. *Euro Physics Letters*, 16(3):265–270, 1991.

[120] R. I. Smith, S. Hull, M. G. Tucker, H. Y. Playford, D. J. McPhail, S. P. Waller, and S. T. Norberg. The upgraded Polaris powder diffractometer at the ISIS neutron source. *Review of Scientific Instruments*, 90, 2019.

[121] Christopher J. Howard, Brendan J. Kennedy, and Caroline Curfs. Temperature-induced structural changes in CaCl2, CaBr2, and CrCl2: A synchrotron x-ray powder diffraction study. *Physical Review B - Condensed Matter and Materials Physics*, 72, 2005.

[122] Patrick Woidy, Antti J. Karttunen, Thomas G. Müller, and Florian Kraus. The unusual coordination sphere in the octaammine calcium(II) ions of [Ca(NH3)8]Br2 and [Ca(NH3)8]I2 and the thermal decomposition of the iodide to [Ca(NH3)6]I2. *Zeitschrift fur Naturforschung - Section B Journal of Chemical Sciences*, 69:1141–1148, 2014.

[123] H. M. Rietveld. A profile refinement method for nuclear and magnetic structures. *Journal of Applied Crystallography*, 2(2):65–71, Jun 1969.

[124] TOPAS Academic. `http://www.topas-academic.net/`, 2024.

[125] W. Kohn and L. J. Sham. Self-Consistent Equations Including Exchange and Correlation Effects. *Physical Review Letters*, 140(4A), 1965.

[126] John P. Perdew, Kieron Burke, and Matthias Ernzerhof. Generalized Gradient Approximation Made Simple. *Physical Review Letters*, 77(18), 1996.

[127] CASTEP. `http://www.castep.org/`.

[128] P. P. Ewald. Die Berechnung optischer und elektrostatischer gitterpotentiale. 1921.

[129] Erwin Madelung. Das elektrische feld in systemen von regelmäßig angeordneten punktladungen. *Physikalische Zeitschrift*, 19:524–533, 1919.

[130] Ewald.py. `https://github.com/materialsproject/pymatgen/blob/master/pymatgen/analysis/ewald.py`, 2024.

[131] Atkins, Peter and Overton, Tina and Rourke, Jonathan and Weller, Mark and Armstrong, Fraser and Hagerman, Michael. *Shriver and Atkins' Inorganic Chemistry (Fifth Ed.)*. W.H. Freeman and Company, 2010.

[132] CRC Handbook. *CRC Handbook of Chemistry and Physics, 97th Edition*. CRC Press, 2016-2017.

[133] F London. The general theory of molecular forces. *Transactions of The Faraday Society*, 33:8–26, 1937.

[134] R. D. Shannon. Revised effective ionic radii and systematic studies of interatomic distances in halides and chalcogenides. *Acta Crystallographica Section A*, 32(5):751–767, Sep 1976.

[135] Rasmus Z. Sørensen, Jens S. Hummelshøj, Asbjørn Klerke, Jacob Birke Reves, Tejs Vegge, Jens K. Nørskov, and Claus H. Christensen. Indirect, reversible high-density hydrogen storage in compact metal ammine salts. *Journal of the American Chemical Society*, 130(27):8660–8668, 2008.

[136] W.E. Wentworth, D.W. Johnston, and W.M. Raldow. Chemical heat pumps using a dispersion of a metal salt ammoniate in an inert solvent. *Solar Energy*, 26(2):141–146, 1981.

[137] Calcium Chloride - A Guide to Physical Properties. `https://www.oxy.com/siteassets/documents/chemicals/products/other-essentials/173-01791.pdf`, 2021.

[138] V.V. Tyagi and D. Buddhi. Thermal cycle testing of calcium chloride hexahydrate as a possible pcm for latent heat storage. *Solar Energy Materials and Solar Cells*, 92(8):891–899, 2008.

[139] Mingyang Sun, Tianze Liu, Xinlei Wang, Tong Liu, Mulin Li, Guijun Chen, Haonan Sha, and Dongyue Jiang. Calcium chloride hexahydrate based supercooling phase change material for a long-term recovery of low-grade thermal energy. *Applied Thermal Engineering*, 243:122663, 2024.

[140] Peter Pang. *A Thermodynamic Study of High Temperature Equilibria involving Zinc Chloride*. PhD thesis, University of London, 1988.

[141] Shuiliang Zhou, Shaobo Shen, Dalong Zhao, Zhitao Zhang, and Shiyu Yan. Evaporation and decomposition of eutectics of cupric chloride and sodium chloride. *Journal of Thermal Analysis and Calorimetry*, 129:1445–1452, 2017.

[142] E. Döneges. *Handbook of Preparative Inorganic Chemistry, 2nd Ed.* 1963.

[143] Dieter Fischer and Martin Jansen. Synthesis and Structure of Na3N. *Angewandte Chemie International Edition*, 41(10):1755–1756, 2002.

[144] D. Fischer, Z. Cancarevic, J. C. Schön, and M. Jansen. Zur Synthese und Struktur von K3N. *Zeitschrift für anorganische und allgemeine Chemie*, 630(1):156–160, 2004.

[145] Matthias Müller and Magnus R. Buchner. Preparation and crystal structures of the beryllium ammines [be(nh3)4]x2 (x = br, i, cn, scn, n3) and be(nh3)2x'2 (x' = cl, br, i). *Chem. Commun.*, 55:13649–13652, 2019.

[146] Egon Wiberg. *Inorganic Chemistry*. Elsevier, 2001.

[147] Fujian Zong, Chunzhan Meng, Zhiming Guo, Feng Ji, Hongdi Xiao, Xijian Zhang, Jin Ma, and Honglei Ma. Synthesis and characterization of magnesium nitride powder formed by Mg direct reaction with N2. *Journal of Alloys and Compounds*, 508(1):172–176, 2010.

[148] P. Ehrlich. *Handbook of Preparative Inorganic Chemistry, 2nd Ed.* 1963.

[149] K.S. Weil. The synthesis of transition metal nitrides via thermolysis of metal–ammine complexes, part i: Chromium nitride. *Journal of Solid State Chemistry*, 181(1):199–210, 2008.

[150] Si Ping-Zhan, Jiang Wei, Wang Hai-Xia, Zhong Min, Ge Hong-Liang, Choi Chul-Jin, and Lee Jung-Goo. The high nitrogen pressure synthesis of manganese nitride. *Chinese Physics Letters*, 29(12):128101, 2012.

[151] Janet M. Newman, Malcolm Binns, Trevor W. Hambley, and Hans C. Freeman. Redetermination of the crystal structure of hexaamminecobalt(ii) chloride. *Inorganic Chemistry*, 30(18):3499–3502, 1991.

[152] M. T. Lowry. *Inorganic Chemistry*. Macmillan, 1922.

[153] Herbert Jacobs and Felix O. Schröder. Penta-Ammoniates of Aluminium Halides: The Crystal Structures of AlX3·5NH3 with X = Cl, Br, I. *Zeitschrift für anorganische und allgemeine Chemie*, 628(5):951–955, 2002.

[154] Samuel Rogers, Matthew Dargusch, and Damon Kent. Impacts of temperature and time on direct nitridation of aluminium powders for preparation of aln reinforcement. *Materials*, 16(4), 2023.

[155] Hisanori Yamane, Yutaka Mikawa, and Chiaki Yokoyama. Penta-amminechlorogallium(III) dichloride. *Acta Crystallographica Section E*, 63(2):i59–i61, Feb 2007.

[156] M Shibata, T Furuya, H Sakaguchi, and S Kuma. Synthesis of gallium nitride by ammonia injection into gallium melt. *Journal of Crystal Growth*, 196(1):47–52, 1999.

[157] FACT Salt Phase Diagrams - Centre for Research in Computational Thermochemistry. `https://www.crct.polymtl.ca/fact/documentation/FTsalt/FTsalt_Figs.htm`.

[158] Willhelm Biltz and Carl Messerknecht. Uber die Ammoniakate der Zinkhalogenide. 1923.

[159] D. Zagorac, H. Müller, S. Ruehl, J. Zagorac, and S. Rehme. Recent developments in the Inorganic Crystal Structure Database: theoretical crystal structure data and related features. *Journal of Applied Crystallography*, 52(5):918–925, Oct 2019.

[160] Simon A. Cotton, Paul R. Raithby, Alexander Shield, and Jack M. Harrowfield. A comparison of the structural chemistry of scandium, yttrium, lanthanum and lutetium: A contribution to the group 3 debate. *Coordination Chemistry Reviews*, 455:214366, 2022.

[161] H. L. Yakel and J. Brynestad. Refinement of the crystal structure of orthorhombic zinc chloride. *Inorganic Chemistry*, 17(11):3294–3296, 1978.

[162] H. Winkler and B. Brehler. Ueber das alpha- und beta-Zn Cl2. *Naturwissenschaften*, 46:553–554, 1959.

[163] Kristallstrukturuntersuchungen an ZnCl2. *Zeitschrift für Kristallographie*, 115(5-6):373–402, 1961.

[164] A. F. Kapustinskii. Lattice energy of ionic crystals. *Q. Rev. Chem. Soc.*, 10:283–294, 1956.

[165] Roy Overstreet and W. F. Giauque. Ammonia. the heat capacity and vapor pressure of solid and liquid. heat of vaporization. the entropy values from thermal and spectroscopic data. *Journal of the American Chemical Society*, 59(2):254–259, 1937.

[166] Herbert Jacobs and Martin Friedriszik. Synthese und Kristallstruktur der Monoammoniakate von Lithiumhalogeniden: LiBr·NH3 und LiI·NH3. *Zeitschrift für anorganische und allgemeine Chemie*, 630(1):167–170, 2004.

[167] H. W. W. Adrian and D. Feil. The structure of NH_4F as determined by neutron and X-ray diffraction. *Acta Crystallographica Section A*, 25(3):438–444, May 1969.

[168] Yulia V. Nelyubina, Alexander A. Korlyukov, and Konstantin A. Lyssenko. Experimental charge density evidence for pnicogen bonding in a crystal of ammonium chloride. *ChemPhysChem*, 16(3):676–681, 2015.

[169] Herbert Jacobs, Holger Barlage, and Martin Friedriszik. Vergleich der Kristallstrukturen der Tetraammoniakate von Lithiumhalogeniden, LiBr·4NH3 und LiI·4NH3, mit der Struktur von Tetramethylammoniumiodid, N(CH3)4I. *Zeitschrift für anorganische und allgemeine Chemie*, 630(5):645–648, 2004.

[170] Steen Lysgaard, Andreas L. Ammitzbøll, Rune E. Johnsen, Poul Norby, Ulrich J. Quaade, and Tejs Vegge. Resolving the stability and structure of strontium chloride amines from equilibrium pressures, XRD and DFT. *International Journal of Hydrogen Energy*, 37(24):18927–18936, 2012. 2011 International Workshop on Molten Carbonates & Related Topics.

[171] A. Leineweber, H. Jacobs, and H. Ehrenberg. Crystal Structure of Ni(NH3)Cl2 and Ni(NH3)Br2. *Zeitschrift für anorganische und allgemeine Chemie*, 626(10):2146–2152, 2000.

[172] K. N. Semenenko, E. B. Lobkovskii, O. V. Kravchenko, V. B. Polyakova, and I. I. Korobov. Structure and vibrational spectra of aluminium chloride monoammoniate. *Koordinatsionnaya Khimiya*, 4:1649–1652, 1978.

[173] Herbert Jacobs and Felix O. Schröder. Monoammoniates of Aluminium Halides: The Crystal Structures of AlBr3 · NH3 and AlI3 · NH3. *Zeitschrift für anorganische und allgemeine Chemie*, 628(2):327–329, 2002.

[174] Gerd Meyer and Diana Klein. Zwei neue Ammoniakate des Scandiumtrichlorides, ScCl3(NH3) und ScCl3(NH3)2. *Zeitschrift fur Anorganische und Allgemeine Chemie*, 628:1447–1450, 2002.

[175] H. Jacobs and B. Nöcker. AlCl3 2NH3 - eine Verbindung mit der Kristallstruktur eines Tetraammindichloroaluminium-tetrachloroaluminats - [AlCl2(NH3)4]+[AlCl4]-. *Zeitschrift für anorganische und allgemeine Chemie*, 614(8):25–29, 1992.

[176] Stephan Bremm and Gerd Meyer. Metallampullen als Mini-Autoklaven: Synthese und Kristallstrukturen der Ammoniakate [Al(NH3)4Cl2][Al(NH3)2Cl4] und (NH4)2[Al(NH3)4Cl2][Al(NH3)2Cl4]Cl2. *Zeitschrift für anorganische und allgemeine Chemie*, 627(3):407–410, 2001.

[177] Herbert Jacobs and Felix O. Schröder. Penta-Ammoniates of Aluminium Halides: The Crystal Structures of AlX3·5NH3 with X = Cl, Br, I. *Zeitschrift für anorganische und allgemeine Chemie*, 628(5):951–955, 2002.

[178] A. Brager. An X-ray examination of titanium nitride III. *Acta Physicochimica (USSR)*, 9:617–632, 1939.

Appendix A

The definition of deuterium occupancies in the mono-ammoniate structure must be symmetric around $\theta = 0°$ and $\theta = 180°$, due to the mirror plane symmetry. The function used must also satisfy $\theta = \theta + 120°$ due to the three-fold symmetry of the ND_3 molecule. A function of the below form achieves this:

$$\text{occ} = \frac{1}{6}\big(1.5 + \alpha_3 \cos(3\theta) + \alpha_6 \cos(6\theta)\big) \tag{1}$$

As $\cos x = \cos(x + 360°)$, this satisfies the requirement of local three-fold symmetry ($\cos 3\theta = \cos(3(\theta + 120°)) = \cos(3\theta + 360°)$). The same logic applies to the $\cos 6\theta$ term with $\cos x = \cos(x + 720°)$. Similarly, $\cos x = \cos -x$, and thus this function is symmetric around $\theta = 0°$. This function is also symmetric around $\theta = 180°$ as $\cos(180° - x) = \cos(180° + x)$.

Offsets are commonly used in circular harmonic equations. However, this is not done here as the inclusion of an offset breaks the mirror plane symmetry. Including an offset would use the function below:

$$\text{occ} = \frac{1}{6}\Big(1.5 + \alpha_3 \cos\big(3(\theta + \phi)\big) + \alpha_6 \cos\big(6(\theta + \phi)\big)\Big) \tag{2}$$

This function breaks the mirror plane symmetry as it is not symmetric about $\theta = 0°$, as $\cos(x + \phi) \neq \cos(-x + \phi)$. The same logic can be applied to show that it is also not symmetric about $\theta = 180°$.

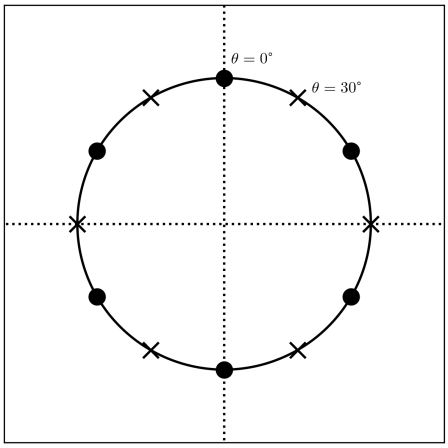


Figure A.1: The definition of 'equivalent' deuterium sites in the Cmmm di-ammoniate structure. The circle depicts the circle of possible deuterium positions (viewed along the N-Ca vector). The markers denote positions used in refinement (every 30°). Positions with the same marker were assigned the same occupancy. The local three fold rotational symmetry of the ND_3 molecule, and the symmetry of the space group (mirror planes denoted as dotted lines), is preserved under this approach.

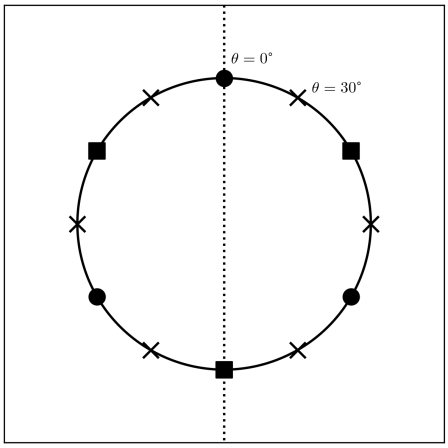


Figure A.2: The definition of 'equivalent' deuterium sites in the Cmce di-ammoniate structure. The circle depicts the circle of possible deuterium positions (viewed along the N-Ca vector). The markers denote positions used in refinement (every 30°). Positions with the same marker were assigned the same occupancy. The local three fold rotational symmetry of the ND_3 molecule, and the symmetry of the space group (mirror plane denoted as a dotted line), is preserved under this approach.

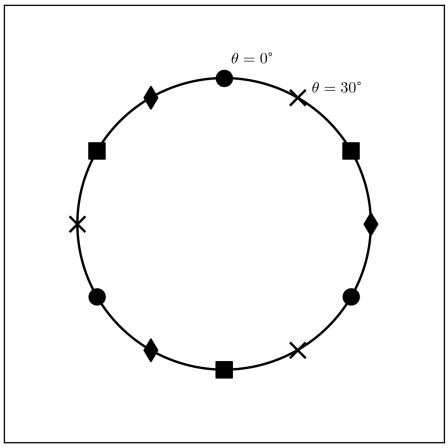


Figure A.3: The definition of 'equivalent' deuterium sites in the tetra-ammoniate structure. The circle depicts the circle of possible deuterium positions (viewed along the N-Ca vector). The markers denote positions used in refinement (every 30°). Positions with the same marker were assigned the same occupancy. The local three fold rotational symmetry of the ND_3 molecule is preserved under this approach.

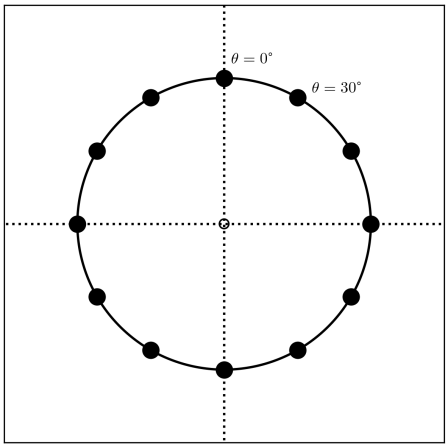
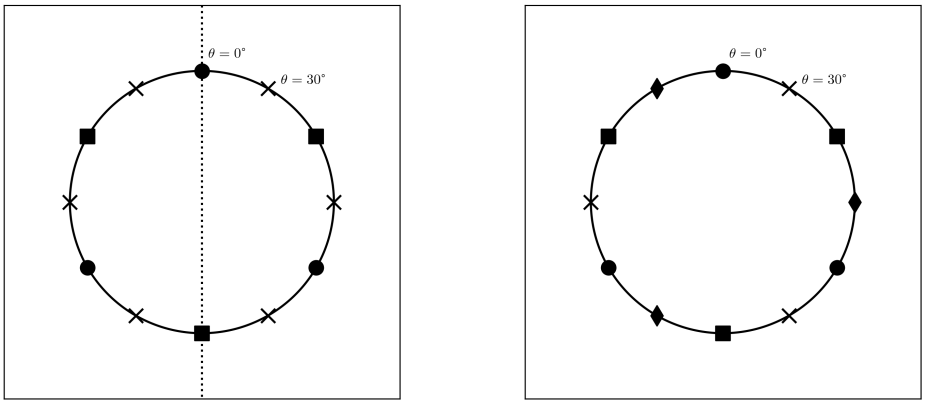


Figure A.4: The definition of 'equivalent' deuterium sites in the hexa-ammoniate structure. The circle depicts the circle of possible deuterium positions (viewed along the N-Ca vector). The markers denote positions used in refinement (every 30°). Positions with the same marker were assigned the same occupancy. The local three fold rotational symmetry of the ND_3 molecule, and the symmetry of the space group (mirror plane denoted as a dotted line, inversion centre as an empty circle), is preserved under this approach.



(a) **(b)**

Figure A.5: The definition of 'equivalent' deuterium sites in the octa-ammoniate structure. The circle depicts the circle of possible deuterium positions (viewed along the N-Ca vector). The markers denote positions used in refinement (every 30°). Positions with the same marker were assigned the same occupancy. The local three fold rotational symmetry of the ND_3 molecule, and the symmetry of the space group (mirror plane denoted as a dotted line), is preserved under this approach. (a) shows the diagram for the ammonia molecule (nitrogen atom) on the 4c Wyckoff site, while (b) shows the diagram for the ammonia molecule on the 8d Wyckoff site.

Table A.1: Data on 'strong' hydrogen bonds in geometry optimised $CaCl_2(NH_3)_2$ phases.

Structure	H-Cl distance (Å)	N-H-Cl angle (°)	N-H distance (Å)
Cmmm	2.519	167.2	1.0280
	2.554	164.5	1.0280
	2.566	165.1	1.0277
	2.612	162.8	1.0273
	2.640	163.2	1.0269
	2.650	161.5	1.0268
	2.671	163.0	1.0272
	2.704	159.4	1.0266
Cmce	2.646	154.0	1.0256
	2.646	154.0	1.0258
	2.648	153.6	1.0255
	2.648	153.6	1.0258
	2.661	154.2	1.0257
	2.662	154.3	1.0256
	2.673	153.3	1.0255
	2.673	153.3	1.0254

Table A.2: Data on 'strong' hydrogen bonds in geometry optimised $CaBr_2(NH_3)_2$ phases.

Structure	H-Br distance (Å)	N-H-Br angle (°)	N-H distance (Å)
Cmmm	2.787	160.2	1.0275
	2.801	159.4	1.0267
	2.806	159.4	1.0269
	2.810	159.2	1.0272
	2.822	159.7	1.0271
	2.831	159.2	1.0271
	2.834	159.3	1.0265
	2.885	157.5	1.0269
Cmce	2.755	155.4	1.0266
	2.755	155.4	1.0272
	2.759	155.0	1.0271
	2.760	155.0	1.0271
	2.762	154.7	1.0267
	2.762	154.7	1.0267
	2.762	154.6	1.0265
	2.762	154.6	1.0265

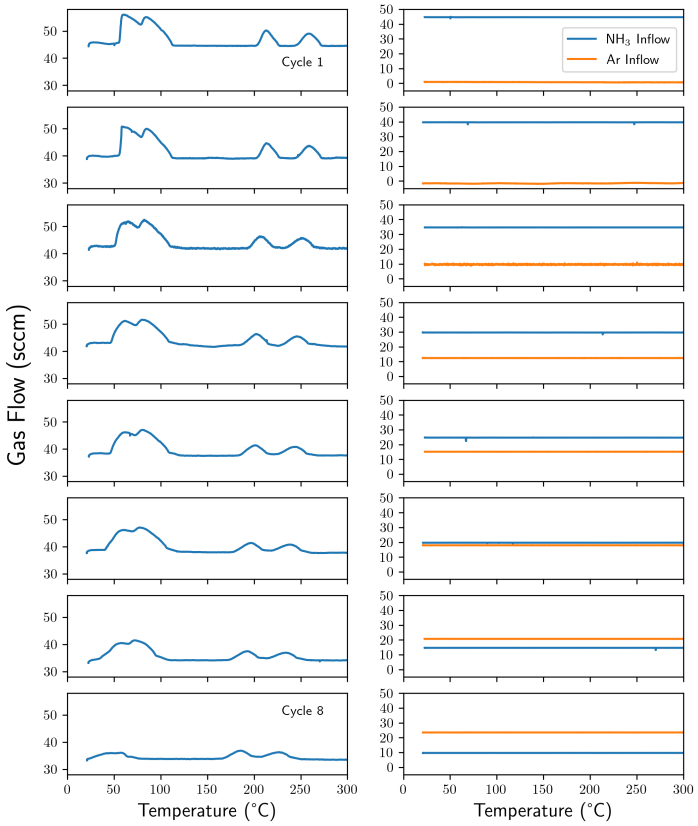


Figure A.6: Variable pressure desorption cycles for $CaCl_2$. Peaks in the MFM reading (left) show a desorption event (phase transitions). Data on the right show the relevant inflows used to modify the partial pressure of NH_3 in the system (total pressure ≈ 4.5 bar). MFC data (right) is shown as recorded i.e. The Ar inflow depicted here has not been adjusted to account for the gas conversion factor. The partial pressure of NH_3 in each cycle can be calculated by adjusting the argon inflow by its GCF (1.80) and multiplying the ammonia gas fraction by the system pressure (4.5 bar).

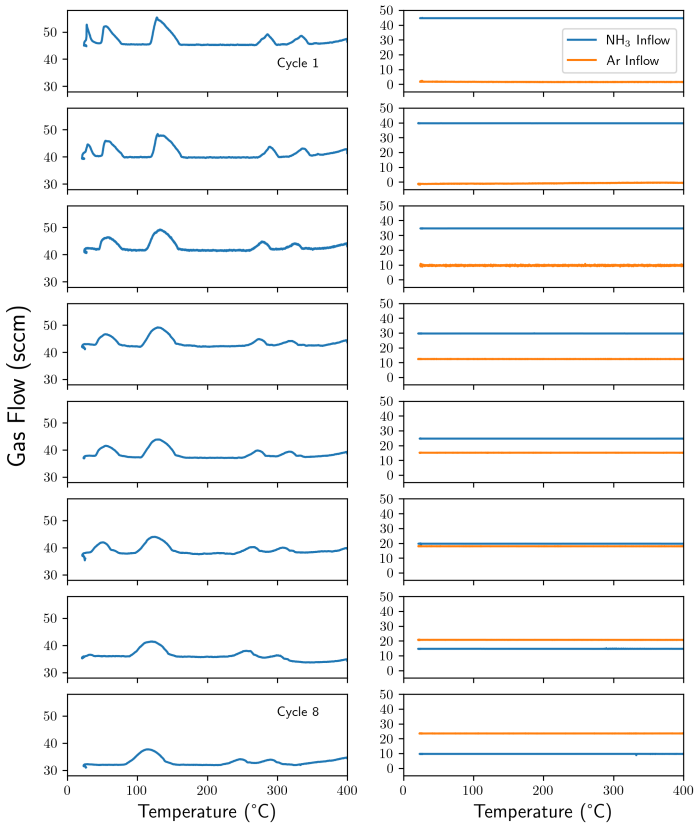


Figure A.7: Variable pressure desorption cycles for $CaBr_2$. Peaks in the MFM reading (left) show a desorption event (phase transitions). Data on the right show the relevant inflows used to modify the partial pressure of NH_3 in the system (total pressure $\approx 4.5\,\text{bar}$). MFC data (right) is shown as recorded i.e. The Ar inflow has not been adjusted to account for the gas conversion factor. The partial pressure of NH_3 in each cycle can be calculated by adjusting the argon inflow by its GCF (1.80) and multiplying the ammonia gas fraction by the system pressure (4.5 bar). Note the disappearance of the deliquescent transition after the initial two high pressure cycles ($P_{NH_3} > 4\,\text{bar}$), and the disappearance of the octa-ammoniate desorption in the final two low pressure cycles ($P_{NH_3} < 1.3\,\text{bar}$).

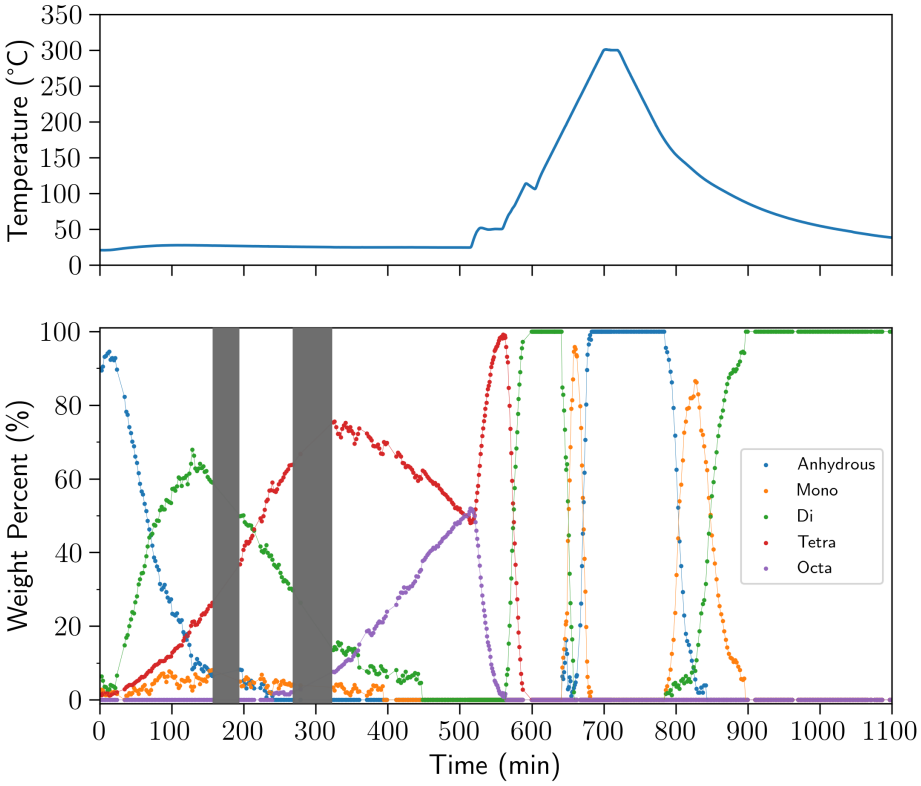


Figure A.8: Weight percent of phases in the $CaCl_2$ PND data.

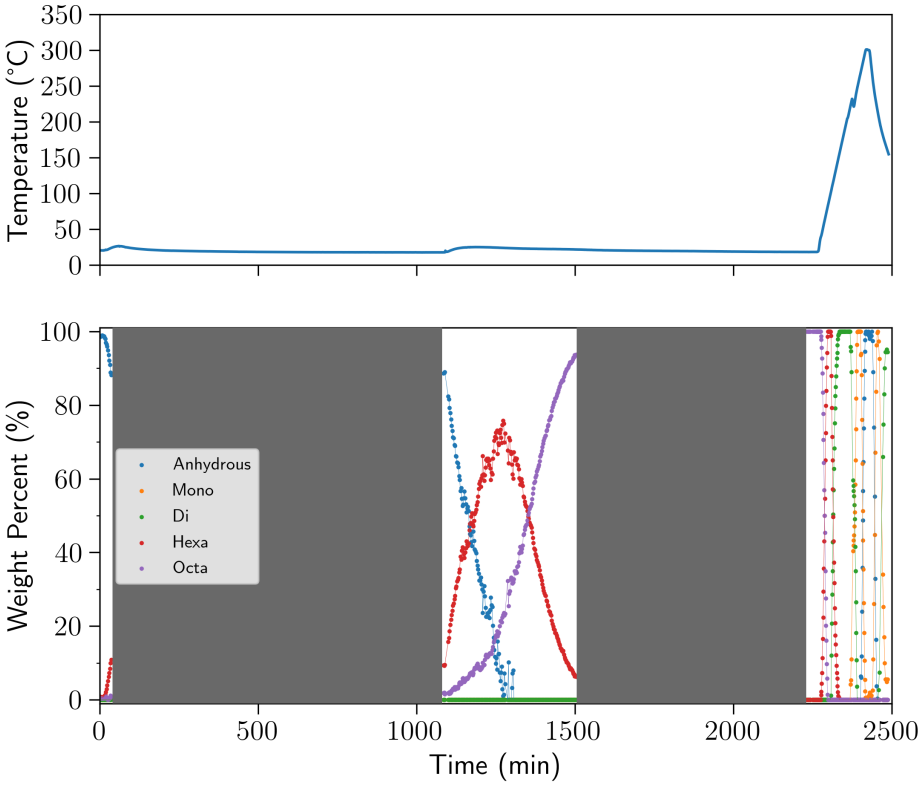


Figure A.9: Weight percent of phases in the $CaBr_2$ PND data.

Appendix B

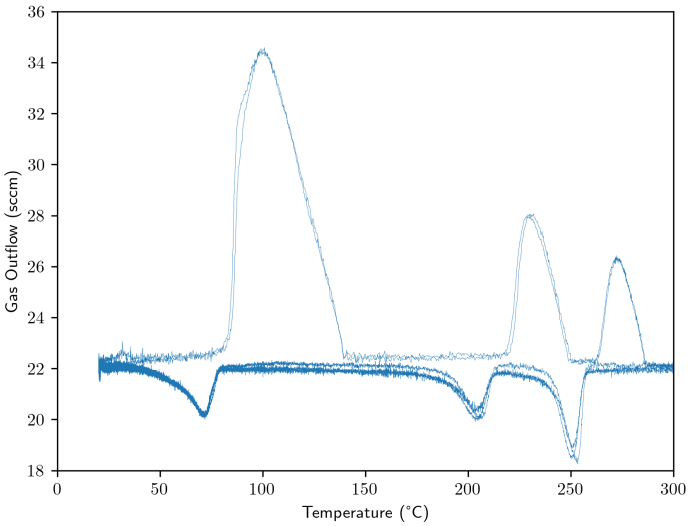


Figure B.1: Gas outflow during temperature cycling of $x = 0$ sample under 1 bar flowing NH_3.

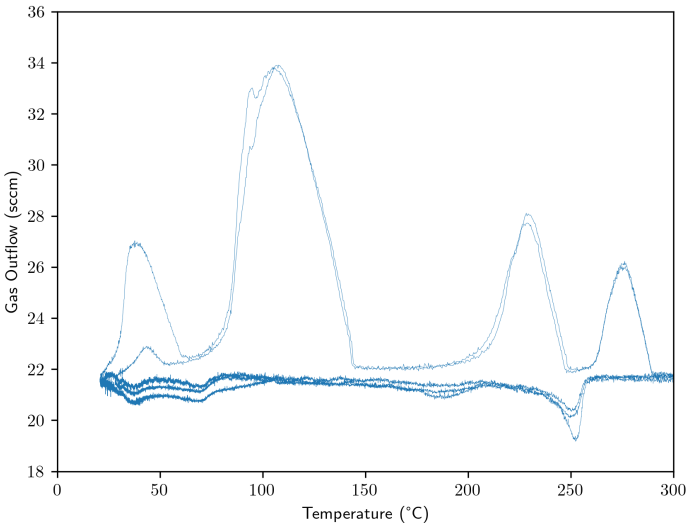


Figure B.2: Gas outflow during temperature cycling of $x = 0.2$ sample under 1 bar flowing NH_3.

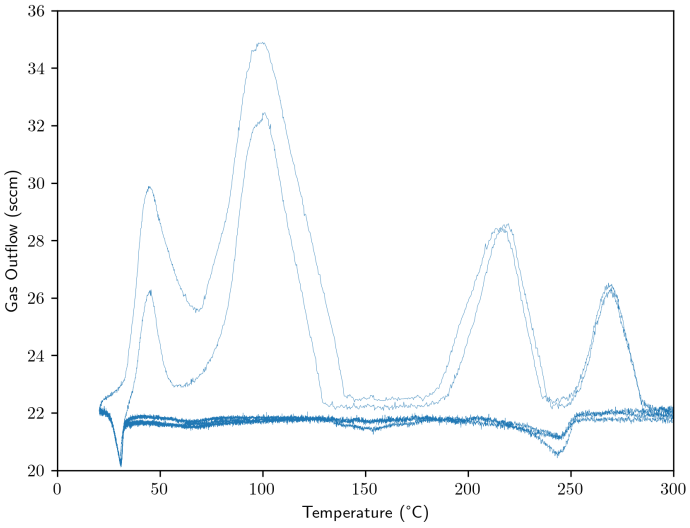


Figure B.3: Gas outflow during temperature cycling of $x = 0.4$ sample under 1 bar flowing NH_3.

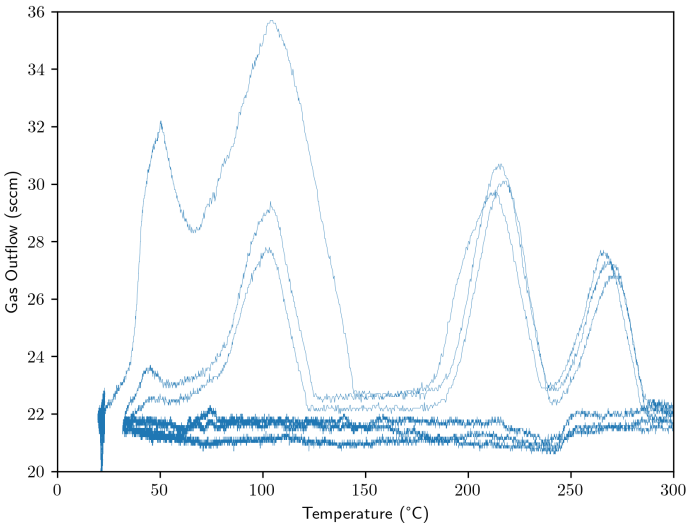


Figure B.4: Gas outflow during temperature cycling of $x = 0.6$ sample under 1 bar flowing NH_3.

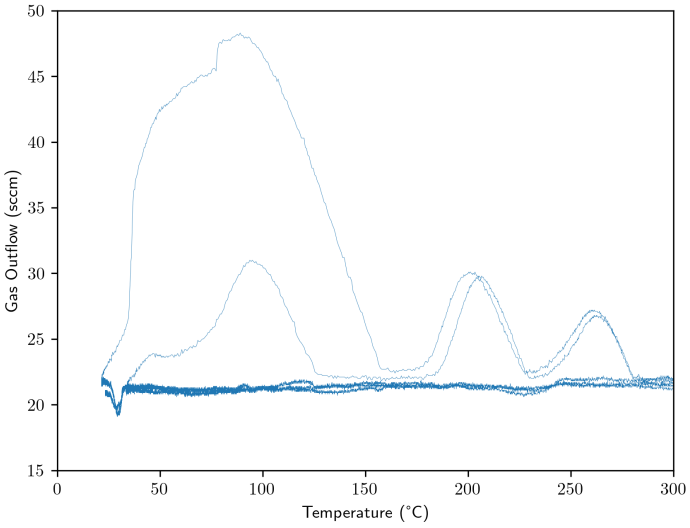


Figure B.5: Gas outflow during temperature cycling of $x = 0.8$ sample under 1 bar flowing NH_3.

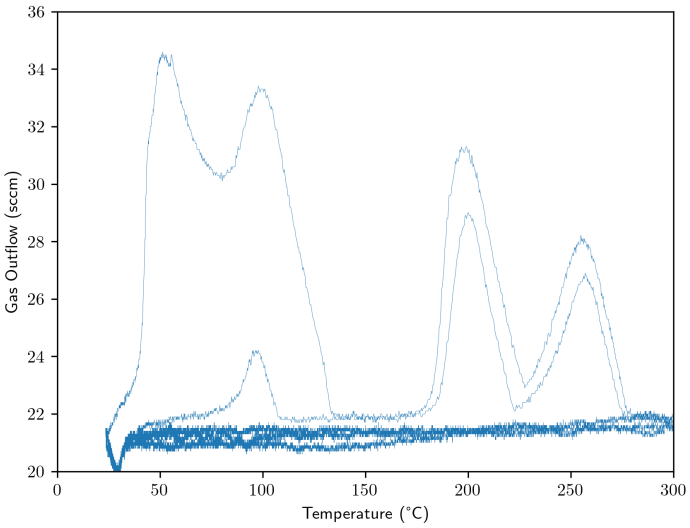


Figure B.6: Gas outflow during temperature cycling of $x = 1$ sample under 1 bar flowing NH_3.

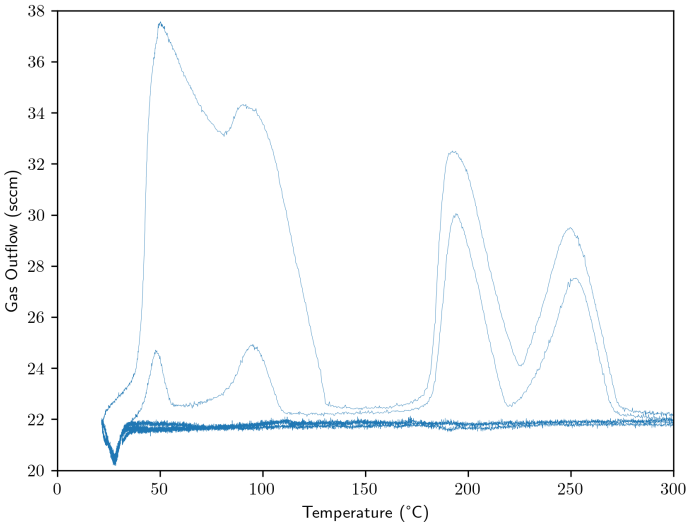


Figure B.7: Gas outflow during temperature cycling of $x = 1.2$ sample under 1 bar flowing NH_3.

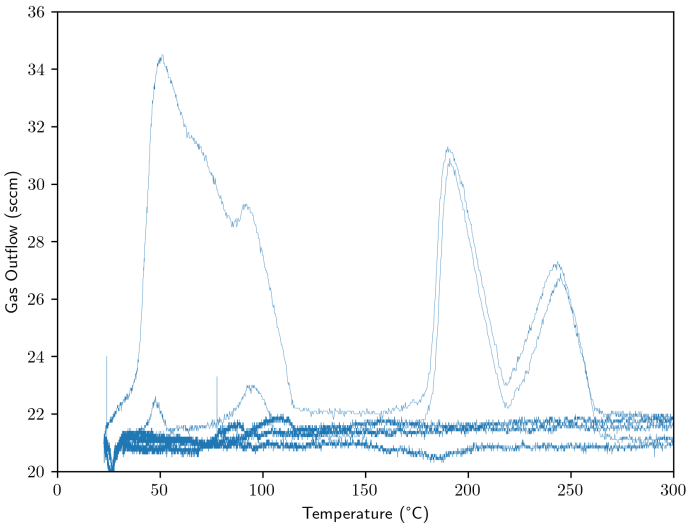


Figure B.8: Gas outflow during temperature cycling of $x = 1.4$ sample under 1 bar flowing NH_3.

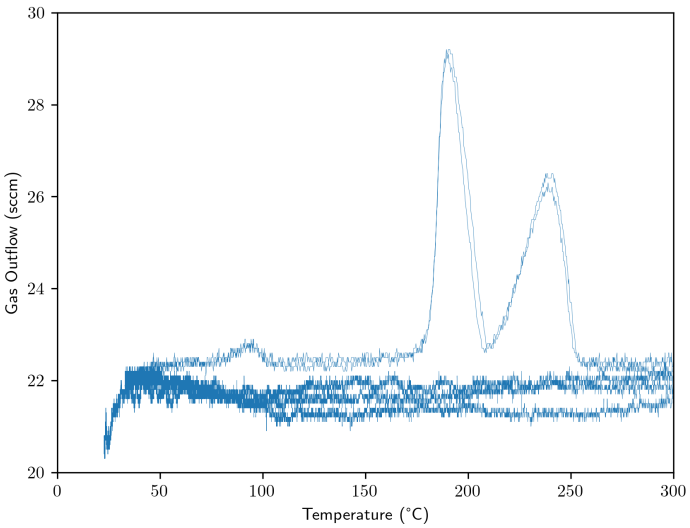


Figure B.9: Gas outflow during temperature cycling of $x = 1.6$ sample under 1 bar flowing NH_3.

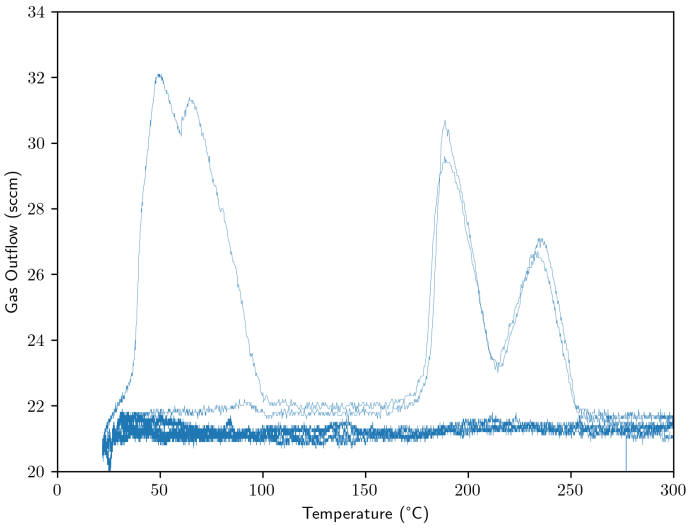


Figure B.10: Gas outflow during temperature cycling of $x = 1.8$ sample under 1 bar flowing NH_3.

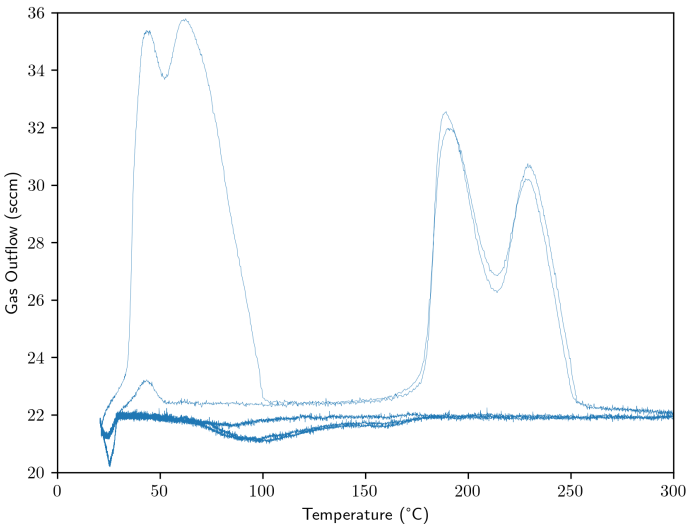


Figure B.11: Gas outflow during temperature cycling of $x = 2$ sample under 1 bar flowing NH_3.

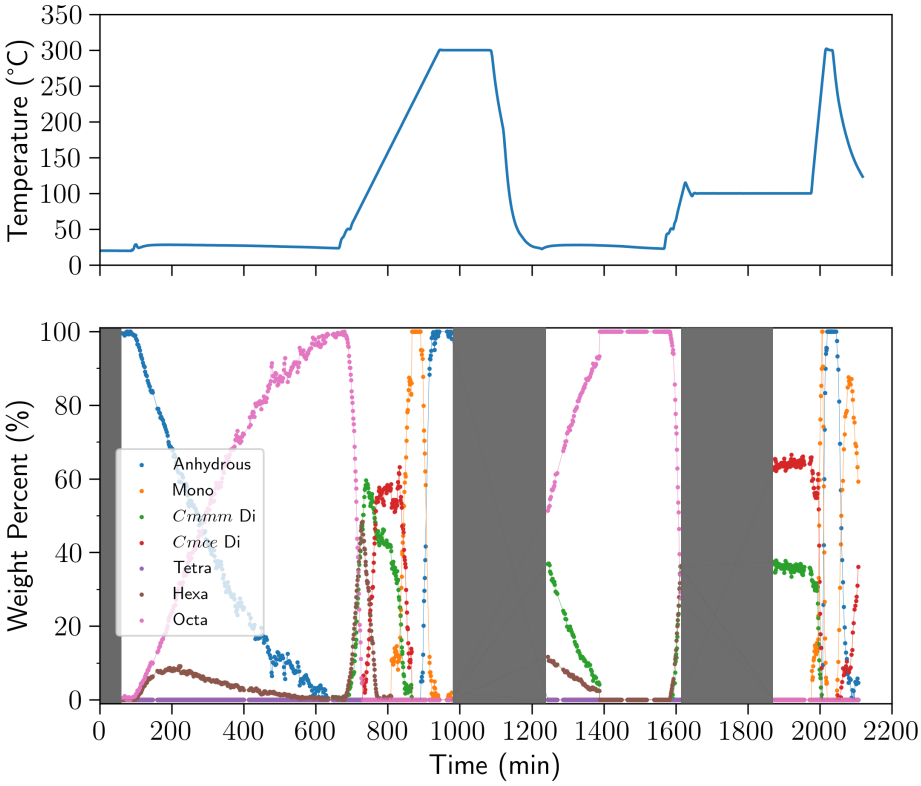


Figure B.12: Weight percent of phases in the CaClBr PND data.

Appendix C

Selected limits of Equation 6.7. These limits exemplify the simple cases where the Hess cycle is dominated by one reaction.

$$\lim_{\gamma_1 \to \infty} \left[\frac{T_{\text{fus}}(1 + \gamma_1 - \gamma_2)}{1 + \frac{T_{\text{fus}}}{T_{\text{des, s}}}\gamma_1 - \frac{T_{\text{fus}}}{T_{\text{fus, amm}}}\gamma_2} \right] = T_{\text{des, s}} \tag{3}$$

$$\lim_{\gamma_2 \to \infty} \left[\frac{T_{\text{fus}}(1 + \gamma_1 - \gamma_2)}{1 + \frac{T_{\text{fus}}}{T_{\text{des, s}}}\gamma_1 - \frac{T_{\text{fus}}}{T_{\text{fus, amm}}}\gamma_2} \right] = T_{\text{fus, amm}} \tag{4}$$

$$\lim_{\gamma_1, \gamma_2 \to 0} \left[\frac{T_{\text{fus}}(1 + \gamma_1 - \gamma_2)}{1 + \frac{T_{\text{fus}}}{T_{\text{des, s}}}\gamma_1 - \frac{T_{\text{fus}}}{T_{\text{fus, amm}}}\gamma_2} \right] = T_{\text{fus}} \tag{5}$$

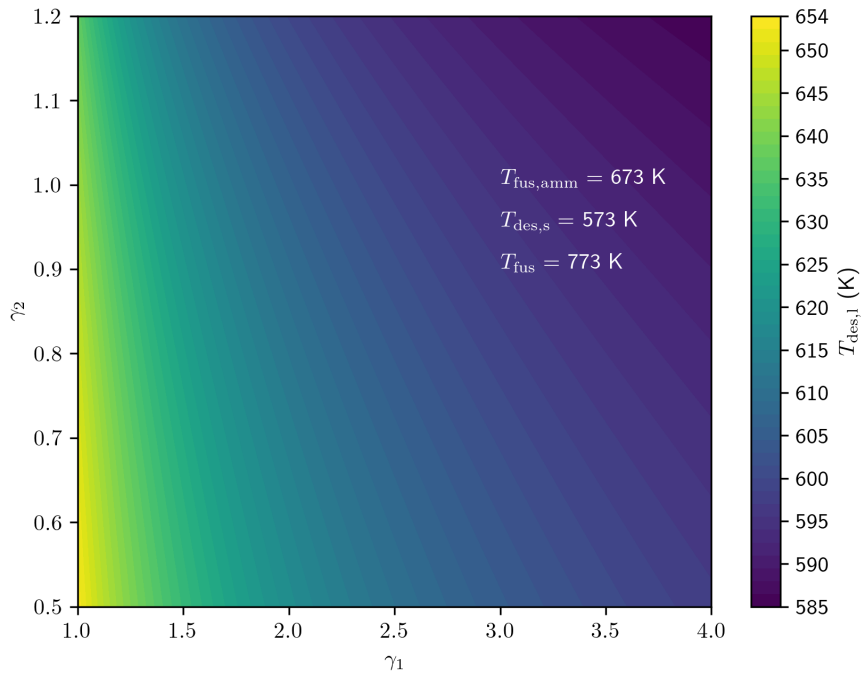


Figure C.1: Colour Map showing $T_{\text{des, l}}$ values as a function of γ_1 and γ_2 for selected $T_{\text{des, s}}$, $T_{\text{fus, amm}}$ and T_{fus} values. Values were chosen to further illustrate the observation that $T_{\text{des, l}} > T_{\text{des, s}}$ when $T_{\text{fus, amm}} < T_{\text{fus}}$, for all reasonable values of γ_1 and γ_2.

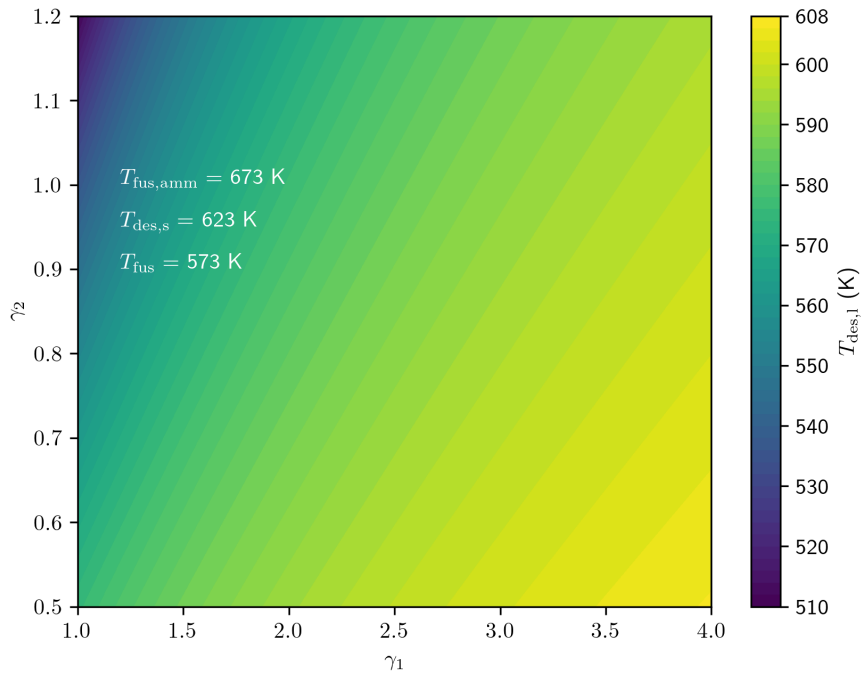


Figure C.2: Colour Map showing $T_{\text{des, l}}$ values as a function of γ_1 and γ_2 for selected $T_{\text{des, s}}$, $T_{\text{fus, amm}}$ and T_{fus} values. Values were chosen to further illustrate the observation that $T_{\text{des, l}} < T_{\text{des, s}}$ when $T_{\text{fus, amm}} > T_{\text{fus}}$, for all reasonable values of γ_1 and γ_2.

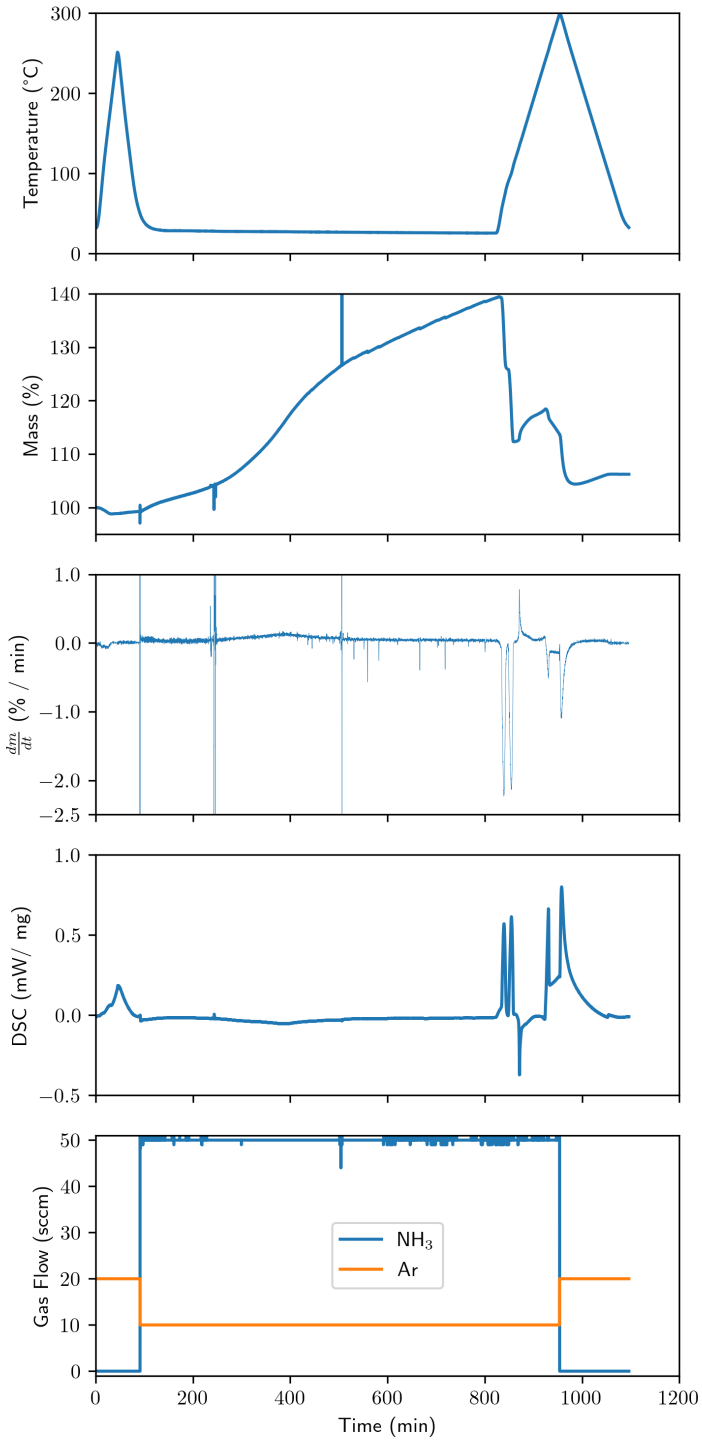


Figure C.3: Ammonia absorption and desorption of $ZnCl_2$, recorded through STA data at an ammonia pressure of 0.83 bar.

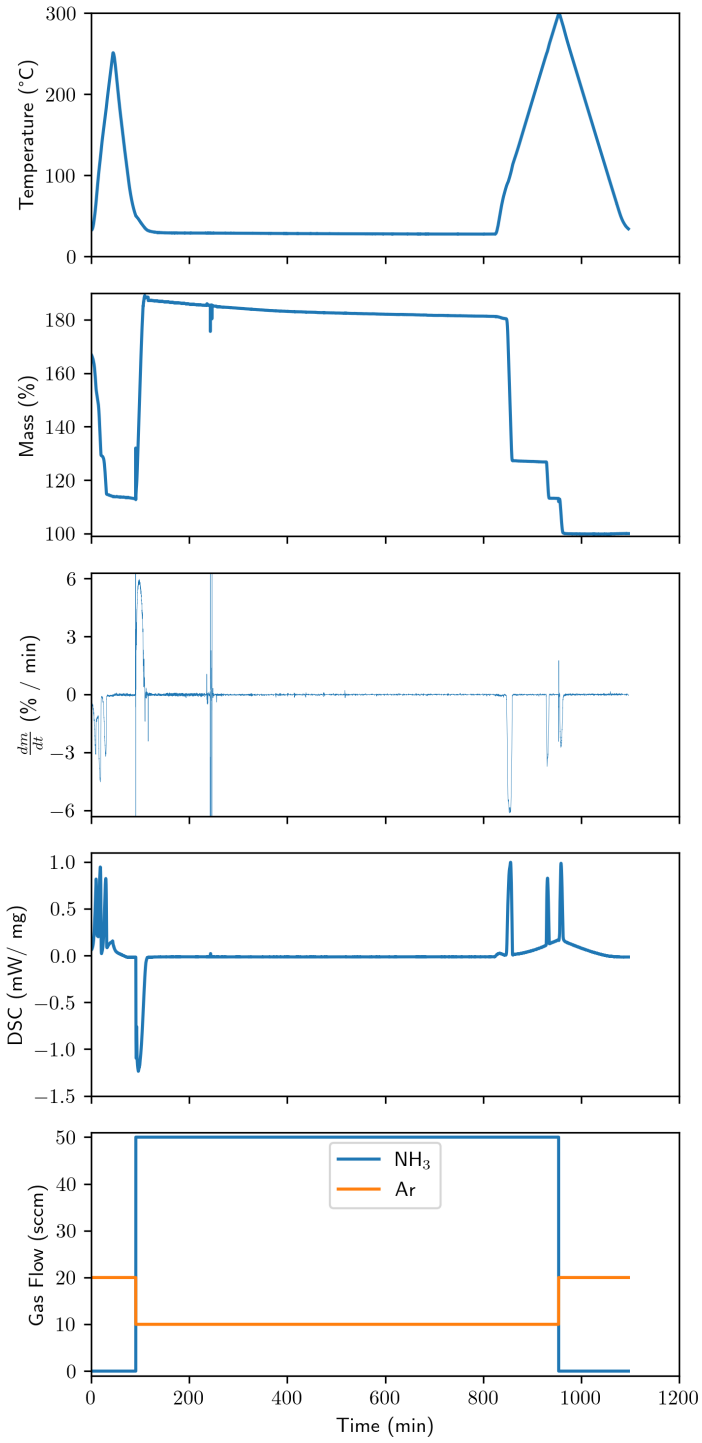


Figure C.4: Ammonia absorption and desorption of $MnCl_2$, recorded through STA data at an ammonia pressure of 0.83 bar.

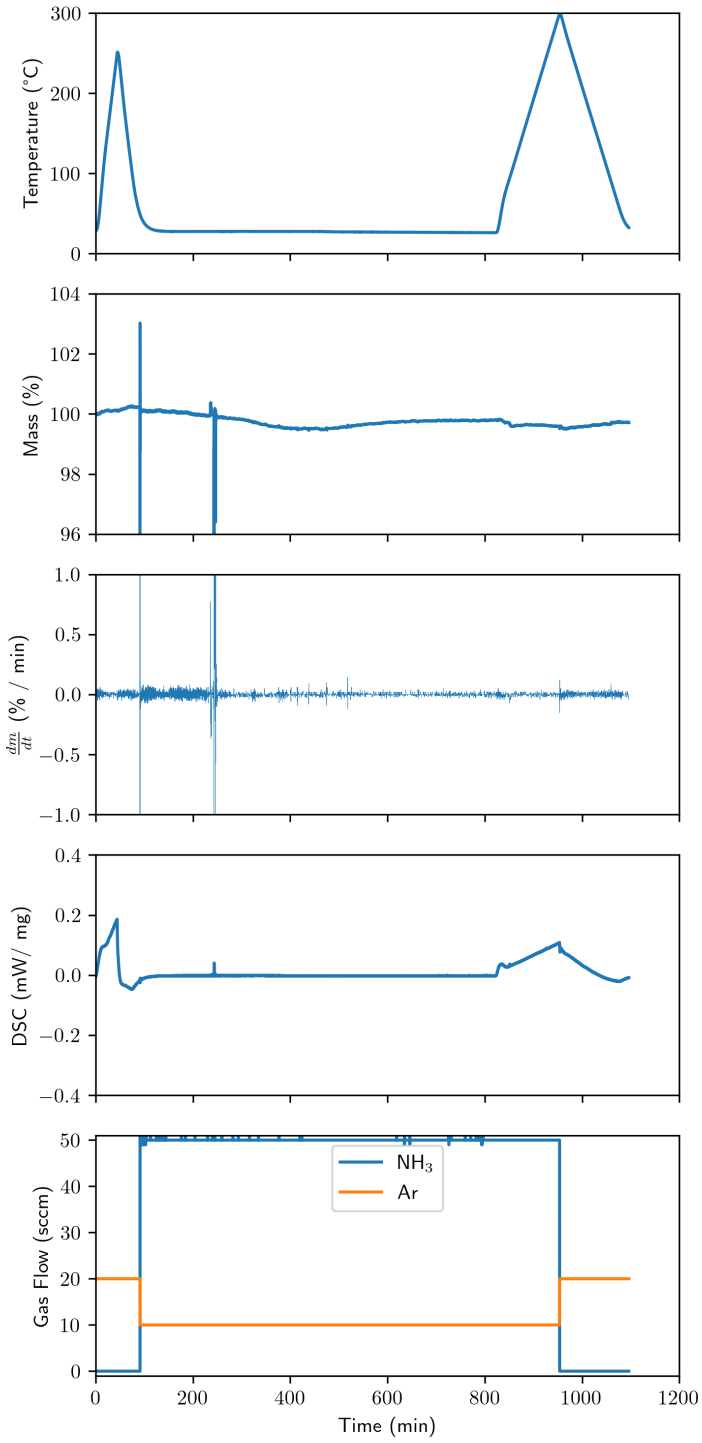


Figure C.5: Ammonia absorption and desorption of NaCl, recorded through STA data at an ammonia pressure of 0.83 bar.

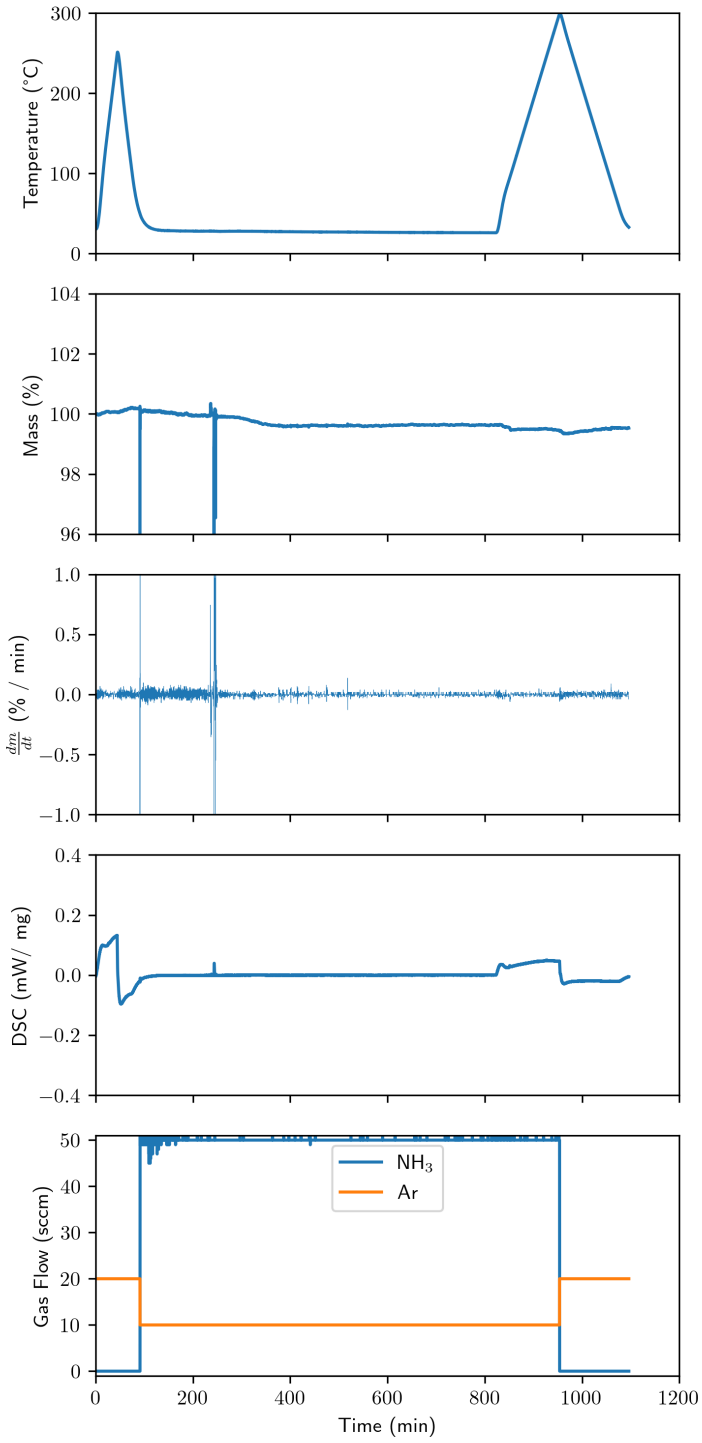


Figure C.6: Ammonia absorption and desorption of KCl, recorded through STA data at an ammonia pressure of 0.83 bar.

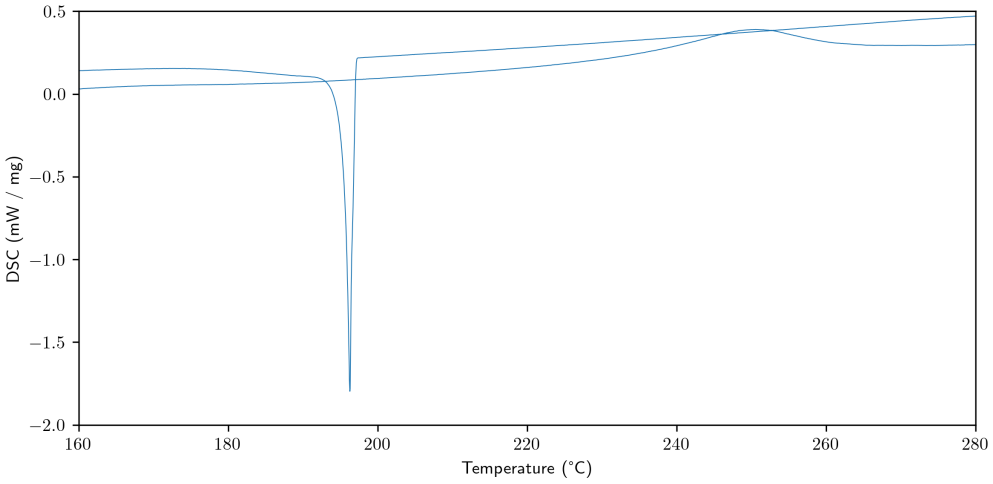


Figure C.7: 60:40 Zn : Na chloride melting point calculation using temperature ramping under an argon atmosphere on the STA. Note the hysteresis (∼50 °C) between solidification and melting.

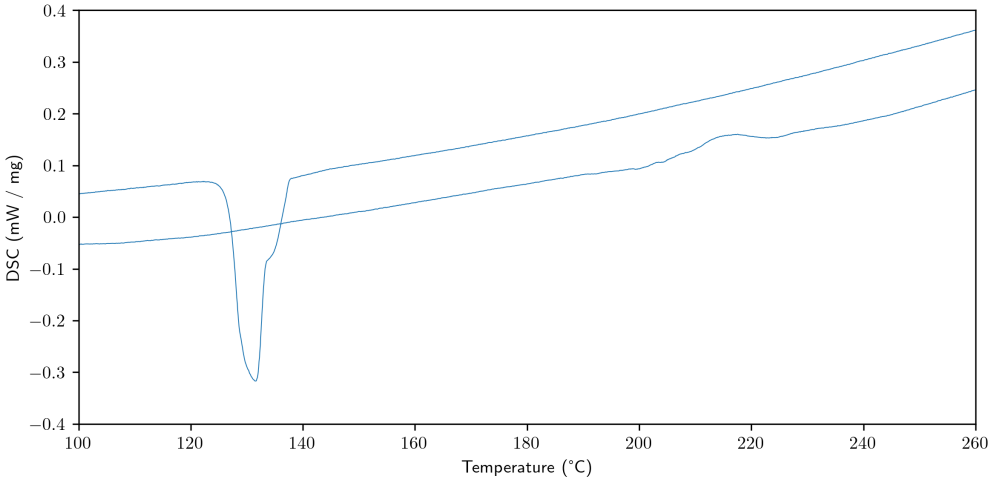


Figure C.8: 60:40 Zn : K chloride melting point calculation using temperature ramping under an argon atmosphere on the STA. Note the hysteresis (∼80 °C) between solidification and melting.

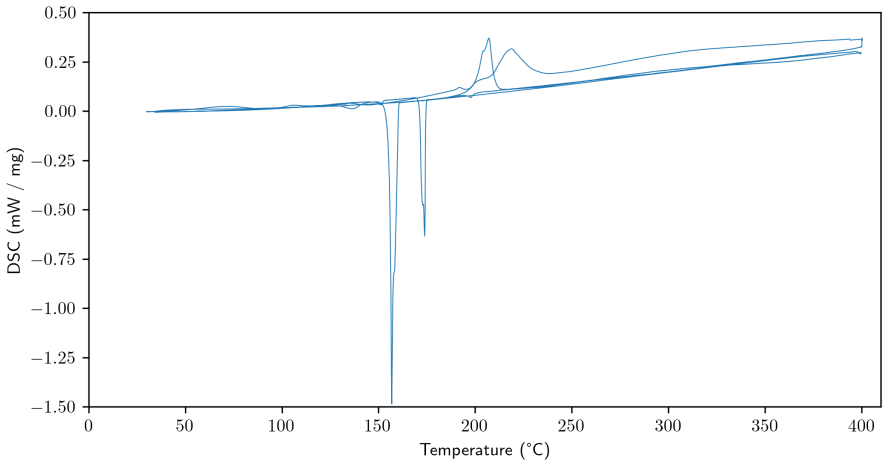


Figure C.9: 60:20:20 Zn : Na : K chloride melting point calculation using temperature ramping under an argon atmosphere on the STA. The difference in melting temperatures between the first and second cycle is likely due to better mixing of different cations after solidification, thus lowering the kinetic barrier to melting. However, it is unclear why different solidification temperatures are seen for each cycle.

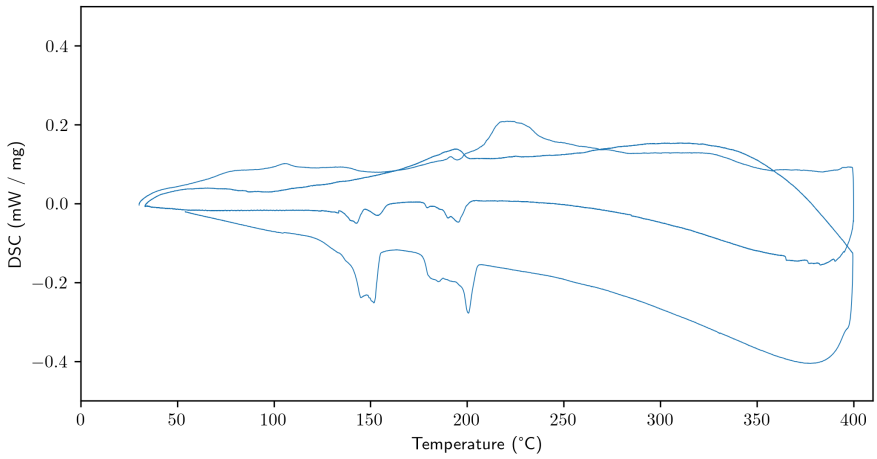


Figure C.10: 70:15:15 Zn : Na : K chloride melting point calculation using temperature ramping under an argon atmosphere on the STA. The difference in melting temperatures between the first and second cycle is likely due to better mixing of different cations after solidification, thus lowering the kinetic barrier to melting.

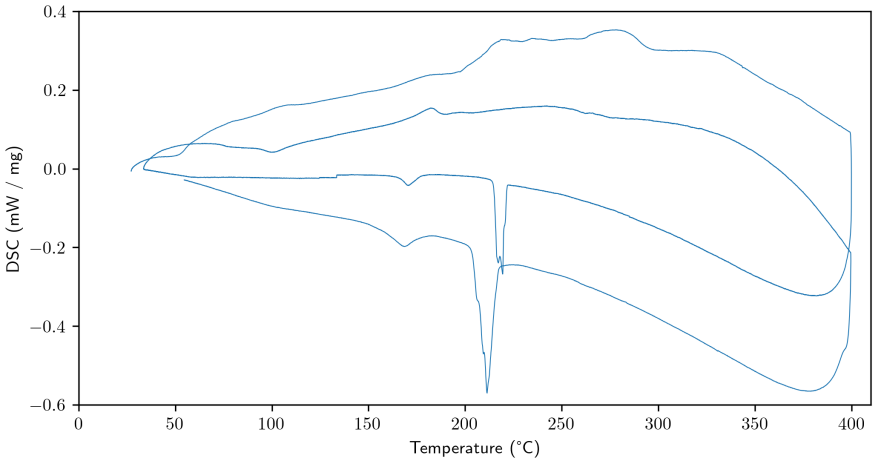


Figure C.11: 80:10:10 Zn : Na : K chloride melting point calculation using temperature ramping under an argon atmosphere on the STA. The difference in melting temperatures between the first and second cycle is likely due to better mixing of different cations after solidification, thus lowering the kinetic barrier to melting.

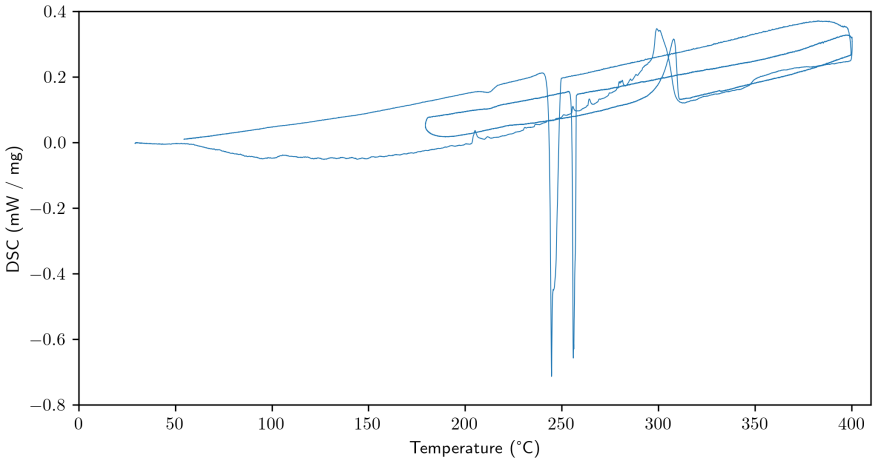


Figure C.12: Zinc chloride melting point calculation using temperature ramping under an argon atmosphere on the STA.

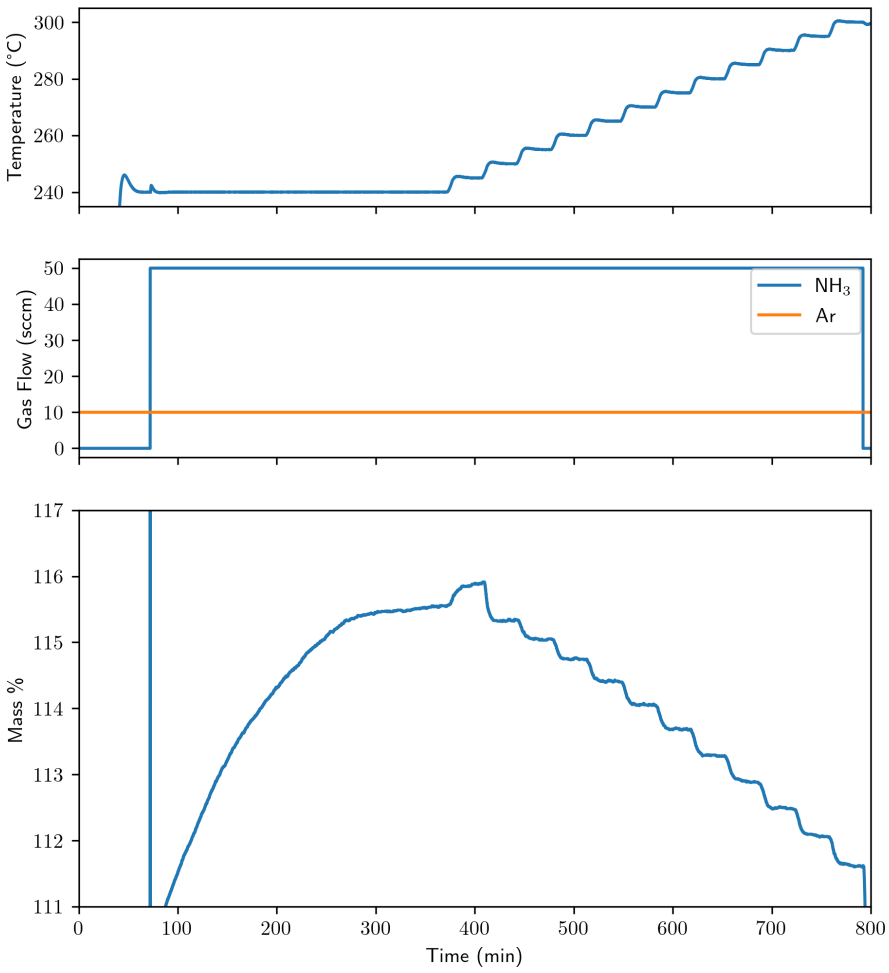


Figure C.13: NH_3 absorption as a function of temperature for the 60:40 Zn : Na chloride sample.

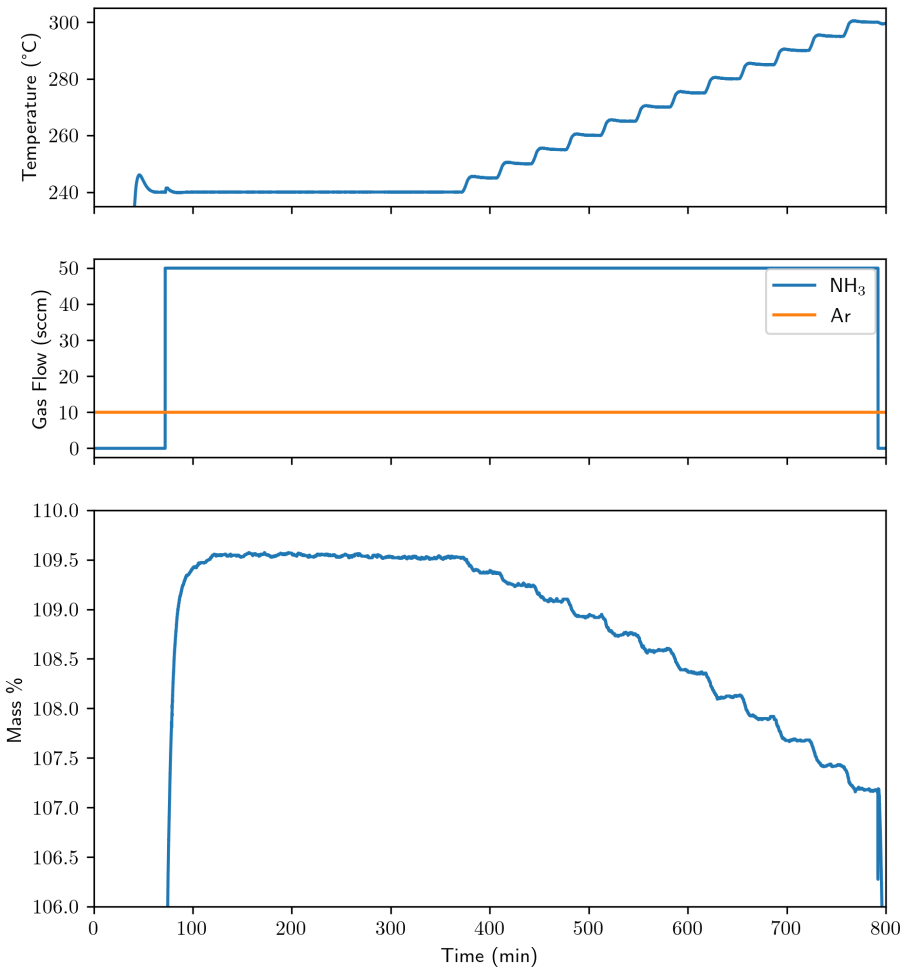


Figure C.14: NH_3 absorption as a function of temperature for the 60:40 Zn : K chloride sample.

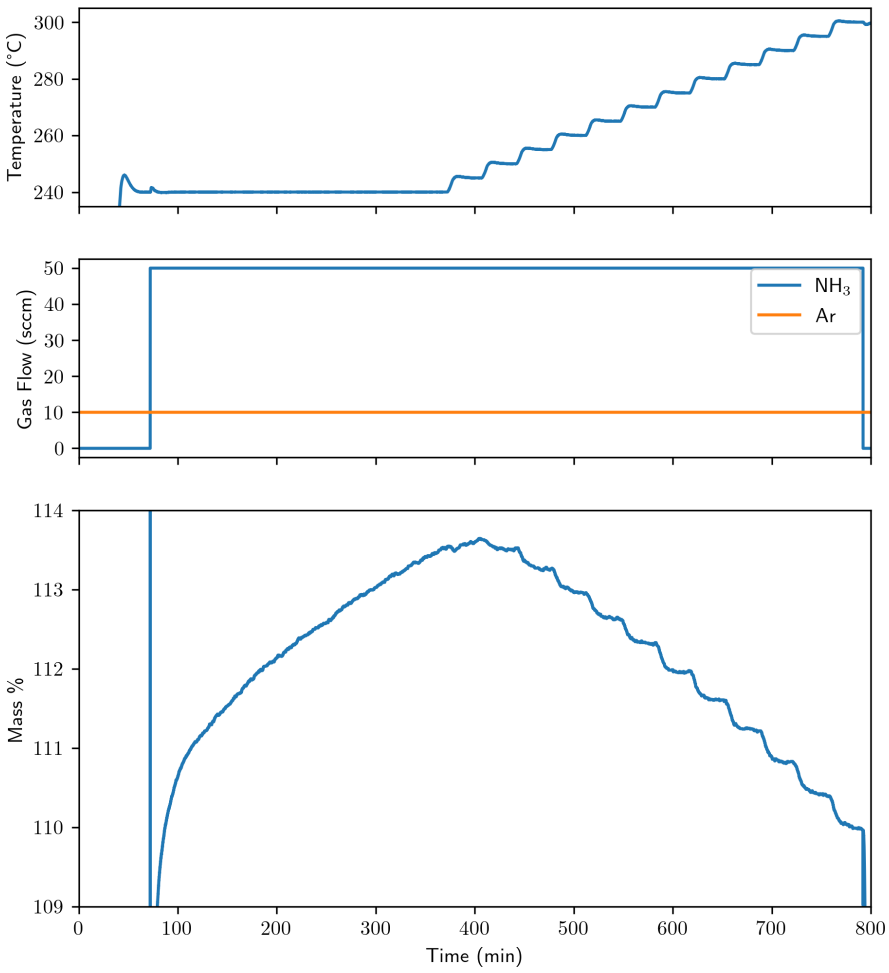


Figure C.15: NH_3 absorption as a function of temperature for the 60:20:20 Zn : Na : K chloride sample.

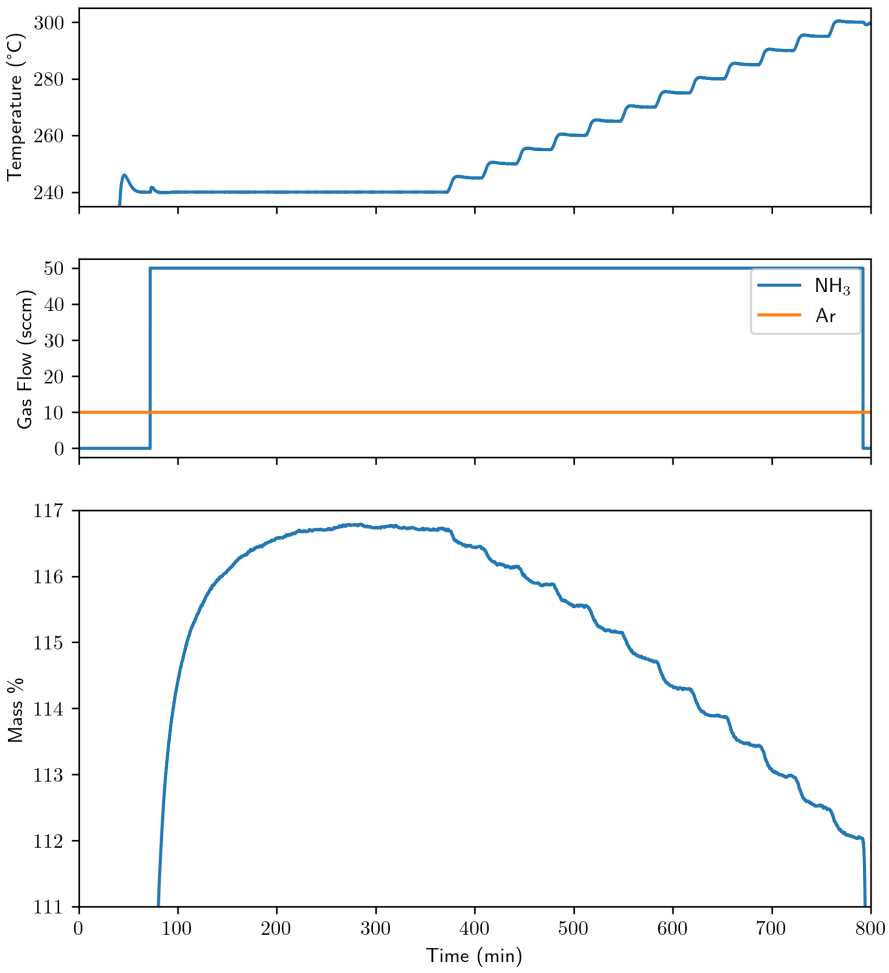


Figure C.16: NH_3 absorption as a function of temperature for the 70:15:15 Zn : Na : K chloride sample.

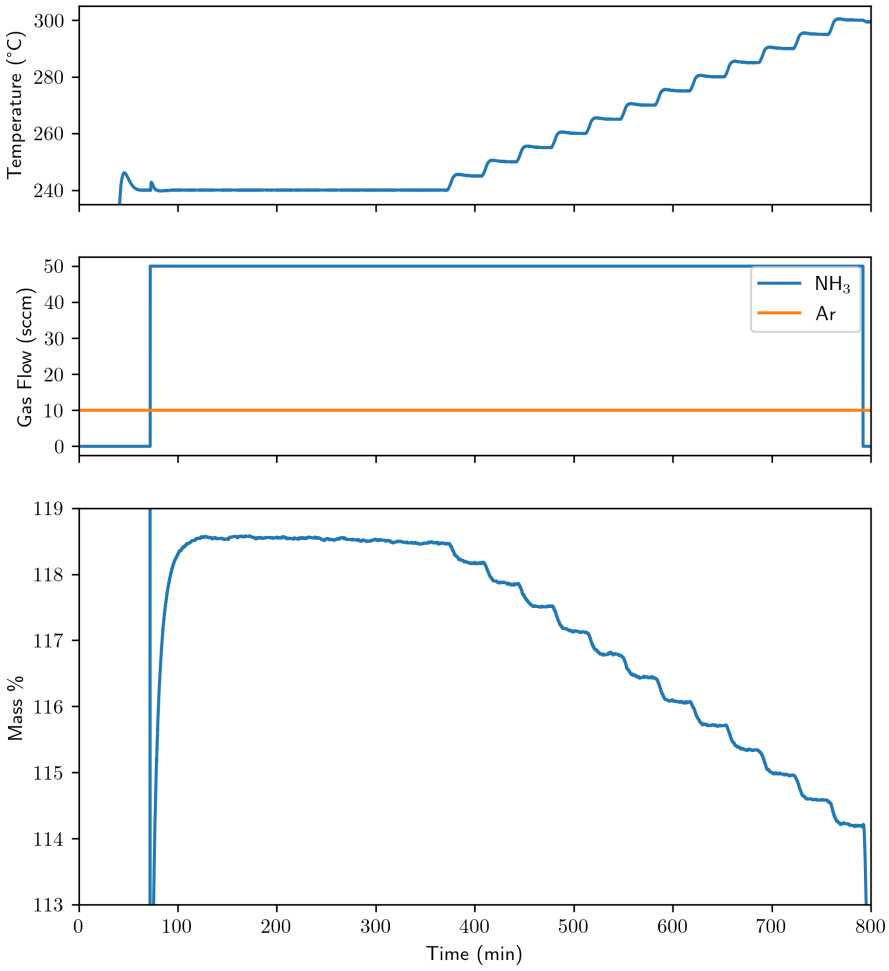


Figure C.17: NH_3 absorption as a function of temperature for the 80:10:10 Zn : Na : K chloride sample.

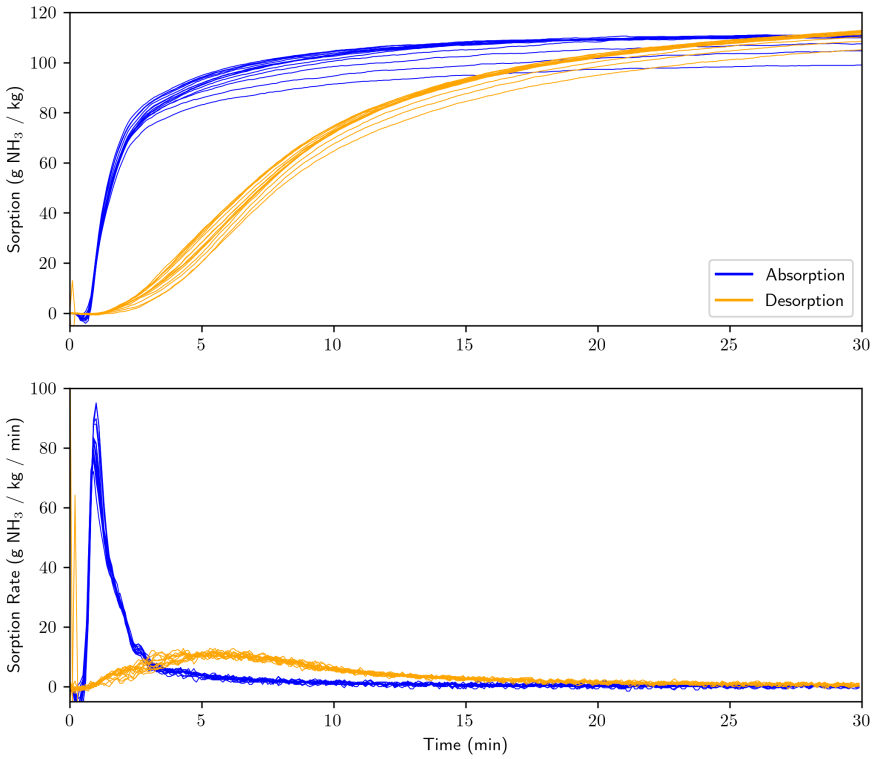


Figure C.18: PSA cycling data for 60:40 Zn : Na chloride at 300 °C and 0–0.83 bar NH_3. t = 0 refers to the switching on/off of ammonia gas flow. There is a slight delay before significant absorption/desorption occurs as the atmosphere is not immediately replaced.

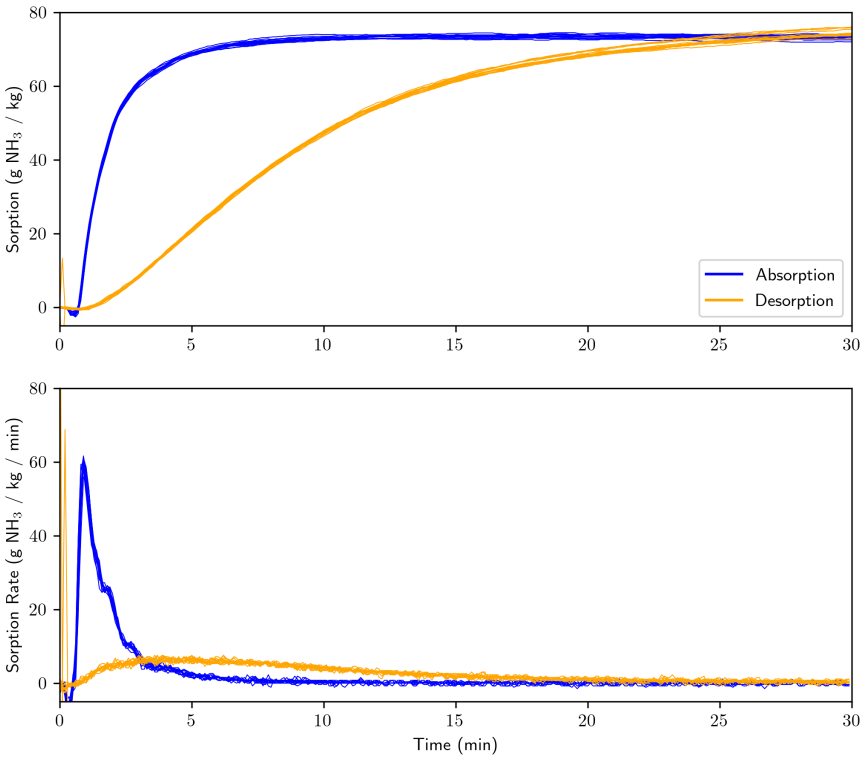


Figure C.19: PSA cycling data for 60:40 Zn : K chloride at 300 °C and 0–0.83 bar NH_3. t = 0 refers to the switching on/off of ammonia gas flow. There is a slight delay before significant absorption/desorption occurs as the atmosphere is not immediately replaced.

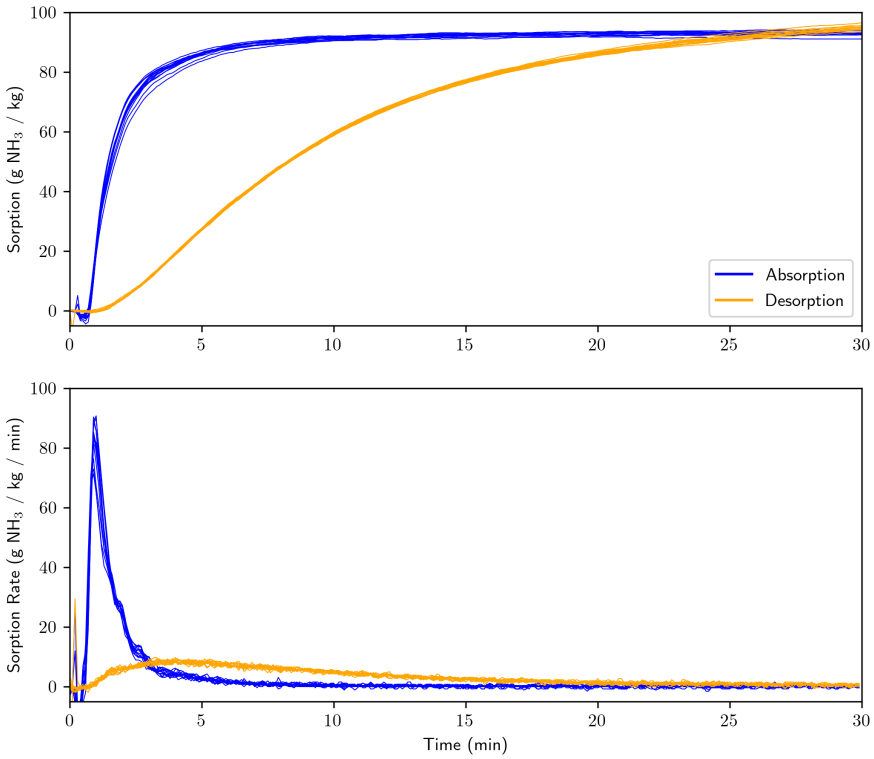


Figure C.20: PSA cycling data for 60:20:20 Zn : Na : K chloride at 300 °C and 0–0.83 bar NH_3. t = 0 refers to the switching on/off of ammonia gas flow. There is a slight delay before significant absorption/desorption occurs as the atmosphere is not immediately replaced.

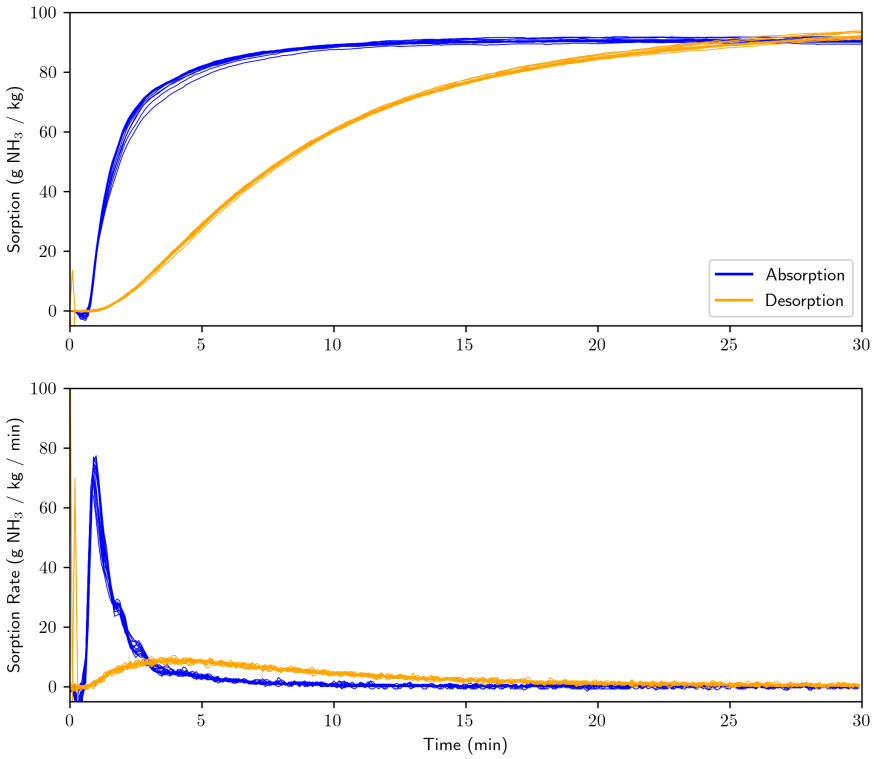


Figure C.21: PSA cycling data for 70:15:15 Zn : Na : K chloride at 300 °C and 0–0.83 bar NH_3. t = 0 refers to the switching on/off of ammonia gas flow. There is a slight delay before significant absorption/desorption occurs as the atmosphere is not immediately replaced.

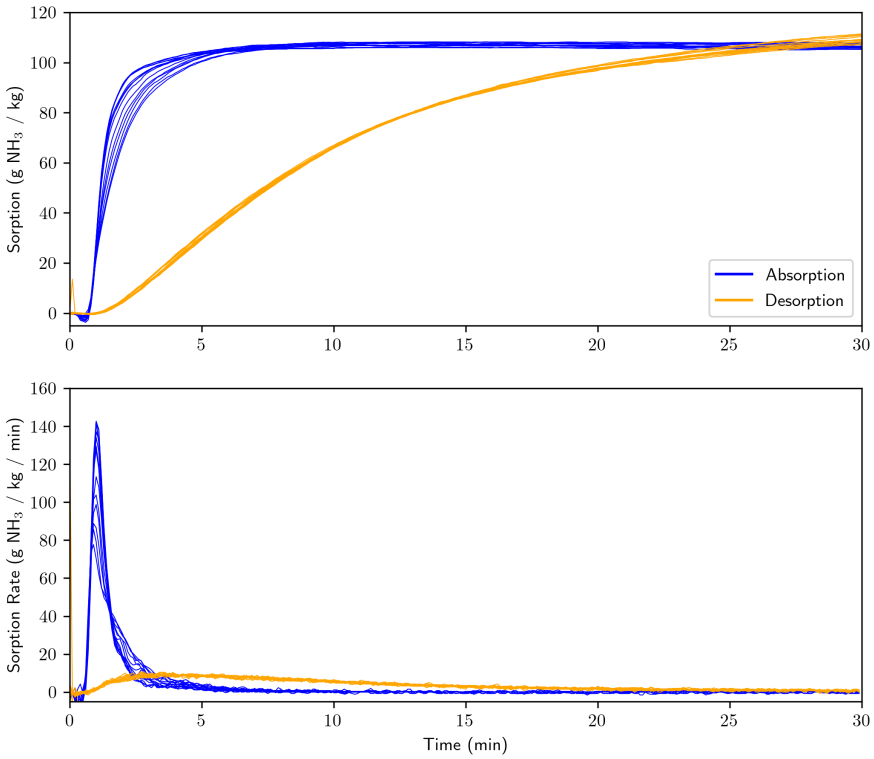


Figure C.22: PSA cycling data for 80:10:10 Zn : Na : K chloride at 300 °C and 0–0.83 bar NH_3. t = 0 refers to the switching on/off of ammonia gas flow. There is a slight delay before significant absorption/desorption occurs as the atmosphere is not immediately replaced.

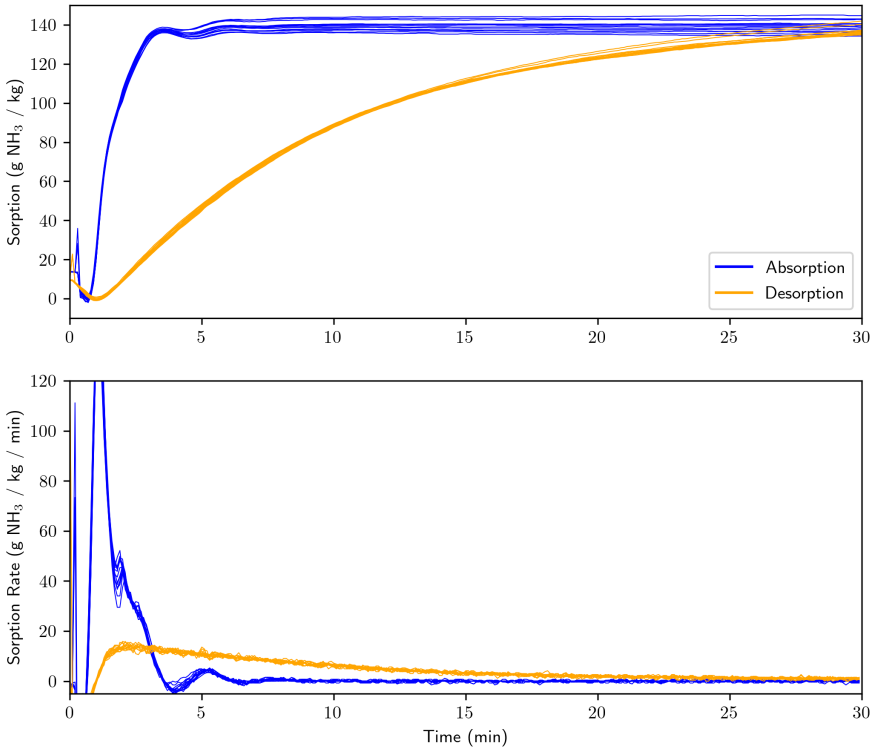


Figure C.23: PSA cycling data for $ZnCl_2$ at 300 °C and 0–0.83 bar NH_3. t = 0 refers to the switching on/off of ammonia gas flow. There is a slight delay before significant absorption/desorption occurs as the atmosphere is not immediately replaced. The data shown is simply a conversion from the raw data. In the raw data, the change in gas flow rate caused a step-shift in the mass reading. This has been corrected for in all presented data, but is the origin of the negative sorption rates immediately after the change in gas flow.

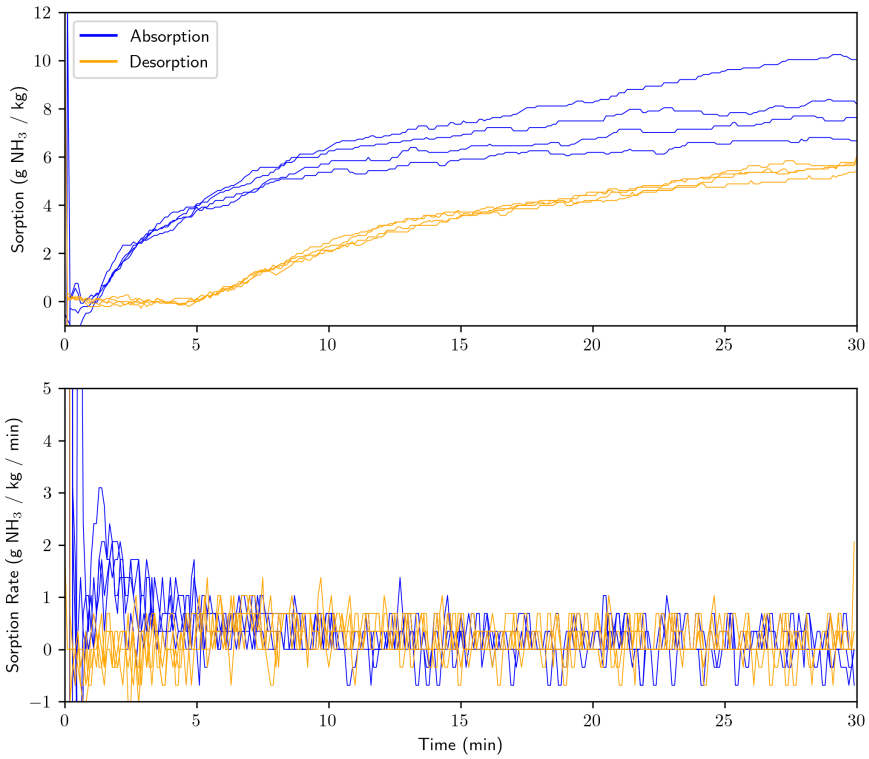


Figure C.24: PSA cycling data for $MnCl_2$ at 300 °C and 0–0.83 bar NH_3. t = 0 refers to the switching on/off of ammonia gas flow. There is a slight delay before significant absorption/desorption occurs as the atmosphere is not immediately replaced.

Appendix D

Table D.1: The ammoniate structures studied for each cation-anion pair in group I. Some cation-anion pairs were not studied in certain ammoniate structures due to the incompatibility of the coordination environments.

		$LiBr(NH_3)$ [166]	$LiI(NH_3)$ [166]	NH_4F [167]	NH_4Cl [168]	$LiBr(NH_3)_4$ [169]
Coordination Number (NH_3 + X^-)		4	4	2	2	4
H	F					
	Cl					
	Br					
	I					
Li	F					
	Cl					
	Br					
	I					
Na	F					
	Cl					
	Br					
	I					

Table D.2: The ammoniate structures studied for each cation-anion pair in group II/XII. Some cation-anion pairs were not studied in certain ammoniate structures due to the incompatibility of the coordination environments.

		Pnnm $CaBr_2(NH_3)$	*Cmc*2_1 $CaBr_2(NH_3)$	$SrCl_2(NH_3)$ [170]	$NiCl_2(NH_3)$ [171]	$BeBr_2(NH_3)_2$ [96]	$CaCl_2(NH_3)_2/MgCl_2(NH_3)_2$ [101]	$MgBr_2(NH_3)_2$ [101]	$CaBr_2(NH_3)_2$	$CaCl_2(NH_3)_4$	$BeCl_2(NH_3)_4$ [96]	$CaBr_2(NH_3)_6$ [122]	$CaCl_2(NH_3)_8$ [122]
Coordination Number ($NH_3 + X^-$)		6	6	7	6	4	6	6	6	6	4	6	8
Be	F												
	Cl												
	Br												
	I												
Mg	F												
	Cl												
	Br												
	I												
Zn	F												
	Cl												
	Br												
	I												
Ca	F												
	Cl												
	Br												
	I												
Sr	F												
	Cl												
	Br												
	I												
Ba	F												
	Cl												
	Br												
	I												

Table D.3: The ammoniate structures studied for each cation-anion pair in group III/XIII. Some cation-anion pairs were not studied in certain ammoniate structures due to the incompatibility of the coordination environments. It should be noted that the $AlCl_3(NH_3)_2$ structure consists of $AlCl_2(NH_3)_4^+$ octahedra and $AlCl_4^-$ tetrahedra. Similarly, the $AlCl_3(NH_3)_3$ structure consists of $AlCl_2(NH_3)_4^+$ octahedra and $AlCl_4(NH_3)_2^-$ octahedra.

		$AlCl_3(NH_3)$ [172]	$AlBr_3(NH_3)$ [173]	$AlI_3(NH_3)$ [173]	$ScCl_3(NH_3)$ [174]	$AlF_3(NH_3)_2$ [99]	$AlCl_3(NH_3)_2$ [175]	$ScCl_3(NH_3)_2$ [174]	$AlCl_3(NH_3)_3$ [176]	$AlCl_3(NH_3)_5$ [177]
Coordination Number (NH_3 + X^-)		4	4	4	6	6	4/6	6	6	6
Al	F									
	Cl									
	Br									
	I									
Sc	F									
	Cl									
	Br									
	I									
Y	F									
	Cl									
	Br									
	I									
Lu	F									
	Cl									
	Br									
	I									

Table D.4: The ammoniate structures studied for each cation-anion pair in group IV. Some cation-anion pairs were not studied in certain ammoniate structures due to the incompatibility of the coordination environments.

		$ZrF_4(NH_3)$ [100]	$TiCl_4(NH_3)_4$ [178]
Coordination Number (NH_3 + X^-)		8	6
Ti	F		
	Cl		
	Br		
	I		
Zr	F		
	Cl		
	Br		
	I		
Hf	F		
	Cl		
	Br		
	I		